

# Identification and Modeling of Coherent Structures in Swirl-Stabilized Combustors at Dry and Steam-Diluted Conditions

vorgelegt von  
Diplom-Ingenieur  
Steffen Terhaar  
aus Bad Oldesloe

Von der Fakultät V – Verkehrs- und Maschinensysteme  
der Technischen Universität Berlin  
zur Erlangung des akademischen Grades

Doktor der Ingenieurwissenschaften  
– Dr.-Ing. –

genehmigte Dissertation

Vorsitzender: Prof. Dr.-Ing. Robert Luckner  
Gutachter: Prof. Dr.-Ing. Christian Oliver Paschereit  
Gutachter: Prof. Dr.-Ing. Ephraim J. Gutmark  
Gutachter: Dr.-Ing. Kilian Oberleithner

Tag der wissenschaftlichen Aussprache: 16. Februar 2015

Berlin 2015  
D83



## Vorwort

Diese Arbeit entstand während meiner Tätigkeit als wissenschaftlicher Mitarbeiter am Fachgebiet für Experimentelle Strömungsmechanik der TU Berlin im Rahmen des von der EU mit einem ERC Advanced Grant geförderten Projektes GREENEST.

Mein aufrichtiger Dank gilt meinem Doktorvater Christian Oliver Paschereit: Sie haben mir ermöglicht, in diesem interessanten Projekt mitzuarbeiten und es zuletzt auch zu leiten. Ich habe dabei viel von Ihnen gelernt. Ihr großes Vertrauen in meine Arbeit, Ihr toller Führungsstil und die Freiheiten, die Sie mir ließen, um meine Ideen zu verwirklichen, waren wichtige Gründe, warum ich immer motiviert und mit viel Freude bei Ihnen gearbeitet habe.

Ephraim J. Gutmark, ich danke Ihnen für die Begutachtung meiner Arbeit. Es ist mir eine große Ehre, dass Sie sich dazu bereit erklärt haben.

Ein großer Dank gilt Kilian Oberleithner: Mit Deinem tiefen Verständnis für die Physik hinter den experimentellen Beobachtungen und Deiner Fähigkeit und Bereitschaft, Dein Wissen mit mir zu teilen, hast Du diese Arbeit erst ermöglicht. Es war und ist mir eine große Freude mit Dir zusammen zu arbeiten.

Für die Hilfe bei der Vorbereitung und Durchführung von vielen langen und teilweise nervenaufreibenden Messkampagnen möchte ich mich bei den Mitarbeitern der Werkstatt und bei Andy Göhrs bedanken. Andy, Du hast mich regelmäßig mit deiner Schnelligkeit, Präzision und Kreativität auch bei den herausforderndsten Arbeiten begeistert. Nicht zuletzt möchte ich auch Heiko Stolpe und meinen Studenten Eduard Höschele, Finn Lückoff und David Borgmann danken. Ohne sie wären die Messkampagnen nicht möglich gewesen. Den Mitarbeiterinnen des Sekretariats und der IT möchte ich für ihre Hilfsbereitschaft und Flexibilität danken. Vielen Dank, Lilli Lindemann, Kristin Halboth, Sandy Meinecke, Maria Lück, Dagmar Pölkow und Angela Pätzold.

Meinen Kollegen bin ich dankbar für die tolle Gemeinschaft: Eure Hilfsbereitschaft hat sich nicht zuletzt durch Eure spontane Unterstützung beim Korrekturlesen dieser Arbeit gezeigt. Ein Dank dafür an Bernhard Bobusch, Bernhard Ćosić, Oliver Krüger, Eric Bach, Panagiotis Stathopoulos, Juliane Wendler, Georg Mensah, Joshua Gray, Moritz Sieber, Phoebe Kuhn, Thoralf Reichel, Lothar Rukes, Sebastian Niether, Christoph Strangfeld, Dominik Wassmer, Sebastian Schimek und Katharina Göckeler. Auch meinen Freunden Matthis Thorade und Kai Loftfield danke ich für ihre Anmerkungen zu dieser Arbeit. Weiterhin möchte ich mich bei meinen Kollegen aus der „Nassen Verbrennung“ für die tolle Zusammenarbeit bedanken. Ich hatte immer große Freude an unseren „Wet Combustion Meetings“.

Für den richtigen Ausgleich zur wissenschaftlichen Arbeit danke ich vor allem Oliver Krüger, Bernhard Bobusch, Bernhard Ćosić und Karsten Liesner. Ich habe mich immer auf unsere oft epischen Duelle am Kickertisch gefreut.

Mit einer Träne im Knopfloch realisiere ich, dass die Jahre, die ich mit meinen Kollegen und Freunden Bernhard Bobusch, Oliver Krüger und Bernhard Ćosić im Büro verbracht habe, zu

Ende sind. Unsere gemeinsame Zeit im CONFET wird immer etwas Besonderes für mich bleiben.

Jupp, Heide, Felix, Janneke und Teresa, ich danke Euch für Eure Liebe, Eure Unterstützung und Euer Vertrauen in mich.



## Zusammenfassung

Gasturbinen sind die Schlüsseltechnologie für eine Sicherstellung der zuverlässigen Stromversorgung, wenn große Teile des Stroms aus fluktuierenden erneuerbaren Energieformen stammen. Um zukünftige Anforderungen, wie Effizienzsteigerungen, Schadstoffreduktionen, schnelle Regelzeiten und Treibstoffflexibilität zu erreichen, werden neue Verbrennungskonzepte wie die *Ultra-Nasse* Verbrennung benötigt. Bei diesem Konzept wird die Wärme des Abgasstrahls genutzt, um Wasserdampf zu erzeugen, der in die Brennkammer eingedüst wird, um die Effizienz zu erhöhen und die Emissionen zu verringern. Dampfzugabe und Brennstoffflexibilität führen zu einer großen Variation der Reaktivität des zu verbrennenden Gemisches und in der Konsequenz zu verschiedenen Flammenformen und Strömungsfeldern in der Brennkammer.

In der vorliegenden Arbeit wird das Strömungsfeld in drallstabilisierten Gasturbinenbrennkammern experimentell und analytisch untersucht. Der Fokus der Arbeit ist auf das Auftreten und die Modellierung von großskaligen kohärenten Strömungsstrukturen und deren Auswirkungen auf die Verbrennung gerichtet. In den ersten Kapiteln dieser Arbeit wird eine bekannte selbsterregte helikale kohärente Strömungsstruktur, der sogenannte präzessierende Wirbelkern (*precessing vortex core*, PVC) untersucht. Es wird gezeigt, dass das Auftreten des PVC eng mit der Flammenform verbunden ist. Die hohe praktische Relevanz des PVC wird durch seinen Einfluss auf Mischungsvorgänge, Flammenoszillationen und die Flammenstabilisierung verdeutlicht. Die Analyse der hydrodynamischen Stabilität der gemittelten Strömungsfelder ermöglicht die Modellierung des PVC und die Identifikation der Schlüsselparameter, die die Anfachung oder Unterdrückung des PVC bestimmen. Auf Basis der Modellierung können weiterhin Kontrollmechanismen entwickelt werden, um den PVC gezielt zu beeinflussen.

Bei der zweiten Form von kohärenten Strukturen, die im Rahmen dieser Arbeit untersucht werden, handelt es sich um achsensymmetrische Ringwirbel. Die Wirbel werden durch eine Kopplung der Flamme mit der Systemakustik angeregt, interagieren mit der Flamme und können thermoakustische Instabilitäten verbunden mit starken Druckschwankungen hervorrufen. In einer experimentellen und analytischen Untersuchung wird das lineare und nicht-lineare Anfachen der Wirbel in den Scherschichten des Strömungsfeldes bestimmt und modelliert. Die Ergebnisse zeigen die Relevanz eines neuartigen Sättigungsmechanismus für die Ringwirbel und damit auch für thermoakustische Instabilitäten.

Basierend auf den vorherigen Ergebnissen wird im letzten Teil der Arbeit die Interaktion der selbsterregten helikalen kohärenten Struktur (PVC) und der Ringwirbel untersucht. Die Experimente zeigen einen starken Einfluss der Ringwirbel auf den PVC. Die Interaktionsmechanismen werden unter Berücksichtigung der hydrodynamischen Stabilität der Strömungsfelder identifiziert und für eine Modellbildung genutzt. Die Modellbildung erlaubt ein tiefergehendes Verständnis der experimentell beobachteten Phänomene.



## *Abstract*

Gas turbines are the key technology for the backup of fluctuating renewable electrical energy sources. Future requirements are low pollutant emissions, high cycle efficiencies at fast start-up and turn-down times, and increased fuel flexibility. Advanced cycles, such as the ultra-wet cycle, are developed to fulfill these requirements, but at the same time impose new challenges to the gas turbine combustor design. In the ultra-wet cycle, steam is produced from the hot exhaust gases and is injected into the combustion process. Thereby, the cycle efficiency is increased and the pollutant emissions are significantly reduced. However, the addition of steam to the combustion further increases the range of reactivities of the fuel–air–steam mixture. This leads to a multitude of different flame shapes in the combustor with different flow fields and flow field dynamics.

In the present thesis the flow fields and flow field dynamics of swirl-stabilized combustors are experimentally investigated and analytically modeled. The focus is placed on the occurrence of large-scale coherent flow structures and their impact on the combustion process. In the first chapters of this thesis, a well-known helical, self-excited coherent flow structure, denoted as the precessing vortex core (PVC), is assessed. Its occurrence is shown to be linked to different flame shapes, which are demonstrated to strongly depend on the reactivity of the fuel–air–steam mixture. The importance of the PVC for flame fluctuations, mixing processes, and the flame stabilization is experimentally demonstrated. In an analytical study employing linear hydrodynamic stability analysis, the PVC is modeled and the key parameters for its excitation and suppression are identified. Furthermore, the modeling allows for the identification of control strategies for the suppression of the PVC by small flow field modifications.

The second type of coherent flow structures investigated in this thesis are axisymmetric, ring-shaped vortices that are excited by the coupling of the flame with the acoustics of the combustion system. This coupling can lead to dangerous high amplitude acoustic pressure oscillations and heat release fluctuations, called thermoacoustic instabilities. One key driver for the flame oscillations is the interaction of the flame with these axisymmetric vortical coherent flow structures. In an experimental and analytical study, the growth of these vortical structures in the linear and non-linear regime is investigated and their important role for the flame oscillation is pointed out. Furthermore, the analytical study reveals an important and new saturation mechanism for the vortical structures and, thus, for the thermoacoustic instabilities.

Finally, the interaction of both types of coherent structures is analyzed. The experiments reveal a strong influence of the axisymmetric structures on the PVC. Employing the same analytical tools as in the previous parts, the mechanisms for the influence are identified and a simple model analogy is presented, which features the most important dynamics and allows for a better insight into the interaction mechanisms.



# Contents

<b>Vorwort</b>	<b>iii</b>
<b>Zusammenfassung</b>	<b>v</b>
<b>Abstract</b>	<b>vii</b>
<b>List of Figures</b>	<b>xiii</b>
<b>Nomenclature</b>	<b>xix</b>
<b>1 Introduction</b>	<b>1</b>
1.1 Motivation . . . . .	1
1.2 Swirl-Stabilized Combustion . . . . .	4
1.3 Coherent Structures in Swirl-Stabilized Combustors . . . . .	7
1.3.1 Helical Coherent Structures: The Precessing Vortex Core . . . . .	8
1.3.2 Axisymmetric Coherent Structures . . . . .	10
1.4 Overview of the Thesis . . . . .	12
<b>2 Theory and Methods</b>	<b>15</b>
2.1 The Precessing Vortex Core as a Global Mode . . . . .	15
2.2 Triple Decomposition . . . . .	18
2.3 Empirical Mode Construction Using Proper Orthogonal Decomposition . . . . .	19
2.4 Physical Mode Construction Using Local Linear Stability Theory . . . . .	20
2.4.1 Theory . . . . .	21
2.4.2 Numerical Implementation and Procedure . . . . .	25
2.5 Data Treatment . . . . .	30
2.5.1 Spatial Averaging . . . . .	30
2.5.2 Phase Averaging of Data Using POD . . . . .	31
2.5.3 Spectra and POD of Symmetric and Antisymmetric Fluctuations . . . . .	32
2.5.4 Flow Field Filtering Employing POD . . . . .	34
<b>3 Experimental Approach</b>	<b>37</b>
3.1 Swirl-Stabilized Combustors . . . . .	37
3.2 Test Rigs . . . . .	38
3.2.1 Water Tunnel Test Rig . . . . .	39
3.2.2 Combustion Test Rigs . . . . .	40

3.3	Measurement Techniques . . . . .	42
3.3.1	Velocity Field Measurements . . . . .	42
3.3.2	Density Estimation . . . . .	44
3.3.3	Heat Release Measurements . . . . .	47
<b>4</b>	<b>Flame Shapes, Flow Fields, and the PVC at Isothermal and Reacting Conditions</b>	<b>51</b>
4.1	Introduction . . . . .	52
4.2	Experimental Procedure . . . . .	53
4.3	Flow Field Topology . . . . .	53
4.4	Classification of Flame Shapes . . . . .	54
4.5	Identification of Coherent Structures . . . . .	60
4.6	Influence of the PVC on the Mixing of the Emanating Jet with the IRZ . . .	65
4.7	Heat Release Fluctuations Caused by the PVC . . . . .	67
4.8	Conclusions . . . . .	69
<b>5</b>	<b>Control of the Vortex Breakdown Type and the PVC with Axial Injection</b>	<b>73</b>
5.1	Introduction . . . . .	73
5.2	Experimental and Numerical Procedure . . . . .	75
5.3	Time-Averaged Flow Fields . . . . .	77
5.4	Classification of Vortex Breakdown Types . . . . .	81
5.5	Identification of the PVC . . . . .	82
5.6	Classification of the PVC . . . . .	87
5.7	Conclusions . . . . .	88
<b>6</b>	<b>Analysis of the Excitation and Suppression Mechanism of the PVC</b>	<b>91</b>
6.1	Introduction . . . . .	92
6.2	Analysis of the Effect of Axial Injection on the PVC . . . . .	94
6.2.1	Local Stability Properties . . . . .	94
6.2.2	Global Stability Properties . . . . .	96
6.2.3	Summary . . . . .	97
6.3	Analysis of the Effect of Combustion and Different Flame Shapes on the PVC	98
6.3.1	Local Stability Properties . . . . .	99
6.3.2	Global Stability Properties . . . . .	101
6.3.3	Comparison to Bi-Global Linear Stability Analysis . . . . .	105
6.3.4	Summary . . . . .	107
6.4	Identification of the Key Parameters Governing the Excitation and Suppression of the PVC . . . . .	108
6.4.1	Parametric Model Profiles . . . . .	108
6.4.2	Results of the Parametric Study . . . . .	110
6.4.3	Summary . . . . .	112
6.5	Conclusions . . . . .	113
<b>7</b>	<b>The Role of the PVC for Flame Shape Transitions</b>	<b>115</b>
7.1	Introduction . . . . .	115
7.2	Experimental Procedure . . . . .	116
7.3	Extraction of the Instantaneous Flame Shape and the Coherent Structures . .	117

7.4	Time-Series Investigation of the Flame Shape Transitions . . . . .	121
7.4.1	Detachment of the Flame . . . . .	121
7.4.2	Attachment of the Flame . . . . .	124
7.5	Transition and Hysteresis Mechanism . . . . .	127
7.6	Conclusions . . . . .	130
<b>8</b>	<b>Axisymmetric Coherent Structures and their Impact on the Flame Response</b>	<b>131</b>
8.1	Introduction . . . . .	132
8.2	Experimental and Analytical Procedure . . . . .	135
8.3	Results . . . . .	138
8.3.1	Flame Response . . . . .	138
8.3.2	Time-Averaged Flow Fields and Flame Positions . . . . .	139
8.3.3	Coherent Structures in the Forced Flow Fields . . . . .	139
8.3.4	Linear Stability Analysis . . . . .	143
8.4	Conclusions . . . . .	145
<b>9</b>	<b>Interaction of Axisymmetric Coherent Structures with the PVC</b>	<b>147</b>
9.1	Introduction . . . . .	147
9.2	Experimental and Analytical Procedure . . . . .	149
9.3	Experimental Observations . . . . .	151
9.3.1	Time-Averaged Flow Fields and Flow Field Dynamics without Acoustic Forcing . . . . .	152
9.3.2	Time-Averaged Flow Fields with Acoustic Forcing . . . . .	154
9.3.3	Flow Field Dynamics with Acoustic Forcing . . . . .	156
9.4	Influence of Axial Forcing on the Stability of the Flow Fields . . . . .	162
9.4.1	Suppression of the PVC in the Isothermal Cases and the Detached Flame Cases . . . . .	163
9.4.2	Excitation of the PVC in the Attached V-Flame Cases . . . . .	166
9.5	Analogy of the Acoustically Forced PVC to a Parametric Oscillator . . . . .	168
9.5.1	Motivation by Phase-Averaged Stability Calculations . . . . .	168
9.5.2	Dynamics of the Parametric Van der Pol Oscillator . . . . .	171
9.6	Conclusions . . . . .	173
	<b>Summary and Concluding Remarks</b>	<b>175</b>
<b>A</b>	<b>Influence of the Outlet Boundary Conditions on the Reacting Flow Field</b>	<b>179</b>
A.1	Introduction . . . . .	179
A.2	Experimental Procedure . . . . .	182
A.3	Concept of an effective swirl number . . . . .	183
A.4	Results . . . . .	184
A.4.1	Isothermal Flow Field . . . . .	184
A.4.2	Reacting Flow Field . . . . .	185
A.4.3	Effect of outlet area contraction on the reacting flow field . . . . .	187
A.4.4	Parametric study . . . . .	188
A.5	Discussion . . . . .	191
A.6	Conclusions . . . . .	194

**Bibliography****197**



# List of Figures

1.1	Temporal fluctuation of the electric energy demand and production in Germany.	2
1.2	Schematic of the ultra-wet gas turbine cycle. . . . .	2
1.3	NO <sub>x</sub> emissions at dry and steam-diluted conditions. . . . .	3
1.4	Industrial swirl-stabilized burners. . . . .	5
1.5	Combustor flow field at increasing swirl intensities. . . . .	5
1.6	Swirl-stabilized flame in the combustor test rig. . . . .	6
1.7	Visualization of the PVC in a crosswise plane near the combustor inlet. . . .	8
1.8	Visualization of the PVC in a streamwise plane. . . . .	9
1.9	Three-dimensional visualization of the PVC. . . . .	10
1.10	Flame oscillation caused by axisymmetric coherent structures. . . . .	11
1.11	Overview of the results chapters of this thesis. . . . .	12
2.1	Schematic of global stability and global instability. . . . .	17
2.2	Example of global flow instability: The von Kármán vortex street. . . . .	17
2.3	Schematic representation of absolute and convective instability. . . . .	18
2.4	Convergence study of the spatial linear stability analysis. . . . .	26
2.5	Flow field and flow profile for the exemplarily presented stability analysis. . .	26
2.6	Eigenvalue spectrum of the temporal stability analysis. . . . .	27
2.7	Growth rate and frequency of the identified eigenmode. . . . .	27
2.8	Identification of the absolute growth rate and frequency. . . . .	28
2.9	Axial evolution of the absolute growth rate and frequency. . . . .	28
2.10	Extrapolation of the absolute growth rate and frequency onto the complex x-plane. . . . .	29
2.11	Example of the spatial averaging of the flow field. . . . .	31
2.12	Example of the POD results for a single-tone coherent structure that is used for a-posteriori phase averaging. . . . .	32
2.13	Examples of symmetric and antisymmetric spectra for a flow field, which fea- tures helical and axisymmetric coherent structures. . . . .	33
2.14	Examples of flow field filtering using POD. . . . .	34
3.1	Sketch of the moveable block swirl generator. . . . .	38
3.2	Sketches of the combustor variations. . . . .	39
3.3	Sketch of the water tunnel test rig. . . . .	40
3.4	Sketch of the combustor test rigs. . . . .	41
3.5	Sketch of the combustor test rig and the experimental setup. . . . .	43
3.6	Process of density estimation from seeding pictures. . . . .	46

3.7	Comparison of the scaled estimated temperatures from the QLS technique to point measurements values. . . . .	47
3.8	Exemplary results of a one-dimensional simulation of a hydrogen flame. . . .	48
4.1	Isothermal flow field. . . . .	54
4.2	Photographs of the flame shapes. . . . .	55
4.3	Parametric classification of the flame shapes. . . . .	56
4.4	Time-averaged reacting flow fields and Abel-deconvoluted OH*-chemiluminescence intensity distribution. . . . .	57
4.5	Flow fields and density fields of the different flame shapes. . . . .	58
4.6	Results of the POD analysis of the isothermal flow. . . . .	60
4.7	Results of the POD analysis of the isothermal flow in a crosswise plane. . . .	61
4.8	Results of the POD analysis of the V-flame. . . . .	62
4.9	Results of the POD analysis of the trumpet flame. . . . .	62
4.10	Results of the POD analysis of the detached annular flame. . . . .	64
4.11	Results of the POD analysis of the short hydrogen flame. . . . .	64
4.12	Time trace of the estimated particle concentration at an arbitrarily chosen point in the region of burnt gases of the V-flame. . . . .	65
4.13	Normalized time-lag distributions. . . . .	66
4.14	Phase-averaged line-of-sight integrated heat release fluctuations caused by the PVC. . . . .	68
4.15	Coherent integral OH*-chemiluminescence fluctuation of the detached flame. . .	69
4.16	Tomographic reconstruction of planar phase-averaged heat release fluctuations. .	70
5.1	Visualization of the bubble VB and cone VB. . . . .	75
5.2	Time-averaged isothermal flow fields at increasing rates of axial injection. . .	77
5.3	Radial velocity profiles of axial and tangential velocities inside the mixing tube and the combustion chamber. . . . .	78
5.4	Time-averaged flow fields at reacting conditions. . . . .	79
5.5	Abel-deconvoluted OH*-chemiluminescence intensity. . . . .	80
5.6	Initial jet opening angle at increasing rates of axial injection. . . . .	80
5.7	Reduction of the resulting swirl number due to axial injection. . . . .	82
5.8	Overview of the occurrence of VB and VB types. . . . .	83
5.9	Spectra of the radial velocity fluctuations at an arbitrarily chosen point in the shear layers. . . . .	83
5.10	Results of the POD analysis of the isothermal flow without axial injection. . .	84
5.11	Normalized radial velocity of the first dominant POD modes for the isothermal flow field in a crosswise plane. . . . .	84
5.12	Results of the POD analysis of the isothermal flow with a high rate of axial injection. . . . .	85
5.13	Normalized through-plane vorticity of the first dominant POD modes for the reacting flow field in the streamwise plane without axial injection. . . . .	86
5.14	Normalized through-plane vorticity of the first two POD modes for the LES of the isothermal flow field without axial injection. . . . .	87
5.15	Overview of the POD analysis and classification of the PVC types. . . . .	88

6.1	Kinetic energy captured by the POD modes for increasing rates of axial air injection. . . . .	94
6.2	Axial distribution of local absolute growth rate and frequency. . . . .	95
6.3	Results of the local linear stability analysis. . . . .	97
6.4	Abel-deconvoluted OH*-chemiluminescence intensity for two different flame positions. . . . .	98
6.5	Abel-deconvoluted OH*-chemiluminescence intensity and normalized density distributions of the analyzed flame shapes. . . . .	99
6.6	Axial distribution of local absolute growth rate and frequency for the detached flame. . . . .	100
6.7	Axial distribution of local absolute growth rate and frequency for the V-flame. . . . .	101
6.8	Axial distribution of local absolute growth rate and frequency for the trumpet flame. . . . .	101
6.9	Axial distribution of local absolute growth rate and frequency for the short hydrogen flame. . . . .	102
6.10	Comparison of the frequencies predicted by the stability analysis to measured frequencies. . . . .	102
6.11	Empirical and physical construction of the coherent radial velocity component of the global mode of the trumpet flame. . . . .	103
6.12	Comparison of the predicted wavemaker location to the location of maximum phase of the through-plane vorticity. . . . .	104
6.13	Phase of the through-plane vorticity along the centerline. . . . .	104
6.14	Eigenvalue spectrum of the Bi-global stability analysis and comparison to the results of the local analysis. . . . .	106
6.15	Model profiles for the axial velocity, density, and tangential velocity. . . . .	109
6.16	Influence of the model parameters on the absolute growth rate and absolute frequency of the model profiles. . . . .	111
6.17	Fit of the model parameters to the measured profiles for the different flame shapes. . . . .	112
7.1	Distribution of the antisymmetric velocity fluctuations. . . . .	118
7.2	Flow field and flame parameters for the transient measurement. . . . .	119
7.3	Time trace of the integral OH*-chemiluminescence intensity during the periodic variation of the equivalence ratio. . . . .	120
7.4	Flow field and flame parameters for the detachment process of the V-flame. . . . .	122
7.5	Flow field and flame parameters for the detachment process of the trumpet flame. . . . .	123
7.6	Flow field and flame parameters for the attachment process of the flame. . . . .	125
7.7	Flow field and flame parameters for the transition from the trumpet flame to the V-flame. . . . .	126
7.8	Schematic of the proposed stabilization mechanism for detached and attached flames. . . . .	127
7.9	Laminar burning velocities for methane flames and at different equivalence ratios at increasing inlet temperatures. . . . .	128
7.10	Abel-deconvoluted OH*-chemiluminescence images at decreasing and increasing equivalence ratios. . . . .	129

8.1	Schematic representation of the determination of the limit-cycle amplitude. .	133
8.2	Schematic of the mechanisms that are involved in the transfer function of velocity fluctuations at the combustor inlet to the flame response. . . . .	134
8.3	Preliminary investigation of the influence of the Reynolds number on the eigenvalue of the axisymmetric mode. . . . .	136
8.4	Preliminary investigation of the influence of the tangential velocity on the eigenvalues of the axisymmetric mode. . . . .	137
8.5	Flame response for acoustic forcing at $f_a = 196$ Hz for three swirl numbers. .	138
8.6	Time-averaged flow field superimposed on the normalized Abel-deconvoluted OH*-chemiluminescence distribution at increasing forcing amplitude. . . . .	140
8.7	Phase-averaged flow fields and flame positions at four equidistant phase angles.	141
8.8	Streamwise development of the coherent fluctuation intensity. . . . .	142
8.9	Maximum coherent fluctuation intensity at increasing forcing amplitudes. . .	142
8.10	Empirical and physical construction of the coherent radial velocity component.	143
8.11	Comparison of predicted to empirically obtained amplitude ratios. . . . .	144
9.1	Comparison of the tangential velocity component for the isothermal case, the detached flame, and the V-flame. . . . .	151
9.2	Time-averaged flow fields without acoustic forcing. . . . .	152
9.3	Time-averaged Abel-deconvoluted OH*-chemiluminescence intensity of the unforced flames. . . . .	152
9.4	Results of the POD analysis of the isothermal flow, the detached flame, and the V-flame without acoustic forcing. . . . .	153
9.5	Flow fields and heat release distributions of the encountered flow field and flame shapes at increasing forcing amplitudes. . . . .	155
9.6	Spectra of the isothermal flow field dynamics at increasing forcing amplitudes.	156
9.7	Results of the symmetric and antisymmetric POD analysis of the isothermal flow with forcing at $f_a = 158$ Hz. . . . .	158
9.8	Results of the antisymmetric POD analysis of the isothermal flow with forcing at $f_a = 110$ Hz. . . . .	158
9.9	Spectral analysis of the detached flame. . . . .	159
9.10	Results of the symmetric and antisymmetric POD analysis of the detached flame with forcing at $f_a = 158$ Hz. . . . .	161
9.11	Results of the antisymmetric POD analysis of the detached flame with forcing at $f_a = 110$ Hz. . . . .	161
9.12	Spectral analysis of the attached V-flame. . . . .	162
9.13	Results of the symmetric and antisymmetric POD analysis of the attached V-flame with forcing at $f_a = 110$ Hz. . . . .	163
9.14	Results of the stability analysis on the time-averaged forced flow fields. . . .	164
9.15	Comparison of the normalized axial velocity distribution of the unforced V-flame and trumpet flame to the forced V-flame. . . . .	167
9.16	Results of the stability analysis on the time-averaged forced flow fields of the attached V-flame. . . . .	167
9.17	Results of the phase-resolved stability analysis of the isothermal flow and the detached flame. . . . .	170

9.18 Phase of the absolute growth rate predicted by the stability analysis in the wavemaker region. . . . .	171
9.19 Spectra of the parametrically forced VdP oscillator. . . . .	172
9.20 Frequency dependence of the parametrically forced VdP oscillator. . . . .	173
A.1 Measured and calculated flame temperatures. . . . .	183
A.2 Isothermal flow field with and without area contraction. . . . .	185
A.3 Radial velocity profiles at isothermal conditions with and without area contraction. . . . .	186
A.4 Radial velocity profiles without area contraction. . . . .	186
A.5 Radial velocity profiles for various swirl numbers at combustion conditions. . . . .	187
A.6 Reacting flow fields at $S = 1.2$ with area contraction. . . . .	188
A.7 Radial velocity profiles at $S = 1.5$ for high acceleration due to heat release. . . . .	189
A.8 Radial velocity profiles at $S = 1.5$ for low acceleration due to heat release. . . . .	189
A.9 Influence of the density ratio on the parameters $p_x$ and $p_\Theta$ . . . . .	190
A.10 Influence of the effective swirl number on the parameters $p_x$ and $p_\Theta$ . . . . .	191
A.11 $\text{NO}_x$ emissions for premixed flames at subcritical conditions. . . . .	191
A.12 Criticality parameter for different effective swirl numbers. . . . .	193
A.13 Influence of the criticality parameter on $p_x$ and $p_\Theta$ . . . . .	193



# Nomenclature

## Latin letters

$A_{MT}$	Area of the mixing tube (m <sup>2</sup> )
$A_{PVC}$	Normalized integral amplitude of the PVC fluctuation (-)
$A_i$	Outlet area of the axial injection (m <sup>2</sup> )
$A_n$	$n$ 'th expansion coefficient (-)
$A_r$	Amplitude ratio (-)
$C$	Particle density (1/m <sup>3</sup> )
$C_h$	Homogeneous particle density (1/m <sup>3</sup> )
$C^* = C/C_h$	Normalized particle concentration (-)
$C_d$	Discharge coefficient (-)
$D_{cc}$	Combustion chamber diameter (m)
$D_{cb}$	Centerbody diameter (m)
$D$	Camera current due to the background (A)
$D_h$	Hydraulic diameter of the burner outlet (m)
$\dot{G}_\Theta$	Axial flux of angular momentum (Nm)
$\dot{G}_x$	Axial flux of axial momentum (N)
$H$	Camera current due to reflections (A)
$I$	Camera current (A)
$IL$	Normalized local light sheet intensity (-)
$I_h$	Camera current with homogeneous particle concentration (A)
$I_0$	Reference camera current (A)
$I_{OH}$	Planar normalized OH*-chem. intensity (-)
$I_{OH,LOS}$	Line-of-sight integrated normalized OH*-chem. intensity (-)
$J$	Bessel functions
$K$	Normalized coherent fluctuation amplitude (-)
$K_I$	Camera correction factor for different viewing angles (-)
$K_j$	Energy share of the $j$ 'th POD mode (-)
$N$	Shear layer thickness parameter (-)
$N_{cheb}$	Number of Chebychev collocation points (-)
$ OH^c /\overline{OH}$	Normalized integral heat release fluctuation (-)
$P$	Combustor Power (W)
$ Q^c /\overline{Q}$	Normalized flame response (-)
$R_{OH}$	Parameter describing the OH*-chem. intensity in the vicinity of the centerbody (-)
$R_\rho$	Parameter describing the density in the vicinity of the centerbody (-)

$Re$	Reynolds number based on $D_h$ and $U_0$ (-)
$Re_{\nu_t}$	Reynolds number considering the eddy viscosity (-)
$R$	Radius of the combustion chamber (m)
$R_b$	Burner outlet radius (m)
$R_c$	Correlation coefficient (-)
$S$	Inlet swirl number (-)
$S_{\text{eff}}$	Effective swirl number downstream of the flame (-)
$S_{\text{res}}$	Resulting swirl number (-)
$S_{\text{prim}}$	Swirl number of the swirler (-)
$S_L$	Laminar burning velocity (m/s)
$St$	Strouhal number based on $D_h$ and $U_0$ (-)
$T$	Temperature (K)
$T_{\text{in}}$	Inlet temperature (K)
$T_{\text{ad}}$	Calculated adiabatic flame temperature of the mixture (K)
$T_{\text{fl}}$	Calculated flame temperature (K)
$Tu = \sqrt{\frac{2}{3}k}/U_0$	Normalized turbulence intensity (-)
$U_0$	Bulk velocity at combustor inlet (m/s)
$U_c$	Bulk velocity at combustor outlet (m/s)
$U_j$	$j$ 'th Chebychev polynomial of the second kind of order $j$ (-)
$ u^c /U_0$	Normalized forcing amplitude (-)
$\mathbf{V} = (U, V, W)$	Mean velocity vector (m/s)
$Z$	Zernike polynomial (-)
$a$	Backflow parameter (-)
$a_j$	Temporal coefficient of the $j$ 'th POD mode (-)
$f$	Frequency (Hz)
$f_a$	Frequency of the acoustic forcing (Hz)
$f_h$	Frequency of the helical instability (Hz)
$k = 0.5 (\overline{u'u'} + \overline{v'v'} + \overline{w'w'})$	Turbulent kinetic energy ( $\text{m}^2/\text{s}^2$ )
$m$	Azimuthal wavenumber (-)
$\dot{m}$	Mass flow (kg/s)
$p$	Pressure (Pa)
$p_x$	Parameters describing the outlet influence on the axial velocity profiles (-)
$p_{\Theta}$	Parameters describing the outlet influence on the tangential velocity profiles (-)
$q$	Normalized solid body rotational speed (-)
$\mathbf{q} = (\mathbf{v}, p)$	Perturbation vector ([m/s, m/s, m/s, Pa])
$r_p$	Radial distance of the peak of the axial velocity (m)
$t$	Time (s)
$x_{\text{fl}}$	Axial center of the flame (m)
$x_s$	Axial location of the wavemaker (m)
$\mathbf{x} = (x, y, z)$	Cartesian coordinates (m)
$\mathbf{x} = (x, r, \Theta)$	Cylindrical coordinates (m)
$\mathbf{v} = (u, v, w)$	Time-dependent velocity vector in Cartesian coordinates (m/s)



$\mathbf{v} = (v_x, v_r, v_\Theta)$	Time-dependent velocity vector in cylindrical coordinates (m/s)
$w_{H2}$	Mass fraction of hydrogen in the fuel (-)

### Greek letters

$\Omega$	Steam-to-air mass ratio(-)
$\mathbf{\Omega} = (\Omega_{xy}, \Omega_{xz}, \Omega_{yz})$	Vorticity vector ( $s^{-1}$ )
$\Phi_j$	$j$ 'th spatial POD mode (-)
$\Psi$	Phase of the acoustic forcing (rad)
$\Sigma_{us}$	Normalized upstream asymmetry parameter (-)
$\Sigma_{ds}$	Normalized downstream asymmetry parameter (-)
$\theta$	Phase of the helical instability (rad)
$\alpha = \alpha_r + \alpha_i$	Complex axial wave number (1/m)
$\alpha_x$	Local opening angle of the swirling jet (rad)
$\alpha$	Initial opening angle of the swirling jet (rad)
$\beta$	Parameter for the eigenfrequency of the parametric Van der Pol oscillator (-)
$\gamma$	Parameter for the linear damping of the parametric Van der Pol oscillator (-)
$\kappa$	Criticality parameter (-)
$\mu$	Parameter for the nonlinearity of the parametric Van der Pol oscillator (-)
$\nu$	Kinematic viscosity ( $m^2/s$ )
$\nu_t$	Eddy viscosity ( $m^2/s$ )
$\omega$	Angular frequency (rad/s)
$\omega_0 = \omega_{0,r} + \omega_{0,i}$	Complex local absolute frequency (-)
$\omega_g = \omega_{g,r} + \omega_{g,i}$	Complex global frequency (-)
$\omega_m$	Measured solid body rotational speed (1/s)
$\omega_c$	Critical solid body rotational speed (1/s)
$\phi$	Equivalence ratio (-)
$\rho$	Fluid density ( $kg/m^3$ )
$\rho^* = \frac{\rho - \rho_b}{\rho_u - \rho_b}$	Normalized fluid density (-)
$\rho_u$	Density of unburnt gasses ( $kg/m^3$ )
$\rho_b$	Density of burnt gasses ( $kg/m^3$ )
$\rho_r$	Density ratio of burnt to unburnt gasses (-)
$\sigma$	Normalized asymmetry parameter (-)
$\tau$	Specific Reynolds stress tensor ( $m^2/s^2$ )
$\tau_c$	Convective time delay (s)
$\tau_d$	Dispersive time delay (s)
$\chi$	Axial injection rate (-)
$\hat{\zeta}$	Amplitude of the parametric excitation of the Van der Pol oscillator (-)

**Subscripts and superscript**

$(\cdot)^c$	Coherent part
$(\cdot)^s$	Stochastic part
$(\cdot)'$	Fluctuating part
$(\cdot)^h$	Phase-resolved data with respect to the helical instability
$(\cdot)^a$	Phase-resolved data with respect to the acoustic forcing
$(\cdot)^{ha}$	Doubly phase-resolved data
$\hat{(\cdot)}$	Amplitude function
$(\cdot)^*$	Normalized quantities of model profiles

**Operators**

$\langle \cdot \rangle$	Phase averaging operator
$\langle \langle \cdot, \cdot \rangle \rangle$	Inner product
$\overline{(\cdot)}$	Temporal averaging operator
$\widetilde{(\cdot)}$	Spatial averaging operator

**Abbreviations**

CB	Centerbody
CC	Combustion chamber
DMD	Dynamic mode decomposition
FFT	Fast Fourier transform
IRZ	Inner recirculation zone
LDV	Laser Doppler velocimetry
LIF	Laser induced fluorescence
LOS	Line-of-sight
LSA	Linear stability analysis
MT	Mixing tube
ORZ	Outer recirculation zone
PIV	Particle image velocimetry
POD	Proper orthogonal decomposition
PVC	Precessing vortex core
QLS	Quantitative light sheet
RMS	Root mean square
TKE	Turbulent kinetic energy
VB	Vortex breakdown
VdP	Van der Pol

# Chapter 1

## Introduction

Allow me to express now, once and for all, my deep respect for the work of the experimenter and for his fight to wring significant facts from an inflexible Nature who says so distinctly “No” and so indistinctly “Yes” to our theories.

---

*(Hermann Weyl, 1950)*

### 1.1 Motivation

The detrimental consequences of global warming and the scarceness of fossil energy resources make an increasing use of renewable energy sources imperative. An inherent problem of most renewable energy sources, such as wind power and solar power, is the fluctuation of the energy supply. Figure 1.1 exemplarily demonstrates the possible mismatch between the electrical energy demand and the electrical energy supply provided by solar and wind power for two days in Germany. The demand follows a rather regular pattern with the peak demand between 6:00 and 18:00. This time frame agrees reasonably well with the peak hours of electrical energy provided by solar power. In strong contrast to this, the electrical energy provided by wind power shows strong and irregular fluctuations. To cope with these fluctuations, flexible energy sources, such as gas turbines, are required. In the foreseeable future, when the share of renewable energies is supposed to be substantially increased, effective storage techniques and fast backup electrical energy sources will be increasingly important to ensure a reliable electrical energy supply.

Gas turbines are most probably the number one choice over other energy conversion techniques, such as coal combustion and nuclear power conversion, to complement a power economy largely based on renewable sources, due to their comparably fast start-up times and clean combustion. Furthermore, gas turbines are able to cooperate with energy storage facilities, where excess electrical energy is used to synthesize fuel, which is stored and subsequently fed to the gas turbine.

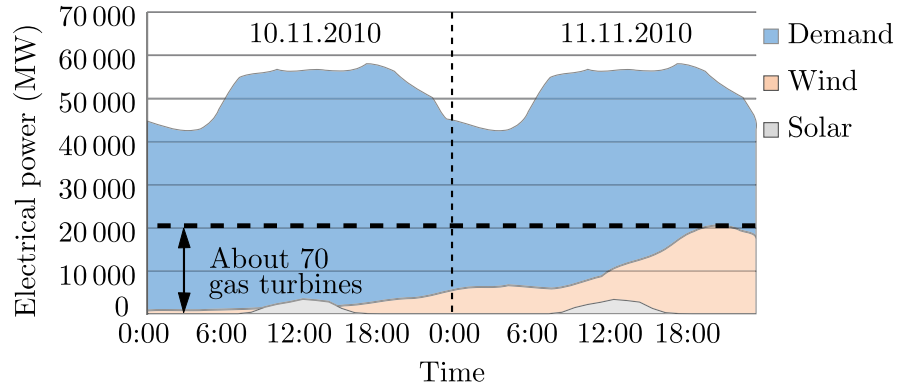


Figure 1.1: Temporal fluctuation of the electric energy demand and production in Germany. Data from the European Energy Exchange AG.

Nevertheless, current gas turbine technology is not ready to fully meet the future requirements of high efficiency, low pollutant emission and fast start-up and turn-down times. High cycle efficiencies are only achieved in complex, expensive, and slow combined-cycle plants, where the gas turbine cooperates with an additional steam turbine. Single-cycle gas turbines, without a separate steam-cycle, can feature very short response times, but do not achieve the required efficiencies.

The present thesis documents work that was carried out in the scope of project GREEN-EST, which is funded by the European Research Council. In this project, the concept of an ultra-wet gas turbine cycle is developed, which promises to combine the three defined requirements, low emissions, high efficiency, and fast response time, in a very convincing way.

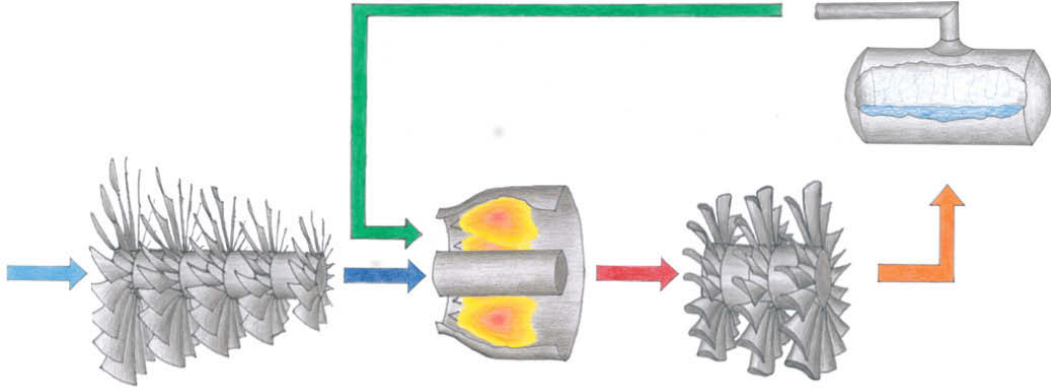


Figure 1.2: Schematic of the ultra-wet gas turbine cycle. Illustration by C. Schrödinger.

The key idea of the ultra-wet cycle, depicted in Fig. 1.2, is the usage of hot exhaust gases to evaporate pressurized water. The produced steam is injected directly into the combustion chamber and is expanded with the main air through the turbine. This single-cycle ultra-wet gas turbine can reach efficiencies comparable to combined-cycle power plants at considerably lower costs, a much smaller footprint, and with significantly faster response times.

The second main advantage of the ultra-wet cycle is the reduction of the pollutant emissions. One of the most toxic pollutants are nitric oxides ( $\text{NO}_x$ ) that are responsible for acid rain and participate in the depletion of the ozone layer. In conventional gas turbines the level of  $\text{NO}_x$  emissions is closely coupled to the maximum achievable efficiency. High flame temperatures are needed for high cycle efficiencies, but at the same time, they cause an exponential increase of the  $\text{NO}_x$  emissions. Thus, a trade-off between efficiency and acceptable  $\text{NO}_x$  emissions is imposed. The ultra-wet cycle overcomes these limitations due to the beneficial effect of steam dilution on the pollutant emissions. This effect is depicted in Fig. 1.3. At dry conditions, without steam dilution, the  $\text{NO}_x$  emissions strongly increase with the flame temperature. This temperature sensitivity of the  $\text{NO}_x$  emissions is very well known since the seminal work of Zeldovich (1946). Steam dilution significantly reduces the  $\text{NO}_x$  emissions even at the same flame temperature.

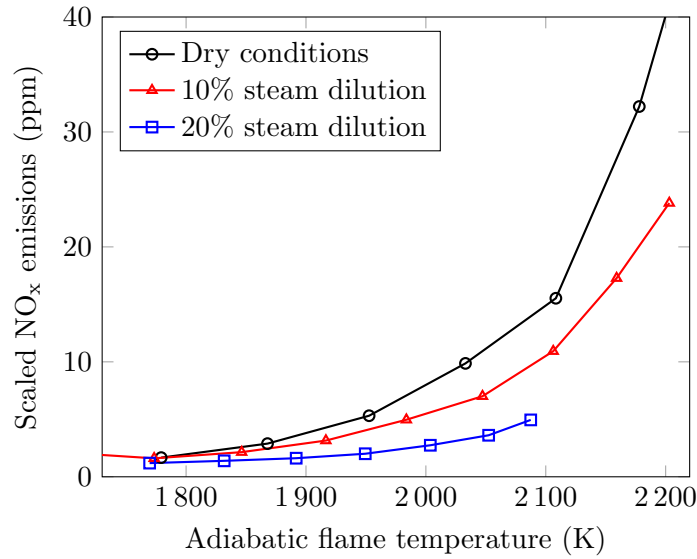


Figure 1.3: Measured  $\text{NO}_x$  emissions at dry and steam-diluted conditions.

The lower flame temperatures that are required at dry conditions for acceptable  $\text{NO}_x$  emissions are usually achieved by burning the fuel with large amounts of excess air that does not take part in the oxidation process. These large amounts of excess air have to be compressed in the engine, creating additional losses and, thereby, further decrease the cycle efficiency. Additionally, combustion at lean conditions, i.e., with excess air, makes the combustion system much more prone to undesirable thermoacoustic oscillations. The onset of these oscillations may limit the gas turbine operation to non-optimal points in terms of the efficiency and the pollutant emissions (Lieuwen and Yang, 2005).

The concept of ultra-wet combustion is able to mitigate these problems by allowing the clean combustion without excess air, at so-called stoichiometric conditions, and furthermore enables for the safe and clean combustion of a large variety of fuels. However, the introduction of large amounts of steam does also introduce new challenges to the combustor design. It

is intuitive that the reactivity of a fuel–air mixture is significantly reduced if it is heavily diluted with steam. Consequently, the main task of a combustor designed for the ultra-wet cycle gas turbine is to ensure a stable combustion without flame blow out under all operating conditions. The range of operating conditions is even further extended by the requirement for the combustor to operate with different types of fuel. Due to the scarcity of fossil fuels, such as natural gas, the use of bio-fuels and hydrogen is of increasing importance. Consequently, the combustor has to be able to operate at different levels of steam dilution and with varying fuel types reaching from low reactivity bio-fuels over natural gas to highly reactive hydrogen fuel.

These extreme changes in the operating conditions give rise to very different flame shapes and flow fields in the combustor. At some operating conditions very strong flow oscillations occur, while at other conditions these flow oscillations are completely suppressed. If the oscillations are excited, they manifest in large-scale coherent structures and cause strong deformations of the flame, substantially affect the mixing processes, and influence the flame stability.

The characterization of the different flow fields and the detailed investigation of the associated flow dynamics is the original motivation for the research work of this thesis. However, different flame shapes also frequently occur at non-diluted conditions, especially when different fuel types are used. Therefore, the emphasis of the present thesis is placed on the understanding of the mechanisms that govern the occurrence of the flame shapes and the flow field dynamics. These mechanisms are independent of the operating conditions and can be transferred to different combustor designs and operating concepts. Thus, the relevance of the findings of this thesis is in no way restricted to steam-diluted flames.

## 1.2 Swirl-Stabilized Combustion

The combustor used in this thesis is based on the principle of swirl-stabilization. Nowadays, these combustors are used in the majority of gas turbines by all leading manufacturers. Examples of industrially applied combustors are shown in Fig. 1.4 from ALSTOM and GE. ALSTOM's EV burner consists of two displaced cones and the flow enters the burner tangentially through the slots in between the cones. As a result angular momentum is imparted on the flow and it swirls around the centerline. In the combustor array by GE, the swirl is imparted on the flow by axial vanes. The designs of the two combustors seem very different, but the basic principles remain the same in a sense that a strongly swirling flow is created. This swirling flow is the basis for flame stabilization.

The main advantage of swirl-stabilized combustors, in comparison to jet flames or bluff-body-stabilized combustors, is the hydrodynamic flame stabilization. No parts of the combustor are in the direct vicinity of the flame and require extensive cooling efforts. This is achieved due to a phenomenon called vortex breakdown (VB). This phenomenon takes place in a wide variety of natural and technical flows, such as tornadoes or the flow around a delta wing.

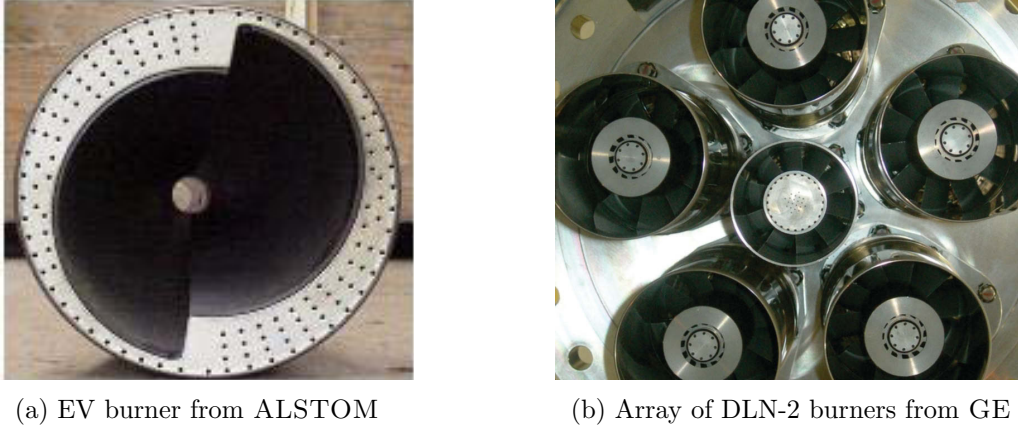


Figure 1.4: Industrial swirl-stabilized burners.

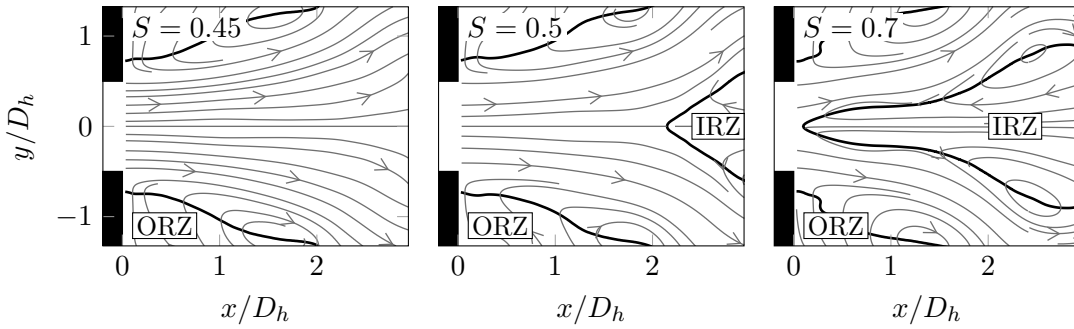


Figure 1.5: Combustor flow field at increasing swirl intensities from left to right. Thick black lines enclose regions of negative axial velocities.

A flow undergoes vortex breakdown if the flow has a sufficient amount of angular velocity, also termed swirl. A representation of the onset of vortex breakdown is depicted in Fig. 1.5. The images show streamlines of typical time-averaged combustor flows at increasing swirl intensities. The leftmost flow field is measured at the lowest swirl, described by the so-called swirl number  $S$ . The flow is recirculating at the corners of the confinement, the outer recirculation zone (ORZ). Near the centerline some divergence of the streamlines is evident, but positive velocities prevail. At a critical swirl intensity (here  $0.45 < S_{crit} < 0.5$ ), a stagnation point occurs and moves further upstream for increasing swirl intensities. The result is a second zone of negative axial velocities along the centerline, the inner recirculation zone (IRZ). A convenient criterion for the onset of vortex breakdown is the existence of negative axial velocities on the centerline of the combustor.

Comprehensive reviews about the mechanisms that are involved into vortex breakdown are available by Hall (1972), Leibovich (1978, 1984), Escudier and Keller (1985), and Lucca-Negro and O'Doherty (2001). Different explanations for the onset of VB have been proposed in the last decades. Jones (1964) related the onset of vortex breakdown to the hydrodynamic stability of the flow, while Benjamin (1962) and Squire (1962) promoted the concept of flow

criticality to explain the onset of vortex breakdown. The dominant role of the criticality of the flow by Benjamin (1962) and Squire (1962) was backed up by later studies (e.g., Escudier and Keller, 1985) and is regarded nowadays as the most suitable explanation. A swirling flow undergoes vortex breakdown if it is subcritical. This state is defined by the ability of the flow to sustain long inertia waves, by which pressure information is transported upstream (Benjamin, 1962; Squire, 1962).

Qualitatively, a tangible explanation for vortex breakdown is also possible. Due to the swirling motion, centrifugal forces lead to radial pressure gradients and a lower static pressure at the center of the swirling flow compared to the surrounding fluid. If the swirl intensity decays in axial direction, e.g., due to viscous forces or geometric changes, these centrifugal forces decay in axial direction and an axial pressure gradient along the centerline is present. If this gradient is sufficiently strong, the flow decelerates, stagnates and eventually reverses: The flow undergoes vortex breakdown.

The post vortex breakdown flow field is very beneficial for flame stabilization. The large zones of reversed flow provide an excellent anchor for the flame since the flow field features a wide range of velocities. This allows for a match of the flow velocity to the turbulent burning velocity of the fuel–air mixture. This match is required for the flame not to be swept away and to be quenched. Furthermore, the recirculation due to the flow reversal causes a sustained upstream transport of hot combustion products to the flame. Thereby, the flow is preheated and important radicals are provided to start the chemical reaction. Moreover, vortex breakdown significantly enhances the turbulence intensity. At higher turbulence levels the turbulent burning velocity of the fuel–air mixture is increased, and the flame stability is even further increased. A photograph of a swirl-stabilized flame is shown in Fig. 1.6. The arrows represent the flow recirculating into the IRZ and ORZ. The flame is mostly located along the inner shear layers, where the flow velocity is comparably low and the turbulence intensity is very high.

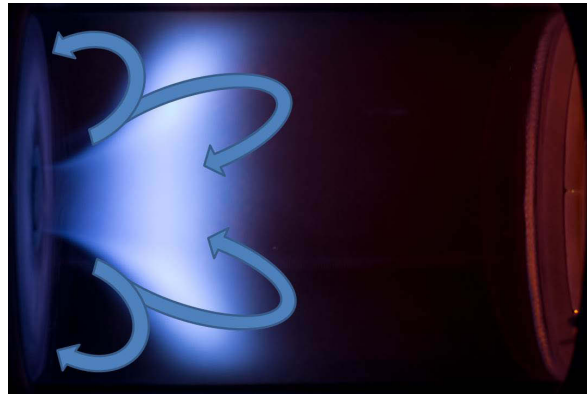


Figure 1.6: Swirl-stabilized flame in on of the combustor test rigs employed for the experimental part of this thesis.

The possibility of purely aerodynamic flame stabilization, where no parts of the combustor are in direct contact with the flame, and the excellent flame holding characteristics, led to the



success of swirl-stabilized combustors in several applications. However, the complex flow field also poses some important challenges. One example is the increased risk of flame flashback. Flashback denotes the undesired upstream movement of the flame into parts of the combustor that are not designed for flame holding. Such parts often serve as premixing sections where fuel and air are mixed prior to combustion to achieve lower emissions. If the location of vortex breakdown is not geometrically fixed, it may move too far upstream and into the premixing section. The flame can easily follow the recirculation zone and advance into the premixing section, where it can cause severe damages to the combustor.

To exploit the immense possibilities of swirl-stabilized combustion and simultaneously circumvent the challenges imposed by the complex mechanisms involved into vortex breakdown, the flow fields of swirling flames and swirl-stabilized combustors have been a frequent topic of combustion research in the last 40 years. Early works primarily focused on the comparability of isothermal to reacting measurements, while later works investigated the interaction of unsteady flow features with the flame. Comprehensive overviews about the beginnings of the research were provided in early reviews by Syred and Beér (1974) and Lilley (1977) in the 70s. The former review compares the isothermal flow field created by different types of swirl generators under the aspects of flow recirculation and turbulence characteristics. The work by Lilley (1977) reviews the first comprehensive data sets dedicated to the comparison of the isothermal to the reacting flow field (Baker et al., 1975), which was enabled due to the advent of the laser Doppler velocimetry (LDV) technique. This early work already describes the strong changes the flame induces on the flow field.

The advent of more powerful lasers and sensitive cameras allowed for the application of spatially resolved particle image velocimetry (PIV) to swirling reacting combustor flows (Ji and Gore, 2002). Following works (e.g., Wicksall et al., 2005b; Stöhr and Meier, 2007; Sadanandan et al., 2008; Stöhr et al., 2009) focused on the importance of unsteady flow structures and their interaction with the flame. The recent introduction of high speed lasers and cameras, ultimately, allowed for the study of transient phenomena (e.g., Konle et al., 2007) as well as new insights into vortex–flame interactions. Other works pointed out the role of large-scale coherent structures for the flame dynamics (e.g., Boxx et al., 2010b; Galley et al., 2011; Stöhr et al., 2011b, 2012).

### 1.3 Coherent Structures in Swirl-Stabilized Combustors

The flow reversal due to vortex breakdown has very beneficial effects on flame stabilization, but the resulting complex flow also causes strong unsteady phenomena in the flow field. Manifestations of an unsteady flow are coherent flow structures. These coherent, large-scale structures can occur in very different shapes and at very different frequencies. In this thesis a clear separation is based on the azimuthal order  $m$  of the structure. The azimuthal order is defined as the ratio of the circumference to the azimuthal wavelength of the structure. That is, an azimuthal order of  $|m| = 1$  means that exactly one wave of the structures is present in circumferential direction, and the structure is antisymmetric with respect to the centerline.

One important type of coherent structures, which will be investigated in the scope of this thesis, is of this azimuthal order  $|m| = 1$ . The second treated type of coherent structures is of an azimuthal order of  $m = 0$ . Thus, the structures are axisymmetric with respect to the centerline. In the following both type of coherent structures, the antisymmetric helical structures and the axisymmetric structures are briefly introduced.

### 1.3.1 Helical Coherent Structures: The Precessing Vortex Core

Already in the early reviews on swirling combustor flows by Syred and Beér (1974) and Lilley (1977), an unsteady behavior of the flow was reported. The center of the vortex seemed to be precessing at a fixed frequency around the geometrical center of the combustor. Hence, the phenomenon was denoted as the precessing vortex core (PVC). Figure 1.7 shows an example of the precession of the vortex core. Streamlines at four different phases of the precession cycle are shown. At all instances the vortex core is displaced from the geometrical center and rotates around it. The direction of the precession is in the same direction as the flow rotation and the vortex core precession frequency is usually of the order of the rotational frequency of the flow but not necessarily equal to it.

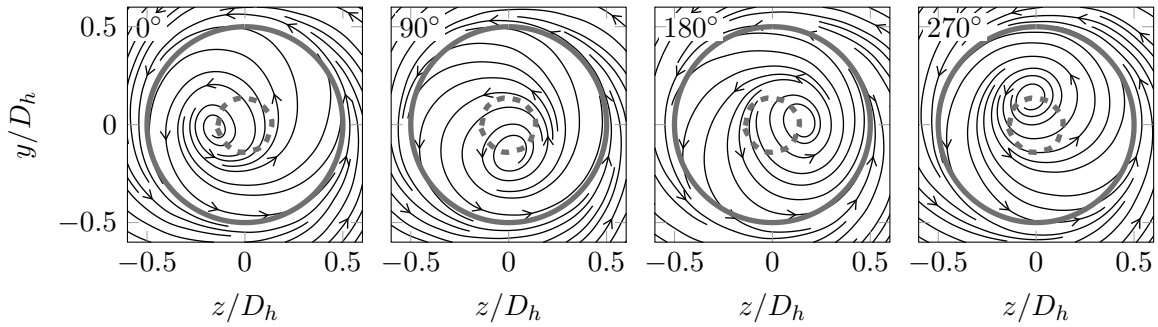


Figure 1.7: Visualization of the PVC in a crosswise plane near the combustor inlet ( $x/D_h = 0.1$ ) at four different phases of the oscillation. The solid circle is the inlet diameter and the dotted circle denotes the trajectory the vortex core prescribes during a precession cycle.

The occurrence of unsteady structures in swirling flow is not limited to combustor flows but was reported in all types of swirling flows (e.g., Leibovich, 1978). In early studies it was distinguished between a steady, axisymmetric bubble type vortex breakdown type and an unsteady, helical spiral vortex breakdown type (Lambourne and Bryer, 1961; Escudier and Zehnder, 1982). Later investigations (Escudier and Keller, 1985) came to the conclusion that vortex breakdown is essentially axisymmetric, and the so-called spiral type vortex breakdown is a superposition of the axisymmetric vortex breakdown and a helical flow instability. At this point it is important to follow the theory of Benjamin (1962) and Squire (1962) that vortex breakdown is caused by the criticality of the flow and not by the hydrodynamic stability. The flow criticality is the ability of the swirling flow to sustain long inertia waves, whereas the hydrodynamic stability describes the temporal and spatial growth of perturbations. Ruith et al. (2003) and Gallaire et al. (2006) confirmed the assumptions of Escudier and Keller

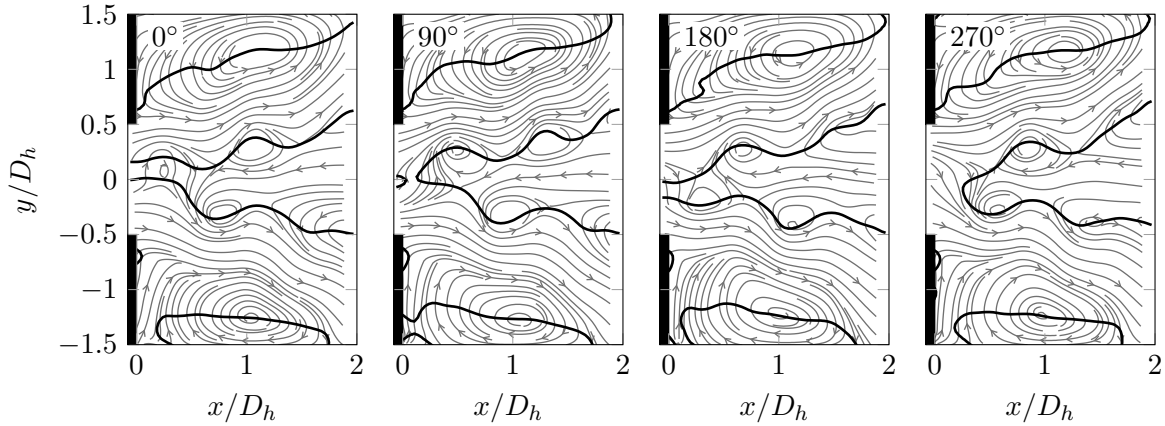


Figure 1.8: Visualization of the PVC in a streamwise plane at four different phases of the oscillation. Thick black lines enclose the regions of negative axial velocity.

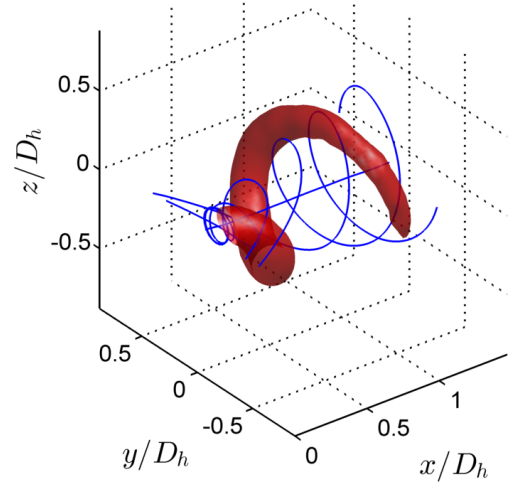
(1985) (and Benjamin (1962) and Squire (1962)) in numerical and analytical studies. They showed that the onset of vortex breakdown depends on the criticality of the flow. The post vortex breakdown flow field shows an axisymmetric bubble-type breakdown. At the onset of a hydrodynamic instability, the appearance of the vortex breakdown changes from bubble type to spiral type. In other words, a flow field undergoing vortex breakdown and featuring a helical instability (the PVC) is called a spiral-type vortex breakdown.

It must be noted that the term PVC is mostly used in research dealing with combustion systems and it is not used in the studies of Ruith et al. (2003) and Gallaire et al. (2006), as other structures were more salient than the precession of the vortex core. This can be made plausible if the same flow field presented in Fig. 1.7 is depicted in a streamwise plane, as shown in Fig. 1.8. Instead of the precession of the vortex core, now a helical train of vortices in the inner shear layer is evident. These vortices are caused by the strong velocity gradient across the shear layers between the jet and the recirculation zones and are a manifestation of Kelvin-Helmholtz instabilities. Furthermore, the IRZ also clearly shows a spiral shape. This is in line with the denotation of the same flow structure as the PVC as a spiral type vortex breakdown. In Fig. 1.9 isocontours of the  $Q$ -criterion (Kolář, 2007) calculated for a three-dimensional reconstruction of the phase-averaged flow field are shown to visualize the helical vortices in shear layers. It is evident that the vortices form a helical structure, which is counter-winding with respect to the mean flow.

It is important to emphasize that both symptoms, the precession of the vortex core and the helical Kelvin-Helmholtz instabilities, are different manifestations of the same global flow structure. For convenience reasons, in the following, the abbreviation PVC is often used without mentioning the helical Kelvin-Helmholtz instabilities. However, it refers to the entire flow structure including the precession of the vortex core and the synchronized Kelvin-Helmholtz instabilities.

The PVC and the Kelvin-Helmholtz instabilities have strong influence on the instantaneous flow fields and, thus, a considerably influence on the flame is to be expected. Paschereit et al.

Figure 1.9: Three-dimensional visualization of the helical Kelvin-Helmholtz instabilities related to the PVC. Blue: Streamlines of the time-average flow field (blue). Red: Isocontours of the phase-averaged  $Q$ -criterion, indicating the vortices in the shear layers.



(2000) reported large-scale antisymmetric heat release fluctuations with the frequency of the PVC. Galley et al. (2011) and Duwig et al. (2012) showed that the PVC alters the fuel-air mixing and thereby the flame stabilization and, consequently, the heat release distribution. Detailed vortex-flame interactions were reported in a series of works by the group at DLR Stuttgart (Boxx et al., 2009, 2010a,b; Stöhr et al., 2012), using simultaneous time-resolved measurements of flow field and flame. Moeck et al. (2012) developed a method to extract the three dimensional heat release rate from phase-averaged line-of-sight integrated measurements. They showed two intertwining helices: one of higher and one of lower than average heat release rates. Furthermore, it is pointed out that due to the antisymmetric nature of the PVC, and the induced heat release fluctuation, no oscillation of the integral heat release is caused. However, in an analytical study Acharya et al. (2013) predicted that this is only true for perfectly axisymmetric time-averaged flows and flames. Thus, asymmetries, as they can be expected in annular combustors (Samarasinghe et al., 2013), may cause also integral heat release fluctuations induced by the PVC. These integral heat release fluctuations are of utmost importance for the combustion system since they can couple to the systems acoustics and cause dangerous pressure fluctuations. The role of integral heat release fluctuation and their excitation by axisymmetric coherent structures will be further elaborated in the following section.

### 1.3.2 Axisymmetric Coherent Structures

In the previous section, the helical PVC was introduced. The oscillation of the PVC is self-excited and determined by the stability of the flow. Generally, in strongly swirling flows the PVC is the dominating self-excited structure, and, without external forcing, no axisymmetric coherent structures usually occur. Nevertheless, axisymmetric coherent structures frequently occur in combustion systems as *forced* coherent structures. In this case the term *forced* does not mean that always an external forcing is required but that the structures are excited by the acoustics of the system and not by the flow itself.

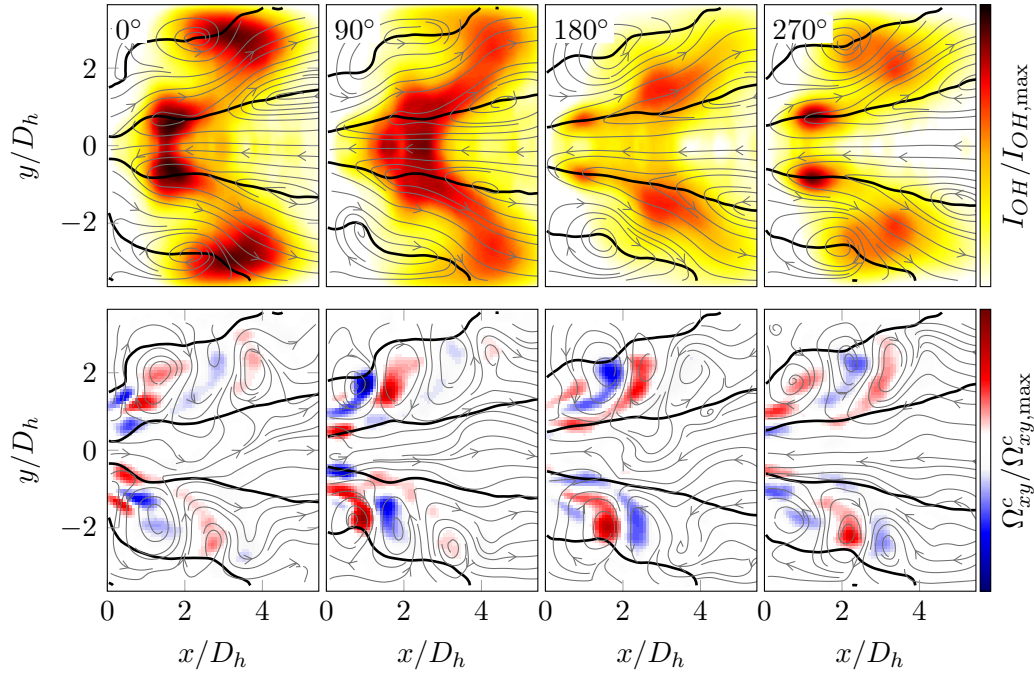


Figure 1.10: Normalized flame oscillation ( $I_{OH}/I_{OH,max}$ ) caused by axisymmetric coherent structures (top row) and the corresponding velocity and trough-plane vorticity fluctuations ( $\Omega_{xy}^c$ ) (bottom row) at four phase angles of the forcing cycle. Acoustic forcing amplitude is 30% of the mean inlet velocity.

The effect of acoustically forced axisymmetric coherent structures on the flame is exemplary shown in the top row of Fig. 1.10. It is evident that in the first phase the intensity of the reaction, indicated here by the amount of OH\*-chemiluminescence ( $I_{OH}$ ) radiated from the flame, is much stronger than in the other phases. This fluctuation is essentially caused by the interaction of the forced vortices, as can be identified from the coherent through-plane vorticity ( $\Omega_{xy}^c$ ) in the bottom row of Fig. 1.10, and the flame. Integral heat release fluctuations are of very high importance, as they close the feedback cycle between the heat release and the system acoustics. If the acoustic pressure fluctuations are in-phase with the heat release fluctuations, the feedback is positive and energy is transferred from the flame into the acoustic field (Rayleigh, 1878). High amplitude thermoacoustic instabilities can lead to increased emissions and very high pressure amplitudes that can cause severe damages to the combustion chamber or even to the entire gas turbine. In the present thesis the effect of the coherent vortices on the flame oscillation will be investigated. However, the main focus is placed on the experimental and analytical characterization of the strength of the vortices and the mechanisms determining their growth. No detailed introduction to combustion instabilities shall be provided here and the reader is referred to the literature for a comprehensive review on combustion instabilities (Lieuwen and Yang, 2005).

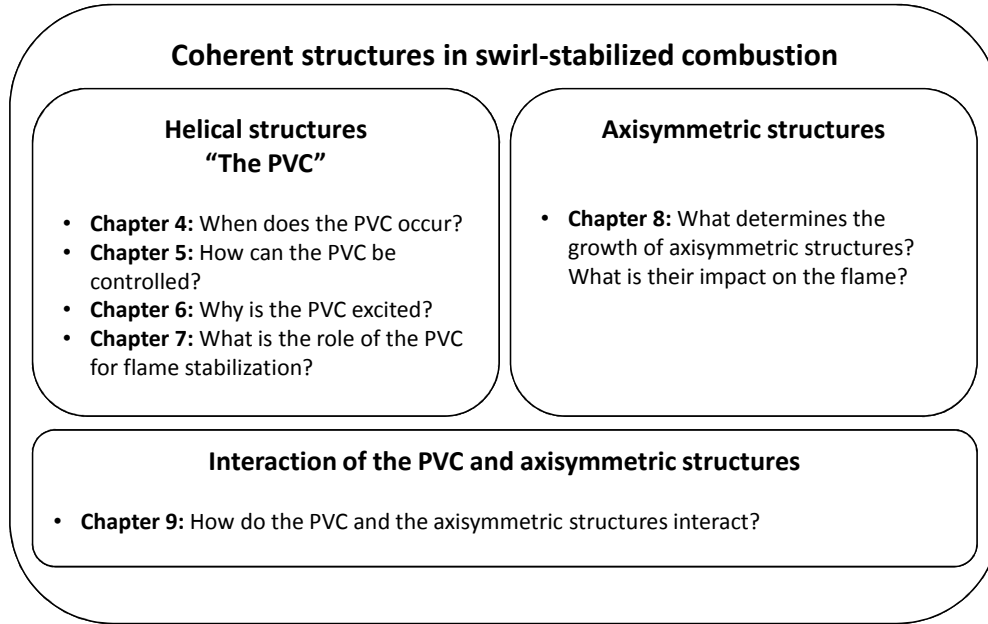


Figure 1.11: Overview of the results chapters of this thesis.

## 1.4 Overview of the Thesis

The aim of the present thesis is to provide new insights into the two most important types of coherent structures in swirl-stabilized combustion. These are self-excited helical coherent structures, the PVC, and forced axisymmetric structures. Both are investigated based on detailed experimental measurements and analytical modeling. Chapter 2 provides a brief introduction into the concept of flow stability and the role of stability for the observed coherent structures. Subsequently, theoretical methods for the empirical and analytical assessment of these structures are introduced. This includes an outline of the linear stability analysis and the proper orthogonal decomposition. In the following Chapter 3, the experimental facilities, namely the investigated combustors and the test rigs, are presented next to the applied measurement techniques. The main part of this thesis is composed of six additional chapters, where the experimental results and the results of the analytical modeling are presented and discussed. A brief overview of these chapters is presented in Fig. 1.11 based on the main questions, for which the individual chapters aim at providing answers. The first four results chapters focus on the occurrence, modeling and impact of the helical PVC structure. In contrast to that, in Chapter 8 the role of axisymmetric structures is investigated. Chapter 9 considers the case where both types of coherent structures occur simultaneously and interact with each other. In the following, a short overview about the different results chapters is provided.

- **Chapter 4** In this chapter the occurrence of the PVC in the swirl-stabilized combustor is empirically investigated. First, the type of the flame shape and the corresponding

flow field is determined for a range of reacting combustor operating conditions. A classification of the results yields four different flame shapes, which are shown to be dominated by the reactivity of the fuel–air–steam mixture. The application of proper orthogonal decomposition shows that the isothermal flow and the reacting flow fields of three of the four flame shapes feature PVCs of different appearances, while the PVC is suppressed for the fourth flame shape. Additionally, the strong influence of the PVC on flame dynamics and mixing characteristics is pointed out. The results of this chapter provide the starting point for the analytical investigation of the impact of the flame on the PVC carried out in Chapter 6.

- **Chapter 5** The second chapter of the main part focuses on the control of the PVC by modifications of the inflow conditions. An experimental study is carried out in a swirl-stabilized combustor where a part of the flow can be injected as a non-swirling jet on the centerline. The results of this axial injection are small changes in the inflow profile into the combustion chamber. It is shown that these small changes substantially affect the global flow field. A classification of two different vortex breakdown types and PVC shapes identifies the operating conditions for a stable flow field. These conditions are furthermore shown to be very favorable in terms of flame stabilization and safety against undesired flame flashback.
- **Chapter 6** While the focus in Chapter 4 and 5 is placed on the empirical description of the PVC, this chapter aims at analyzing how the PVC is excited and which regions in the flow field are determining its excitation, shape, and frequency. To this end, linear hydrodynamic stability analysis is employed on the time-averaged isothermal and reacting flow fields. The concept is first validated against the experimental results by showing that the analysis correctly predicts the excitation and suppression of the PVC at different combustor operating conditions. Subsequently, the validated theory is used to carry out a parametric study isolating the influence of important flow parameters, such as the backflow intensity, the shear intensity, the density ratio, and the amount of swirl, on the instability. The identification of the most important parameters for the excitation of the PVC is of paramount importance for the explanation of the phenomena observed in the following chapters.
- **Chapter 7** In the previous chapters the occurrence of the PVC in different flame configurations is investigated and general conclusion about the PVC and its role for flame stabilization are drawn. In this chapter the assessment is extended to transient conditions featuring flame shape transitions. The focus is placed on the role of the PVC for the stabilization process of the different flame shapes. Transient measurements are presented to illustrate the course of actions that finally leads to the transitions. The experiments show that the transition between the flame shapes is not continuously, but takes place on a very short timescale. Furthermore, a considerable region of hysteresis is encountered between the transitions. Based on the results of the previous chapters, a conceptual model is developed for the transition process. This conceptual model shows

the importance of the PVC for the transition and suggests the PVC as an important driver for the observed hysteresis.

- **Chapter 8** The previous chapters dealt with the PVC, which is a self-excited helical instability. In this chapter the second type of coherent structures, forced axisymmetric coherent structures, are investigated. These structures are of high relevance for the gas turbine industry as they are directly related to the occurrence of thermoacoustic instabilities. The focus of this chapter is placed on the growth of these coherent structures. In the first part of the chapter, it is shown experimentally that the structures are amplified in the flow field when forced at a low acoustic forcing amplitude. At high amplitudes, however, a saturation is observed. This saturation of the flow structures is shown to cause a saturation of the flame response to acoustic excitation. In the second part of the chapter, the mechanisms that cause the saturation of the growth of the coherent structures (and, thus, also of the flame response) are identified employing linear stability analysis. It is shown that the saturation of the growth is essentially a result of changes to the mean flow field caused by the axisymmetric coherent structures themselves.
- **Chapter 9** In swirl-stabilized combustors, often a PVC and acoustically excited axisymmetric structures are present at the same time. In this chapter the effect of the axisymmetric structures on the PVC is investigated. Two different phenomena are observed. A PVC, which is excited in the absence of acoustic axial forcing, is attenuated and suppressed by axial forcing. In strong contrast to that, in a naturally stable flow field without a PVC, the PVC can be excited by acoustic axial forcing. These, at the first glance contradictory, findings are explained in this chapter with the application of linear hydrodynamic stability theory. Moreover, it is shown that the PVC at axially forced conditions behaves essentially as a parametrically excited oscillator.

In the concluding remarks of this thesis, the questions posed in Fig. 1.11 are answered based on the findings of the results chapters. Additionally, the implications of the findings of the present thesis are pointed out.



## Chapter 2

# Theory and Methods

In the following the theoretical methods and concepts employed in this thesis are briefly introduced. First, the occurrence of the PVC is described as a global hydrodynamic mode. Subsequently, tools to empirically and analytically investigate hydrodynamic modes, such as the PVC, are presented. Finally, the set of data treatment measures that was applied in the scope of the present thesis is introduced.

### 2.1 The Precessing Vortex Core as a Global Mode

At isothermal conditions the onset of the PVC is closely linked to the amount of swirl imparted on the flow. This amount of swirl is usually described by the swirl number, which is defined as the relation of the axial flux of angular momentum ( $\dot{G}_\Theta$ ) to the axial flux of axial momentum ( $\dot{G}_x$ ).

$$S = \frac{\dot{G}_\Theta}{R_b \dot{G}_x}. \quad (2.1)$$

The axial fluxes of the axial and angular momentum of an inviscid, incompressible, and axisymmetric jet are obtained using the following equations (Rajaratnam, 1976):

$$\dot{G}_\Theta = 2\pi\rho \int_0^R (UW + v'w') r^2 dr \quad (2.2)$$

$$\begin{aligned} \dot{G}_x = 2\pi\rho \int_0^R \left[ \left( U^2 - \frac{W^2}{2} + \overline{u'^2} - \frac{\overline{v'^2} + \overline{w'^2}}{2} \right) r \right. \\ \left. + \left( U \frac{\partial V}{\partial x} + V \frac{\partial V}{\partial r} + \frac{\partial}{\partial x} \overline{u'v'} \right) \frac{r^2}{2} \right] dr. \end{aligned} \quad (2.3)$$

Here,  $W$  denotes the tangential velocity,  $U$  is the axial velocity,  $\rho$  is the fluid density,  $R$  denotes the radius of the combustion chamber, and  $R_b$  is the burner outlet radius. The calculation of the swirl number using the above stated equations includes spatial derivatives of the Reynolds stresses. Therefore, it is very sensitive to the measurement quality and requires very precise and spatially resolved data. A more commonly used definition was introduced by Chigier and

Beer (1964). It is assumed that  $\overline{u'^2} \approx \overline{v'^2} \approx \overline{w'^2}$  and that the turbulent shear stresses and the radial velocity component can be neglected. These assumptions result in the following equation for the axial flux of angular and axial momenta:

$$\dot{G}_\Theta = 2\pi\rho \int_0^R UW r^2 dr \quad (2.4)$$

$$\dot{G}_x = 2\pi\rho \int_0^R \left( U^2 - \frac{W^2}{2} \right) r dr. \quad (2.5)$$

Oberleithner et al. (2012a) showed that the required swirl number for the excitation of the PVC is slightly above the critical amount of swirl ( $S_{\text{crit}}$ ) for vortex breakdown to occur. If the swirl is strong enough, the flow undergoes a supercritical Hopf bifurcation and the PVC sets in. The amplitude of the PVC increases with increasing swirl number (Anacleto et al., 2002; Oberleithner et al., 2012a). At reacting conditions the situation is much more complex (Syred, 2006). In many cases, the PVC, which was present at isothermal conditions, is completely suppressed at reacting conditions (e.g., Giauque et al., 2005; Roux et al., 2005). In other cases it remained (Froud et al., 1995; Galley et al., 2011; Moeck et al., 2012) or the suppression depended on the operating conditions (Boxx et al., 2010b).

Recently, large progress in the understanding of the PVC was made by its interpretation as a global hydrodynamic mode (Liang and Maxworthy, 2005; Gallaire et al., 2006; Oberleithner et al., 2011). This interpretation allows for the use of hydrodynamic stability theory to understand the underlying mechanisms for its occurrence and suppression. In terms of linear stability theory, a flow is either stable, unstable, or exactly critically stable. Figure 2.1 schematically depicts the stable and the unstable state. In the stable state, a small perturbation leads to an oscillation of a finite amplitude (the ball is dislocated from the center), but the oscillation is damped, and the amplitude the oscillation is zero in the time asymptotic behavior of the system. The system returns to a steady state (the ball returns to the center). In the representation of the unstable state, the displacement of the small ball has to be interpreted as the oscillation amplitude. A small disturbance leads to an oscillation of a finite amplitude (the ball is dislocated from the center). In contrast to the stable system, the oscillation amplitude is not reduced but grows in time with each periodic oscillation (the ball rolls down).

In strictly linear theory this would result in infinite amplitudes in the time asymptotic solution. However, in real systems (or flows) nonlinearities always restrict the growth of the amplitude when an equilibrium state of energy added to the system and energy dissipated by the system is reached. In this state the system has reached its limit-cycle. A very famous example of a global flow instability in its limit-cycle is the von Kármán vortex street, where alternating vortices are shed behind a cylinder (or behind an island, see Fig. 2.2) at a well-defined frequency (Wille, 1960) and create a sinusoidal wake. No external forcing is required, since the flow acts as a self-sustained oscillator.

In the present study, linear hydrodynamic stability theory is employed to investigate the occurrence of the PVC. Generally it has to be distinguished between global and local stability

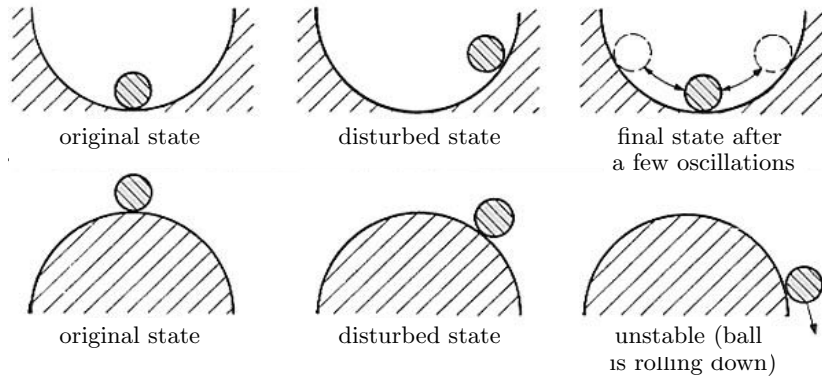


Figure 2.1: Schematic of global stability (top) and global instability (bottom). For an unstable oscillating system, the displacement of the small ball represents the amplitude of the oscillation. Reproduced from Cook (2007).

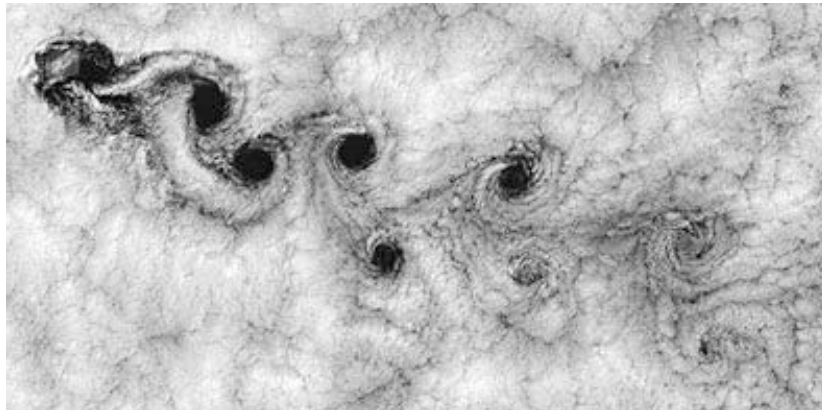


Figure 2.2: Example of global flow instability: A von Kármán vortex street leeward of an island in Chile. Source: NASA.

concepts. In the global concept (Theofilis, 2011), the stability of the entire flow field is calculated in one step. Global stability analysis is very precise but also requires very high computational efforts. With some assumptions (e.g., locally parallel flow, for details see Section 2.4), the global calculation can be transferred into a series of local calculations, where the flow field is sliced into radial slices and the calculations are carried out for every slice separately (Michalke, 1965). Beside the drastic reduction in computational costs, local analysis provides superior insight into the role of different flow sections for the occurrence of a hydrodynamic instability.

In the local stability concept, two different classes of unstable flow slices are possible. A flow slice is termed locally absolutely unstable if perturbations may grow in time at a fixed location (Fig. 2.3a). If a perturbation grows but is convected downstream, leaving its origin unperturbed, the flow slice is called convectively unstable and absolutely stable (Fig. 2.3b). Only absolutely unstable flow slices can lead to self-excited global flow instabilities, the so-called global modes, such as the PVC (Chomaz et al., 1988). The global mode is triggered by an inherent flow resonance (Liang and Maxworthy, 2005; Gallaire et al., 2006; Oberleithner et al., 2011, 2012a), and a necessary condition for the resonance is a sufficiently large region of absolutely unstable flow (Huerre and Monkewitz, 1990).

Since the global stability can be deduced from the local absolute stability (Chomaz et al., 1991), the local stability properties are essential for the self-excited global mode investigated in this thesis, the PVC. In isothermal flows, the growth rate of a convective instability mainly

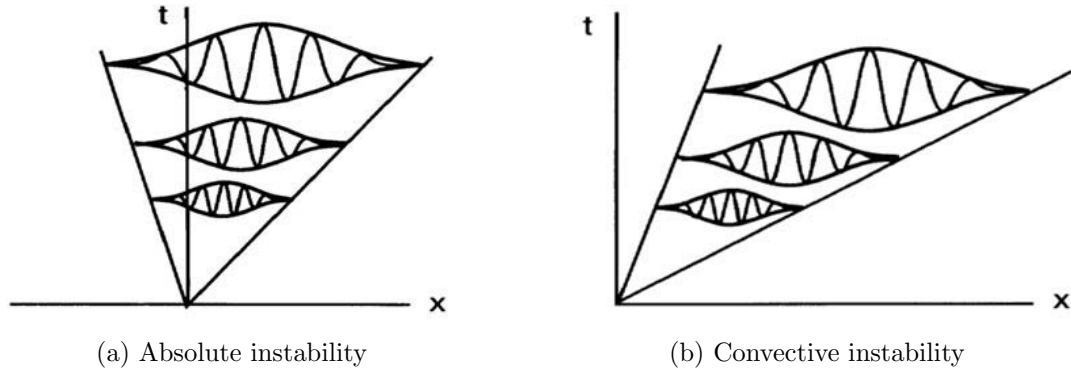


Figure 2.3: Schematic representation of an absolutely unstable flow and a convectively unstable flow. Reproduced from Oertel and Delfs (2005).

scales with the inverse of the shear layer thickness (Michalke, 1965). That is, the thinner the shear layers and the steeper gradients of the shear layer, the stronger is the amplification of a perturbation in the shear layer. The growth rate of an absolute instability, on the other hand, depends on both the shear layer thickness and the velocity level. Qualitatively speaking, the former determines the temporal growth rate and the latter the convective velocity. In a wake like profile, where the velocity deficit is high, or in a jet like profile with very low coflow or even counterflow, the perturbations convectively growing in the shear layers are not swept away but can grow in time at a fixed location. This results in an absolutely unstable flow. Thus, in general terms, a sufficiently large region of low or even negative velocities with strong shear make the flow prone to feature a global flow oscillation.

In the case of non-isothermal flows, not only the velocity distribution, but also the temperature/density field has a significant influence on the perturbation growth rates and consequently on the absolute instability. As shown by Monkewitz and Sohn (1988), a hot (low density) jet emanating in cold (high density) fluid is destabilized due to the density stratification. Consequently, a cold jet into a hot environment, as it is generally the case for a combustor flow, is stabilized. An explanation for this phenomenon was found by Soteriou and Ghoniem (1995), who showed that in the presence of density stratification, the convection speed of an instability is biased towards the velocity of the high-density stream. Thus, in the case of a hot jet and a cold wake, the convection speed is decreased, making the flow more prone to an absolute instability. In contrast to that, in the case of a cold jet and a hot wake, the convection speed is increased, making the flow less prone to an absolute instability.

## 2.2 Triple Decomposition

The cornerstone for the analysis of coherent structures in highly turbulent flows is the triple decomposition concept (Reynolds and Hussain, 1972). The time and space-dependent flow  $\mathbf{v}(\mathbf{x}, t)$  is decomposed into a time-averaged part,  $\mathbf{V}(\mathbf{x})$ , a part representing the coherent

fluctuations, such as the PVC,  $\mathbf{v}^c(\mathbf{x}, t)$ , and a randomly fluctuating (stochastic) part,  $\mathbf{v}^s(\mathbf{x}, t)$ .

$$\mathbf{v}(\mathbf{x}, t) = \mathbf{V}(\mathbf{x}) + \mathbf{v}^c(\mathbf{x}, t) + \mathbf{v}^s(\mathbf{x}, t) \quad (2.6)$$

The three components of Eqn. 2.6 are defined as

$$\mathbf{V}(\mathbf{x}) = \frac{1}{N} \sum_{n=0}^{N-1} \mathbf{v}(\mathbf{x}, t_n) \quad (2.7)$$

$$\mathbf{v}^c(\mathbf{x}, t) = \langle \mathbf{v}(\mathbf{x}, t) \rangle - \mathbf{V}(\mathbf{x}) \quad (2.8)$$

$$\mathbf{v}^s(\mathbf{x}, t) = \mathbf{v}(\mathbf{x}, t) - \langle \mathbf{v}(\mathbf{x}, t) \rangle, \quad (2.9)$$

where  $N$  is the number of measured (or simulated) velocity fields. The phase average  $\langle \cdot \rangle$  is defined as

$$\langle \mathbf{v}(\mathbf{x}, t) \rangle = \frac{1}{N} \sum_{n=0}^{N-1} \mathbf{v} \left( \mathbf{x}, t + \frac{n}{f} \right), \quad (2.10)$$

where  $f$  is the frequency of the coherent fluctuation and  $N$  the number of cycles used for the phase average.

In the present work the focus is placed on the coherent fluctuations  $\mathbf{v}^c(\mathbf{x}, t)$ . These fluctuations can be empirically extracted from experimental measurements or analytically modeled. Both approaches are employed in this thesis and will be presented in the following.

## 2.3 Empirical Mode Construction Using Proper Orthogonal Decomposition

The aim of the empirical mode construction is the extraction of the coherent velocity fluctuations from measured turbulent velocity fields. If the flow oscillates at a discrete frequency, such as a forced flow, equations 2.8 and 2.10 can be used to obtain the coherent fluctuations. If the phase ( $\theta$ ) of the coherent oscillation is known, for instance due to an observer (e.g., a time-resolved pressure signal (Gütke and Schuermans, 2007)), the coherent fluctuations are obtained as

$$\mathbf{v}^c(\mathbf{x}, \theta) = \frac{1}{N} \sum_{n=0}^{N-1} \mathbf{v}(\mathbf{x}, \theta + 2\pi n) - \mathbf{V}(\mathbf{x}). \quad (2.11)$$

However, the considered coherent structures associated with the PVC are self-excited flow oscillations. Thus, the phase of the velocity snapshots and the frequency of the oscillation is not known a priori. In the present thesis, instead of an observer, the proper orthogonal decomposition (POD) is used to construct the coherent fluctuations. The POD is a well-established technique in fluid mechanics (Berkooz et al., 1993), to extract coherent velocity fluctuations from experimental and numerical data of turbulent flows. It consists of the projection of  $N$  measured (or simulated) velocity fields on an orthogonal  $N$ -dimensional vector base that maximizes the turbulent kinetic energy content for any subset of the base. In other words, the POD modes provide a least-order expansion of the fluctuating flow field,

such as

$$\mathbf{v}(\mathbf{x}, t) = \mathbf{V}(\mathbf{x}) + \sum_{j=1}^N a_j(t) \Phi_j(\mathbf{x}) + \mathbf{v}_{res}(\mathbf{x}, t), \quad (2.12)$$

by minimizing the residual  $\mathbf{v}_{res}$ . The  $a_j(t)$  are called temporal POD coefficients, while the  $\Phi_j(\mathbf{x})$  are the spatial POD modes or simply POD modes. The amount of the fluctuating kinetic energy contained in each POD mode is given by

$$K_j = \overline{\langle \mathbf{v}, \Phi_j \rangle^2} / 2 = a_j^2 / 2, \quad (2.13)$$

with  $\langle \mathbf{v}, \Phi_j \rangle$  being the inner product of the vectors  $\mathbf{v}$  and  $\Phi_j$ .

The POD approach provides an orthogonal set of spatial and temporal modes that are energy ranked. The spatial modes  $\Phi_j(\mathbf{x})$  provide the shape of the mode, while the Fourier spectra of the POD coefficients  $a_j(t)$  readily reveal any dominant frequencies related to these modes. In the case of a coherent fluctuation in the flow field, the oscillating global mode is usually captured by two modes (Oberleithner et al., 2011) of similar coherent kinetic energy  $K_j$ , of the same dominant frequency, and with a corresponding spatial shape. If such two modes are encountered, the coherent velocity fluctuation  $\mathbf{v}^c$  can be reconstructed from the POD modes as

$$\mathbf{v}^c(\mathbf{x}, \theta) = \Re \left[ \sqrt{a_j^2 + a_k^2} (\Phi_j(\mathbf{x}) + i \Phi_k(\mathbf{x})) e^{-i\theta} \right] \quad (2.14a)$$

$$\mathbf{v}^c(\mathbf{x}, t) = \Re \left[ \sqrt{a_j^2 + a_k^2} (\Phi_j(\mathbf{x}) + i \Phi_k(\mathbf{x})) e^{-i\omega t} \right]. \quad (2.14b)$$

The frequency  $\omega$  of the global mode is obtained from the spectra of the time coefficients ( $a_j$  and  $a_k$ ) of the two POD modes  $j$  and  $k$  describing the global mode. In addition to the direct construction of the coherent fluctuations related to the global mode from Eqn. 2.14, the POD also yields a good estimation of the instantaneous phase of each velocity measurement and other simultaneously captured quantities. This procedure and its application will be further elucidated in Section 2.5.

## 2.4 Physical Mode Construction Using Local Linear Hydrodynamic Stability Theory

The approach to physically construct the coherent fluctuations is fundamentally different from the empirical technique presented in the preceding section. For the physical reconstruction the concept of linear hydrodynamic stability analysis is employed. This is possible since the PVC can be interpreted as a global hydrodynamic mode, whose excitation is determined by the stability of the flow.

### 2.4.1 Theory

The starting point for the stability analysis is the incompressible Navier-Stokes equation 2.15 and the incompressible continuity equation 2.16.

$$\frac{\partial \mathbf{v}}{\partial t} + \mathbf{v} \cdot \nabla \mathbf{v} = -\frac{1}{\rho} \nabla p + \frac{1}{Re} \nabla^2 \mathbf{v} \quad (2.15)$$

$$\nabla \cdot \mathbf{v} = 0 \quad (2.16)$$

Note that the density stratification is only considered in the momentum equation and the flow is regarded as incompressible. Under reacting conditions, however, the divergence of the flow field is not equal to zero, since the combustion causes some dilatation. The negligence of compressibility effects in the continuity equations was validated in the findings of Lesshafft and Huerre (2007). They calculated the stability of a compressible heated jet and compared the results of a full compressible stability analysis to stratified incompressible calculations. When only incompressible modes (i.e., not acoustic modes) were considered, both analyses yielded exactly the same results. Since the interest in this thesis is only placed on incompressible modes, the incompressible analysis (Eqn. 2.16) is justified.

Subsequently, the triple decomposition ansatz Eqn. 2.6 is substituted into the Navier-Stokes equation 2.15 and the continuity equation 2.16. By time-averaging, one obtains the governing equations for the mean field:

$$\mathbf{V} \cdot \nabla \mathbf{V} = -\frac{1}{\rho} \nabla P + \frac{1}{Re} \nabla^2 \mathbf{V} - \nabla \cdot (\overline{\mathbf{v}^c \mathbf{v}^c} + \overline{\mathbf{v}^s \mathbf{v}^s}) \quad (2.17)$$

$$\nabla \cdot \mathbf{V} = 0. \quad (2.18)$$

The term  $-\nabla \cdot (\overline{\mathbf{v}^c \mathbf{v}^c} + \overline{\mathbf{v}^s \mathbf{v}^s})$  determines how the mean flow field is changed due to the stochastic and coherent Reynolds stresses. Thus, if the analysis is carried out on the measured mean flow fields at the limit-cycle oscillation, the mean-coherent and the mean-turbulent interactions are already reflected in the mean flow field. The governing equations for the coherent fluctuations are obtained by subtracting the time-averaged equations of motion from the phase-averaged equations (Reynolds and Hussain, 1972). The continuity equation has to be fulfilled for each component of Eqn. 2.6.

$$\frac{\partial \mathbf{v}^c}{\partial t} + \mathbf{v}^c \cdot \nabla \mathbf{V} + \mathbf{V} \cdot \nabla \mathbf{v}^c = -\frac{1}{\rho} \nabla p^c + \frac{1}{Re} \nabla^2 \mathbf{v}^c - \nabla \cdot (\tau^R + \tau^N) \quad (2.19)$$

$$\nabla \cdot \mathbf{v}^c = 0 \quad (2.20)$$

In the framework of the linear stability analysis, the response of the flow to small-amplitude perturbations is calculated. Therefore, the non-linear term  $\tau^N = \mathbf{v}^c \mathbf{v}^c - \overline{\mathbf{v}^c \mathbf{v}^c}$  is neglected in the following assuming small-amplitude perturbations. The remaining term  $\tau^R = \langle \mathbf{v}^s \mathbf{v}^s \rangle - \overline{\mathbf{v}^s \mathbf{v}^s} = \widetilde{\mathbf{v}^s \mathbf{v}^s}$  is the difference between the phase-average and the time-average of the stochastic Reynolds stresses. It can be regarded as the oscillation of the stochastic Reynolds stresses due to the passage of the coherent perturbation (Reynolds and Hussain, 1972). To implement

these stresses, one has to find an appropriate model. Here, a Newtonian eddy viscosity model is employed

$$\tau^R = -\widetilde{u_i^s u_j^s} = \nu_t \left( \frac{\partial u_i^c}{\partial x_j} + \frac{\partial u_j^c}{\partial x_i} \right). \quad (2.21)$$

The indices  $i, j = 1, 2, 3$  represent the three velocity components and  $\nu_t$  is the eddy viscosity of the unperturbed flow (Reau and Tumin, 2002). To model these stresses, the eddy viscosity has to be estimated from the experimental results. For a three-dimensional flow, like the swirling jet, the turbulence is not isotropic. An optimal representation of  $\nu_t$  is obtained using a least-square fit over all resolved Reynolds stresses (Ivanova et al., 2012)

$$\nu_t = \frac{\left( -\overline{u_i^s u_j^s} + \frac{2}{3} k \delta_{ij} \right) \cdot \left( \frac{\partial U_j}{\partial x_i} + \frac{\partial U_i}{\partial x_j} \right)}{\left( \frac{\partial U_l}{\partial x_n} + \frac{\partial U_n}{\partial x_l} \right) \cdot \left( \frac{\partial U_l}{\partial x_n} + \frac{\partial U_n}{\partial x_l} \right)}, \quad (2.22)$$

where the turbulent kinetic energy  $k$  is introduced to avoid an inconsistency with the continuity equation, and the summation is done over the repeating indices  $i, j, l$ , and  $n = 1, 2, 3$ . Subsequently, the eddy-viscosity  $\nu_t$  is lumped into the Reynolds number  $Re_{\nu_t}$  and the well-known Orr-Sommerfeld equation is obtained as

$$\frac{\partial \mathbf{v}^c}{\partial t} + \mathbf{v}^c \cdot \nabla \mathbf{V} + \mathbf{V} \cdot \nabla \mathbf{v}^c = -\frac{1}{\rho} \nabla p^c + \frac{1}{Re_{\nu_t}} \nabla^2 \mathbf{v}^c. \quad (2.23)$$

In the local linear stability concept, the flow field is sliced into velocity profiles and the stability analysis is performed at each axial location separately. This approach is, in principal, only valid if the flow under consideration is strictly parallel. In contrast to this, the velocity fields of a swirling jet undergoing vortex breakdown exhibit a strong non-parallelity in the vortex breakdown region. Nevertheless, nonparallel effects are not incorporated into the stability analysis. The reason for this is twofold: First, progress in the analysis of the global mode has so far been made by applying the concept of a so-called wavemaker (e.g., Pier, 2002; Juniper, 2006; Gianetti and Luchini, 2007; Juniper et al., 2011). This is an intrinsically local concept, which is best described in the context of a local analysis. Second, the validity of the parallel analysis of significantly nonparallel flows has been demonstrated several times (e.g., Pier, 2002; Sevilla and Martínez-Bazán, 2004; Gallaire et al., 2006; Pier, 2008). Nevertheless, one has to find an a posteriori justification for the negligence of the nonparallel effects. This benchmark is the frequency of the global mode. For selected cases, furthermore, a comparison to a global analysis will be presented, where the non-parallelity is included in the analysis.

The treatment of the flow to be *locally parallel* allows for the decomposition of the coherent fluctuations into normal modes, which are periodic in time and two spatial directions

$$\mathbf{q}^c(\mathbf{x}, t) = \Re \left[ \hat{\mathbf{q}}(r) e^{i(\alpha x + m\Theta - \omega t)} \right]. \quad (2.24)$$



Here,  $\alpha$  is the complex streamwise wave number,  $\omega$  the complex frequency,  $m$  the real azimuthal wave number,  $\hat{\mathbf{q}} = [\hat{\mathbf{v}}, \hat{p}]^T$  the vector of amplitude functions,  $\mathbf{q}^c = [\mathbf{v}^c, p^c]^T$  the vector of the coherent perturbations, and  $\Re$  refers to the real part.

For a given mean velocity profile, equations 2.20, 2.23, and 2.24 can be solved with the appropriate boundary conditions. At the combustor wall, the no-slip condition yields:

$$\mathbf{v}^c = 0 \quad (2.25)$$

$$\frac{\partial p^c}{\partial r} = 0 \quad (2.26)$$

On the centerline ( $r = 0$ ), the enforcement of bounded and smooth physical quantities, as well as the fulfillment of the continuity equation, lead to the following set of boundary conditions (Khorrami et al., 1989):

$$\left. \begin{aligned} \mathbf{v}^c = (v_x^c, v_r^c, v_\Theta^c)^T &= (0, 0, 0)^T \\ p^c &= 0 \end{aligned} \right\} \quad \text{if } |m| > 1 \quad (2.27)$$

$$\left. \begin{aligned} v_x^c &= p^c \\ v_r^c + mw^c &= 0 \\ \frac{2\partial v_r^c}{\partial r} + m\frac{2\partial v_\Theta^c}{\partial r} &= 0 \end{aligned} \right\} \quad \text{if } |m| = 1 \quad (2.28)$$

$$\left. \begin{aligned} v_r^c &= v_\Theta^c \\ v_x^c \text{ and } p^c &\text{ finite} \end{aligned} \right\} \quad \text{if } m = 0. \quad (2.29)$$

Here, the velocity vector in cylindrical coordinates  $(v_x, v_r, v_\Theta)^T$  corresponds the velocity vector  $(u, v, w)^T$  in Cartesian coordinates. In the resulting eigenvalue problem

$$\mathbf{A}(\alpha)\hat{\mathbf{q}} = \omega\mathbf{B}(\alpha)\hat{\mathbf{q}}, \quad (2.30)$$

the matrices  $\mathbf{A}$  and  $\mathbf{B}$  become

$$\begin{aligned} \mathbf{A} &= \begin{pmatrix} \mathcal{L} & \frac{\partial V_x}{\partial r} & 0 & \frac{i\alpha}{\rho} \\ 0 & \mathcal{L} + \frac{1}{\text{Re}\nu_t r^2} & -\frac{2V_\Theta}{r} + \frac{2im}{\text{Re}\nu_t r^2} & \frac{\mathcal{D}_r}{\rho} \\ 0 & \frac{\partial V_\Theta}{\partial r} + \frac{V_\Theta}{r} - \frac{2im}{\text{Re}\nu_t r^2} & \mathcal{L} + \frac{1}{\text{Re}\nu_t r^2} & \frac{im}{\rho r} \\ i\alpha & \frac{1}{r}\mathcal{D}_r & \frac{im}{r} & 0 \end{pmatrix}, \\ \mathbf{B} &= \begin{pmatrix} i & 0 & 0 & 0 \\ 0 & i & 0 & 0 \\ 0 & 0 & i & 0 \\ 0 & 0 & 0 & 0 \end{pmatrix}. \end{aligned} \quad (2.31)$$

Here,  $\mathcal{L} = V_x i\alpha + \frac{W}{r} im - \frac{1}{\text{Re}\nu_t} \left( \frac{1}{r}\mathcal{D}_r + \mathcal{D}_{rr} - \frac{m^2}{r^2} - \alpha^2 \right)$  and  $\mathcal{D}_r$  and  $\mathcal{D}_{rr}$  represent the first and second order derivative operators with respect to  $r$ , respectively.

Equation 2.30 can be solved for complex  $\omega$  given real  $\alpha$ , for complex  $\alpha$  given real  $\omega$ , or for complex  $\omega$  given complex  $\alpha$ . The first approach is called temporal analysis and provides the temporal growth ( $\omega_i > 0$ ) or decay ( $\omega_i < 0$ ) of a perturbation that is convected along the shear layer. It is best suited for the analysis of flows with negligible convective velocities like the Taylor-Couette flow.

The second approach is called spatial analysis and yields spatially growing ( $\alpha_i > 0$ ) or decaying modes ( $\alpha_i < 0$ ). It is most appropriate for the study of convectively unstable shear flows that act as noise amplifiers (Michalke, 1965)

The third approach, where the eigenvalue problem is solved for complex  $\alpha$  and complex  $\omega$  is termed spatio-temporal analysis. With this approach the growth and decay of perturbations in time and in streamwise direction is considered. The spatio-temporal analysis is suitable for the analysis of self-excited instabilities because it allows for the important distinction between a convectively unstable wavepacket and an absolutely unstable wavepacket (see Fig. 2.3). A convectively unstable wavepacket can only grow in downstream direction from its point of origin. In contrast, an absolutely unstable wavepacket can grow in up- and downstream direction of its origin. Only this type of instability can contaminate the entire flow in the limit of infinite time. It is therefore the only instability that may cause the flow to oscillate at a well-defined frequency in the absence of external excitation. Self-excited instabilities occur frequently in wakes (Provansal et al., 1987; Monkewitz, 1988), hot jets (Monkewitz and Sohn, 1988), and also in strongly swirling jets (Liang and Maxworthy, 2005; Gallaire et al., 2006; Oberleithner et al., 2011).

The cornerstone of the spatio-temporal analysis is the mapping of complex wavenumbers onto the complex frequencies via the stability eigenproblem (Eqn. 2.30) and the identification of saddle points, at which the long term behavior of a disturbance is determined Briggs (1964). The reason for this is that the time-asymptotic response to a disturbance takes the form of a wavepacket. One important feature of a wavepacket is its group speed. To determine whether an instability is absolute or convective, one is interested in the wave with vanishing group velocity. The group velocity is the derivative of the frequency with respect to the wavenumber and this is precisely the condition for a saddle point. The saddle point is numerically searched by minimizing the functional  $F = (\partial\omega_i/\partial\alpha_r)^2 + (\partial\omega_i/\partial\alpha_i)^2$ . The frequency at a saddle point is called the absolute frequency  $\omega_0$ . The imaginary part of the absolute frequency  $\omega_{0,i}$  is the absolute growth rate and determines the nature of the instability. If  $\omega_{0,i} < 0$  the instability is convectively unstable, if  $\omega_{0,i} > 0$  the instability is of an absolute nature. If the flow slice is absolutely unstable, the real part of the absolute frequency  $\omega_{0,r}$  would be the oscillation frequency of a fictitious parallel flow constituted only of this absolutely unstable flow profile.

If the flow is (weakly) nonparallel, the global oscillation frequency and growth rate has to be derived from the evolution of the absolute frequency along the axis. It was shown for wake flows, as in the present study, that the limit-cycle oscillation is most accurately predicted if the stability analysis is carried out on the mean flow field at limit-cycle and a linear frequency selection criterion is applied (Pier, 2002; Barkley, 2006). A necessary condition for the flow to be linearly globally unstable is the existence of a region of absolute instability, which is

sufficiently long (Chomaz et al., 1991). If such a region of absolute instability is present, one can derive the global instability from the local analysis. A criterion for the linear global mode frequency  $\omega_g$  is given by the saddle point criterion (Chomaz et al., 1991)

$$\omega_g = \omega_0(x_s) \quad \text{with} \quad \frac{d\omega_0}{dx}(x_s) = 0. \quad (2.32)$$

This criterion is often not fulfilled along the real  $x$ -axis, since the real and imaginary part of  $\omega_0$  do not necessarily have their maxima or minima at the same  $x$  location. Therefore, in order to fulfill the saddle point criterion, the absolute growth rate curve is continued analytically into the complex  $x$ -plane. This can be accomplished by fitting a rational polynomial to the curve on the real  $x$ -axis and evaluating it in the complex  $x$ -plane. The real part of the frequency at this saddle point determines the frequency and the imaginary part of the frequency determines the growth rate of the global mode. If  $\omega_{g,i} > 0$ , the flow is globally unstable, oscillating at  $\omega_{g,r}$ , while the flow is globally stable for  $\omega_{g,i} < 0$ .

Once the global frequency is determined,  $\mathbf{v}^c$  is reconstructed by solving the system of equations (2.20, 2.23, and 2.24) with  $\omega = \omega_{g,r}$ . The spatial shape of the global mode  $\mathbf{v}^c$  is calculated from the local amplitude functions  $\hat{\mathbf{v}}$  by integrating the spatial growth rates  $\alpha$  from a spatial local analysis.

$$\mathbf{v}^c(\mathbf{x}, t) = \Re \left[ A_0 \hat{\mathbf{v}}(\mathbf{x}) e^{i \left( \int_0^x \alpha(\xi) d\xi + m\theta - \omega t \right)} \right] \quad (2.33)$$

If forced structures are to be analyzed instead of self-excited structures, the spatial analysis can be directly carried out with  $\omega$  determined by the forcing frequency. Subsequently, Eqn. 2.33 is employed to recover the spatial shape of the forced oscillation. The oscillation amplitude depends on the excitation amplitude and phase which determines the factor  $A_0$ . Note that the eigenmodes  $\hat{\mathbf{v}}(\mathbf{x})$  stem from the eigenvalue problem 2.30. Thus, their magnitude depends on the applied norm, while their relative phase is unknown a priori. For the construction of the global mode shape, the magnitude of the eigenvectors is scaled with the 2-norm and their phase (before the application of Eqn. 2.33) is adjusted to achieve a maximum correlation with the corresponding upstream eigenvector. Thereby, the phase and magnitude of the constructed mode only stem from the evolution of the complex wavenumber  $\alpha(x)$ .

### 2.4.2 Numerical Implementation and Procedure

The numerical implementation of the solution of the eigenvalue problem closely follows the implementation by Oberleithner et al. (2011, 2013). The Orr-Sommerfeld operator is discretized using a Chebyshev pseudospectral collocation technique (Khorrami et al., 1989) and the eigenvalue problem is solved using the MATLAB<sup>TM</sup> routine EIG. Once the suitable eigenvalue and eigenmode has been identified, it is efficiently tracked using the MATLAB<sup>TM</sup> Arnoldi-iteration-based routine EIGS.

For the determination of the required number of collocation points ( $N_{\text{cheb}}$ ), a sensitivity analysis was carried out with a typical combustor flow profile. The dependence of the most

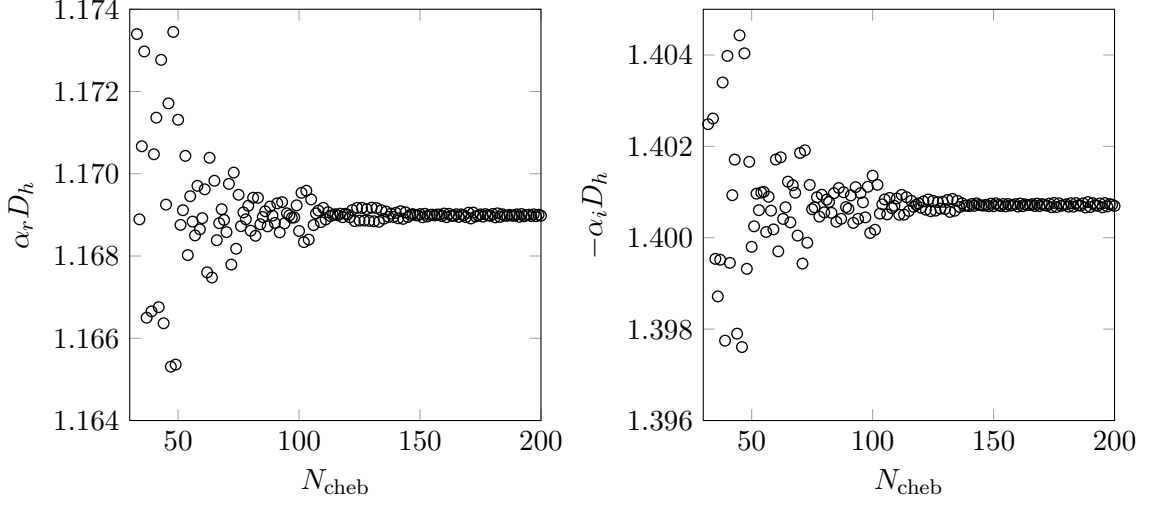
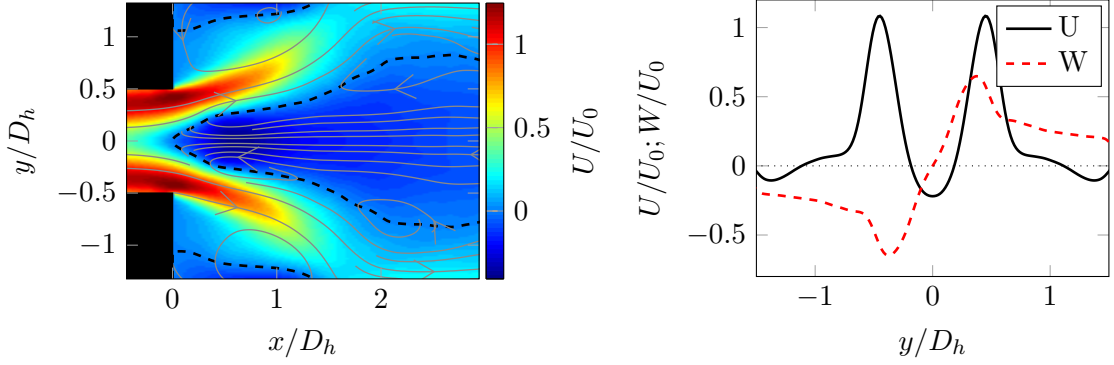


Figure 2.4: Convergence of the spatial linear stability analysis for increasing number of collocation points ( $N_{\text{cheb}}$ ).



(a) Streamlines imposed on the normalized axial velocity. Dashed lines indicate zero axial velocity.

(b) Radial profiles of axial ( $U$ ) and tangential ( $W$ ) velocity extracted at  $x/D_h = 0.29$ .

Figure 2.5: Flow field and flow profile for the exemplarily presented stability analysis.

unstable eigenvalue of the spatial analysis on the number of collocation points is shown in Fig. 2.4. It is evident that the eigenvalues converge for  $N_{\text{cheb}} > 120$ , whereas for  $N_{\text{cheb}} < 75$  the eigenvalues show some variance in the order of 0.5% of the converged value. In the present study, a value of  $N_{\text{cheb}} = 180$  is chosen, where the eigenvalues are well converged.

In the following the steps for the spatio-temporal stability analysis will be presented exemplarily for the swirling combustor flow shown in Fig. 2.5a. The first step is the temporal analysis of one flow slice (see Fig. 2.5b) for a given value of the axial wavenumber  $\alpha$  and an azimuthal wavenumber  $m$ . Employing Eqn. 2.30, the eigenvalue spectrum for an axial wavenumber of  $\alpha = 1$  and the azimuthal wavenumber  $m = 1$  is calculated and presented in Fig. 2.6. It is evident that most of the eigenvalues are stable ( $\omega_i < 0$ ). However, the

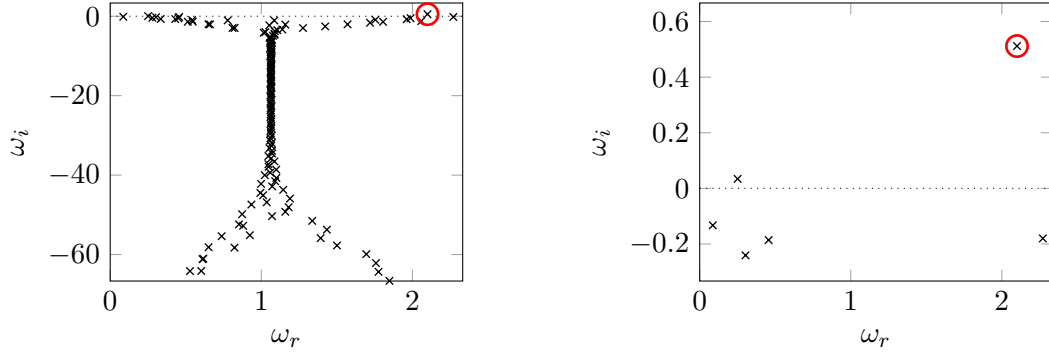


Figure 2.6: Eigenvalue spectrum of the temporal analysis of the profiles shown in Fig. 2.5b for a real axial wavenumber of  $\alpha = 1$  and an azimuthal wavenumber of  $m = 1$ . Right picture shows a close-up view containing the most unstable eigenvalue( indicated by the red circle).

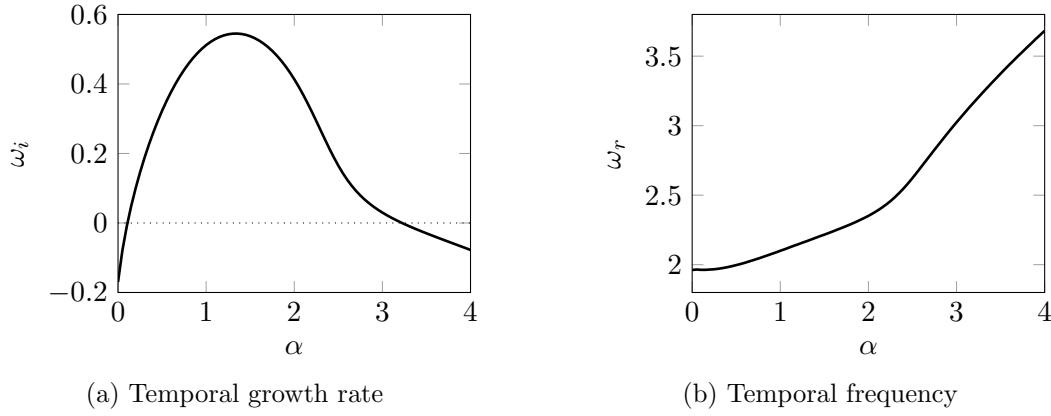


Figure 2.7: Growth rate  $\omega_i$  and frequency  $\omega_r$  of the eigenmode indicated by the red circle in Fig. 2.5 for a variation of the real axial wavenumber  $\alpha$ .

close-up view reveals two unstable modes. The eigenvector of the marginally unstable mode at  $\omega = 0.25 + 0.03i$  (not shown here) shows that this mode is dominated by the outer shear layer. Furthermore, it gets quickly stable at more downstream positions. The most unstable mode indicated by the red circle at  $\omega = 2.10 + 0.51i$  is mainly located in the inner shear layer (eigenvector is not shown) and is the mode of interest for the following investigations.

In the next step, the identified eigenmode is tracked for a variation of the axial wavenumber  $\alpha$ . This is shown for real values of  $\alpha$  in Fig. 2.7. This figure shows the dispersion relation of  $\alpha$  to  $\omega$  and provides information about the temporal amplification ( $\omega_i$ ) and the oscillation frequency ( $\omega_r$ ) of instabilities of different axial wavelengths ( $\alpha$ ). It is evident that the perturbations are most amplified for  $\alpha \approx 1.25$ . However, in the present example, the focus is placed on the identification of self-excited instabilities, such as the PVC. Therefore, the instability with a vanishing group velocity has to be found. This is numerically done by searching for a saddle point of  $\omega$  in the complex  $\alpha$ -plane. This is demonstrated in Fig. 2.8, where the saddle point at  $\alpha_0 = 1.34 - 0.41i$  is depicted. The complex frequency at this point, the absolute

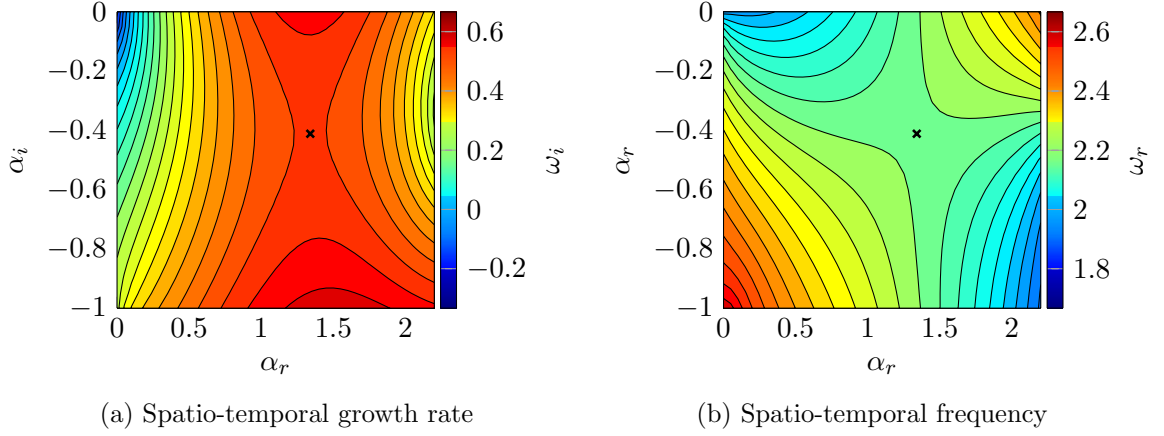


Figure 2.8: Identification of the absolute growth rate  $\omega_i$  and absolute frequency  $\omega_r$  of the eigenmode indicated by the red circle in Fig. 2.5. The black cross indicates the identified saddle point in the complex  $\alpha$ -plane.

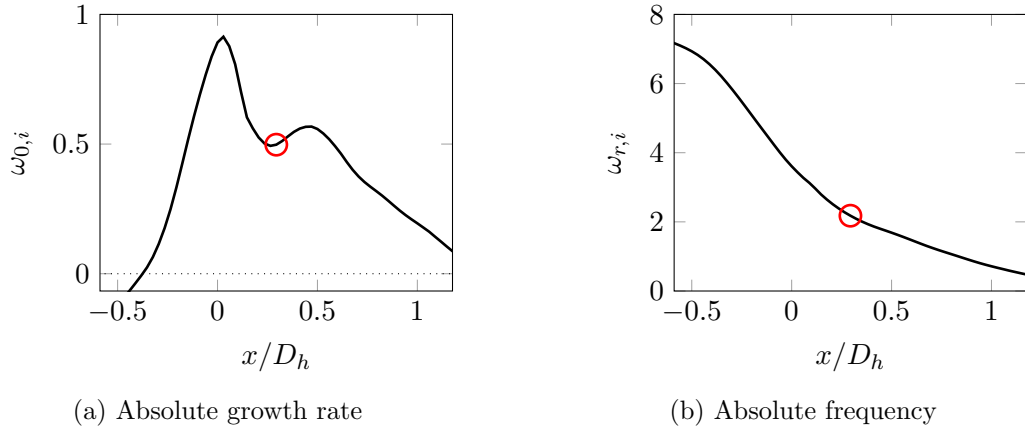


Figure 2.9: Axial evolution of the absolute growth rate  $\omega_{0,i}$  and frequency  $\omega_{0,r}$ . Red circles indicate the absolute frequency and growth rate identified from Fig. 2.8 for  $x/D_h = 0.29$ .

frequency, is  $\omega_0 = \omega(\alpha_0) = 2.18 + 0.50i$ . Thus,  $\omega_{0,i}$  is positive, and the flow slice is absolutely unstable.

In order to extend the investigation from the flow slice to the complete flow field, the absolute frequency has to be identified for each flow slice. Since the manual identification at every flow slice is a very cumbersome task, a search strategy is employed, where the result of one slice is the starting point for the neighboring flow slice. Details about the very efficient iterative search procedure are provided by Rees (2009). The results of the tracking of the complex absolute frequency are provided in Fig. 2.9 for the example flow field. A large region of absolute instability ( $\omega_{0,i} > 0$ ) is evident, whereas the absolute frequency  $\omega_{0,r}$  decays monotonically. In order to obtain a smooth transition of  $\omega_0$  at the area jump at  $x = 0$ , the

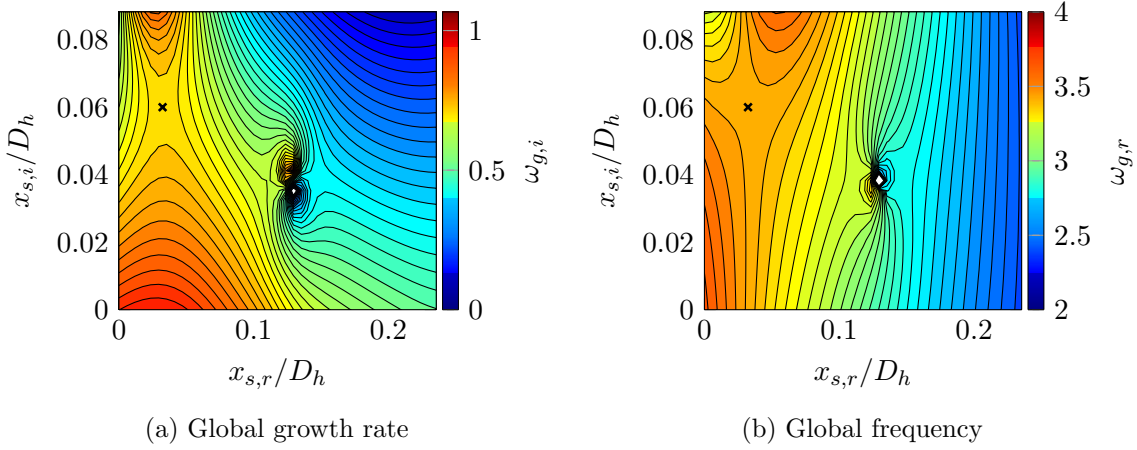


Figure 2.10: Extrapolation of the absolute growth rate  $\omega_{0,i}$  and frequency  $\omega_{0,r}$  onto the complex  $x$ -plane and identification of the global growth rate  $\omega_{g,i}$  and frequency  $\omega_{g,r}$  at the saddle point. The black cross indicates the identified saddle point. Values of  $\omega_0$  for  $x_i = 0$  correspond to Fig. 2.9.

radius for the imposition of the boundary conditions was linearly increased from  $y = 0.5D_h$  to  $y = 1.54D_h$  over a region extending from  $x = 0$  to  $x = 0.1D_h$ .

The final step for the determination of the global stability of the flow field, i.e., the prediction whether the flow field develops a self-sustained oscillation, is the application of the frequency selection criterion (Eqn. 2.32). This criterion is based in the determination of saddle points of the absolute frequency. It is evident from Fig. 2.9 that the real and imaginary part of  $\omega_0(x)$  have no common minima or maxima. Therefore, in order to find saddle points,  $\omega_0(x)$  has to be extrapolated onto complex values of  $x$  (Chomaz et al., 1991). To this end, a rational polynomial is fitted to  $\omega_0(x)$  at the real  $x$ -axis and is subsequently evaluated at complex values of  $x$ . The results are presented in Fig. 2.10. Saddle points at  $x_s/D_h = 0.032 + 0.06i$  and  $x_s/D_h = 0.112 + 0.038i$  are evident. When  $\omega_0(x)$  is evaluated in the complex  $x$ -plane, frequently more than one saddle point can be observed. It is therefore crucial to identify the dominating saddle point. In the present work, rational polynomials of different orders are fitted to  $\omega_0(x)$  at the real  $x$ -axis. The saddle points that mainly depended on the fitting, such as the saddle close to the singularity at  $x/D_h = 0.12 + 0.041i$ , significantly change their location when the order of the fitted polynomials is changed. In contrast to that, the physical saddle point at  $x_s/D_h = 0.032 + 0.06i$  remains virtually constant when the degree of the fitted rational polynomial is varied. The absolute frequency at this saddle point is termed the global frequency  $\omega_g = \omega_0(x_s) = 3.42 + 0.71i$ . Since the imaginary part  $\omega_{g,i}$  is positive, the flow is predicted to be globally unstable and to be oscillating at the frequency determined by  $\omega_{g,r}$ . In terms of Hz,  $\omega_{g,r}$  corresponds to a frequency of  $f = \omega_{g,r}U_0(2\pi D_h)^{-1} = 23.99$  Hz, which is close to the empirically obtained frequency of  $f = 24.72$  Hz. The good frequency match is important to show that, despite the multitude of simplifications made for the sta-

bility analysis (e.g., parallel flow, isotropic turbulence, small amplitude oscillations), it is still able to capture the most important flow dynamics.

In the local stability framework, also a second frequency selection criterion was proposed (Chomaz et al., 1988; Chomaz, 2005) when the absolutely unstable region appears at the inlet and is a few wavelengths long. In this case, the frequency is not selected at the saddle point, as defined in Eqn. 2.32, but at the flow inlet. It may be argued that the area jump at  $x/D_h = 0$  can be regarded as a new flow inlet. In this case the global frequency is predicted as  $f = \omega_{0,r}(x=0)U_0(2\pi D_h)^{-1} = 25.33$  Hz. Since the saddle point frequency selection criterion already located the wavemaker in the vicinity of the area jump, both frequency selection criteria yield similar frequencies.

## 2.5 Data Treatment

In the scope of this thesis, different methods of data treatment were employed in order to prepare the data for the stability analysis, perform a-posteriori phase averaging, and investigate the flow field dynamics. The most important techniques will be presented briefly in the following.

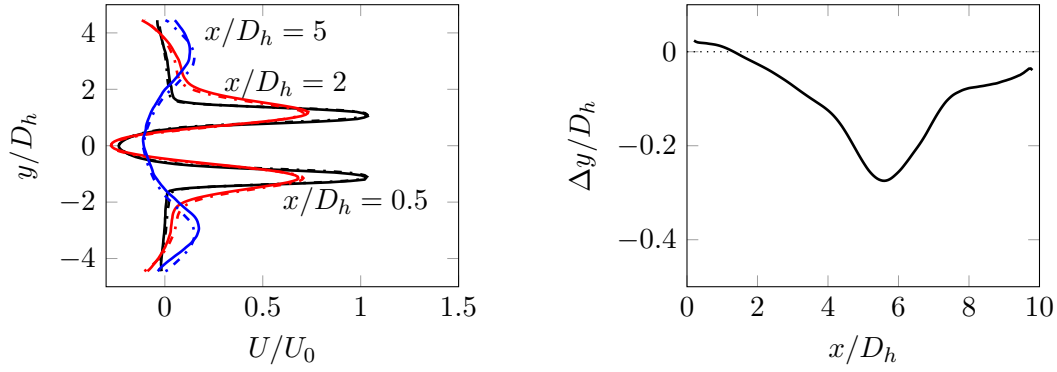
### 2.5.1 Spatial Averaging

The geometry of the swirl-stabilized combustors investigated in the scope of this thesis is basically axisymmetric. However, swirling jets are known to show more pronounced asymmetries than non-swirling jets even in the absence of strong geometric deviations from perfect axisymmetry (Escudier et al., 2006). An explanation for this phenomenon was recently found by Oberleithner et al. (2014). They showed that the addition of swirl increases the ability of the flow field to promote steady modes at considerably high amplification rates. These modes do not rotate with the mean flow but rather appear as asymmetries of the mean flow. This behavior is observed, to a limited extent, also in this thesis. Figure 2.11a shows examples of radial profiles of the time-averaged axial velocity. For the profiles close to the combustor inlet, only very small deviations from perfect symmetry are present, whereas the downstream profile at  $x/D_h = 5$  shows a perceivable asymmetry. In this thesis a strategy was applied to eliminate even these weak asymmetries. The reason for this is that for the analytical assessment of the flow field using linear stability analysis, rotational symmetry is an important prerequisite.

The averaging process contains two steps. First, the deviation of the flow field center from the geometrical center  $\Delta y$  is determined for every flow slice. This is done by maximizing the correlation between the radial profile of the axial velocity with the same profile shifted by  $\Delta y$  and mirrored with respect to the combustor centerline.

$$R_c(x, \Delta y) = \frac{\int_0^R U(y, x)U(-y + \Delta y, x)dy}{\sqrt{\int_0^R U(y, x)^2 dy \int_0^R U(-y + \Delta y, x)^2 dy}} \quad (2.34)$$





(a) Comparison of measured axial velocity profiles with slight asymmetries (solid lines) to the symmetric profile with spatial averaging (dashed lines).

(b) Deviation  $\Delta y$  of the flow center from the geometrical center.

Figure 2.11: Example of the spatial averaging of the flow field.

The evolution of  $\Delta y(x)$  for the exemplary flow field is shown in Fig. 2.11. Again, it can be observed that the center of symmetry of the flow is very close to the geometrical centerline near the combustor inlet. Only in a region of  $3 < x/D_h < 8$  stronger deviations are evident and are to be corrected by the spatial averaging:

$$\tilde{U}(x, y) = 0.5 (U(x, y) + U(x, -y + \Delta y(x))) \quad (2.35)$$

$$\tilde{V}(x, y) = 0.5 (V(x, y) - U(x, -y + \Delta y(x))) \quad (2.36)$$

$$\tilde{W}(x, y) = 0.5 (W(x, y) - U(x, -y + \Delta y(x))). \quad (2.37)$$

For the sake of simplification the superscript  $\widetilde{(\cdot)}$ , is omitted in the remainder of this thesis.

### 2.5.2 Phase Averaging of Data Using POD

In a flow field with turbulent and coherent periodic fluctuation, the coherent velocity fluctuations  $\mathbf{v}^c$  (see Eqn. 2.6) can be empirically obtained via a POD when the outcome of the POD is sufficiently clear. Here, *sufficiently clear* means that the POD yields two modes of a similar spatial shape, and whose temporal coefficients oscillate at the same frequency but shifted in time by a quarter period. An example for a POD analysis that clearly identifies an oscillating coherent structure is provided in Fig. 2.12. The first two modes span a convective vortex pattern. Analogously to a traveling sine wave, expressed by a superposition of a sine and cosine, the global flow oscillation is expressed by a superposition of these two POD modes. Consistently, the time traces of the temporal POD coefficients  $a_1$  and  $a_2$  show a sinusoidal oscillation and  $a_2$  has a time-lag of a quarter wavelength with respect to  $a_1$ .

If  $a_2$  is plotted versus  $a_1$ , one obtains a so-called Lissajous plot. The circular shape is evident and a direct result of the similar amplitudes of  $a_1$  and  $a_2$  and the constant phase difference between  $a_1$  and  $a_2$  of  $\pi/2$ . Similar to the phase plot of a pendulum (speed vs.

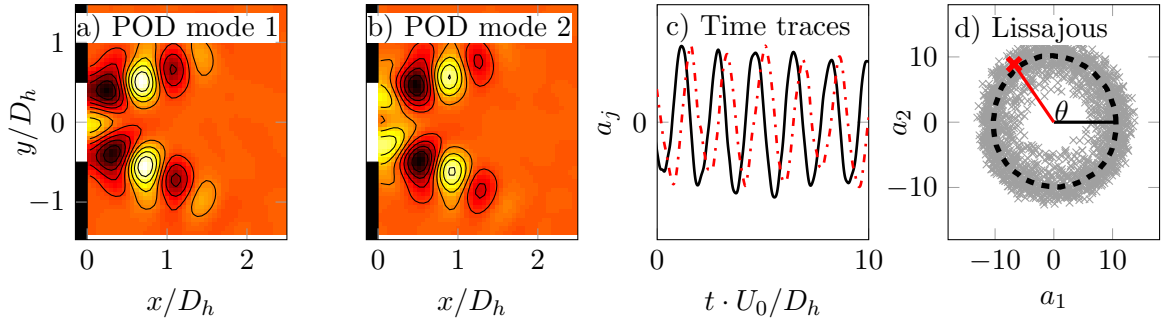


Figure 2.12: Example of the POD results for a single-tone coherent structure that is used for a-posteriori phase averaging.

displacement angle), the angle of each point (in polar coordinates) is identical to the phase angle  $\theta$  of the oscillation.

$$\theta(t) = \arg(a_1(t) + ia_2(t)) \quad (2.38)$$

Thus, from the representation shown in Fig. 2.12d, the phase angle  $\theta$  corresponding to each measurement point can be obtained. This technique has been very successfully employed for swirling jets (Oberleithner et al., 2011) and swirling flames (Stöhr et al., 2011b; Dolan et al., 2014). Its big advantage is that no time-resolved observer is required, as for conventional a-posteriori phase averaging (e.g., Güthe and Schuermans, 2007). If the velocity data itself is time-resolved, one could also use a velocity time-series at one characteristic point as the observer. Compared to this approach, phase averaging using POD provides significantly better results since the complete flow field is used to extract the phase information. Moreover, no selection of a characteristic point for the phase extraction is required.

Once the phase angle is obtained, it is used for phase averaging. Since the measurements are taken at discrete times and are limited in their number, the direct phase averaging using Eqn. 2.10 cannot be employed. The employed approach is to calculate the average of all measurements whose phases fall into a certain interval around the phase to be obtained. Usually, a phase overlap of 50% is used to increase the number of data points available for each phase calculation.

Different quantities, such as the velocity field and heat release distribution, are often measured simultaneously. In this case, the phase angle obtained for one quantity, in the present thesis the velocity field, is used also for the phase averaging of the heat release distribution.

### 2.5.3 Spectra and POD of Symmetric and Antisymmetric Fluctuations

The spectra of velocity fluctuations are conveniently calculated by means of a fast Fourier transform (FFT). In the present study the focus is either placed on forced axisymmetric fluctuations with an azimuthal wavenumber of  $m = 0$  or on self-excited helical oscillations ( $m = 1$ ). In the case of axisymmetric oscillation, Eqn. 2.24 obviously yields that the planar representation of the coherent fluctuation for  $y$  and  $-y$  (i.e., for  $\Theta$  and  $\Theta + \pi$  in cylindrical coordinates) is in phase. Consequently, for the helical coherent structures, the upper half

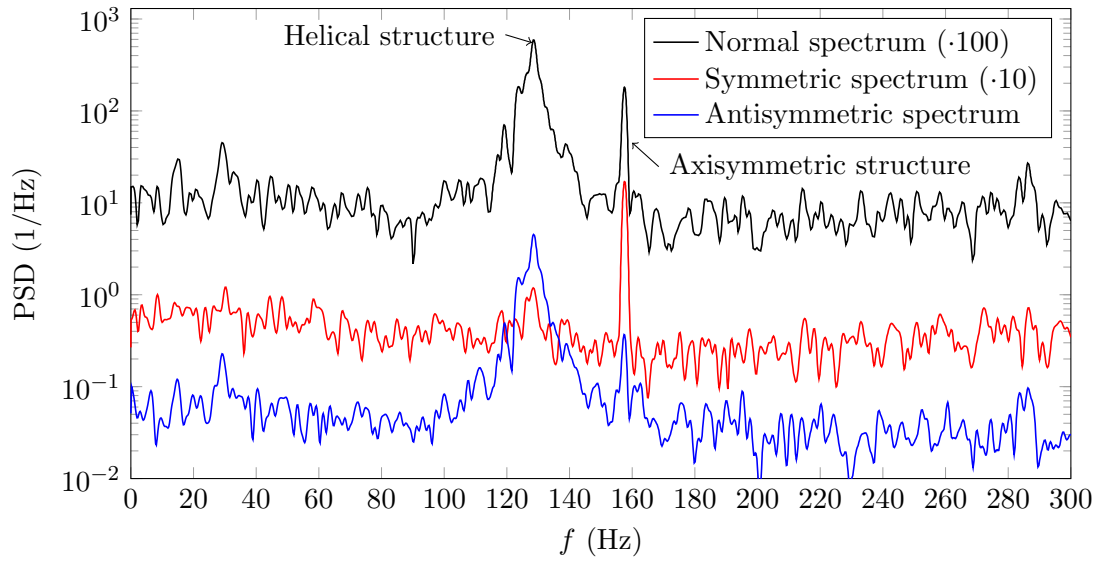


Figure 2.13: Examples of symmetric and antisymmetric spectra for a flow field, which features helical and axisymmetric coherent structures. To enhance the clarity of the representation, the normal spectrum and the symmetric spectra are multiplied by factors of 100 and 10, respectively.

( $y > 0$ ) and the lower half ( $y < 0$ ) are  $180^\circ$  out of phase. Thus, a summation of both sides of the instantaneous velocity fields eliminates the coherent fluctuation of the helical mode, and the subtraction of both sides eliminates the axisymmetric fluctuations. In the following the term *symmetric spectrum* is used for the spectrum of the sum of the upper and lower half of the instantaneous velocity fields and the term *antisymmetric spectrum* denotes the spectrum of the difference of the upper and lower half of the instantaneous velocity fields. The concept is shown for a flow field that features both self-excited helical (at 128 Hz) and forced axisymmetric oscillations (at 158 Hz) in Fig. 2.13. The normal spectrum of the velocity fluctuations shows peaks at both frequencies. In contrast to that, the symmetric spectrum only captures the peak of the helical mode at 128 Hz, whereas the symmetric spectrum only captures the forced oscillations at 158 Hz. Minor contributions of the helical structure to the symmetric spectrum, and vice versa, are presumably caused by non-perfect axisymmetric, and antisymmetry, respectively. The calculation of symmetric and antisymmetric spectra provides a very convenient way to assess the contribution of helical and forced coherent structures to the flow field dynamics. In the same way, a POD analysis of solely the symmetric and antisymmetric fluctuations can be carried out in order to provide additional insight into the flow field dynamics.

Care has to be taken when flows are investigated that feature helical fluctuations of an azimuthal order of  $|m| = 2$  and higher. The planar representation of modes of even (odd) azimuthal numbers is purely (anti)symmetric. Therefore, their oscillation is lumped in the (anti)symmetric spectra. In the investigated flows, however, the main contribution consists

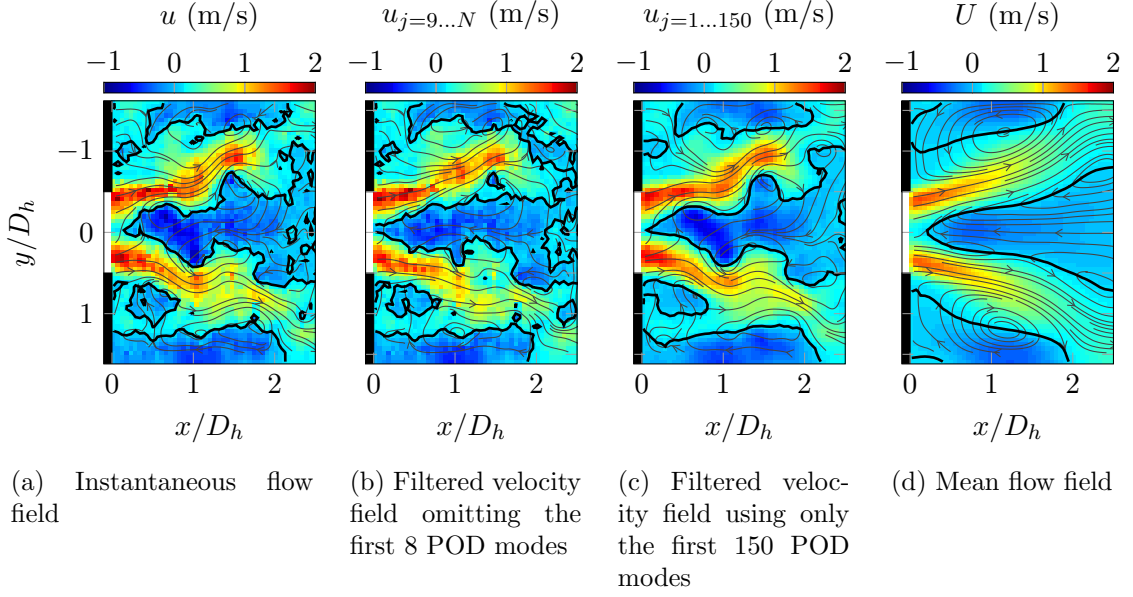


Figure 2.14: Examples of flow field filtering using POD. Streamlines of the non-reacting combustor flow are imposed on the axial velocity distribution. Thick black lines indicate zero axial velocity.

of axisymmetric and single helical structures. The contribution of higher azimuthal modes ( $|m| > 1$ ) is assumed to be negligible.

#### 2.5.4 Flow Field Filtering Employing POD

The decomposition of the turbulent flow fields into energy sorted spatial POD modes allows for the filtering of the instantaneous flow fields. The flow field at every time step is exactly represented by a linear combination of the spatial POD modes

$$\mathbf{v}(\mathbf{x}, t) = \mathbf{V}(\mathbf{x}) + \sum_{j=1}^N a_j(t) \Phi_j(\mathbf{x}). \quad (2.12)$$

The first modes capture most of the turbulent kinetic energy, which is often related to large-scale structures. The higher modes usually capture the smaller incoherent scales that have lower energy contents. By reconstructing the instantaneous flow fields based on a cropped number of POD modes, the instantaneous flow fields can be decomposed into different scales (Adrian et al., 2000). This procedure is demonstrated in the example provided in Fig. 2.14. In the instantaneous flow field, both the small-scale noise and the contribution of large-scale fluctuations are visible. If the instantaneous flow field is reconstructed omitting the first modes, most of the large-scale fluctuations are eliminated and the flow field features some similarity to the mean flow field with added noise. The operation works similar to a high-pass filter on the velocity fluctuations. In contrast to that, the construction of the instantaneous

flow field considering only the first modes shows very little small-scale noise, whereas the large-scale fluctuations remain visible. Consequently, this filtering approach has the effect of a low-pass filter.

In the present thesis the high-pass filtering technique is employed for the estimation of the eddy viscosity, as provided in Eqn. 2.22. To avoid the contribution of the coherent fluctuations to the estimation, the instantaneous flow fields are reconstructed omitting the first eight POD modes. Note that the specific number of eight modes is not physical but was found to be a good guess for the modes describing large-scale structures (Lacarelle, 2011). For the representation of instantaneous velocity fields in Chapter 7, the low-pass technique is employed to enhance the perceptibility of the images.



## Chapter 3

# Experimental Approach

In the following the different combustor types investigated in the scope of this thesis are presented. Subsequently, the test rigs and their instrumentation are briefly introduced. Furthermore, an overview about the employed measurement techniques, including a newly development technique for spatially resolved density estimations, is provided.

### 3.1 Swirl-Stabilized Combustors

The experimental work of this thesis was carried out with two different swirl-stabilized model combustors. Both combustors are based on the same moveable block swirl generator as proposed by Leuckel (1967). The swirl generator (Fig. 3.1) consists of fixed and moveable blocks. By rotating the moveable blocks in clockwise direction, the size of radial entrances into the swirl generator is increased and the size of the tangential inlets is decreased. Consequently, the amount of swirl is decreased. Analogue to that, the counter-clockwise rotation of the moveable blocks increases the amount of swirl. The amount of swirl in a flow is usually described by the swirl number ( $S$ ) and measured as the relation of the axial flux of angular momentum to the axial flux of axial momentum. For simple geometries, such as the moveable block swirl generator, the swirl number can be estimated very well from the swirler geometry. In the presented configuration, the theoretical swirl number is adjustable in a range of  $0 \leq S \leq 2$ .

Sketches of the two combustor models used in this thesis are provided in Fig. 3.2. The combustor that was used for the majority of the experiments is shown in Fig. 3.2a. Air enters the moveable block swirl generator from the upstream plenum and the gaseous fuel is injected through 16 circumferentially distributed holes. Downstream of the swirl generator, an annular duct ensures a very homogeneous fuel–air mixing (Göke et al., 2011). The combustion chamber consists of a 300 mm long quartz glass tube of  $D_{cc} = 200$  mm diameter.

The main differences between the two combustor models are the shape and length of the centerbody, the diameter of the mixing tube and the diameter of the combustion chamber. The combustor shown in Fig. 3.2b is considerably smaller and closer to an industrially applicable combustor due to the truncation of the centerbody, which increases the acceptable

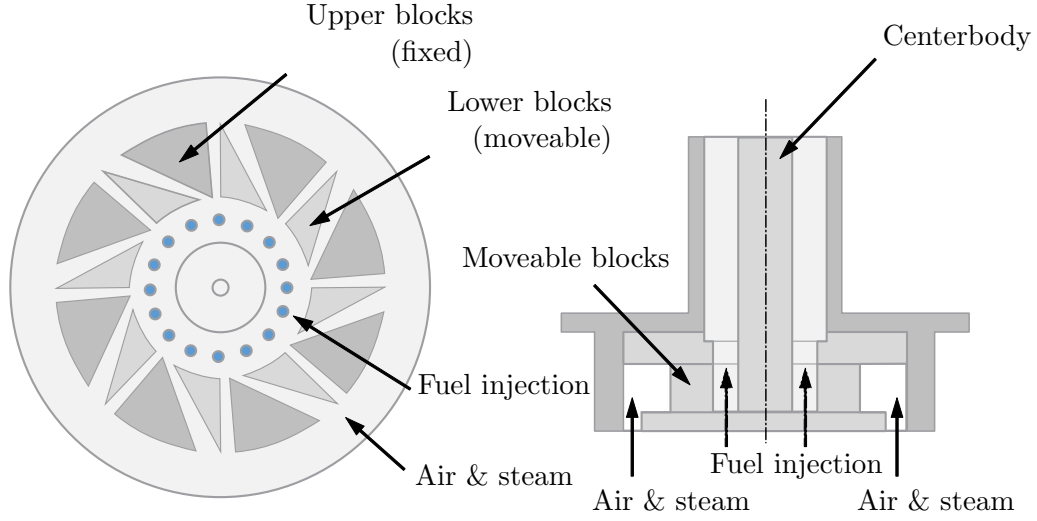


Figure 3.1: Sketch of the moveable block swirl generator.

combustor power. If a centerbody is present, such as in the combustor presented in Fig. 3.2a, the flame often stabilizes in its vicinity. Therefore, at high combustor powers and high combustor pressures, the centerbody must be extensively cooled, rendering its application difficult and expensive in practical combustion systems. However, without the centerbody, which prevents the upstream movement of the onset of vortex breakdown, the combustor can become prone to flame flashback. In order to overcome the flashback propensity, the concept of low momentum axial air injection is employed as proposed by Burmberger and Sattelmayer (2011). A non-swirling axial jet of a velocity, which is similar to bulk velocity, is injected through the truncated centerbody, as displayed in Fig. 3.2b. During the course of the present PhD work, this concept was further developed in the work by Reichel et al. (2013, 2014), where the potential of the combustor was demonstrated.

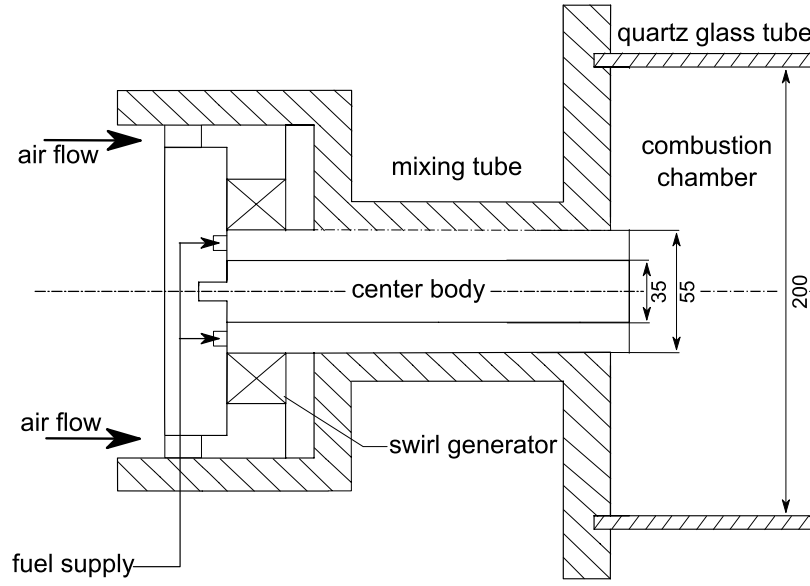
The secondary air, which is injected through the truncated centerbody, leads to lower swirl numbers of the flow than the theoretical swirl number of the swirl generator. Thus, for the operation of the combustor with axial injection, two swirl numbers are defined. The swirl number of the swirler, the primary swirl number, is denoted as  $S_{\text{prim}}$  and the resulting swirl number, incorporating the reduced swirl due to axial injection, is denoted as  $S_{\text{res}}$ . Furthermore, the axial injection rate  $\chi$  is defined as the ratio of axially injected mass flow to the total mass flow.

The characteristic length scales of the combustor are the hydraulic diameters  $D_h$  of the combustor inlets. For the combustor presented in Fig. 3.2a,  $D_h$  varies with the centerbody size and for the centerbody-free combustor (Fig. 3.2b) it has a constant value of  $D_h = 34$  mm.

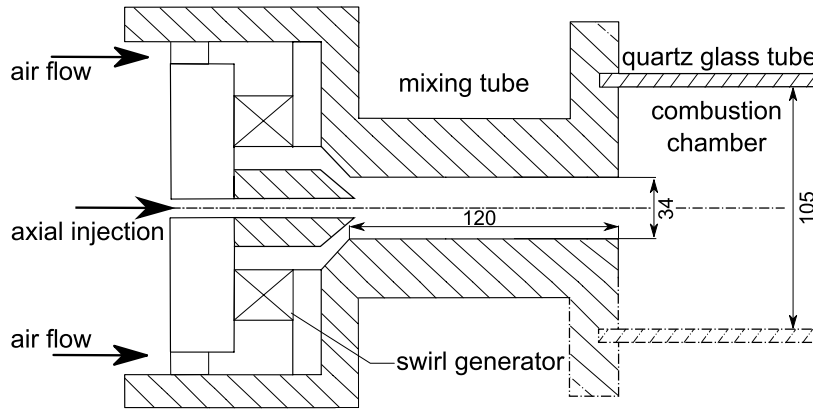
## 3.2 Test Rigs

The two combustors were experimentally investigated under non-reacting and reacting conditions in different test rigs at TU Berlin. For the assessment of the flow field under isothermal





(a) Combustor with centerbody



(b) Axial injection combustor

Figure 3.2: Sketches of the combustor variations.

conditions, a water tunnel test rig is used. The combustion tests were carried out in two different atmospheric combustion test rigs. The water tunnel and the combustion test rigs are briefly presented in the following.

### 3.2.1 Water Tunnel Test Rig

The water tunnel, as shown in Fig. 3.3, consists of a  $400 \text{ mm} \times 400 \text{ mm}$  measurement cross-section, two  $3.5 \text{ m}^3$  water tanks, a main pump, and a secondary pump. The mass flow was measured employing rotating wheel mass flow meters and maintained in a range of  $\pm 3\%$  of the set value by a closed-loop control scheme. However, to obtain the mass flow through

the combustor model, the amount of leakage around the model has to be estimated. This was done by a rotameter, which was placed in the combustion chamber. The uncertainty of the reading of the rotameter increases the uncertainty of the mass flow to  $\pm 5\%$ . The secondary flow employed for the testing of the combustor presented in Fig. 3.2b is injected with a separate pump from the secondary clean water tank.

The vertical test-section provides full optical access from all four sides and from the top. The whole system can be operated in open and closed-loop configuration. The water enters the water tunnel upstream of the test-section and the incoming velocity profile is conditioned by a flow straightener. For the water tunnel experiments, polycarbonate models of the combustors were used. The models were fixed on a plate and mounted in the test-section.

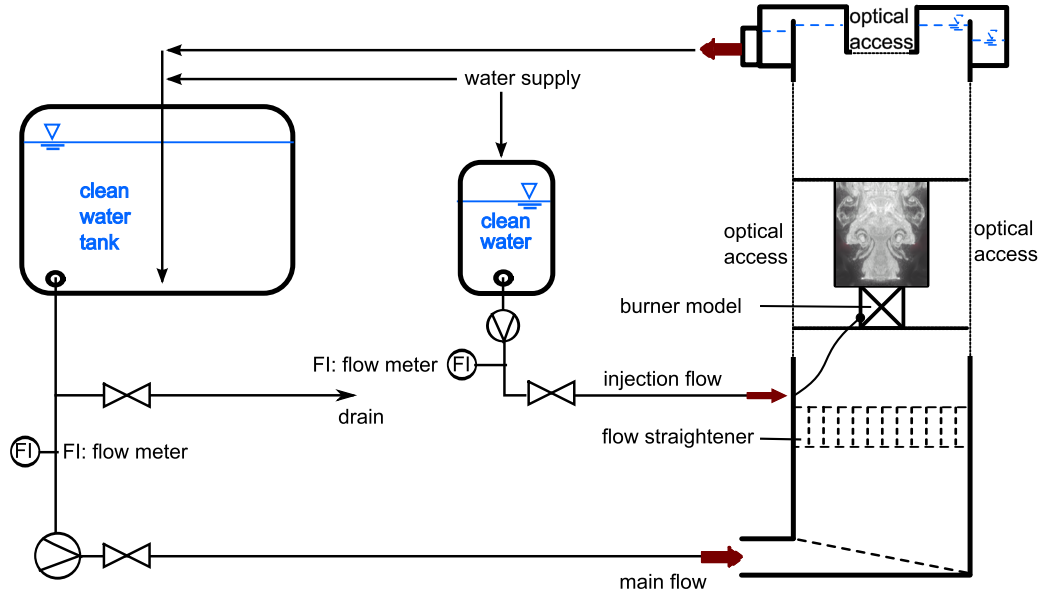


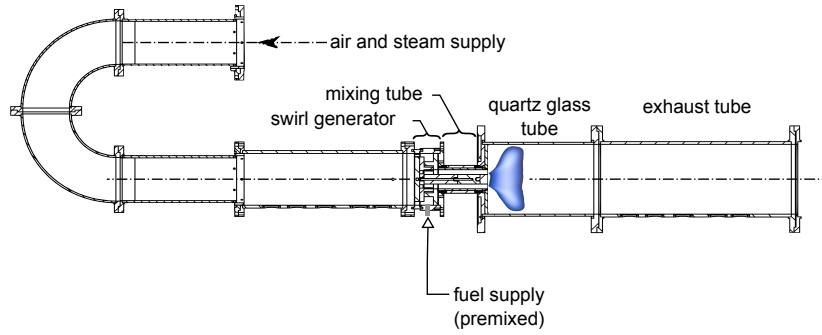
Figure 3.3: Sketch of the water tunnel test rig.

### 3.2.2 Combustion Test Rigs

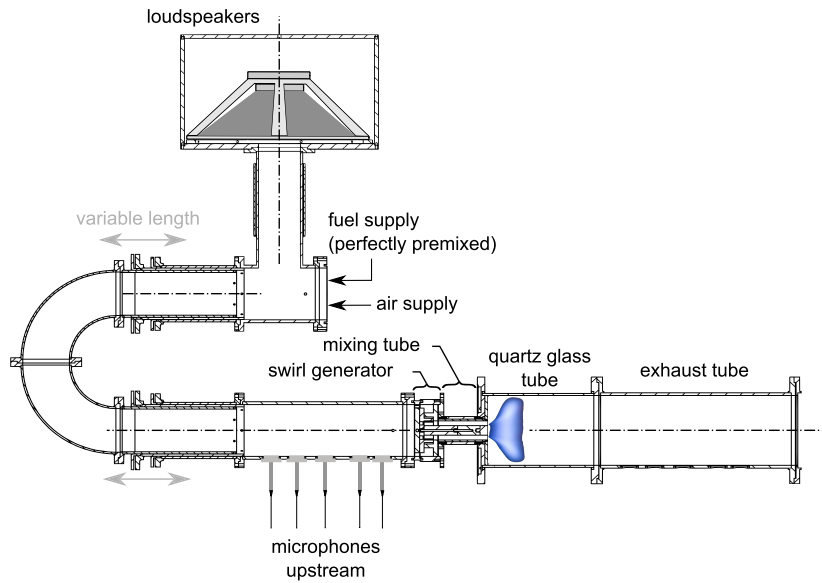
For the experiments at reacting conditions two similar test rigs were used. As shown in Fig. 3.4, both test rigs are similar in terms of the combustor, the exhaust tube, the upstream section, and the air preheating system. However, the test rigs are specifically designed to meet different needs. The fuel-flexible test rig shown in Fig. 3.4a is able to operate with natural gas, hydrogen, and blends of both. Additionally, the fuel-air mixture can be diluted using diluent gases, such as nitrogen and, most importantly, steam. The steam is produced in an electric steam generator and superheated prior to mixing it with the combustion air well upstream of the combustor. Throughout the study the steam content  $\Omega$  is described by the steam-to-air mass ratio

$$\Omega = \frac{\dot{m}_{steam}}{\dot{m}_{air}}. \quad (3.1)$$

Details about the fuel-flexible test rig can be found in the thesis by Göke (2012).



(a) Fuel-flexible combustion test rig



(b) High-amplitude acoustic forcing test rig

Figure 3.4: Sketch of the combustor test rigs.

The purpose of the test rig shown in Fig. 3.4b is the investigation of the flame response to high-amplitude axial forcing. To this end, four loudspeakers are installed upstream of a variable length bent. This bent, similar to a trombone, is adjusted to ensure resonance and to achieve maximum forcing amplitudes of the order of the mean flow velocity. Details on the acoustic test rig were provided by Schimek et al. (2009).

In order to suppress self-excited thermoacoustic instabilities, an area contraction with a ratio of 8:1 was applied downstream of the exhaust tube. The upstream effect of the area contraction strongly varies from non-reacting to reacting conditions and also with the operating conditions. A detailed investigation of this phenomenon and a quantitative estimation of the effect are provided in the Appendix A. In the present work, all reacting measurements were taken with the mounted orifice and all non-reacting measurements were taken without the orifice unless noted otherwise.

### 3.3 Measurement Techniques

#### 3.3.1 Velocity Field Measurements

The spatially and temporally resolved measurements of the non-reacting and reacting flow fields are the key prerequisite for the analysis of coherent structures and, hence, for the present thesis. Due to the harsh environment of reacting flows, the range of possible measurement techniques is limited to non-intrusive laser-based techniques. Two of these techniques, laser Doppler velocimetry (LDV) and particle image velocimetry (PIV) were used in this thesis due to their comparably high accuracy, their ease of use, and their availability. In the following the application of both techniques is presented briefly. For detailed descriptions of the working principles, the reader is referred to the literature (Nitsche and Brunn, 2006; Raffel et al., 2007; Tropea et al., 2007).

#### Particle Image Velocimetry

The particle image velocimetry technique is by far the most important velocity measurement technique employed during this thesis. Its most striking feature is the ability to measure instantaneous two-dimensional velocity distributions with high spatial resolution. On the one hand, this drastically reduces the measurement time compared to one-dimensional or point-wise measurement techniques, such as LDV, and, on the other hand, provides superior insight into large-scale coherent structures. PIV requires a laser with adequate optics to create a high-intensity, pulsed light sheet of low thickness and at least one camera. The laser light is scattered at liquid or solid particles that have to be seeded into the flow. This scattered light is measured by the camera with two images separated in time by the pulse distance of the two laser pulses. The particle displacement is extracted from the images using specific algorithms and subsequently converted into velocities (Raffel et al., 2007).

Two types of PIV setups were used in the course of this thesis: conventional monoscopic PIV and stereoscopic PIV. Monoscopic PIV requires only one camera and provides the spatial distribution of the two in-plane velocity components in a planar section. Stereoscopic PIV requires two cameras with significantly different viewing angles on the plane. Using an appropriate calibration, out of the two views the spatial distribution of all three velocity components are calculated (for details see Raffel et al. (2007)).

Figure 3.5 shows a sketch of the PIV setup for the reacting measurements. The laser used for most of the experiments was a QUANTRONIX Darwin Duo 100 high-speed Nd:YLF laser. This laser provides up to 50 W (per cavity) at a pulse frequency of 3 kHz and up to 30 mJ pulse energy at 1 kHz. The cameras were PHOTRON SA1.1 CMOS high-speed cameras with a frame rate of 5.4 kHz in full frame mode (1 MP). The camera mounted perpendicular to the light sheet was used in the monoscopic and the stereoscopic setup. In the latter setup the second camera was equipped with a Scheimpflug adapter and mounted at an angle of 35° with respect to the light sheet. This setup with one camera looking perpendicular and one tilted camera is not optimal in terms of measurements uncertainty of the out-of-plane

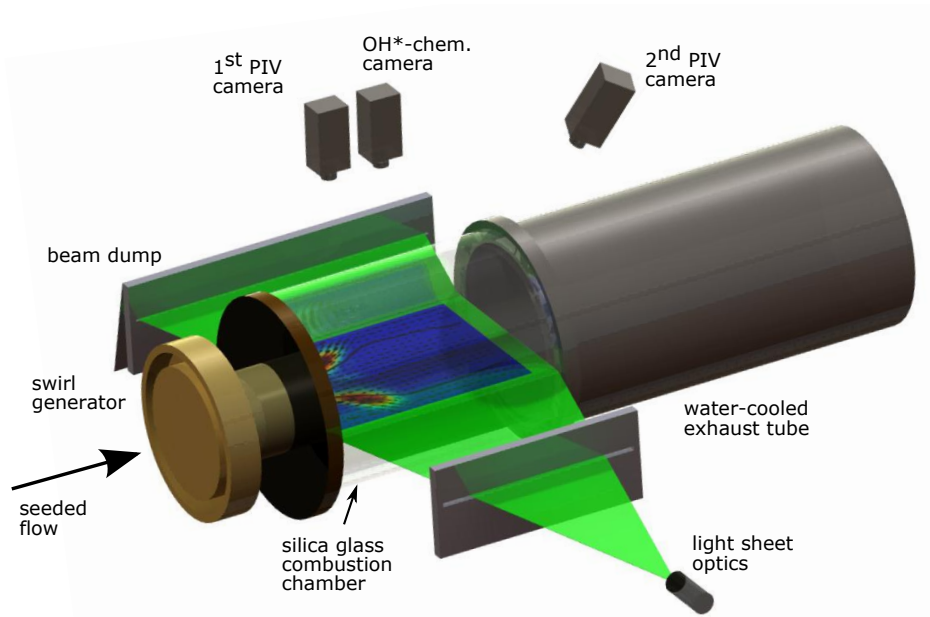


Figure 3.5: Sketch of the combustor test rig and the experimental setup.

component. However, geometrical restrictions and restriction due to laser light reflections did not allow for a better positioning. Furthermore, a comparative study by Willert et al. (2006) came to the conclusion that this configuration is the most suitable in terms of data quality and reflections. In the present setup, reflections of the incoming laser light from the silica glass were minimized by using beam dumps for the sheet and primary reflections. Further reflections were eliminated by sandblasting parts of the silica glass. For the monoscopic PIV setup, the second camera was used for simultaneous  $\text{OH}^*$ -chemiluminescence imaging and mounted close to the first camera.

Zirconium dioxide seeding of a nominal diameter of  $2\text{ }\mu\text{m}$  was introduced into the combustion air employing an RGB 1000 brush based particle disperser from PALAS. The seeding in the water tunnel consisted of silver-coated hollow glass spheres of a nominal diameter of  $15\text{ }\mu\text{m}$ . All PIV images were post-processed with a final interrogation area of  $16\text{ px} \times 16\text{ px}$ . The interrogation window overlap of 50% resulted in spatial resolutions of 1.2 to 1.8 mm of the overlapped vectors. The data was filtered for outliers (typically less than 3%) and interpolated from adjacent interrogation areas.

The measurement uncertainty of the instantaneous in-plane PIV velocity data can be estimated between 1.8 to 2.2 m/s and 0.25 to 0.31 m/s for measurements in air and water, respectively. The exact value depends strongly on the pulse separation (ITTC, 2008). In all cases the error was less than approximately 2% of the bulk velocity. Due to the required reconstruction, the error in the out-of-plane component is estimated to be two to three times larger than the error for the in-plane component (Lawson and Wu, 1997). The errors are mostly randomly distributed and mainly contribute to the RMS error and only to a minor extent to the mean flow field.

### Laser Doppler Velocimetry

The laser Doppler velocimetry is based on four intersecting laser beams (two for each velocity component) that create an interference pattern. A particle passing this pattern scatters light at a characteristic frequency and enables the system to calculate the velocity of the particle. For details about the measurement principle the reader is referred to the literature (Nitsche and Brunn, 2006; Tropea et al., 2007). LDV, in contrast to PIV, is a pointwise measurement technique. Its advantages are the smaller measurement uncertainty, the lower measurement effort, and the excellent temporal resolution (especially compared to low-speed PIV). However, due to the pointwise measurements, no instantaneous spatial structures can be measured and the measurement of one, two, or three-dimensional fields requires a traversing of the measurement system, which leads to long measurement times. In the present work LDV is used as a supplement to monoscopic PIV to measure the third velocity component, wherever it seemed more applicable to setup a LDV system than to set up a stereoscopic PIV system. In the water tunnel measurements, the possible measurement time is not restricted by fuel costs and seeding accumulation, thus, the LDV technique was frequently employed here. In the combustion test rig, LDV was only employed for the measurement of the effect of outlet boundary conditions on the flow field (see Appendix A).

### 3.3.2 Density Estimation

Distributions of the density and temperature field inside the combustor were estimated using the quantitative light sheet (QLS) technique. The QLS technique is mainly used as an alternative to laser induced fluorescence (LIF) measurements for mixing experiments, where the flow is only partly seeded (Voigt et al., 1997; Roehle et al., 2000; Findeisen et al., 2005). However, in the present work a novel approach is employed, where the QLS technique is used for density measurements in homogeneously seeded flows. The big advantage of the QLS technique is the simplicity of the setup compared to techniques based on Rayleigh or Raman scattering. The experimental setup is almost identical to the PIV setup, what makes the QLS technique very suitable to be used simultaneously to PIV measurements. In the QLS technique, the amount of scattered light is used to derive the spatial distribution of the seeding density, which is correlated to either mixture fractions at non-premixed conditions or the fluid density at premixed conditions. The recorded intensity signal does not only depend on the seeding particle density but also on several other factors. However, the most important parameters are described by a simplified model (Findeisen et al., 2005; Freund et al., 2011):

$$I(x, y) = C(x, y)IL(x, y)K_I(x, y) + H(x, y) + D(x, y). \quad (3.2)$$

In this model the measured intensity of the scattered light ( $I$ ) consists of three parts. The first term represents the light intensity scattered by the seeding particles. It depends on the distribution of the particle density ( $C$ ), on the local light sheet intensity ( $IL$ ), and on a factor ( $K_I$ ) that accounts for different viewing angles in the measurement plane. For details see the work of Findeisen et al. (2005) and Freund et al. (2011). The second term stems from

reflections of the light at the silica glass combustion chamber ( $H$ ), and the last term ( $D$ ) represents the camera's dark current. Other physical effects such as light extinction, multiple scattering, and illumination of the background due to seeding are assumed to be of secondary importance (Freund et al., 2011) and are neglected in this simple model and in the scope of this study. In order to correct for the background light and dark current ( $H$  and  $D$ ), reference pictures ( $I_0$ ) without seeding ( $C = 0$ ) were recorded and subtracted from the raw images:

$$I_0(x, y) = H(x, y) + D(x, y). \quad (3.3)$$

For the correction of the local light sheet intensity ( $IL$ ) and the viewing angle ( $K_I$ ), images at isothermal conditions and, hence, an almost homogeneous particle density distribution ( $C_h$ ) were recorded:

$$I_h(x, y) = C_h IL(x, y) K_I(x, y) + D(x, y) + H(x, y). \quad (3.4)$$

With the known homogeneous particle density  $C_h$ , the particle density distribution  $C$  for a measured light intensity distribution ( $I$ ) can be obtained:

$$C(x, y)/C_h = (I(x, y) - I_0(x, y))/(I_h(x, y) - I_0(x, y)). \quad (3.5)$$

This process is exemplarily displayed in Fig. 3.6. First, the mean light intensity  $I$  is obtained by time-averaging the instantaneous images (Fig. 3.6a,b). Subsequently, the background illumination  $I_0$  is eliminated by subtracting an unseeded background picture (Fig. 3.6c). The inhomogeneous light intensity  $IL$ , due to the Gaussian shaped laser profile, is visible in Fig. 3.6d ( $I_h - I_0$ ). The final estimated normalized particle density  $C/C_h = (I - I_0)/(I_h - I_0)$  is shown in Fig. 3.6e.

In order to convert particle density distributions into fluid density distributions, it must be assumed that the scattering cross section of the particles does not change inside the measurement plane and that the velocity field does not cause changes in the particle density. The melting temperature for the  $\text{ZrO}_2$  seeding is higher than any temperatures reached in the combustor. Hence, it is assured that the size distribution of the particles does not change due to heat release. Changes in the seeding density inside of smaller eddies could be observed to a limited extent, even in the homogeneously seeded isothermal case. This is assumed to stem from the higher density of  $\text{ZrO}_2$  compared to air. Particles are transported out of the core of the eddy due to centrifugal forces. However, these inhomogeneities disappear in the averaged raw image. Thus, only averaged density and temperature fields can be extracted with the proposed technique. Inhomogeneities in the mean seeding density distribution caused by the swirling motion of the flow are accounted for in Eqn. 3.5, as they also occur when measuring  $I_h$ . However, this correction only provides a first order correction as it assumes similar tangential velocities under isothermal and reacting conditions. Due to the fact that several parameters determine the total amount of scattered light, the QLS technique is commonly used as a relative technique only. This means that a reference value is necessary to deduce absolute quantities from the measurements. From Eqn. 3.4, it follows that an estimation of the density distribution can be obtained if the density  $\rho_h$  of the homogeneous image  $I_h$  is

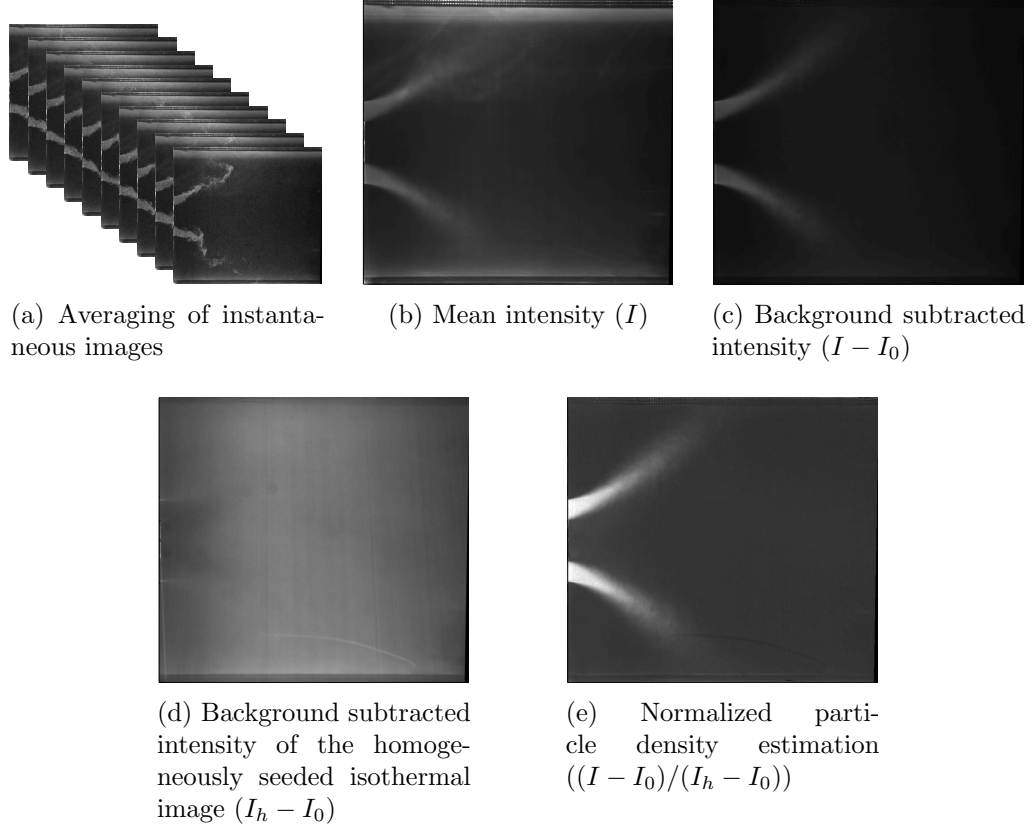


Figure 3.6: Process of density estimation from seeding pictures.

known and it is assumed that the particle density is proportional to the fluid density:

$$\tilde{\rho}(x, y) = \rho_h C(x, y) / C_h. \quad (3.6)$$

From the density distribution, an estimation of the temperature distribution can be derived if ideal gas behavior and a negligible pressure drop over the flame are assumed.

$$\tilde{T}(x, y) = T_h(x, y) \frac{\rho_h}{\tilde{\rho}(x, y)} \quad (3.7)$$

A comparison with point-wise measured temperature data obtained using a precise suction pyrometer (Göke and Paschereit, 2013) showed that the absolute values of  $\tilde{T}$  differed up to 20% from the suction pyrometer data, although the shape of the temperature field was reproduced very well. This is assumed to stem from long term variations of the seeding intensity, which directly influences the measured light intensity and is not corrected for in the present setup.

A better quantitative estimation is obtained, when the density distribution (or temperature distribution) is scaled with (pointwisely measured) temperatures of the burned gases (Terhaar et al., 2012). The good agreement of the scaled QLS temperature data to pointwise measured



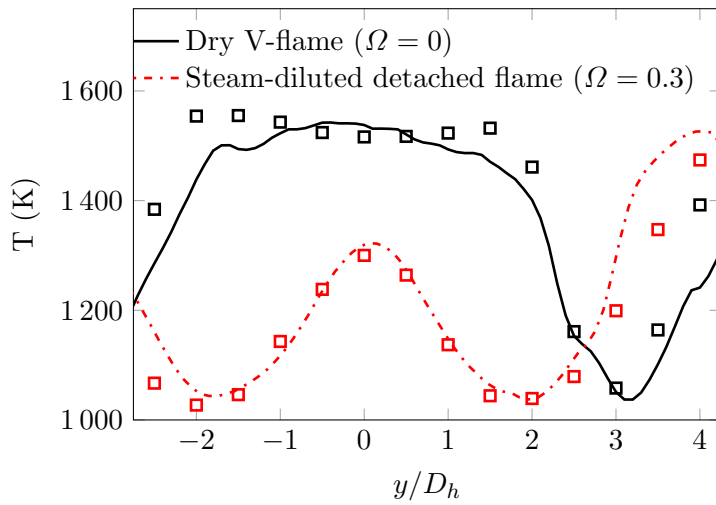


Figure 3.7: Comparison of the scaled estimated temperatures from the QLS technique (lines) to point measurements from Göke and Paschereit (2013) (squares).

data is evident in Fig. 3.7. In other words, the proposed temperature estimation employing the QLS technique provides a very convenient way to obtain qualitative temperature distributions of reacting flows. If pointwise temperature data are available, a reasonable quantitative estimation is possible.

### 3.3.3 Heat Release Measurements

During the oxidation of natural gas and/or hydrogen, several short-living radicals are produced. The concentration of the hydroxyl radical (OH) is shown in Fig. 3.8 for a one-dimensional chemical simulation of the oxidation of hydrogen. The flame front can be observed as the thin location of maximum heat release causing the steep gradient of the temperature. Very close to this region, the concentration of the hydroxyl radical OH increases significantly to superequilibrium conditions. Measurements of the OH radical concentration are possible and have been successfully carried out in a number of studies (e.g., Drake and Pitz, 1985; Balachandran et al., 2005; Konle et al., 2007; Li et al., 2010; Meier et al., 2010). The flame front location is determined by the maximum gradient of the OH concentration. However, the measurement technique, termed planar laser induced fluorescence (OH-PLIF), requires tunable laser light sources and supposes high measurement efforts and costs.

A more convenient way to measure the location of heat release is by measuring the chemiluminescence of the OH radical, termed OH\*-chemiluminescence. In contrast to fluorescence, chemiluminescence requires no external excitation from laser light and is measured directly using a camera that is sensitive in the UV range. Figure 3.8 shows that only close to the flame front, the amount of OH\*-chemiluminescence reaches high levels.

In contrast to planar measurements of laser induced fluorescence (e.g., OH-PLIF), the OH\*-chemiluminescence images are line-of-sight integrated. Thus, reconstruction techniques have to be employed in order to obtain a planar representation. For axisymmetric distributions, such as time-averaged OH\*-chemiluminescence images of swirling flames, the well-known Abel inversion is frequently applied. The present work, however, also deals with helical instabil-

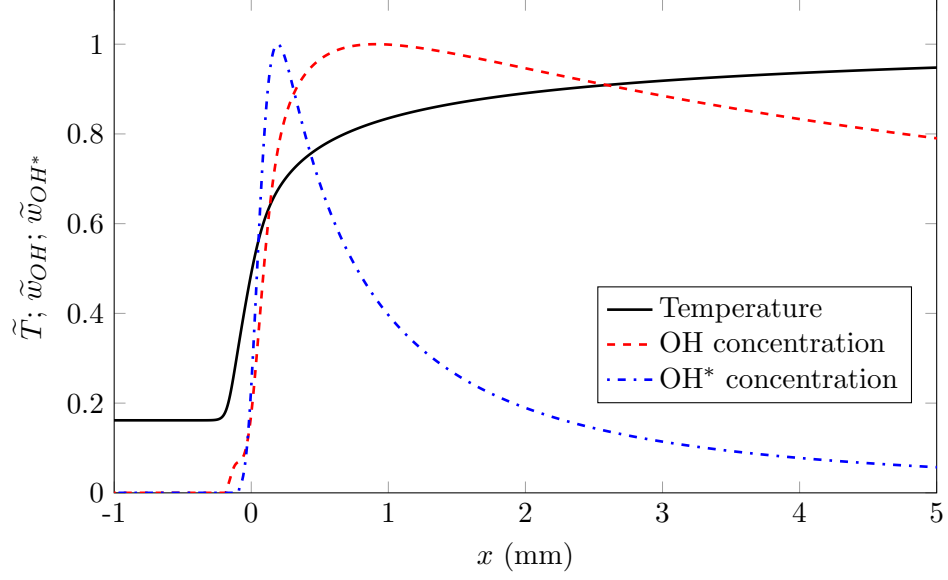


Figure 3.8: Exemplary results of a one-dimensional simulation of a hydrogen flame. All quantities are normalized with their relative maxima.

ities, which are assumed to cause helical heat release fluctuations that are antisymmetric with respect to the combustor axis (Moeck et al., 2012). Therefore, a recently developed tomographic reconstruction technique (Moeck et al., 2013) was employed. In contrast to conventional reconstruction techniques, this algorithm only requires one camera making use of the rotation of the helical structure. Instead of taking images from various views at the same time, different measurements from one view are taken at different phase angles of the rotating structure. An important assumption is that the signal only contains contributions of the single helical structure. For the heat release fluctuations caused by the PVC, this was shown by Moeck et al. (2013).

In the employed tomographic reconstruction algorithm, the coherent fluctuation of the line-of-sight (LOS) integrated images  $I_{OH,LOS}$  is approximated by a sum of Chebyshev polynomials

$$I_{OH,LOS}(x, r) = e^{i\theta} \sqrt{1 - r^2} \sum_{n=0}^{\infty} \frac{A_n(x)}{n+1} U_{2n+1}(r/R), \quad (3.8)$$

where the  $U_{2n+1}$  are Chebyshev polynomials of the second kind of the order of  $2n+1$ , and the  $A_n$  are the corresponding expansion coefficients. The coefficients are obtained from the experimental data as

$$A_n(x) = 2 \frac{n+1}{\pi} \int_{-1}^1 I_{OH,LOS}(x, r) U_{2n+1}(r/R) dr. \quad (3.9)$$

According to Deans (2007, p. 175), the inverse Radon transform of the expansion, which yields the reconstruction of the planar fluctuation, takes the form

$$I_{OH}(x, r, \theta) = e^{i\theta} \sum_{n=0}^{\infty} A_n(x) Z_{1+2n}^1(r/R), \quad (3.10)$$

where the  $Z_{2n+1}^1$  are Zernike polynomials and the  $A_n$  are the expansion coefficients determined from Eqn. 3.9. This reconstruction method does not require any numerical inversion and is therefore very robust to noise in the data (Moeck et al., 2013).

The processing of the time averaged OH\*-chemiluminescence images prior to the tomographic reconstruction involved the elimination of minor asymmetries before the Abel inversion. For the antisymmetric coherent fluctuations induced by the helical instability, in contrast to this, minor deviations from perfect antisymmetry were eliminated prior to smoothing the phase-resolved images.



## Chapter 4

# Flame Shapes, Flow Fields, and the PVC at Isothermal and Reacting Conditions

<sup>1</sup>*The present chapter is dedicated to the experimental assessment of the flow field and the flow field dynamics at different combustor operating conditions. To this end, detailed experimental results are presented for a wide range of operating conditions including different fuel compositions and rates of steam dilution. Emphasis is placed on the occurrence of four different flame shapes. The conclusion is drawn that the reactivity of the fuel-air-steam mixture, as represented by the laminar burning velocity, is the main driver for the selection of the flame shape. At dry conditions, a V-shaped flame stabilizes in a broad inner recirculation zone with low levels of local turbulent kinetic energy; at moderate steam content, the flame changes into a trumpet-like shape; and at very high rates of steam dilution, the flame detaches and shows an annular shape. With pure hydrogen fuel, a very short flame with a distinct flow field is also possible. The importance of the flame shape is pointed out by its correlation to strong changes in the time-averaged combustor flow field and density distribution. Moreover, the occurrence of the PVC is extracted from the flow field data. The excitation of the PVC seems to depend solely on the flame shape present in the combustor. Lastly, the strong effect of the PVC on the flame dynamics and mixing characteristics is shown using heat release measurements and tracer experiments, respectively. Both the shift of the flame position and the excitation of the PVC can affect the thermoacoustic stability of the combustion system.*

---

<sup>1</sup>The results presented in the present chapter were previously published in Terhaar et al. (2014b, 2015a). Oliver Krüger conducted the calculations of the laminar burning velocities and Kilian Oberleithner assisted with the interpretation of the POD results. All other tasks were carried out by the author.

## 4.1 Introduction

To cope with the scarcity of fossil fuels and to facilitate renewable energy sources, modern gas turbine combustors will presumably be required to operate at a very wide range of operating conditions. The fuel composition may vary from highly reactive hydrogen to natural gas and low reactivity syngases. Furthermore, the ultra-wet cycle requires very high rates of steam dilution, which significantly reduce the reactivity of the mixture. Changes of the operating conditions have been shown to significantly change the appearance of the flame (Vanoverberghe et al., 2003a,b; Boxx et al., 2010a; Hermeth et al., 2014). Vanoverberghe et al. (2003a) carried out a parametric study with a similar swirl-stabilized combustor as in the current study and identified various flame configurations. Transitions of the flame state were found to depend on the equivalence ratio, swirl number and the degree of fuel-air unmixedness. In the studies of Boxx et al. (2010a) and Hermeth et al. (2014), alterations of the operating conditions not only induced changes of the flame shape, but also changes of the flow field dynamics. In one case a helical flow instability, the PVC as introduced in Section 1.3, was strongly excited. In another case at different operating conditions, the PVC was completely suppressed.

The large-scale flow structures related to the PVC have a significant influence on the instantaneous flow field. For instance, they were shown to affect the fuel-air mixing (Galley et al., 2011; Duwig et al., 2012) and the mixing of burnt and unburnt gases (Göckeler et al., 2013). The helical flow instability, moreover, induces helical heat release fluctuations. Moeck et al. (2012) showed two intertwining helices, one of higher and one of lower than average heat release rates. Furthermore, their study demonstrated that due to the antisymmetric nature of the PVC and the induced heat release fluctuations, no oscillation of the integral heat release is caused. However, in an analytical study, Acharya et al. (2013) predicted that this is only true for perfectly axisymmetric time-averaged flows and flames. Thus, asymmetries, as they can be expected in annular combustors (Samarasinghe et al., 2013), may cause also integral heat release fluctuations induced by the PVC. Such integral heat release fluctuations are of utmost importance for the combustion process, as they can interact with the system acoustics and cause high-amplitude thermoacoustic instabilities (Lieuwen and Yang, 2005).

The influence on the excitation of the PVC is, however, not the only mechanism how different flame shapes (e.g., attached and detached flames) can affect thermoacoustic instabilities. Durox et al. (2009) and Thumuluru and Lieuwen (2009) showed for non-swirling and swirling flames, respectively, that different flame geometries resulted in different flame responses to velocity fluctuations. The same was observed in flame transfer function measurements by Schimek et al. (2012a), which were conducted in the same combustor, as used in the present work. Recently, Hermeth et al. (2014) numerically investigated the transition between two flame states, a detached flame and an attached flame, in an industrial swirl-stabilized burner type. Their simulations predicted a strong influence of the flame state on the transfer function of velocity to heat release perturbations. Therefore, understanding the mechanisms that cause the different flame shapes and the relation to the occurrence of the PVC is of high im-

portance to ensure stable combustion. Moreover, the understanding of different flame states and the mechanisms involved in their occurrence is vital to avoid undesired flame shape transitions. Such flame transitions can strongly impact the combustion process in terms of cooling requirements, emissions, operational range, etc. Therefore, flame shape transitions have to be either avoided or considered already in the combustor design process to avoid detrimental effects on the combustion performance and the lifetime of the combustor components.

## 4.2 Experimental Procedure

For the experiments presented in this chapter, the combustor shown in Fig. 3.2a was used with a centerbody diameter of  $D_{cb} = 35$  mm. The velocity field was measured using high-speed particle image velocimetry and the heat release distribution was determined with high-speed  $\text{OH}^*$ -chemiluminescence imaging. For every operating condition two runs were carried out. In the first run, a stereoscopic PIV setup was employed to yield all three velocity components in a planar section. In a second run, the PIV setup was changed to a monoscopic view and  $\text{OH}^*$ -chemiluminescence intensity was measured simultaneously. All presented results are normalized with the hydraulic diameter  $D_h = 20$  mm and the bulk velocity  $U_0$  at the combustor inlet.

The flow was seeded upstream of the swirl generator using a brush-based seeding generator with Zirconium Dioxide ( $\text{ZrO}_2$ ) particles of a nominal diameter of  $2\ \mu\text{m}$ . The tracer particles were used for the velocity measurements, an estimation of the fluid density, and an estimation of the mixing processes. Using a quantitative light sheet (QLS) technique, as described in Section 3.3.2, planar density information was recovered from the amount of scattered light. For the assessment of the mixing, the flow was not continuously seeded, but the seeding was introduced as a step input. By evaluating the spatially resolved transient particle concentration, conclusions about the mixing processes inside the combustor were drawn. The same technique was successfully used for the determination of combustor residence times by Gökeler et al. (2013), who also provided details about the measurement procedure and the image post-processing.

During the measurements a very wide range of operating conditions was assessed. The variation included the amount of steam dilution defined by the steam-to-air mass ratio  $\Omega = \dot{m}_{\text{steam}}/\dot{m}_{\text{air}}$ , the equivalence ratio  $\phi$ , the inlet temperature  $T_{\text{in}}$ , and the mass fraction  $w_{\text{H}_2}$  of hydrogen in the fuel. An overview of the investigated operating conditions is provided in Tab. 4.1.

## 4.3 Flow Field Topology

Before the effect of combustion on the flow field and the observed flame shapes is described, the reference flow field topology of the isothermal case is presented in Fig. 4.1a-c. Streamlines of the two dimensional velocity vectors measured on a radial-axial plane are superimposed on the normalized axial velocity magnitude, the normalized tangential velocity, and the normalized

Table 4.1: Range of investigated operating conditions for the flame shape classification.

Inlet temperature	$T_{\text{in}}$	450 - 620 K
Equivalence ratio	$\phi$	0.3 - 0.9
Reynolds number	Re	22 000 - 32 000
Steam content	$\Omega$	0 - 0.5
Hydrogen content	$w_{H_2}$	0 - 1
Combustor power	$P$	30 - 120 kW

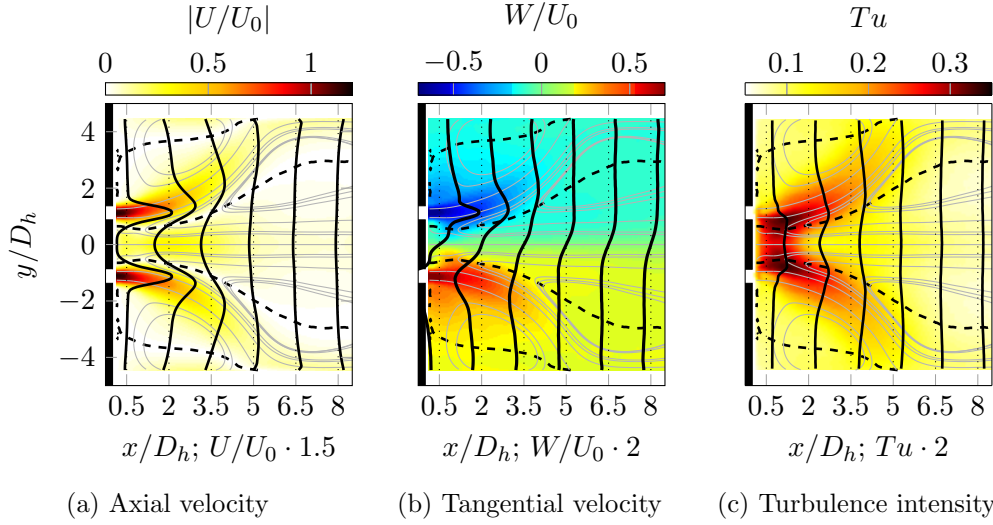


Figure 4.1: Isothermal flow field. Streamlines of the time-averaged flow field and radial profiles are superimposed on the corresponding quantity. Dashed lines indicate zero axial velocity.

turbulence intensity. Additionally, radial profiles of the presented quantity are extracted and are presented for various axial locations. Three regions can be identified in the flow field: An annular jet emanating from the mixing tube, an internal recirculation zone (IRZ) generated by vortex breakdown, and an outer recirculation zone (ORZ) induced by the area change and the confinement. In between the jet and the large recirculation regions, turbulent shear layers are produced, with very high levels of turbulence. The distribution of the tangential velocities shows almost a solid body rotation up to axial location of  $x/D_h = 3.5$ . Farther downstream the tangential velocities decay very fast.

## 4.4 Classification of Flame Shapes

Under reacting conditions several flame shapes were encountered. An overview is given by the flame photographs shown in Fig. 4.2. In order to find a parametric description of the flow fields and flame shapes, two simple parameters are introduced. The first parameter is the



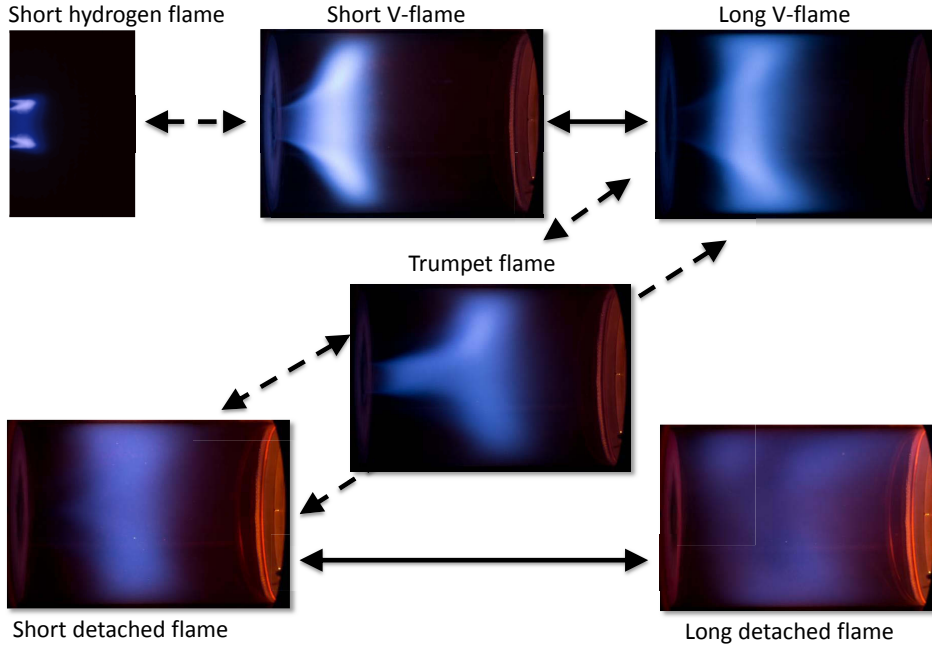


Figure 4.2: Photographs of the flame shapes. Solid arrows are continuous transitions and dashed arrows indicate sudden transitions. The picture of the short hydrogen flame is a false-colored OH\*-chemiluminescence image due to the lack of emitted visible light.

axial location of the center of gravity of the OH\*-chemiluminescence intensity  $x_{fl}$ :

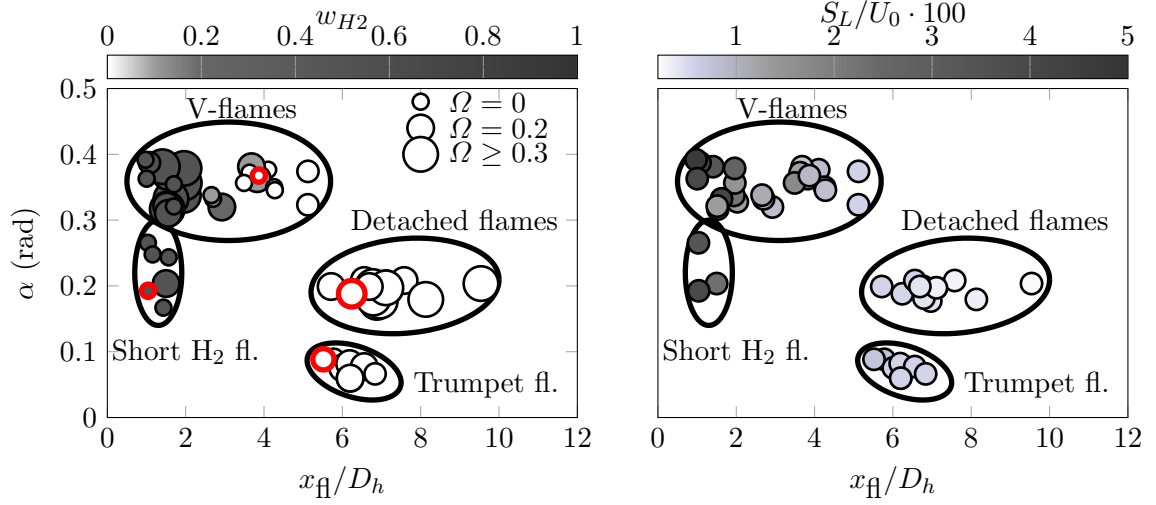
$$x_{fl} = \frac{\int I_{OH}(x, r) x dV}{\int dV}. \quad (4.1)$$

Here,  $I_{OH}$  is the Abel-deconvoluted OH\*-chemiluminescence intensity. The second parameter describes the initial opening angle  $\alpha$  of the jet averaged over  $0.5 < x/D_h < 4$  with

$$\alpha_x(x) = \text{atan}\left(\frac{dr_p}{dx}\right) \quad \text{and} \quad \alpha = \frac{1}{(4 - 0.5)D_h} \int_{x/D_h=0.5}^{x/D_h=4} \alpha_x dx. \quad (4.2)$$

The encountered parameter combinations  $x_{fl}$  and  $\alpha$  are summarized in Fig.4.3 for a wide range of operating conditions (see Tab. 4.1).

From Fig. 4.3a it is evident that parameters resulting in a decrease of the mixture reactivity, such as steam dilution, shift the flame downstream. An increase of the reactivity, e.g., due to hydrogen addition, causes an upstream shift of the flame. This is even more evident when the combinations of  $x_{fl}$  and  $\alpha$  are color-coded with the ratio of the laminar burning velocity to the inlet flow velocity, as presented in the Fig. 4.3b. The laminar burning velocity is the dominating parameter for the reactivity of the mixture. It strongly influences if a flame at a given flow velocity, turbulence intensity, and strain rate can be stabilized or is quenched (Williams, 2000). In Fig. 4.3b, the laminar burning velocity is calculated with



(a) The size of the marker indicates the rate of steam dilution and the color the mass fraction of hydrogen. Red bold circles indicate the selected operating conditions for the detailed investigation (Tab. 4.2).

(b) The color of the marker indicates the normalized calculated laminar flame speed.

Figure 4.3: Parametric classification of the flame shapes.

Table 4.2: Operating conditions of the selected cases representing the four flame shapes.

Parameter	$T_{in}$ (K)	$T_{ad}$ (K)	$\phi$	Fuel	$\Omega$	$u_0$ (m/s)	$S_L$ (m/s)
Detached	620	1850	0.8	CH <sub>4</sub>	0.2	72.9	0.39
Trumpet	620	1850	0.68	CH <sub>4</sub>	0.1	69.6	0.48
V-flame	620	1850	0.56	CH <sub>4</sub>	0	66.1	0.59
Short H <sub>2</sub>	540	1850	0.5	H <sub>2</sub>	0	65.8	2.58

one-dimensional simulations employing Cantera (Goodwin, 2003) with the GRI mechanisms (Smith et al., 2000) and the reaction mechanism developed by Burke et al. (2012). Some operating conditions (e.g., very lean hydrogen flames) are outside of the validity range of the reaction mechanisms and are omitted. Details about the calculation can be found in a recent publication by Krüger et al. (2013).

From Fig. 4.3 four separated regions are evident and correspond to the flame shapes presented in Fig. 4.2. The shortest flames occurred at dry conditions with hydrogen fuel. Substituting hydrogen with natural gas leads to a rather sudden change of the flame opening angle. At dry conditions with natural gas fuel, the flame usually showed the typical V-shape. Leaning out the flame or mildly steam diluting the air, leads to a continuous enlargement of the flame. Further reducing the equivalence ratio or increasing the rate of steam dilution leads to a sudden change of the flame shape into the trumpet shape. At high rates of steam dilution, the flame shape changes again abruptly and shows detached annular shapes of dif-

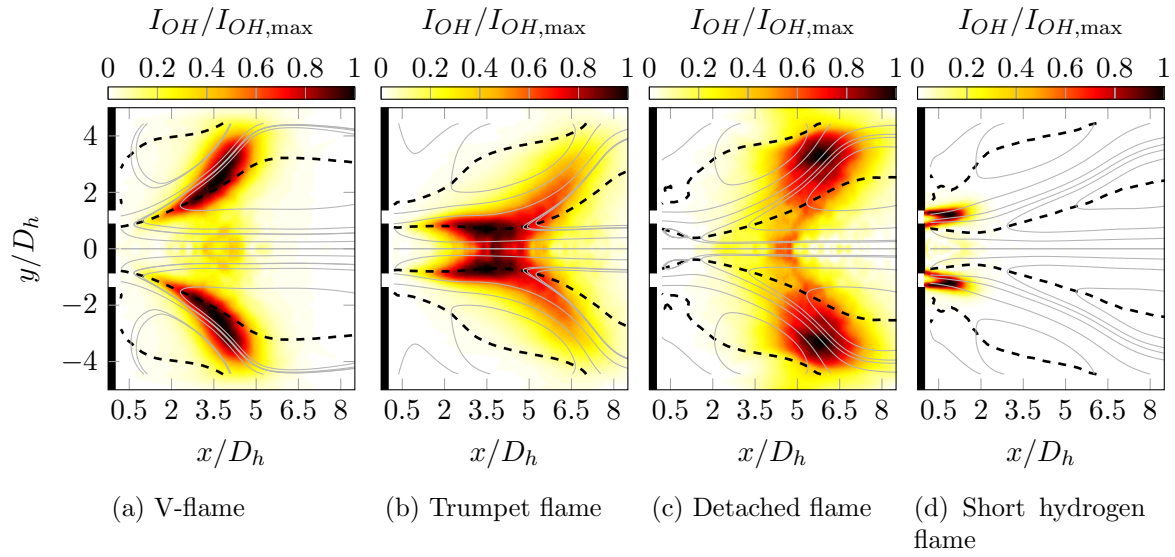


Figure 4.4: Streamlines of the time-averaged flow fields superimposed on the normalized Abel-deconvoluted OH\*-chemiluminescence intensity distribution. Dashed lines indicate zero axial velocity.

ferent lengths. The flow fields corresponding to the same flame shape are very similar (for details see Terhaar et al., 2011), whereas flow fields of different flame shapes show significant differences. In order to assess the different flame shapes and the corresponding velocity fields, representative examples were chosen and are presented in Figs. 4.4 and 4.5. The first example represents a typical V-shaped flame with a wide opening angle. The second example has a very narrow flame opening angle and features a trumpet like shape. Next, an example of a detached flame located comparably far downstream in the combustor is provided in Fig. 4.3c. Finally, in Fig. 4.3d a very short hydrogen flame with a small opening angle is depicted. All experiments were conducted at the same flame temperature and all but one at the same inlet temperature. This way, the dilatation over the flame is comparable. The selected operating conditions are presented in Tab. 4.2 and are indicated by red markers in Fig. 4.3.

The typical V-flame (Fig. 4.4a), which is anchored at the centerbody and along the inner shear layer, has a wide jet opening angle and negative axial velocities in the IRZ that are very uniform in radial direction and comparably low (see Fig. 4.5a). This comes along with much lower levels of the local turbulence in the IRZ, compared to the other investigated cases. Additionally, the radial gradient of the tangential velocity, i.e., the rotational speed of the vortex core, remains very low up to an axial location of  $x/D_h = 2$ . This indicates a very low transport of angular momentum from the annular swirling jet at the combustor inlet into the IRZ. The estimated density distribution of the V-flame case shows that the IRZ is completely filled with hot burned gases. Similarly to the tangential momentum, the fluid interchange between the jet and the IRZ seems to be rather low, causing steep density gradients in radial direction.

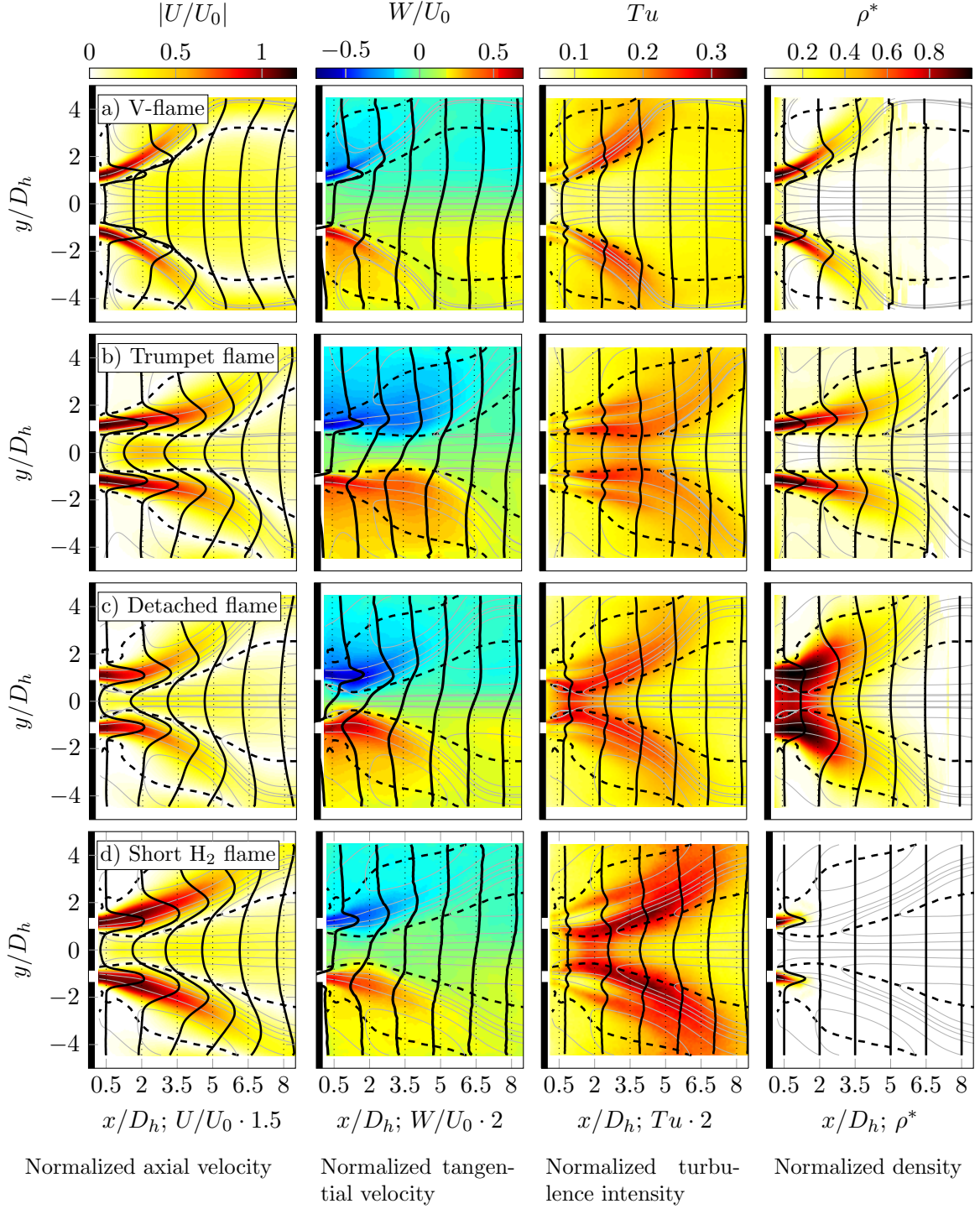


Figure 4.5: Flow fields and density fields of the different flame shapes. First row (a): V-flame, second row (b): trumpet flame, third row (c): detached flame, and fourth row (d): short hydrogen flame. Streamlines of the time-averaged flow field and radial profiles are superimposed on the corresponding quantity. Dashed lines indicate zero axial velocity.

The flow field shown in Fig. 4.5b corresponds to the region of very narrow flame opening angles (see Fig. 4.3) and, thus, to the trumpet-like flame shown in Fig. 4.4b. This flame, which is denoted as a trumpet flame in the following, is anchored near the centerbody and along the inner shear layer. Compared to the V-flame, the flow field of the trumpet flame has a considerably narrower IRZ with much higher recirculating velocities. The very low jet divergence near the combustor inlet and the small axial decay of the tangential velocities indicate a downstream shift of the onset of vortex breakdown. Consequently, the strong backflow on the centerline is assumed to depend on the recirculation bubble downstream of the centerbody. This assumption is supported by the observation that the trumpet flame is much less prone to appear with higher swirl numbers and smaller centerbody sizes. Compared to the V-flame, the transfer of tangential momentum from the jet to the IRZ is significantly increased, leading to a much higher rotational speed of the solid body vortex core. However, this transfer does not set in before  $x/D_h = 2$  corresponding to a significant increase of the normalized turbulence intensity. The density distribution of the trumpet flame is similar to the V-flame with the IRZ being completely filled with burned gases. Downstream of  $x/D_h = 2$  the higher transfer of angular momentum is accompanied by a smoothing of the density gradients.

Both the V-flame and the trumpet flame anchor at the centerbody. If the flame root is quenched, for instance due to high strain rates near the combustor inlet, it detaches and takes an annular shape (Fig. 4.4c). The density distribution of the detached flame (Fig. 4.5c) shows a large region of cold unburned gases near the combustor inlet. This region includes the jet and the upstream part of the IRZ. The tangential velocity distribution of the detached annular flame shows a considerable amount of angular momentum transfer from the jet into the IRZ. This results in solid body rotational speeds of the vortex core that are similar to the isothermal case. The high radial transport is assumed to be linked to the high turbulence intensity in this region. Consistently, also very low density gradients from the jet to the IRZ are evident.

For very high laminar burning velocities, the flame gets very short and is also able to reside in the inner and outer shear layer (Fig. 4.4d). Interestingly, the flow field of the short hydrogen flame (Fig. 4.5d) features a similar jet opening angle and similar axial and tangential velocity distributions in the IRZ as the flow field of the detached flame. Obviously, the hydrogen flame is much shorter, leading to significantly higher axial velocities close to the combustor inlet. Only a very small region near the combustor inlet remains at the combustor inlet temperature, while almost the complete combustor is filled with the hot combustion products. Note that the resolution of the used density estimation technique did not allow for the assessment of smaller density gradient in the downstream section of the combustor. Therefore, the profiles for  $x/D_h > 2.5$  are set to  $\rho = \rho_{\text{burnt}}$  (i.e.,  $\rho^* = 0$ ). The transfer of angular momentum seems to be slightly lower compared to the detached flame, resulting in lower solid body rotational speeds. However, compared to the V-flame, still considerably more angular momentum is transferred. This is consistent with the much higher turbulence intensities.

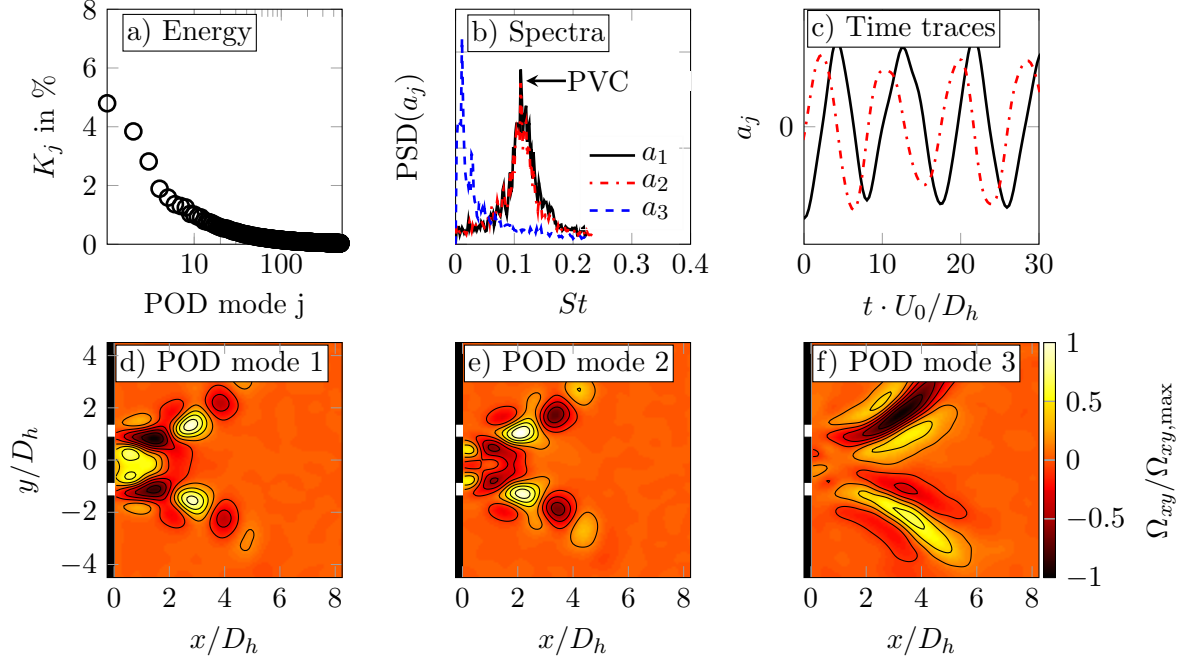


Figure 4.6: Results of the POD analysis of the isothermal flow. a) Distribution of the turbulent kinetic energy over the modes. b) Power spectra of the temporal POD coefficients. c) Time traces of the temporal coefficients related to the PVC. d-f) Normalized through-plane vorticity  $\Omega_{xy}$  of the spatial POD modes.

## 4.5 Identification of Coherent Structures

From the evaluation of the time-averaged fields, significant differences were found between the four flame shapes. In the following, the results of a POD analysis are presented. The focus is placed on the identification of large-scale coherent structures, such as the PVC. Before assessing the occurrence of coherent structures in the different flame configurations, the outcome of the POD analysis at isothermal conditions, where a PVC is present (Strangfeld et al., 2011), is described. Figures 4.6a-c show the energy distribution  $K_j$  of the POD modes, the normalized power spectral density (PSD) of the POD coefficients  $a_j(t)$ , and the corresponding time traces. It can be observed that around 9% of the fluctuating kinetic energy is captured by the first two modes. The spectra of these two modes reveal a distinct peak at around  $St = 0.11$  and the corresponding time traces show that the first two modes oscillate in time at a phase shift of a quarter period. Consistently, the first two spatial POD modes (Figures 4.6d-e) span a convective vortex pattern, which is very typical for the PVC (Oberleithner et al., 2011; Stöhr et al., 2011b). Analogously to a traveling sine wave expressed by a superposition of a sine and a cosine, the global flow oscillations encountered here can be expressed by a superposition of the two most energetic POD modes.

Ideally, the spectral peaks of the first modes, shown in Fig. 4.6b, should be discrete and equally high. The encountered broadening of the peak is associated with jitter in the phase



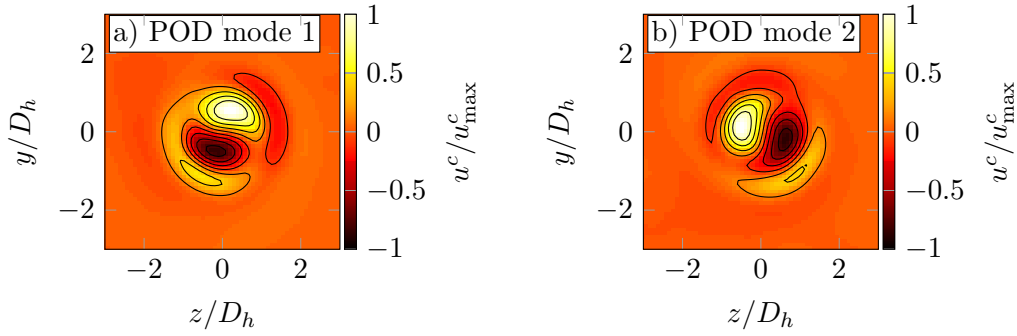


Figure 4.7: Results of the POD analysis of the isothermal flow in a crosswise plane at  $x/D_h = 1.5$ .

and in the spatial structure due to the strong turbulence. The slight difference of the energy captured by the modes is assumed to stem from the finite number of snapshots used for the POD. Nonetheless, the POD is sufficiently clear to conclude that the isothermal flow features a helical coherent structure at a Strouhal number of  $St = 0.11$ . The third POD mode (Fig. 4.6f) shows a peak in the spectrum at a very low frequency. The spatial distribution shows that this mode describes a slow axisymmetric longitudinal movement of the shear layers. The low frequency content of this mode indicates that the dynamics captured by the third mode are not related to shear instability.

The helical nature of the coherent structure described by the two POD modes (Figs. 4.6d,e) was confirmed by results from isothermal measurements of the same geometry in a water tunnel (for details see Strangfeld et al. (2011)), where the geometry also allows for measurements in crosswise planes. The results of the crosswise POD analysis are presented in Fig. 4.7, where it is evident that the structure is of an azimuthal wavenumber of  $|m| = 1$ . Thus, the structure is helical and it is confirmed that the dominating coherent structure in the isothermal field is the PVC.

For the V-flame (Fig. 4.8), the spectrum of the first mode reveals no prominent peaks except some low frequency contributions that are associated with long time flow variations. Similar to the slow mode observed in the isothermal case, the spatial shape of this mode (Fig. 4.8d) reveals that it describes a slow axisymmetric longitudinal movement of the shear layers. The second mode (Fig. 4.8e) corresponds to a peak in the spectrum at  $St = 0.02$ . The spatial distribution of this mode shows a lateral movement of the shear layers. In contrast to the isothermal case, neither a clear vortex pattern nor a complementary POD mode can be found. This indicates that the encountered frequency may not be associated to shear flow instability. In any case, there is no velocity contribution of this mode on the centerline. Thus, no precession of the vortex core can be caused by this mode. The third mode looks complementary to the first mode. Consequently, it also describes a slow axisymmetric longitudinal movement of the shear layers.

The spectra of the trumpet flame (Fig. 4.9b) show a very slow oscillation for the first mode. The spatial shape of this mode is similar to the first POD mode of the V-flame. It describes a

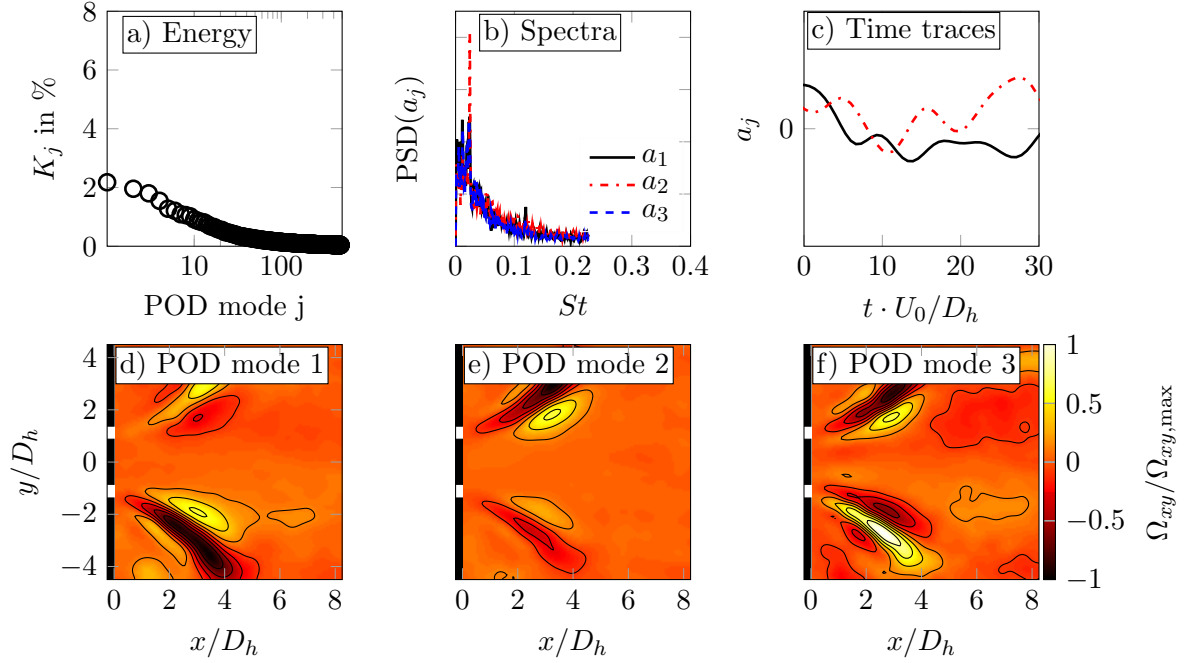


Figure 4.8: Results of the POD analysis of the V-flame. a) Distribution of the turbulent kinetic energy over the modes. b) Power spectra of the temporal POD coefficients. c) Time traces of the temporal coefficients related to the PVC. d-f) Normalized through-plane vorticity  $\Omega_{xy}$  of the spatial POD modes.

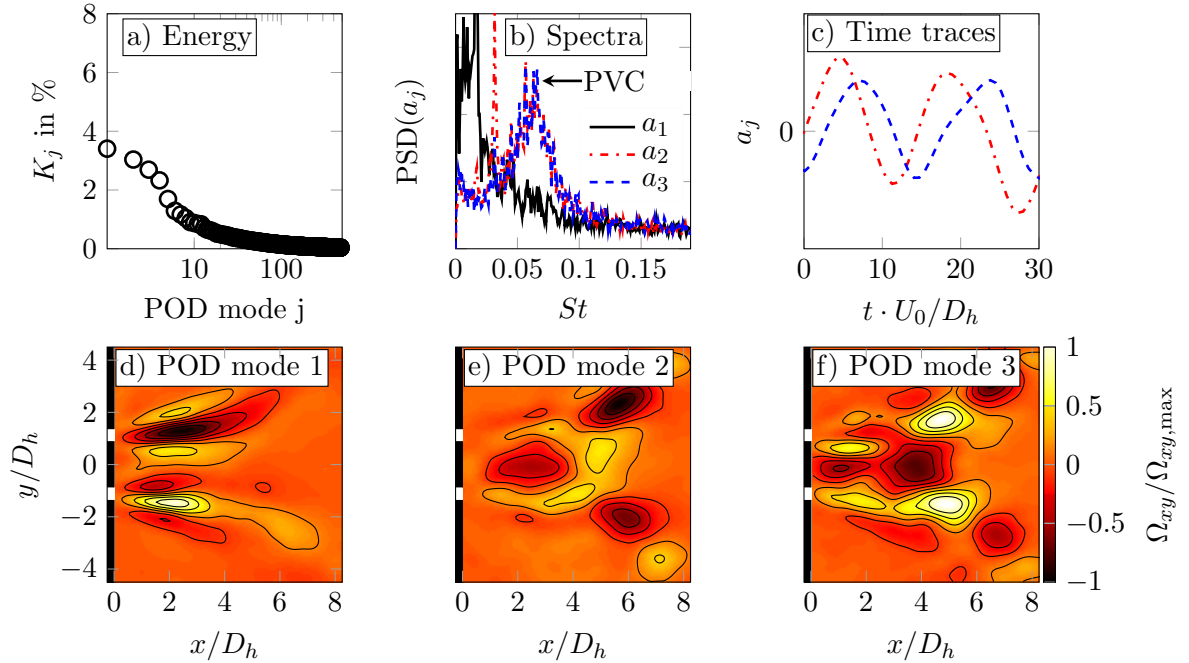


Figure 4.9: Results of the POD analysis of the trumpet flame. a) Distribution of the turbulent kinetic energy over the modes. b) Power spectra of the temporal POD coefficients. c) Time traces of the temporal coefficients related to the PVC. d-f) Normalized through-plane vorticity  $\Omega_{xy}$  of the spatial POD modes.



slow axisymmetric longitudinal movement of the shear layers. Additionally, a distinct peak for the second and third mode at a frequency ( $St = 0.056$ ) is evident in Fig. 4.9b. The frequency of this peak is somewhat lower than the PVC frequency for the isothermal case but clearly above the frequency of the first mode. These two modes (Fig. 4.9e,f) represent a dynamical feature that is similar to the isothermal flow, indicating that the reacting flow of the trumpet flame is subjected to a flow instability that manifests in a PVC. Additionally, the spatial POD modes reveal that the coherent flow pattern in the inner shear layer, corresponding to the PVC, is significantly shifted downstream compared to the isothermal case. Note that the spectrum of the second POD mode also shows a sharp peak at  $St = 0.02$ . This is the same frequency as the second POD mode of the V-flame. In fact, the fourth POD mode of the trumpet flame, not shown here, has its only peak at  $St = 0.02$  and describes an antisymmetric movement of the shear layers similar to the second POD mode of the V-flame. In the case of the trumpet flame, the POD fails to completely separate these two antisymmetric modes and lumps parts of the antisymmetric shear layer movement into the modes describing the PVC. However, the flow phenomena are not the same and are clearly separated by the very distinct frequencies. Decomposition techniques, such as the dynamic mode decomposition (DMD, see e.g. Schmid, 2010), which decompose the flow dynamics into different frequency contributions, yield no contribution of one flow structure to the modes of the other. However, due to the frequency jitter of the helical oscillation, the DMD does not yield a single dynamic mode representing the PVC, making this technique less suitable for the analysis of the present data compared to the POD.

The POD analysis of the detached flame configuration (Fig. 4.10) shows a strong helical instability that is surprisingly similar to the isothermal case. The spectra of the two most energetic POD modes, which account for 9% of the fluctuating kinetic energy, peak clearly at the same frequency ( $St = 0.11$ ) as in the isothermal case. The spatial POD modes (Fig. 4.10d,e) reveal slightly stronger vortical structures and slower streamwise decay. For these operating conditions, the helical instability and associated coherent structures are not suppressed by combustion. In fact, they seem to be almost not affected at all. The third mode (Fig. 4.10f) represents slow axisymmetric movements similar to the isothermal case.

For the short hydrogen flame, the POD (Fig. 4.11) reveals a strong (6%) first mode, which describes an axisymmetric broadening and contraction of the jet. The second and third mode show the typical vortex pattern already observed for the PVC of the detached flame, the isothermal case, and the trumpet flame. Compared to the isothermal case and the detached flame, it is slightly shifted downstream, still remaining upstream of the structure found for the trumpet flame. The time traces and their spectra show that the PVC in the case of the short hydrogen flame oscillates at a frequency of  $St = 0.096$ , which is slightly lower than for the isothermal case and the detached flame. The energy distribution (Fig. 4.11a) shows that the fourth mode still contains 3% of the fluctuating kinetic energy. However, it shows no clear spatial distribution and no peak in its spectrum and is, therefore, omitted here. A compilation of the occurrence of the PVC, its frequency, and axial location is provided in Tab. 4.3 for the four observed flame shapes and the isothermal flow field.

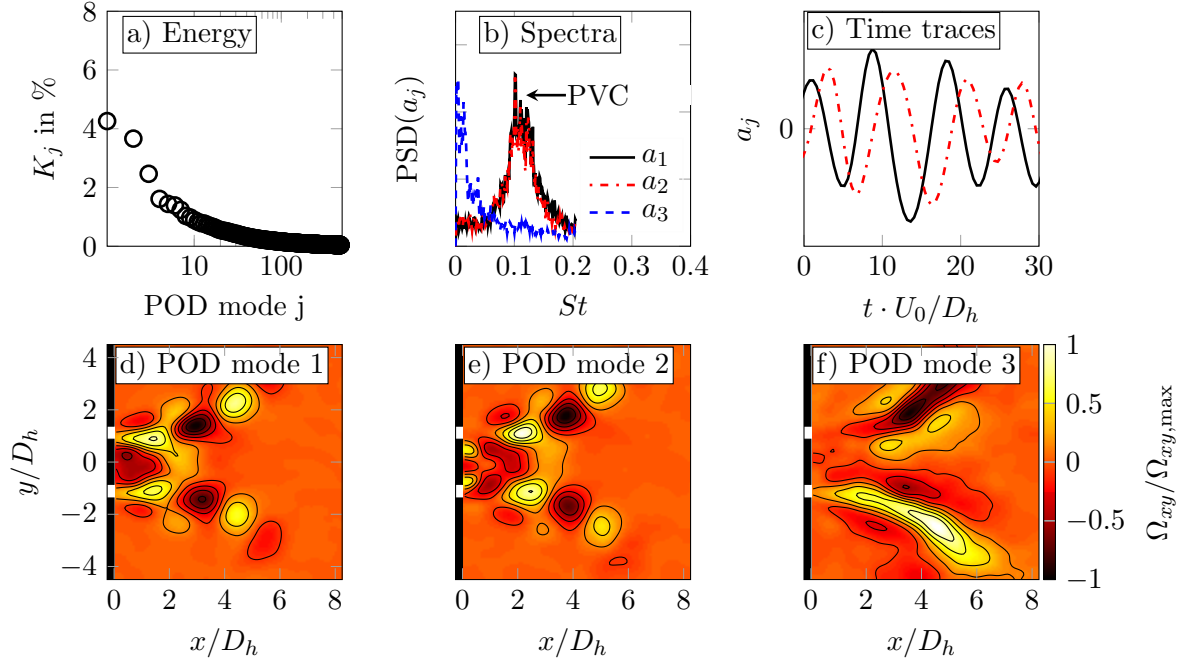


Figure 4.10: Results of the POD analysis of the detached flame. a) Distribution of the turbulent kinetic energy over the modes. b) Power spectra of the temporal POD coefficients. c) Time traces of the temporal coefficients related to the PVC. d-f) Normalized through-plane vorticity  $\Omega_{xy}$  of the spatial POD modes.

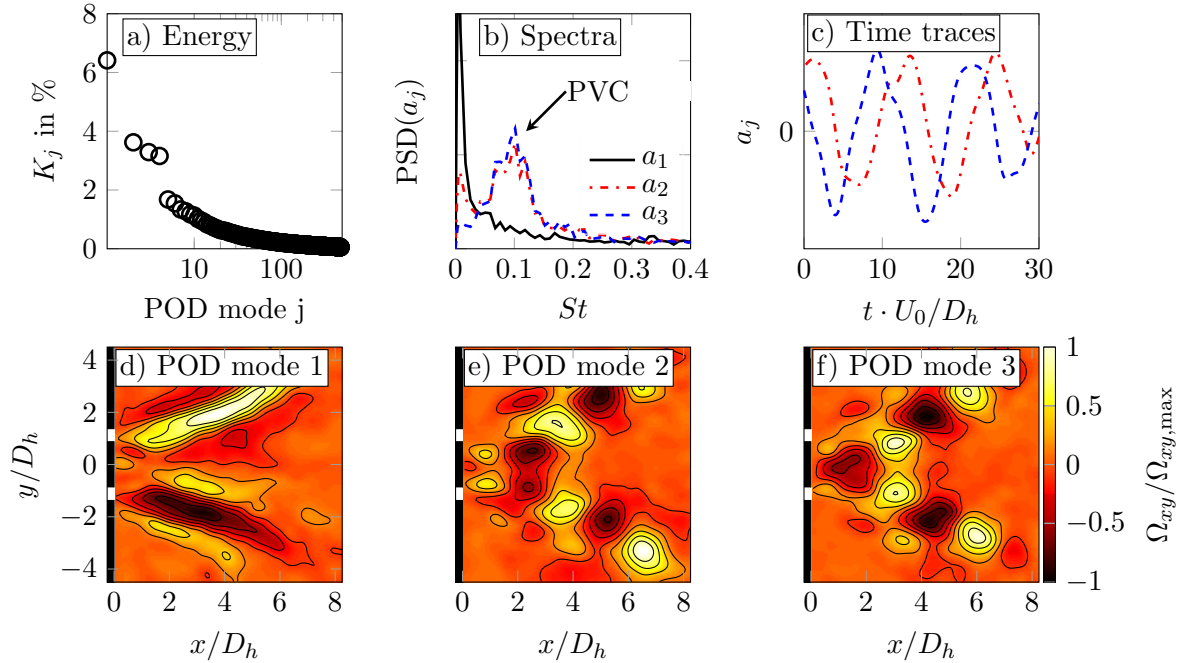


Figure 4.11: Results of the POD analysis of the short hydrogen flame. a) Distribution of the turbulent kinetic energy over the modes. b) Power spectra of the temporal POD coefficients. c) Time traces of the temporal coefficients related to the PVC. d-f) Normalized through-plane vorticity  $\Omega_{xy}$  of the spatial POD modes.

Table 4.3: Compilation of the occurrence of the PVC for the observed flame shapes.

Flame shape	PVC	Frequency	Axial location
Isothermal flow	Yes	St= 0.11	Reference case
Detached flame	Yes	St= 0.11	Similar to isothermal PVC
Trumpet flame	Yes	St=0.056	Downstream of isothermal PVC
V-flame	No	-	-
Short H <sub>2</sub> flame	Yes	St= 0.096	Slightly downstream of isothermal PVC

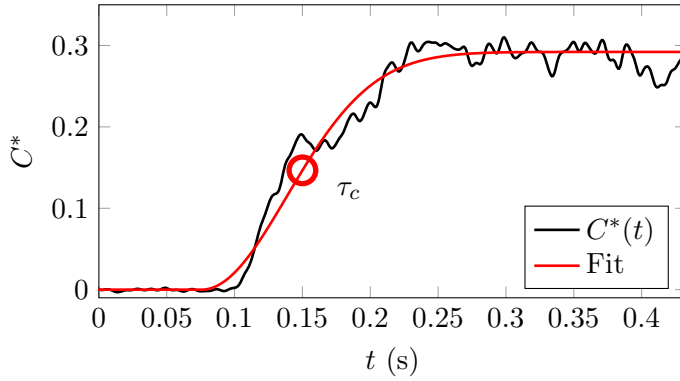


Figure 4.12: Time trace of the estimated normalized particle concentration at an arbitrarily chosen point ( $x/D_h = 1.5$  and  $y/D_h = 0$ ) in the region of burnt gases of the V-flame. Red line represent the analytical fit (Eqn. 4.3) and the red circle indicates the estimated time-lag  $\tau_c$ .

## 4.6 Influence of the PVC on the Mixing of the Emanating Jet with the IRZ

One of the effects of the PVC and the associated Kelvin-Helmholtz instabilities is the increased mixing of the emanating annular jet with the IRZ, also denoted as the *premixing-core phenomenon* (Coats, 1996). To assess this phenomenon in the present thesis, time-lags from the combustor inlet to the different locations in the combustor are estimated. To this end, the transient particle concentration is measured for a steep input of the seeding particle concentration. The time-lag is defined as the time it takes for the concentration to reach 50% of its final value. It is extracted from the transient normalized particle concentration  $C^*(t, \mathbf{x})$  with the fitting of an analytical profile of the form:

$$C^*(t, \mathbf{x}) = \overline{C^*}(\mathbf{x}) \left[ 1 - \left( e^{\left( \frac{t-\tau_c}{\tau_d} + \sqrt{\log 2} \right)^2} \right)^{-1} \right]. \quad (4.3)$$

Here,  $\overline{C^*}(\mathbf{x})$  is the density-dependent steady state particle concentration,  $\tau_c$  is the convective time-lag, and  $\tau_d$  describes the broadening of the step (low-pass filter characteristic). An example of the fitting of the analytical profile on the measured data is depicted in Fig. 4.12. For the investigation of the mixing processes of the emanating jet to the IRZ, the interest is placed on the convective time-lag, as it indicates very well if the fluid particles can enter the IRZ quickly via mixing or slowly through the large recirculation system (IRZ).

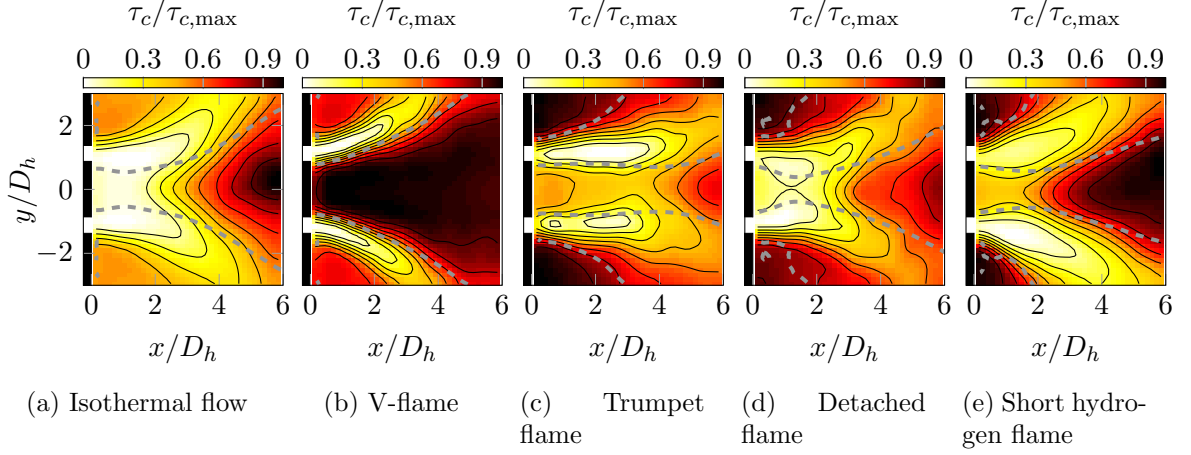


Figure 4.13: Normalized time-lag distributions. Gray dashed lines indicate zero axial velocity of the time-averaged flow field.

From Fig. 4.13, different convective time-lag distributions are evident between the different configurations. The most significant difference can be observed in between the V-flame and all other configurations. While in the V-flame case, very high convective time-lags prevail in the IRZ, they are much lower in the isothermal case, for the detached flame, the trumpet flame, and the short hydrogen flame.

One of the main differences regarding the flow field dynamics between the V-flame and the other investigated cases is the suppression of the PVC, which is known to significantly affect mixing processes (Galley et al., 2011; Duwig et al., 2012) inside the combustor. Therefore, it seems plausible that the PVC and the associated axial-radial eddies, the Kelvin-Helmholtz instabilities, are the cause for the rapid mixing in the isothermal case and their suppression is the reason for the slow mixing in the V-flame case. This assumption is supported by a closer view at the time-lag distributions of the different flame configurations. In the cases where the PVC is strong already close to the combustor inlet (isothermal flow and detached flame), the time-lags are very short close to the combustor inlet. Obviously, the fluid in the jet is immediately mixed with the IRZ. In the trumpet flame case, where the PVC is shifted downstream, the time-lags are higher close to the inlet. Interestingly, the lowest time-lags in the IRZ are found at  $x/D_h \approx 2.5$ . This corresponds very well to the axial location, where the PVC oscillation starts to be strong. The time-lag distribution suggests that the particles enter the IRZ at  $x/D_h \approx 2.5$  and are subsequently transported upstream. The time-lags in the case of the short hydrogen flame are slightly longer close to the centerbody. This is in good agreement to the somewhat weaker PVC and its location slightly more downstream compared to the isothermal and detached case.

The strong differences in the mixing characteristics, caused by the PVC, are also very important for the density distribution as shown in Fig. 4.5. Due to the strong mixing in the upstream region of the IRZ, almost no density gradients are present for the detached flame. For the trumpet flame the strong mixing does not set in upstream of  $x/D_h < 2.5$ .

Consequently, the density gradients are very steep upstream of the PVC. In the case of the V-flame, the suppression of the PVC leads to lower mixing intensities and, thus, to steeper density gradients. For the short hydrogen flame, the PVC is entirely located in the region of burnt gases. Thus, the axial-radial eddies have no significant effect on the density gradient. Their effect can be seen, however, in the tangential velocity profiles. Analog to the density, the transport of angular momentum from the jet into the IRZ seems to be dominated by the helical instability. In the absence of the PVC, the tangential velocity gradient near the centerline is very low, while for the cases with a strong PVC, the gradient is considerably higher (see Fig. 4.5).

## 4.7 Heat Release Fluctuations Caused by the PVC

In the following, the influence of the PVC on the heat release rate distribution is investigated. Since the measurement of the heat release is subject to a significant amount of noise, the direct application of the POD on the measured OH\*-chemiluminescence intensity does not provide clear results. The decomposition fails to yield spatial modes that can be associated with the frequency of the PVC. However, since the OH\*-chemiluminescence intensity was captured simultaneously to the velocity data, the POD is carried out on the velocity data. Subsequently, the phase averaging process of the heat release is carried out using the phase information from the POD of the velocity data. The phase angle of the PVC oscillation is obtained as:

$$\theta(t) = \arg[a_j(t) + ia_k(t)], \quad (4.4)$$

where  $j$  and  $k$  are indices corresponding to the POD modes describing the PVC. The procedure is presented in Section 2.5 in more detail. In Fig. 4.14, the phase-averaged OH\*-chemiluminescence images are provided for the three flame shapes featuring the PVC (detached annular flame, trumpet flame, and short hydrogen flame) at four different phase angles.

For the detached flame and the trumpet flame (Fig. 4.14a,b), it can be observed how the PVC causes large-scale heat release fluctuations, where the upper and the lower half of the combustor are perfectly out-of-phase. The heat release peaks at one side of the combustor when the other side has a minimum. Thus, no integral heat release fluctuations were measured. This is also evident in the integral OH\*-chemiluminescence intensity shown in Fig. 4.15 for the detached flame. If the intensity is integrated over one half of the combustor, a strong sinusoidal oscillation is evident. In contrast to that, the full integration yields no clear oscillation. It is inherent to the antisymmetry of the velocity fluctuations that also the induced heat release oscillations are antisymmetric. Thus, no integral heat release fluctuations are caused by the helical instability. However, in the presence of pronounced asymmetries, this may not be the case (Acharya et al., 2013), and the integral heat release rate may fluctuate with the PVC frequency. For the short hydrogen flame (Fig. 4.14d), only very weak heat release fluctuations are evident.

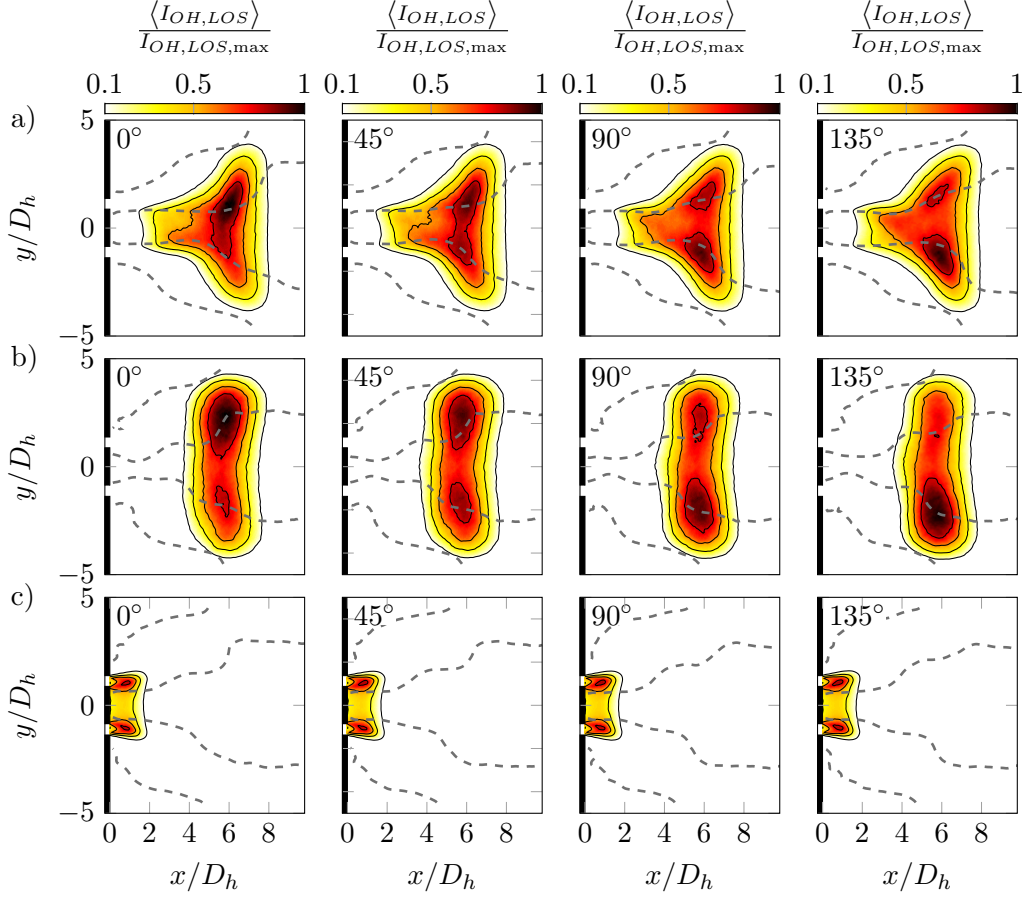


Figure 4.14: Phase-averaged line-of-sight integrated heat release fluctuations caused by the PVC. Gray dashed lines indicate zero phase-averaged axial velocity. a) trumpet flame, b) detached flame, and c) short hydrogen flame.

To obtain a planar representation of the line-of-sight  $\text{OH}^*$ -chemiluminescence measurements, a tomographic reconstruction scheme, as developed by Moeck et al. (2013), is applied to the antisymmetric heat release fluctuations (see Section 3.3.3). The reconstructed planar heat release fluctuations are shown in Fig. 4.16. Lines of zero phase-averaged axial velocity are superimposed on the normalized reconstructed coherent  $\text{OH}^*$ -chemiluminescence fluctuations.

For the trumpet flame in Fig. 4.16a, alternating regions of higher and lower heat release rates are evident that travel along the inner shear layer and to a limited extent also in the outer shear layer. The heat release oscillation pattern clearly correlates to the vortical pattern identified from the POD analysis shown in Fig. 4.9. It can be observed that the heat release fluctuations emanate from the flame root and are subsequently amplified. Since fuel, air, and steam are mixed well upstream of the combustor inlet, it is assumed that the heat release fluctuations are mainly caused by vortex-flame interaction.

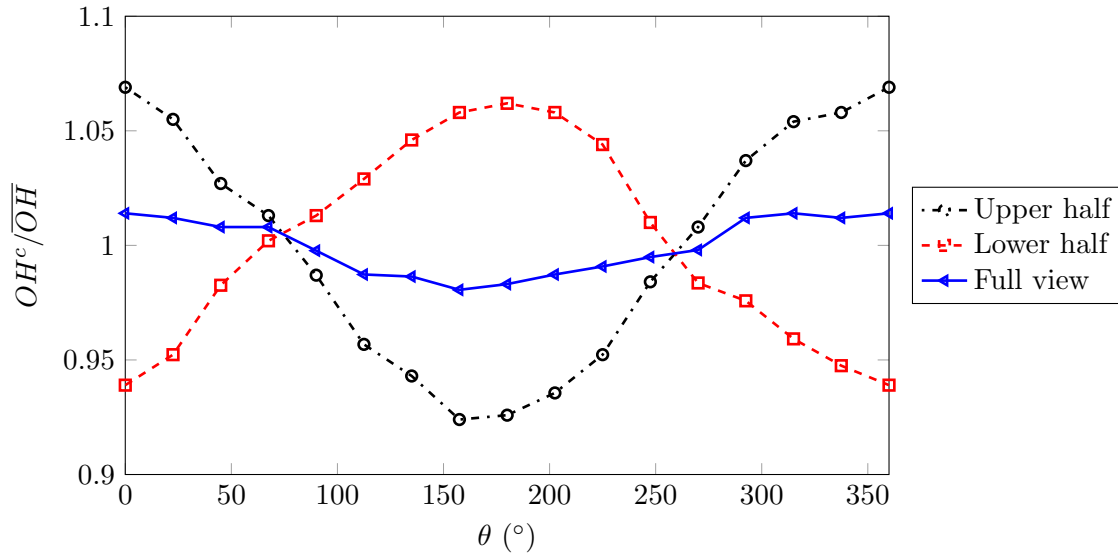


Figure 4.15: Coherent integral  $\text{OH}^*$ -chemiluminescence fluctuation of the detached flame.

For the detached flame presented in Fig. 4.16b, a similar antisymmetric pattern of alternating regions of high and low  $\text{OH}^*$ -chemiluminescence intensities is evident. Again the wavelength and frequency corresponds to the flow field fluctuations (see Fig. 4.10). The region of  $\text{OH}^*$ -chemiluminescence fluctuations is limited to the flame region, whereas the helical flow instability begins considerably upstream of the flame.

For the short hydrogen flame, the majority of the helical flow structure is located downstream of the flame. Nevertheless, small heat release fluctuations of the flame are caused (Fig. 4.16c). The flame seems to tumble slightly, which causes a skew symmetric heat release fluctuation field. However, it is to be reminded that the heat release fluctuations of the short hydrogen flame are very small (see Fig. 4.14c). No clear convection of the regions of high and low heat release can be identified due to the short flame length.

## 4.8 Conclusions

In the presented chapter four flame shapes in a swirl-stabilized combustor were classified and described.

- Dry flames and steam-diluted hydrogen or hydrogen enriched flames exhibited a V-shape. The flow fields showed low negative velocities in the IRZ and a wide jet opening angle, resulting in a broad IRZ. The turbulence intensity near the burner outlet was significantly reduced compared to the isothermal flow. In particular, inside the IRZ very low turbulence levels were measured.

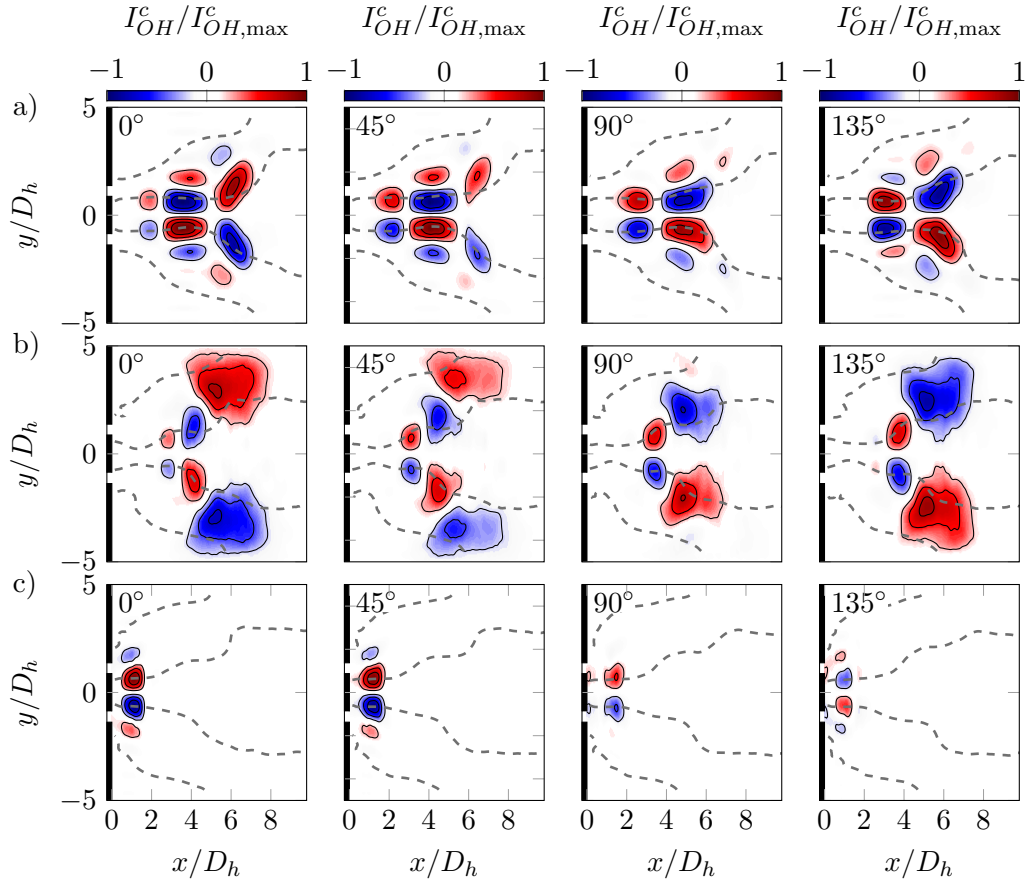


Figure 4.16: Tomographic reconstruction of the planar phase-averaged heat release fluctuations corresponding to Fig. 4.14. Red color indicates values higher than the time-averages and blue color lower values. Gray dashed lines indicate zero phase-averaged axial velocity. a) trumpet flame, b) detached flame, and c) short hydrogen flame.

- A trumpet-like flame was found at intermediate steam levels. The flow field as well as the flame showed a particular form with a very narrow IRZ and the main zone of heat release located along the inner shear layer.
- At high steam dilution rates, the flames detached and showed annular shapes located in a broad range of axial positions further downstream compared to the other flame shapes. The flow fields of the annular flames showed a good agreement with the isothermal flow. The shape of the velocity and turbulence profiles remained nearly unaltered near the burner outlet. Further downstream, flow velocities were higher due to dilatation caused by the heat release, and the IRZ became slightly narrower. Turbulence profiles scaled similarly to the velocity profiles.
- For very short, dry hydrogen flames, the flame angle is comparably narrow and the flow field showed some similarity to the isothermal case and the case of the detached flame.



Coherent structures were extracted from the flow field data by employing the POD technique. At isothermal conditions, a helical flow instability in the form of a PVC was found. This coherent structure was completely suppressed in the case of the V-flame. The trumpet flame featured a helical coherent structure that was located further downstream and precessed at a lower frequency than for the isothermal case. The flow fields of the annular flames at high levels of steam dilution (or very lean mixtures) and the flow field of the short hydrogen flame showed coherent structures that were very similar to the isothermal case in appearance and frequency.

The findings of this chapter show how the operating conditions, in particular the steam dilution rate and hydrogen addition, induce different flow fields and flame shapes, which are of high relevance for gas turbine operation, as they directly influence the stability of the combustor. The influence of the fuel composition and the dilution is generalized by relating the observed results to the reactivity of the mixture. Thereby, the results are not limited to steam-diluted combustion. The presented work empirically describes how the flame shapes and the flame length are related to the occurrence of the PVC. Furthermore, the strong impact of the PVC on the mixing characteristics and the flame dynamics are pointed out. The detailed investigation of the mechanisms involved in the excitation and suppression of the PVC are left for Chapter 6.



## Chapter 5

# Control of the Vortex Breakdown Type and the PVC with Axial Injection

*<sup>2</sup>This chapter presents the results of a combined experimental and numerical study of the occurrence of different vortex breakdown types and helical instabilities in realistic swirling combustor flows. The focus is placed on the investigation of how they can be controlled with axial injection through a truncated centerbody. A parametric study of the isothermal flow field inside the combustion chamber and in the mixing tube upstream of the combustor is carried out in a water tunnel test facility. Selected configurations were further assessed under reacting conditions, and a large eddy simulation was conducted and successfully validated with the experimental data. The results show that at certain combinations of the primary swirl number of the swirler and the amount of axial injection, the vortex breakdown type changes from a bubble type to a cone type. The flow field featuring the cone type VB is shown to provide very suitable conditions for flashback-proof combustor operation. The analysis of the flow field dynamics yields a clear correlation of the vortex breakdown type to the excitation of the PVC. The flow fields containing the bubble vortex breakdown feature a strong, high-frequency PVC. This PVC is gradually damped by axial injection and fully suppressed if the vortex breakdown type changes to the cone type. Simultaneously, a much slower and weaker PVC emerges further downstream.*

### 5.1 Introduction

Swirling flows undergoing vortex breakdown provide an excellent basis for flame stabilization. On the other hand, vortex breakdown can also lead to flame flashback into the premixing section. Modern premixed combustors require a mixing tube for enhanced fuel–air mixing.

---

<sup>2</sup>The results presented in the present chapter were previously published in Terhaar et al. (2015c). The LES was conducted out by Christina Schrödinger. Thoralf Reichel assisted during the non-reacting measurement in the water tunnel. All other tasks were carried out by the author.

The good mixing significantly reduces the emissions, but the vortex breakdown can move upstream into the mixing tube, or the swirl generator, where the high temperatures may cause severe damage. A safe way to prevent flashback is the application of a centerbody in the mixing tube. However, this centerbody is in the direct vicinity of the flame and must be extensively cooled, rendering its application impossible for high pressure operation. The design of a flashback-proof, centerbody-less burner that ensures a high degree of mixing still remains one of the most challenging tasks in combustor development. Burmberger and Sattelmayer (2011) proposed the application of a low momentum non-swirling inner jet (jet velocity is similar to bulk velocity) and a convergent mixing tube to obtain a well-defined vortex breakdown outside of the mixing tube. In the present thesis, the approach of a non-swirling inner jet is employed.

The main focus of this chapter is, however, not placed on the flashback safety of the combustor, but on the understanding of the effect of the low-momentum axial injection on the time-averaged flow field, i.e., the vortex breakdown type, and on the excitation of a PVC. For the detailed assessment of the flashback behavior, the reader is referred to the work published from the author in cooperation with Thoralf Reichel (Reichel et al., 2013, 2014).

Beside the work by Burmberger et al. (2006), who briefly mentioned the observation of a damping effect of the non-swirling jet on the PVC in their numerical simulation, no previous investigations of the damping of the PVC due to a low momentum axial injection into the mixing tube are known to the author. For a fuel injector with a high momentum jet (100 m/s jet velocity and 30 m/s bulk velocity), Jochmann et al. (2005) performed URANS simulations. They found a complete suppression of a PVC that was present without jet. This suppression was accompanied by minor changes to the mean flow field. Other studies investigated a different configuration, featuring a jet that is injected through a centerbody directly into the combustion chamber with high momentum (Spencer et al., 2008; Dunham et al., 2009) or low momentum (Bender and Büchner, 2005; García-Villalba and Fröhlich, 2006; García-Villalba et al., 2007). All observed that the PVC at its original frequency is damped or suppressed. In the high momentum cases, an instability of higher azimuthal wave number appeared instead of the PVC (Spencer et al., 2008; Dunham et al., 2009).

Jochmann et al. (2005) related the suppression of the PVC due to high momentum axial injection to different vortex breakdown types, which are triggered by the inflow profile. In analogy to the DNS simulations of Ruith et al. (2003), they found that a wake-like profile (without jet) caused a spiral type breakdown (with PVC), and the jet like profile with injection caused a bubble-type breakdown (without PVC). These findings are fully in line with the interpretation of the spiral type vortex breakdown as the superposition of a globally unstable bubble type breakdown and a helical instability (Escudier and Keller, 1985; Ruith et al., 2003; Gallaire et al., 2006).

Another distinction for VB, which is used in this chapter, was introduced by Billant et al. (1998). They observed the typical bubble-type VB and a cone-shaped VB, as depicted in Fig. 5.1. Both VB types were produced in the same swirling jet facility at different operating conditions. Depending on the Reynolds number, both VB types were reported in an axisym-

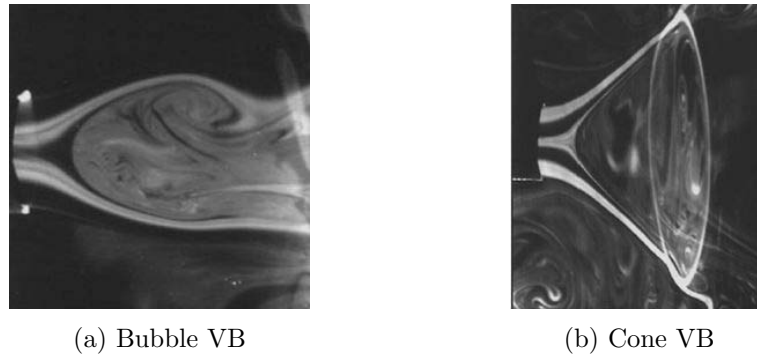


Figure 5.1: Visualization of the bubble VB and cone VB by Billant et al. (1998).

metric and an asymmetric form. The asymmetric form at sufficiently high Reynolds numbers can be interpreted as the basic axisymmetric flow field with the superposed asymmetric global flow oscillation (Gallaire et al., 2006).

In this chapter, the effect of a non-swirling low momentum jet in the mixing tube is investigated in a generic combustor geometry at isothermal conditions. Obviously, for combustor development, the flow field and flow field dynamics are much more relevant at reacting conditions than at isothermal conditions. Regarding the onset of vortex breakdown, it was shown by Kröner et al. (2003) that at reacting conditions, combustion induced vortex breakdown can occur. The stagnation point can move upstream and the risk of flashback is increased. Therefore, complementary reactive measurements are presented to show that the conclusions made in this chapter for isothermal conditions also hold under reacting conditions.

The outline of this chapter is as follows. A brief introduction to the measured and simulated operation conditions is provided, and time-averaged flow fields are presented and classified into different vortex breakdown regimes resembling the bubble and cone type vortex breakdown. Subsequently, the occurrence of the PVC is extracted from the time-resolved flow field data and classified into two different types, closely corresponding to the vortex breakdown regimes. Of the two breakdown types, the cone breakdown is identified as preferable in terms of flow stability and flash back safety. Design rules for the control of the vortex breakdown type with axial injection are obtained.

## 5.2 Experimental and Numerical Procedure

The experiments were carried out in the centerbody-free combustor shown in Fig. 3.2b. This combustor has a primary inflow through a movable block swirl generator and a secondary inflow through a non-swirling jet on the centerline. The swirl number through the swirler is termed the primary swirl number  $S_{\text{prim}}$  and the ratio of axially injected mass flow to the total mass flow is denoted by the axial injection rate  $\chi$ . The majority of the experiments were carried out under non-reacting conditions in the water tunnel facility (Fig. 3.3) and  $S_{\text{prim}}$  and  $\chi$  were systematically varied. The flow field inside the combustor was measured employing high-speed PIV. At a fixed inlet swirl number of  $S_{\text{prim}} = 0.9$ , additional measurements inside

Table 5.1: Operating conditions of the tested cases.

Parameter		Isothermal cond.	Reacting cond.	LES
Water mass flow	$\dot{m}$ (kg/h)	4,900	-	4,900
Air mass flow	$\dot{m}$ (kg/h)	-	130	-
Reynolds number	Re	50 000	75 000	50 000
Swirl number	$S_{\text{prim}}$	0.5 - 1.2	0.9	0.9
Axial injection	$\chi$	0 - 15%	0; 12.5%	0%
Air inlet temperature	$T_{\text{in}}$ (K)	-	450	-
Equivalence ratio	$\phi$	-	0.7	-

the mixing tube in crosswise and streamwise planes were conducted and the tangential flow field velocities were measured employing LDV. Furthermore, measurements under reacting conditions using methane fuel were carried out, where the axial injection rate was varied and the flow field in the combustion chamber was captured using high-speed PIV. The flame position was measured employing OH\*-chemiluminescence imaging.

A small region upstream of the area jump was not accessible to the optical measurement techniques. To obtain insight into this very interesting domain, a large eddy simulation (LES) was conducted. For the simulation, only the mixing tube and the combustion chamber were considered and experimentally obtained inflow profiles from the swirl generator were used as boundary conditions. This drastically reduced the computational and meshing effort and still resulted in a satisfactory simulation of the flow field.

The simulation was performed with the commercial ANSYS CFX 14 software. ANSYS CFX uses a completely coupled solver, which solves the differential equations for the hydrodynamic variables ( $u$ ,  $v$ ,  $w$ ,  $p$ ) as a single system. This solution approach uses a fully implicit discretization of the equations at any given time step. For spatial discretization, the central difference advection scheme was applied, and for temporal discretization a 2nd-order backward Euler scheme was employed. The LES Smagorinsky model was used for subgrid turbulence modeling.

The computational domain was meshed with tetrahedrons. The grid was refined within the mixing tube and in the combustion chamber in the shear layer and recirculation regions, resulting in element volumes smaller than  $4 \cdot 10^{-9} \text{ m}^3$ . Altogether, the mesh consisted of around 1.3 million nodes. Since the isothermal experiments were conducted in a water test rig, the fluid properties in the simulation were also set to those of water. A time step of  $5 \cdot 10^{-4} \text{ s}$  was used so that the rms Courant-Friedrichs-Levy number in the whole domain was smaller than 0.8. Convergence was achieved within 10 inner loop iterations for every time step. An opening was used as outlet condition and no slip conditions were applied at all other boundaries. Table 5.1 gives an overview of the simulated and measured non-reacting and reacting operating conditions.

### 5.3 Time-Averaged Flow Fields

During the non-reacting measurements in the water tunnel, a parametric study was carried out increasing the amount of mass flow injected through the truncated centerbody. All flow fields shown in Fig. 5.2 resemble the typical flow field of swirl-stabilized combustors, similar to the flow field observed in Chapter 4. A jet emanating into the combustion chamber can be observed in Fig. 5.2a. This jet undergoes vortex breakdown, leading to a large region with negative axial velocities around the centerline, the inner recirculation zone (IRZ). A second zone of negative axial velocities can be seen near the combustor wall, the outer recirculation zone (ORZ).

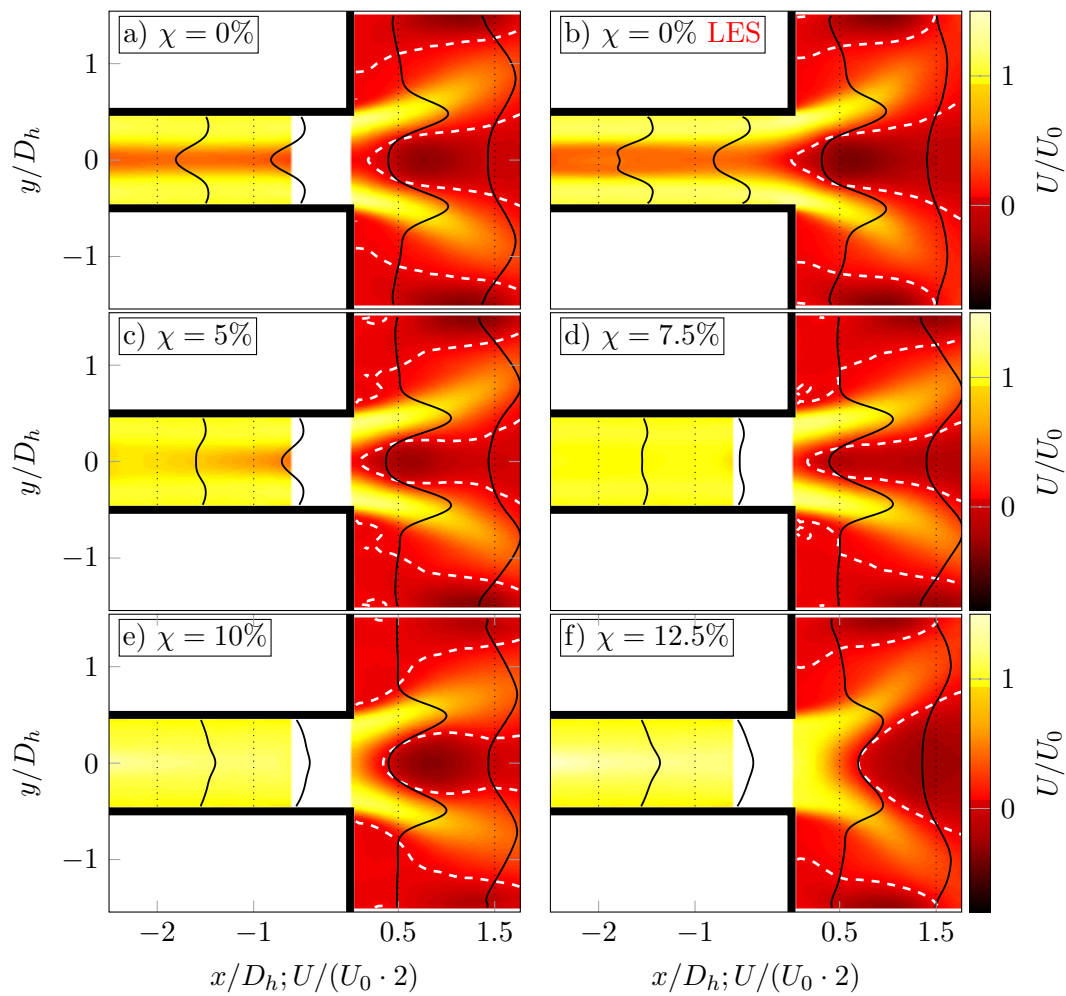


Figure 5.2: Time-averaged flow fields at increasing rates of axial injection. Radial profiles of the axial and tangential velocities superimposed on the normalized axial velocity. White dashed lines indicate zero axial velocity. Inlet swirl number is  $S_{\text{prim}} = 0.9$ . Top right plot (b) is based on LES data, while all other plots are based on experimental data.

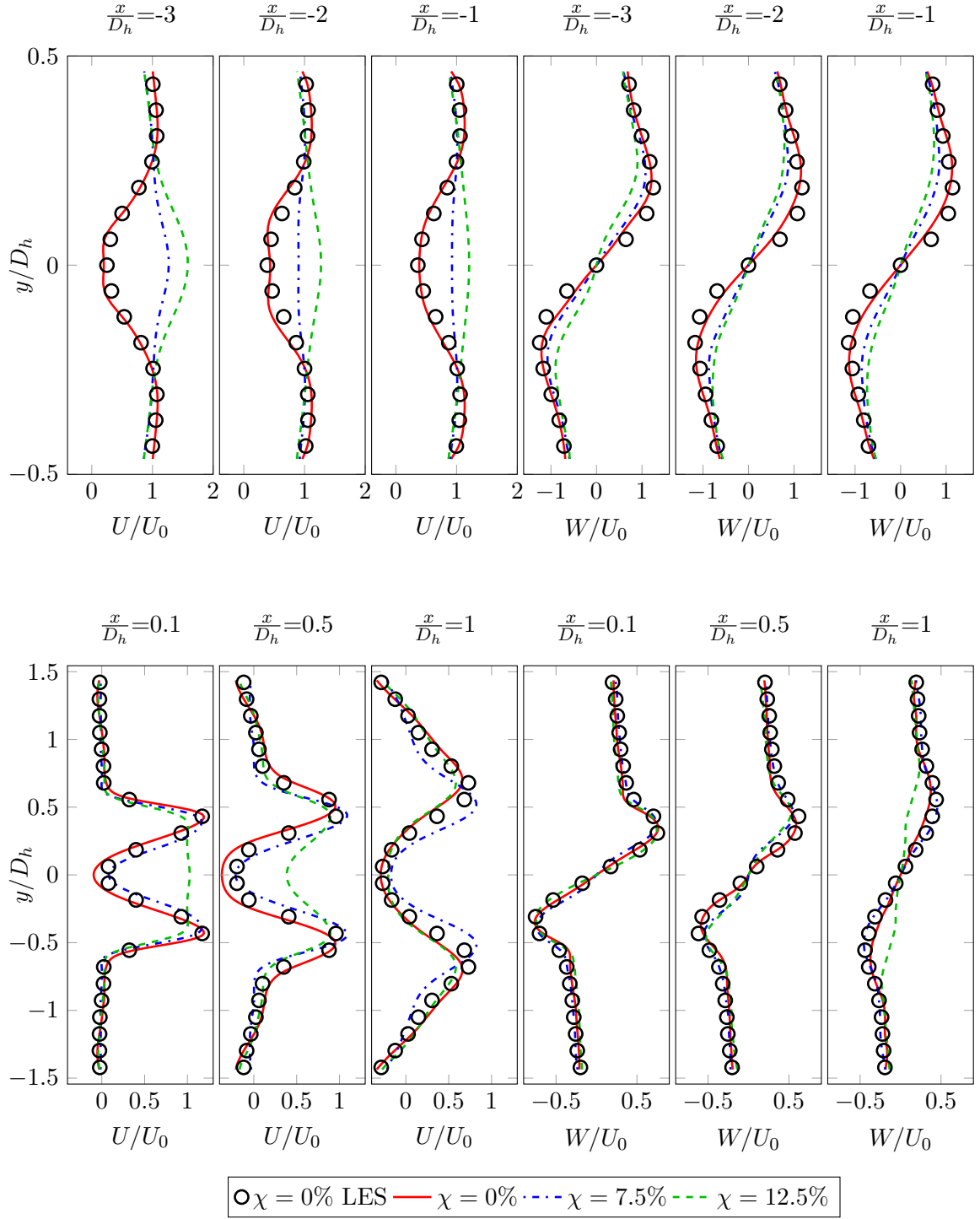


Figure 5.3: Radial velocity profiles of axial and tangential velocities inside the mixing tube (top row) and the combustion chamber (bottom row). Inlet swirl number is  $S_{\text{prim}} = 0.9$ .



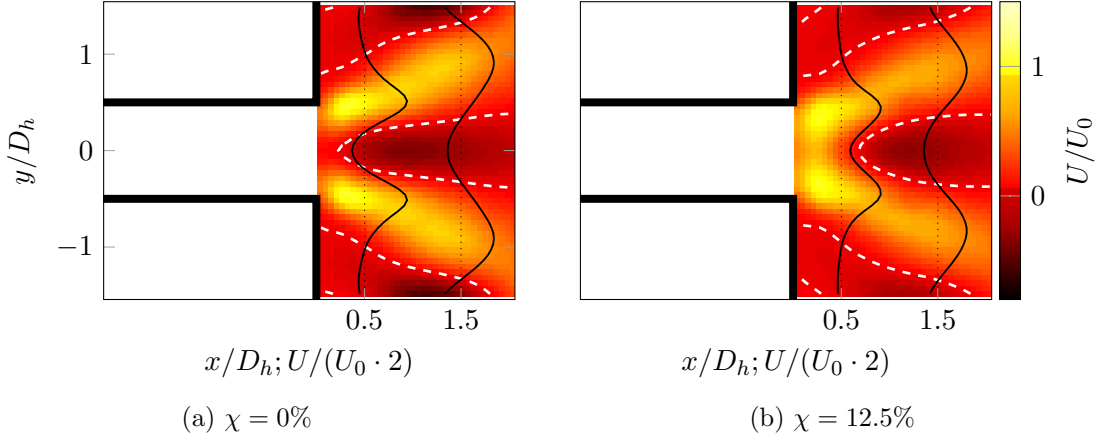


Figure 5.4: Time-averaged flow fields at reacting conditions (methane). Radial profiles of the axial velocity superimposed on the normalized axial velocity. White dashed lines indicate zero axial velocity. Inlet swirl number is  $S_{\text{prim}} = 0.9$ .

The effect of axial injection is evident in the series of mean flow fields shown in Fig. 5.2. For ratios of axial injection up to  $\chi = 7.5\%$  two trends are apparent. First, the axial deficit on the centerline is only reduced in the mixing tube. Near the combustor inlet, the velocity profiles remain similar. Second, the opening angle of the jet becomes narrower while the streamwise location of the stagnation point remains almost unchanged. At an injection ratio of  $\chi = 10\%$ , a different trend is visible. Injection now significantly increases the axial velocities near the centerline, leading to a downstream displacement of the stagnation point. The opening angle of the jet increases significantly, leading to a very wide zone of negative velocities for  $\chi = 12.5\%$  axial injection.

The same trends can be seen in Fig. 5.3, where radial profiles of the axial and tangential velocities are compared at various axial locations for  $\chi = 0, 7.5$ , and  $12.5\%$ . At  $\chi = 12.5\%$ , the axial velocity profile at the entrance of the combustion chamber ( $x/D_h = 0.1$ ) nearly equals a plug-flow. In terms of flashback-safety this is considered as optimal (Lieuwen et al., 2008). Furthermore, an interesting detail can be visible. While axial injection leads to lower tangential velocities in the mixing tube, all profiles converge to a very similar shape slightly downstream of the area jump. This is assumed to be caused by the different locations of vortex breakdown. In the cases with low rates of axial injection, the decay of the azimuthal velocities induced by vortex breakdown approximately counterbalances the lower azimuthal velocities caused by axial injection.

Additionally, the good agreement of the LES simulation to the experimental results is evident from Figs. 5.2 and 5.3. Despite the small upstream shift of the stagnation point, the LES data resembles very well the measured velocities, thus, providing insight into the complete flow field, including the region that was not accessible during the experiments.

Figure 5.4 shows the time-averaged flow fields under reacting conditions without axial injection and with  $\chi = 12.5\%$  axial injection. On the one hand, combustion leads to a smaller IRZ and the dilatation due to heat addition leads to higher velocities in the jet. On the other

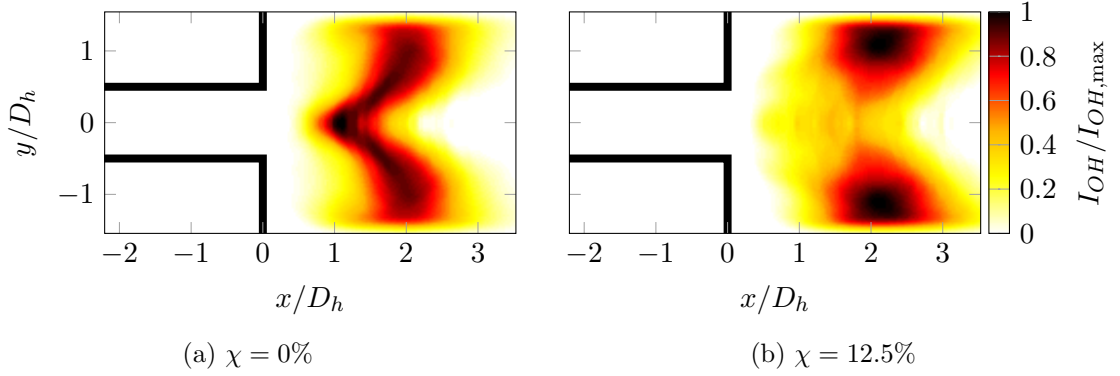


Figure 5.5: Abel-deconvoluted OH\*-chemiluminescence intensity. Inlet swirl number is  $S_{prim} = 0.9$ .

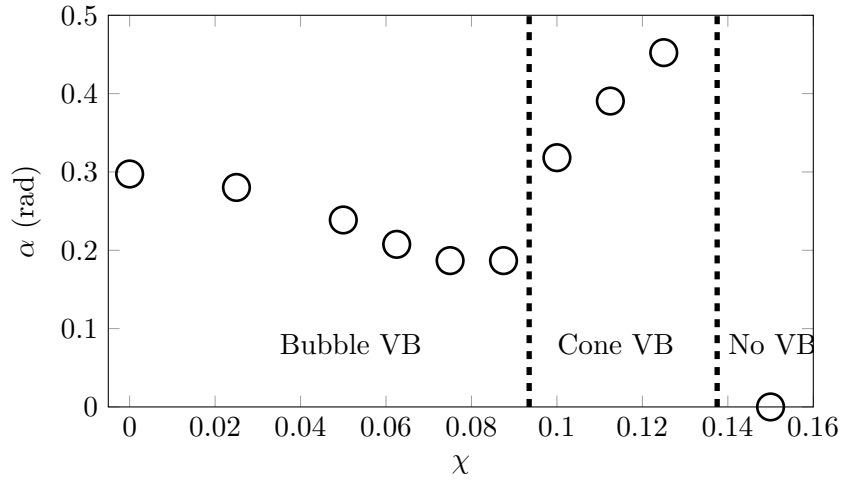


Figure 5.6: Initial jet opening angle (from  $x/D_h = 0.1$  to  $0.6$ ) at increasing rates of axial injection. Inlet swirl number is  $S_{prim} = 0.9$ .

hand, the results clearly show that the basic effects of axial injection on the isothermal flow field remain under reacting conditions. The velocity deficit near the burner outlet vanishes, the vortex breakdown is shifted downstream and the opening angle of the jet is increased. The effect of axial injection on the flame shape is depicted in Fig. 5.5. With axial injection, the reaction in the inner shear layer is reduced and the flame is shifted downstream.

The evolution of the jet opening angle  $\alpha$ , with changes of the axial injection rate is shown in Fig. 5.6. The opening angle is obtained using Eqn. 4.2 with integration boundaries of  $x/D_h = 0.15$  to  $x/D_h = 0.6$ . The trend of decreasing jet divergence with low ratios of axial injection is likely to be a result of the lower resulting swirl of the jet caused by the addition of non-swirling fluid. However, the adverse trend at high injection rates indicates that an additional mechanism is involved into the drastic changes of the mean flow field. The large opening angle and the overall shape of the flow field at  $\chi = 12.5\%$  shows similarity to the

cone-type breakdown, as reported by Billant et al. (1998) (see Fig. 5.1b), whereas the flow field without injection is similar to the typical bubble breakdown (Fig. 5.1a) (Billant et al., 1998; Lucca-Negro and O'Doherty, 2001). In the presented results, the downstream stagnation point is located outside of the measured domain.

## 5.4 Classification of Vortex Breakdown Types

In order to parametrically study the occurrence of the different VB types, the transition from the bubble type to the cone type is defined as the point where the initial size of the IRZ starts to increase with increasing rates of axial injection, as can be seen in Fig. 5.6 for  $\chi > 9\%$ . Furthermore, a resulting swirl number ( $S_{\text{res}}$ ) is introduced that accounts for the reduction of the geometrical swirl number of the swirler ( $S_{\text{prim}}$ ) due to the axial injection. The resulting swirl number is calculated from the measurement applying the reduced definition of the swirl number:

$$S_{\text{res}} = \frac{\dot{G}_{\Theta}}{R_b \cdot \dot{G}_x} = \frac{2\pi\rho \int_0^{R_b} UWr^2 dr}{R_b \cdot 2\pi\rho \int_0^{R_b} (U^2 - 0.5W^2) r dr}, \quad (5.1)$$

where  $\dot{G}_{\Theta}$  and  $\dot{G}_x$  are the axial flux of tangential and the axial flux of axial momentum, respectively, and  $R_b$  is the mixing tube (and burner outlet) radius. The non-swirling air injection causes an additional axial momentum and the tangential momentum is reduced since the total mass flow is kept constant. Thus, with an increasing rate of axial injection the mass flow through the swirler generator is reduced. Both effects can be modeled, and a resulting swirl number  $S_{\text{res}}$  is obtained as:

$$S_{\text{res}} = \frac{\dot{G}_{\Theta, \chi=0} (1 - \chi)^2}{R_b \left( \dot{G}_{x, \chi=0} (1 - \chi)^2 + \dot{G}_{x, i}(\chi) \right)} = \frac{\dot{G}_{\Theta, \chi=0} (1 - \chi)^2}{R_b \left( \dot{G}_{x, \chi=0} (1 - \chi)^2 + \rho \chi^2 u_0^2 \frac{A_{MT}^2}{C_d A_i} \right)} \quad (5.2)$$

The newly introduced variables are the cross section of the mixing tube  $A_{MT}$ , the cross section of the axial injection  $A_i$  and the discharge coefficient  $C_d$  of the axial injection. Both cross sections are defined by the geometry. For the discharge coefficient, a rather low value of  $C_d = 0.6$  had to be used in order to fit the measurement data. This is assumed to be caused by the supply port for the axial injection, which is of a much smaller diameter than the axial injection. Figure 5.7 shows a comparison of the measured swirl number at  $x/D_h = -2$ , that is upstream of the vortex breakdown, and the calculated resulting swirl numbers. The model seems to be in good agreement to the experimental results and is therefore used to calculate the resulting swirl number for the other combinations of geometrical swirl numbers and rates of axial injection, where no experimental data of the tangential velocity component inside the mixing tube is available.

Isolines of the resulting swirl numbers for all measured parameters ( $S_{\text{prim}} = 0.5$  to  $1.2$  and  $\chi = 0$  to  $12.5\%$ ) are provided in Fig. 5.8. The lines of constant resulting swirl are superposed on the zones where a bubble type VB, a cone type VB, and no VB were observed. It is evident that the onset of VB is dominated by the resulting swirl number. A critical swirl

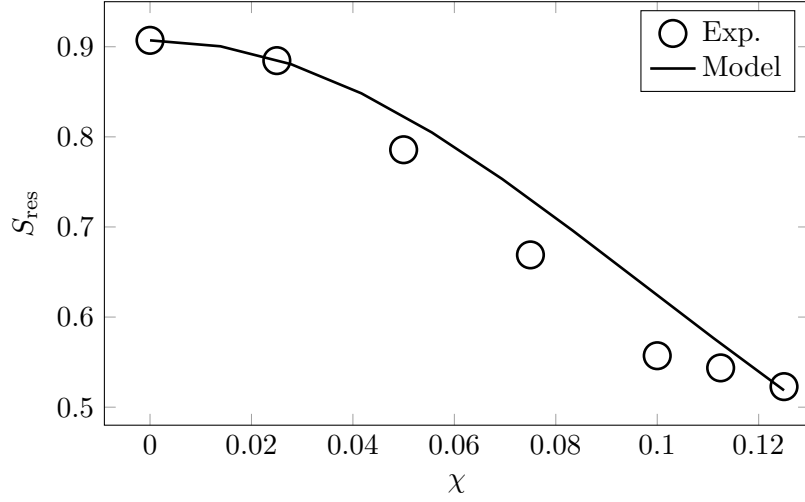


Figure 5.7: Reduction of the resulting swirl number due to axial injection. Comparison of measured to modeled swirl number.  $S_{prim} = 0.9$

number of  $S_{res,crit} \approx 0.47$  can be identified. The zones of bubble type VB and cone type VB, in contrast to this, do not depend on the resulting swirl. This relative insensitivity to the swirl number is in line with the findings of Billant et al. (1998). While Billant et al. (1998) found that small temperature differences triggered the transitions, in the present cases the shape of the inflow profiles seems to determine the selection of the VB type. High primary swirl numbers at high rates of axial injection, i.e, a low axial velocity deficit at the combustor inlet, promote the cone type VB. For low primary swirl numbers, the zone of the cone type VB is rather small and high rates of axial injection lead to resulting swirl numbers  $S_{res}$  below  $S_{crit}$ , where no VB occurs. It is also worth noting that in preliminary measurements, the cone type vortex breakdown could not be achieved using a high momentum jet on the centerline. The flow field transition took place directly from the bubble type VB to the inhibition of VB.

## 5.5 Identification of the PVC

Spectra of the radial velocity fluctuations at an arbitrarily chosen point in the inner shear layer ( $x/D_h = 0.7$ ,  $y/D_h = 0.25$ ) are shown in Fig. 5.9 for the isothermal and the reacting flow fields. For comparison purpose, the results of the LES are also provided. It can be observed that the flow fields without axial injection exhibit very strong periodic oscillations. The spectra at the isothermal and reacting conditions, as well as from the LES, are very similar in terms of the peak Strouhal number ( $St = 0.56$ ). This indicates that, in the presented cases without axial injection, the mechanism that defines the frequency of the self-excited oscillation is not influenced by combustion. This is an important justification for the investigation of the swirling combustor flow and its dynamics under isothermal conditions. The peak in the spectra is completely suppressed for the isothermal and reacting flow fields with a high rate of axial injection ( $\chi = 12.5\%$ ) (Fig. 5.9b). For the sake of comparison, also the spectrum of a

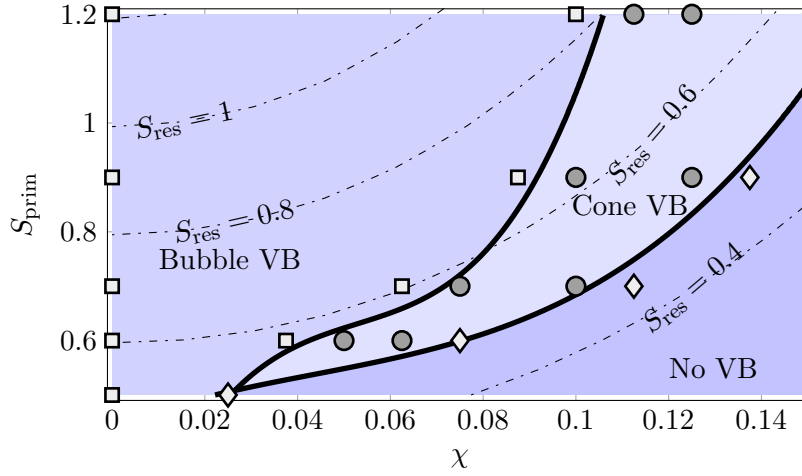


Figure 5.8: Overview of the occurrence of VB and VB types. Squares indicate bubble type VB, circles cone type VB, and diamonds no VB. Solid lines are interpolated boundaries of the domain. Dashed lines are isolines of the modeled resulting swirl number. To enhance the clarity, only the relevant measurement points are displayed.

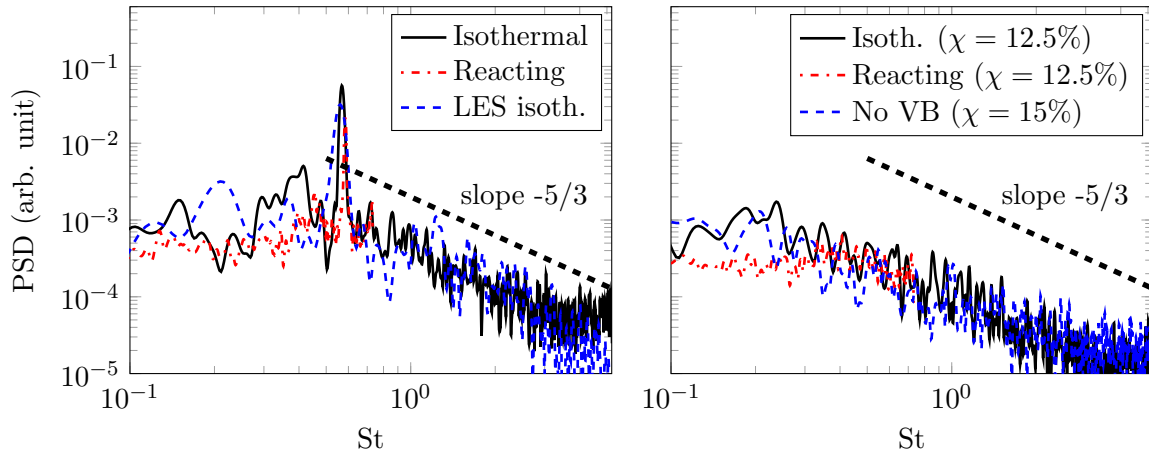


Figure 5.9: Spectra of the radial velocity fluctuations at an arbitrarily chosen point in the shear layers ( $x/D_h = 0.7$ ,  $y/D_h = 0.25$ ) for the isothermal flow field and reacting flow fields without axial injection (left,  $\chi = 0\%$ , bubble type VB) and at high rates of axial injection (right,  $\chi = 12.5 - 15\%$ , cone type VB). Inlet swirl number is  $S_{\text{prim}} = 0.9$ .

case with a very high injection rate ( $\chi = 15\%$ ) is shown. Vortex breakdown is inhibited due to the axial injection (see Fig. 5.8) and no peaks in the spectrum are visible.

The shape of the flow structures that are linked to the peaks in the spectra without axial injection can be extracted from the velocity data using a POD as described in Section 2.3. Before assessing the occurrence of the coherent structures in the different configurations, the outcome of the POD analysis without axial injection is briefly described. The presentation of the results follows the same path as in the previous chapter. Figures 5.10a-c show the energy

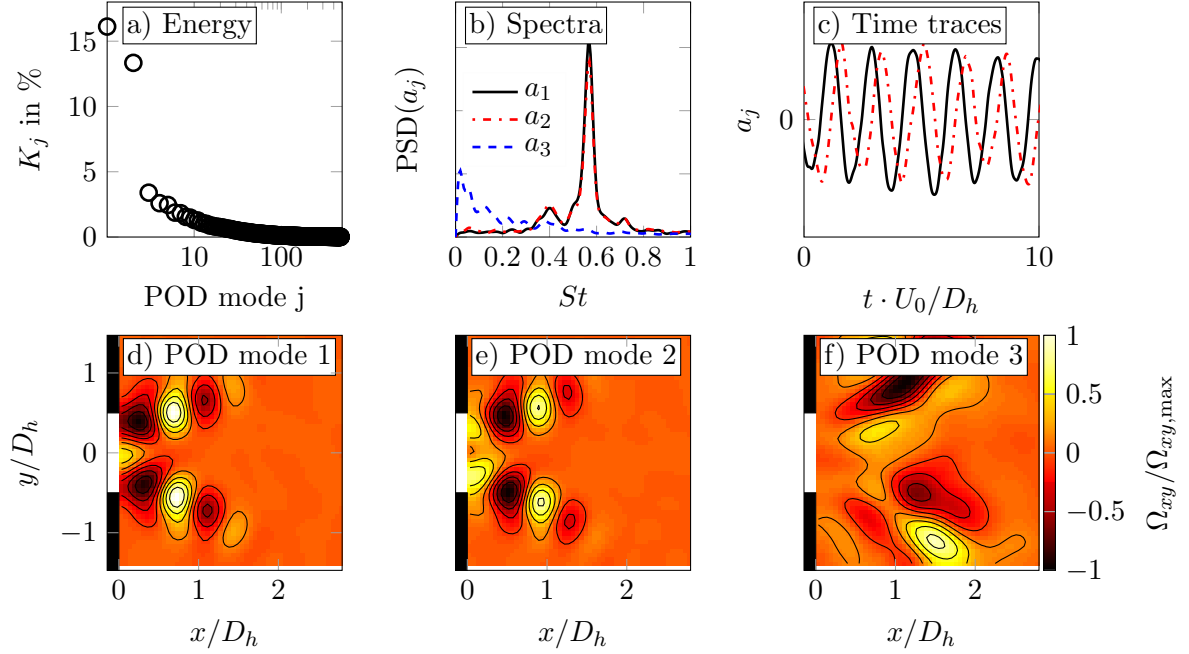


Figure 5.10: Results of the POD analysis of the isothermal flow without axial injection ( $\chi = 0\%$ , bubble VB, PVC type I). a) Distribution of the turbulent kinetic energy over the modes. b) Power spectra of the temporal POD coefficients. c) Time traces of the temporal coefficients related to the PVC. d-f) Normalized through-plane vorticity  $\Omega_{xy}$  of the spatial POD modes. Inlet swirl number is  $S_{\text{prim}} = 0.9$ .

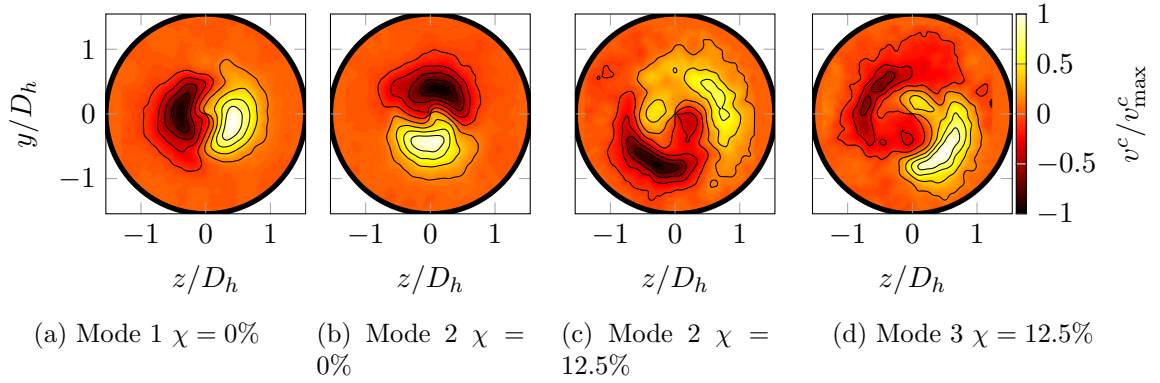


Figure 5.11: Normalized radial velocity of the first dominant POD modes for the isothermal flow field in a crosswise plane at  $x/D_h = 0.7$ . a)-b) Bubble VB / PVC type I; c)-d) Cone VB and PVC type II. Inlet swirl number is  $S_{\text{prim}} = 0.9$ .

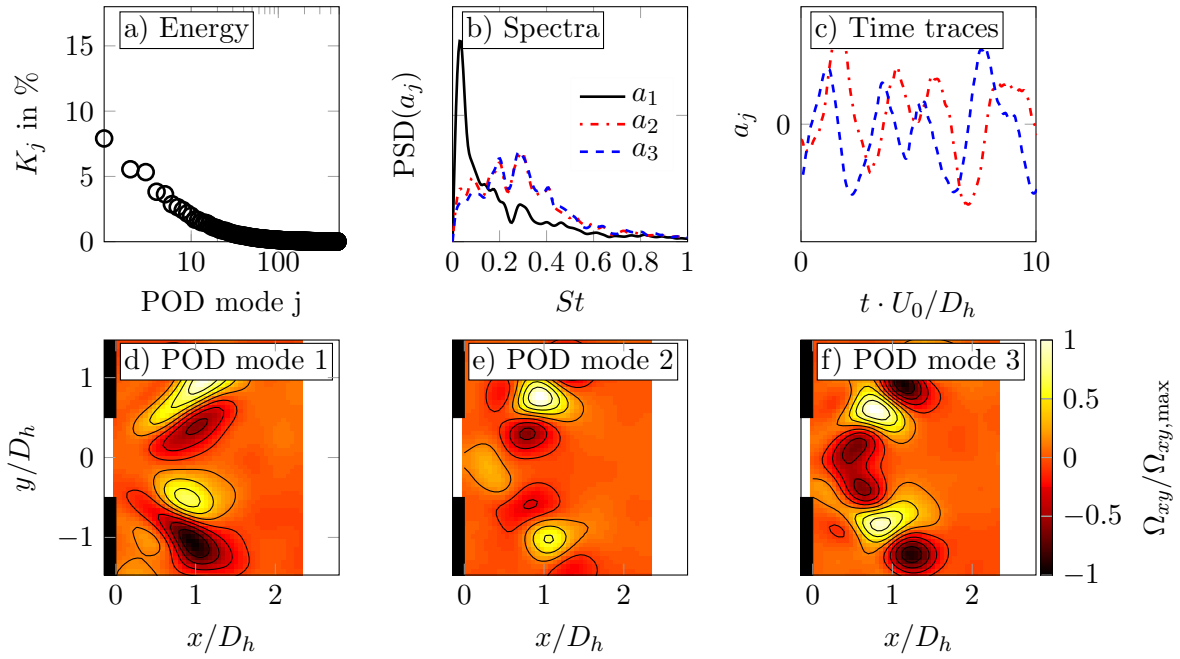


Figure 5.12: Results of the POD analysis of the isothermal flow with a high rate of axial injection ( $\chi = 12.5\%$ ). For the explanation see Fig. 5.10. Inlet swirl number is  $S_{\text{prim}} = 0.9$ .

distribution  $K_j$ , the normalized power spectral density (PSD) of the POD coefficients  $a_j(t)$ , and the corresponding time traces. It can be observed that around 30% of the fluctuating kinetic energy is captured by the first two modes. The spectra of these two modes reveal a distinct peak at  $St = 0.56$  that coincides with the peak in the velocity spectra shown in Fig. 5.9. Thus, the POD clearly identified the coherent structure that caused the strong spectral peak of Fig. 5.9. The corresponding time traces show that the first two modes oscillate in time at a phase shift of a quarter period. Consistently, the first two spatial POD modes (Figures 4.6d-e) span a convective vortex pattern that is very similar to the results of the POD presented in Chapter 4. It is typical for the PVC and the synchronized Kelvin-Helmholtz instabilities (Oberleithner et al., 2011; Stöhr et al., 2011b).

Analogously to a traveling sine wave expressed by a superposition of a sine and cosine, the global flow oscillations encountered here can be expressed by the two most energetic POD modes. The third POD mode (Fig. 5.10f) shows no clear peak in the spectrum. The spatial distribution shows that this mode describes a mostly axisymmetric longitudinal movement of the shear layers and the recirculation zone. The low frequency content of this mode indicates that its dynamics are not related to shear instability. Figure 5.11a,b depicts the radial velocity of the first two spatial POD modes measured in a crosswise plane. The patterns show that the investigated global mode is manifested in a single helical structure, i.e., a structure of an azimuthal wave number of  $|m| = 1$ . Phase-averaged measurements (not presented here) show a precession of the vortex core co-rotating with the mean flow that is well in line with previous findings (Gallaire and Chomaz, 2003; Syred, 2006; Oberleithner et al., 2011). The

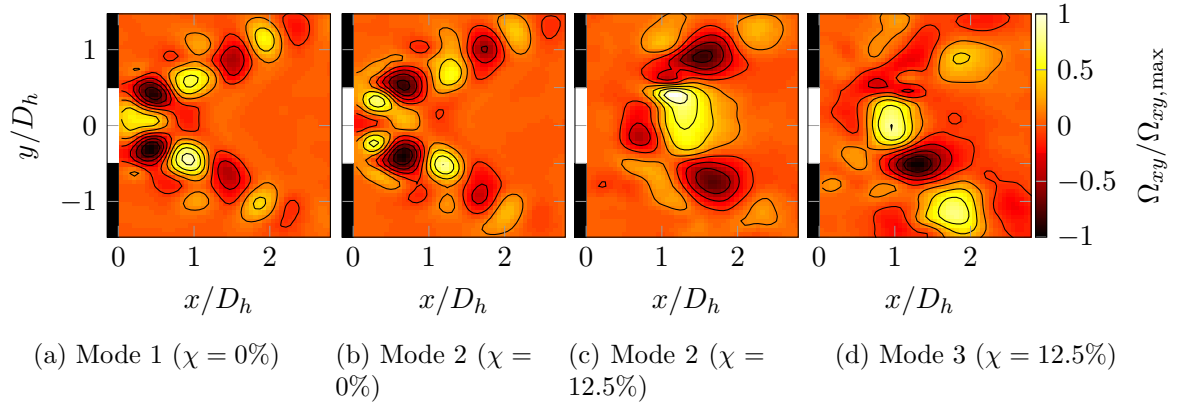


Figure 5.13: Normalized through-plane vorticity of the first dominant POD modes for the reacting flow field in the streamwise plane without axial injection ( $\chi = 0\%$ ) and with a high rate of axial injection ( $\chi = 12.5\%$ ). Inlet swirl number is  $S_{\text{prim}} = 0.9$ .

POD analysis provides strong evidence that the isothermal flow field without axial injection features a helical coherent structure, the PVC, at a Strouhal number of  $St = 0.56$ .

For the flow field with a high rate of axial injection ( $\chi = 12.5\%$ , cone VB), no clear peaks can be identified from the spectrum in Fig. 5.9b. Nevertheless, the POD analysis, as shown in Fig. 5.12, reveals large-scale coherent structures. The first POD mode represents a slow axisymmetric longitudinal movement of the shear layers. Similarly to the third mode of the case without axial injection, it seems unlikely that this mode is related to shear instabilities. In contrast to that, the second and third POD modes show a convective vortex pattern observed already in the case without axial injection. However, the structure is much noisier, shifted downstream, and oscillates at a lower frequency with strong jitter. The POD modes of the crosswise measurements, shown in Fig. 5.11c-d, indicate that the structure is of a single helical type, typical for the PVC. Again, the time-resolved measurements confirm that the structure is co-rotating with the mean flow. The low energy content of the modes and the strong frequency jitter may explain why no peak was found for this case in the single point velocity spectra (Fig. 5.9b). An explanation for the non-constant frequency may be long term flow field variations, as they were also reported by Billant et al. (1998) for the cone VB. Possibly, the long term flow variations are captured by the first POD mode.

The results of the POD analysis of the reacting flow field are presented in Fig. 5.13. For the case without axial injection (Fig. 5.13a,b) the spatial shapes of the modes are very similar to the isothermal case. It can be observed that the axial wavelength is slightly higher and the axial extent of the structure is increased. The frequency of the oscillation, as indicated by the single point spectra in Fig. 5.9, is hardly altered from the isothermal to the reacting case. For the case at a high rate of axial injection (Fig. 5.13a,b), again a similarity between the isothermal and the reacting case is found. However, the structures are even noisier in the reacting case compared to the isothermal case (Fig. 5.12).



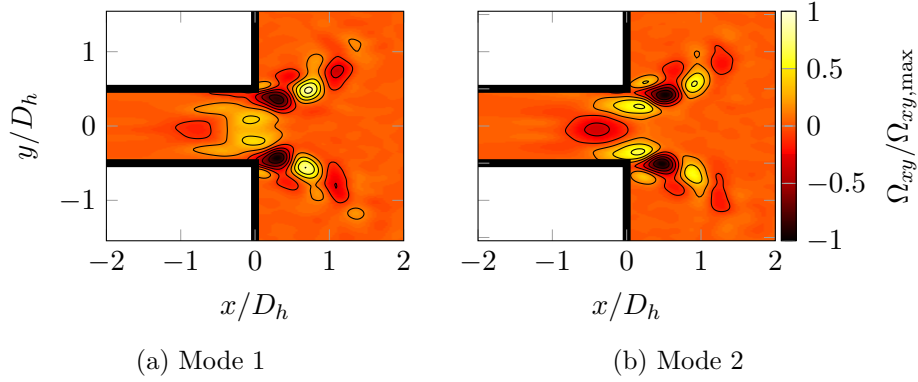


Figure 5.14: Normalized through-plane vorticity of the first two POD modes for the LES of the isothermal flow field without axial injection ( $\chi = 0\%$ ). Inlet swirl number is  $S_{prim} = 0.9$ .

The POD of the LES simulation reveals two POD modes (Fig. 5.14), which are very similar to the POD modes obtained from the experimental data (Fig. 5.10). Additionally the frequency of the global mode, as could be expected from Fig 5.9, and the TKE contribution ( $\approx 30\%$ ) are nearly identical. The excellent agreement of the velocity profiles, the oscillation frequency, and the mode shape proves the validity of the LES simulation in terms of both the mean velocities and the global mode. The benefit of the LES data is that it allows for the continuation of the POD analysis into the mixing tube and shows that the global mode persists up to  $x/D_h \approx -1$ . Furthermore, the LES data will be used for the stability analysis presented in the following chapter.

The strong similarity of the global mode in the isothermal and the reacting case without axial injection and the fact that the global mode changes its shape and structure at high rates of axial injection similarly at isothermal and reacting conditions is an important finding of this chapter. It demonstrates the relevance of the isothermal investigations for the present configuration.

## 5.6 Classification of the PVC

The POD analysis showed two different shapes of the PVC depending on the rate of axial injection. In the following, a PVC, which is similar to the PVC in the flow field without axial injection (Fig. 5.10), is defined as a PVC type I, whereas a PVC, which is similar to the PVC present at high rates of axial injection (shown in Fig. 5.12), is referred to as a PVC type II. It is worth noting that when the rate of axial injection is increased, no continuous transitions from the PVC type I to the PVC type II were observed. Rather, the PVC type I is damped and the PVC type II emerges.

From the POD analysis, the amount of turbulent kinetic energy (TKE) captured by the PVC can be readily obtained as the sum of the TKE ( $K_j$ , see Eqn. 2.13) captured by the two POD modes that describe the PVC. The TKE and the frequency of the highest peak in the spectra is summarized in Fig. 5.15 for the investigated swirl numbers of the primary air

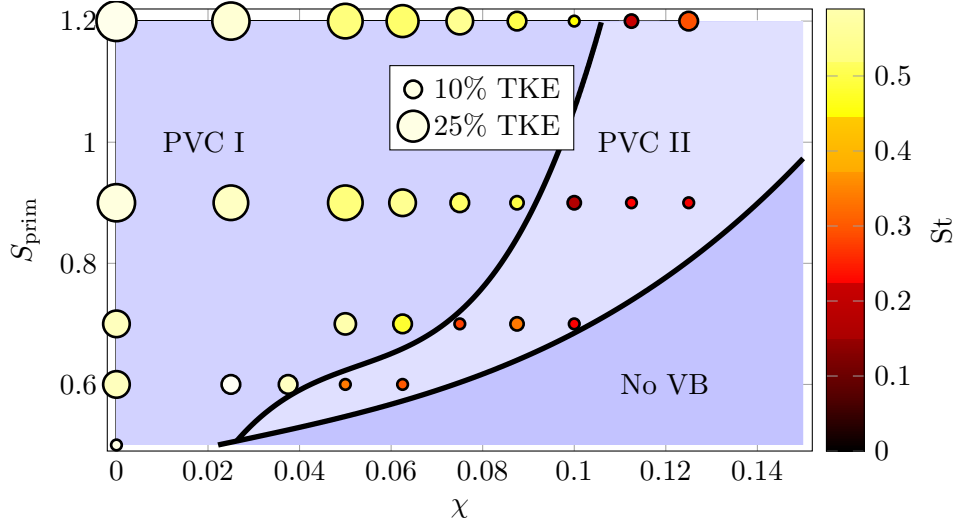


Figure 5.15: Overview of the POD analysis and classification of the PVC types. The marker size indicates the sum of turbulent kinetic energy associated to the two POD modes describing the PVC. The frequency of the highest peak is color coded. Areas show the regions where the PVC type 1 and PVC type 2 were identified.

$S_{\text{prim}}$  and axial injection rates  $\chi$ . Three regions are deduced from the results: At low primary swirl number and/or high rates of axial injection, vortex breakdown is inhibited. The zones representing the two PVC types, as shown in Figs. 5.10 and 5.12, can be clearly separated by a sudden change of the peak frequencies to considerably lower values. Inside the region of the PVC type I, the frequency and TKE increase with higher primary swirl and decrease with axial injection. The increase of the TKE with the swirl number is typical for a global mode arising from a supercritical Hopf bifurcation (Oberleithner et al., 2012a).

No clear trends inside the PVC type II region can be identified, and the TKE is much lower compared to that of the PVC type I. This further demonstrates the ambiguous character of the PVC type II. The parameter space, where the two PVC types were observed, is the same, where the two types of vortex breakdown (bubble and cone type) were observed, as shown in Fig. 5.8. The bubble type VB clearly corresponds to the PVC type I, and the cone type VB promotes a PVC type II.

## 5.7 Conclusions

In this chapter the control of the vortex breakdown type and the PVC in swirling combustor flows by means of axial injection was investigated. The practical application of axial air injection is to provide a suitable flow field for aerodynamic flame stabilization without the risk of flame flashback into the mixing tube. The results of this chapter show that the desired flashback-proof flow field can be achieved very well by changing the vortex breakdown type from the typical bubble to a cone type. The dominating parameters for the transition of

the vortex breakdown type are shown to be the inlet swirl number and the amount of axial injection. Based on the data, design rules are derived. A minimum primary swirl number is identified around  $S_{\text{prim}} = 0.6$ , where the cone type VB first appears for low rates of axial injection. At higher primary swirl numbers  $S_{\text{prim}}$ , the range of axial injection rates, for which the cone type VB occurred, significantly increases, thus, increasing the robustness of the design.

In general terms, the onset of VB is triggered by the resulting swirl, while the selection of the VB type is dominated by the inflow profile into the combustion chamber. High primary swirl numbers  $S_{\text{prim}}$  with high rates of axial injection  $\chi$  are more prone to a cone type VB. The flow field without axial injection and the same resulting swirl number  $S_{\text{res}}$  always showed a bubble type VB.

A POD of the results yielded that the flow field of the bubble type VB featured a strong self-excited global mode, denoted as PVC type I. The POD analysis of the flow fields of the cone type VB reveals a very weak global mode at a location further downstream, denoted as PVC type II. The spectra of the corresponding mode coefficients exhibited more than one peak, indicating that the PVC type II was of a non-constant frequency. The PVC type I of the bubble type VB was only slightly affected by combustion, whereas PVC type II of the cone type seems to be affected stronger by combustion.

The findings of this chapter provide a classification of VB types in swirling combustor flows and the requirements for their occurrence. A physical explanation for the excitation of the PVC and why it is so effectively controlled by small flow field modifications will be provided in the following Chapter.



## Chapter 6

# Analysis of the Excitation and Suppression Mechanism of the PVC

<sup>3</sup>*This chapter deals with the analytical assessment of the excitation of the PVC in swirling combustor flows. Linear hydrodynamic stability theory is applied to the measured flow fields to analyze the excitation and suppression of the PVC. In the first part of the chapter, control of the PVC using axial injection is assessed. Local linear stability analysis yields the absolutely unstable domain inside the flow field. Axial injection is shown to impede a zone of absolute instability near the combustor inlet while a second zone further downstream remains. An excellent agreement of the measured to the calculated frequencies of the global modes is achieved over the whole range of investigated axial injection rates. In the second part of the chapter, the effect of changes of the flame shape on the excitation and suppression of the PVC is analyzed. Local linear hydrodynamic stability successfully predicts the region of the flow field that dominates the excitation and frequency of the PVC. An excellent agreement is achieved between the PVC frequency and shape predicted and those observed in the experiments. The damping effect of density stratification, which is evident from the results, is further generalized in the third part of this chapter by the analysis of parametric model profiles. This model study investigates the role of the backflow velocity, the swirl intensity, and the density distribution. It reveals that the backflow on the jet axis and the density gradient in the shear layer are essentially the parameters that determine the suppression or excitation of the instability.*

---

<sup>3</sup>The results presented in the present chapter were previously published in Terhaar et al. (2015b, 2014c, 2015c). Kilian Oberleithner and Lothar Rukes provided the original version of the stability solver. The Bi-global stability analysis based on the author's experimental data was conducted by Pedro Paredes at the Universidad Politécnica de Madrid. All other tasks were carried out by the author.

## 6.1 Introduction

In the previous two chapters, the occurrence of the PVC and its shape and frequency were analyzed using the proper orthogonal decomposition (POD). This technique is based on experimental or numerical data and extracts the coherent structures related to the PVC empirically. However, the results are rather descriptive and cannot provide a sufficient understanding of the mechanisms involved in the excitation and suppression of the PVC. At this point, the local linear hydrodynamic stability theory, as described in Section 2.4, is a viable tool to complement the POD analysis of the PVC. Thus, the present chapter aims at a further understanding of the PVC mechanisms, the dominating flow regions, and the most important flow parameters by the application of linear stability theory to the measured flow fields.

In the literature, the effect of combustion on the flow instability was reported very ambiguously. In some cases the instability remained (Froud et al., 1995; Moeck et al., 2012; Galley et al., 2011), was suppressed (Roux et al., 2005; Giauque et al., 2005), enhanced (Syred, 2006), or the suppression depended on the operating conditions (Boxx et al., 2010a, see also Chapter 4). The governing mechanisms for the damping of the PVC were suggested to be the increased viscosity (Roux et al., 2005; Kuenne et al., 2011) and low tangential velocities near the centerline (Syred, 2006).

For isothermal swirling jets, linear hydrodynamic stability theory has been used successfully to explain the appearance of the PVC. The starting point for its application is the interpretation of the PVC as a global hydrodynamic mode triggered by an inherent flow resonance (Liang and Maxworthy, 2005; Gallaire et al., 2006; Oberleithner et al., 2011). In the local stability concept, local absolute instability is a necessary condition for a global instability, such as the PVC (Huerre and Monkewitz, 1990). Delbende et al. (1998) identified, for a fixed Reynolds number of  $Re = 667$ , parameter combinations of swirl intensity and back flow intensity that results in a locally absolutely unstable flow field. Ruith et al. (2003) carried out DNS of swirling jets with Reynolds numbers varying from  $Re = 1$  to 500 and found the single helical instability, the PVC, to be the first unstable mode if sufficient swirl was imparted on the flow, and the Reynolds number was of the order of  $Re = 200$  or higher. Gallaire et al. (2006) carried out linear stability analysis on the base flow fields calculated by Ruith et al. (2003) and found a region of absolute instability causing the PVC. The superposition of the helical PVC and the axisymmetric breakdown is also denoted as spiral vortex breakdown. Oberleithner et al. (2011) employed linear stability theory to the measured mean flow field of a turbulent swirling jet and found an excellent agreement between empirically constructed coherent structures and the eigenmodes of the solutions of the stability equations. Juniper (2012) showed the capability of local and global stability concepts by predicting very accurately the eigenfrequencies of the PVC in isothermal combustor flows.

When reacting flows are considered, the mean flow field is often strongly affected by combustion. Additionally, the dilatation due to heat release and the density stratification can directly alter the stability characteristics of the flow field. This can be seen by considering

the inviscid vortex transport equation:

$$\frac{D\boldsymbol{\Omega}}{Dt} = \underbrace{(\boldsymbol{\Omega} \cdot \nabla) \mathbf{V}}_{\text{Tilting and stretching}} - \underbrace{\boldsymbol{\Omega} (\nabla \cdot \mathbf{V})}_{\text{Dilatation}} + \underbrace{\frac{1}{\rho^2} (\nabla \rho \times \nabla p)}_{\text{Baroclinic torque}}. \quad (6.1)$$

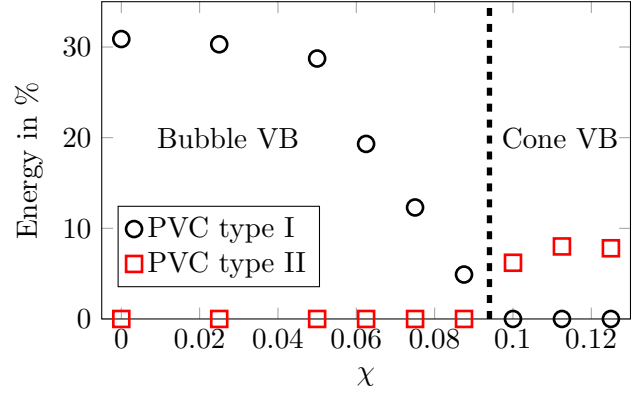
The vorticity generation is caused by stretching and tilting of the stream lines (first term), dilatation due to heat release (second term), and the baroclinic torque due to density stratification (third term). Contributions of viscous diffusion are neglected here. Of the three terms, the last two are affected by combustion.

The influence of density gradients on the hydrodynamic stability was first shown in an analytical study by Monkewitz and Sohn (1988). They found that a heated jet could pass a transition from absolutely stable to absolutely unstable, when the density ratio between the jet and the free stream fell below a critical ratio. A qualitative explanation for this can be found in the numeric and analytical study of Soteriou and Ghoniem (1995). The authors showed that the effect of density stratification is caused by the baroclinic torque. This was confirmed later by Lesshafft and Huerre (2007), who analytically proved that only the baroclinic torque has a significant influence on the flow stability. Soteriou and Ghoniem (1995) showed that the presence of a baroclinic vorticity dipole within a rolled-up eddy causes a lateral displacement of the eddy and, very importantly, the bias of its convection speed towards the velocity of the high-density stream. Thus, in the case of a hot jet and a cold wake, the convection speed is decreased, making the flow more prone to an absolute instability. In contrast to this, in the case of a cold jet and a hot wake, the convection speed is increased, making the flow less prone to an absolute instability. This was confirmed in the experimental and analytical study on the stability of non-isothermal wakes by Emerson et al. (2012).

In the studies of Monkewitz and Sohn (1988) and Emerson et al. (2012), parametric model profiles were employed to study the transition from absolute stability to absolute instability of isothermal free jets and wakes. Both studies found that cosigned temperature and velocity gradients (i.e., a heated jet) destabilized the flow, whereas cosigned density and velocity gradients (i.e., a heated wake) stabilized the flow. To the author's knowledge, no parametric study has so far been carried out that investigates the stability of non-isothermal swirling jets with backflow.

In the present chapter the excitation and suppression of the PVC is analyzed based on experimental results and on a parametric study using model profiles. It is structured in three parts: First, the analysis is applied to the flow field presented in Chapter 5 helping to understand the strong control authority of the axial injection on the PVC. Second, the analysis is extended to the reacting conditions presented in Chapter 4, where the occurrence and shape of the PVC for the different flame shapes are analyzed. Besides providing insight into the most important flow regions, the analysis of the flow fields furthermore serve to validate the local linear stability concept for its application to identify the governing flow parameters. Once the analysis is validated, it is used in the third part of this chapter part

Figure 6.1: Kinetic energy captured by the two POD modes representing PVC type I and PVC type II for increasing rates of axial air injection. At  $\chi \approx 9.5\%$ , the vortex breakdown type changes from bubble type to cone type.  $S_{\text{prim}} = 0.9$ .



in a model study to identify the key parameters for the occurrence, suppression, shape, and frequency of the PVC.

## 6.2 Analysis of the Effect of Axial Injection on the PVC

In Chapter 5 the control of the mean flow field, in particular the vortex breakdown type, with the application of axial injection was demonstrated. At high rates of axial injection ( $\chi$ ), a combustor flow field, which is very suitable for flashback proof combustor operation, was achieved. The changes of the vortex breakdown type were closely related to significant changes in the flow field dynamics. The results from a POD analysis and the spectra of velocity measurements showed that all flow fields exhibit a co-rotating helical self-excited oscillation with an azimuthal wave number of  $m = 1$ , the PVC. However, the frequency, amplitude, and modal shape differed considerably and depended on a combination of swirl number and rate of axial injection. Figure 6.1 summarizes the suppression of the strong PVC that occurred without axial injection (PVC type I) and the excitation of the weak PVC type II at high rates of axial injection.

### 6.2.1 Local Stability Properties

In the following, local linear hydrodynamic stability theory is used to study the influence of mean flow field changes on the local and global stability of the flow field and, thereby, on the PVC. As the interest is placed on self-excited instabilities, the spatio-temporal analysis, as described in Section 2.4, is applied. The flow is treated as locally parallel, and the local complex absolute frequencies  $\omega_0 = \omega_{0,r} + i\omega_{0,i}$  (absolute growth rate  $\omega_{0,i}$  and absolute frequency  $\omega_{0,r}$ ) are calculated for each axial position ( $x/D_h$ ). From the experiments it was confirmed that the global structure is of a co-rotating, single helical structure. Thus, all analysis were carried out at a fixed azimuthal wave number of  $m = 1$ . It is to be recalled that a positive absolute local growth rate ( $\omega_{0,i} > 0$ ) indicates that the flow is absolutely unstable at the given axial location, whereas a negative local growth rate ( $\omega_{0,i} < 0$ ) means that the flow is absolutely stable at this axial position. From the local stability properties, the global stability can be obtained. In any case, a sufficiently large region of absolute instability is a necessary



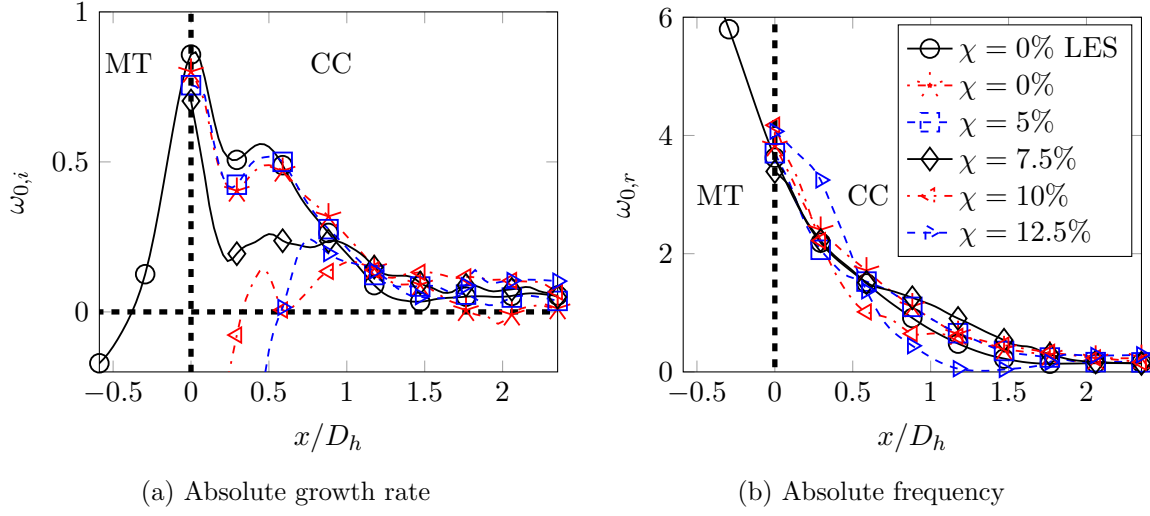


Figure 6.2: Axial distribution of local absolute growth rate ( $\omega_{0,i}$ ) and frequency ( $\omega_{0,r}$ ) in the mixing tube (MT) and the combustion chamber (CC).

condition for the flow field to become globally unstable. The global stability properties, the global growth rate ( $\omega_{g,i}$ ) and global frequency ( $\omega_{g,r}$ ), are subsequently obtained from the local absolute properties ( $\omega_0(x)$ ) with the application of a frequency selection criterion (see Eqn. 2.32). The full procedure of the stability analysis is provided in Section 2.4, where the mean flow field of the LES is exemplarily analyzed.

Figure 6.2 shows the local absolute growth rates and frequencies calculated for the velocity fields of  $S_{\text{prim}} = 0.9$  and axial injection rates of  $\chi = 0, 5, 7.5, 10$ , and  $12.5\%$ . Additionally, the results for the analysis of the LES data for  $\chi = 0\%$  are shown. The validated LES data provides insight into the influence of the mixing tube, which was not accessible to the measurements. The results for the LES show a large region of absolute instability ( $\omega_{0,i} > 0$ ). The region starts inside the mixing tube at  $x/D_h \approx -0.25$  and reaches far downstream  $x/D_h > 2.5$ . The highest local absolute growth rates are in the vicinity of the area jump from the mixing tube to the combustion chamber. The local frequencies strongly decay from the mixing tube to the combustion chamber.

The analysis of the experimental data without axial injection shows very similar results as the LES. This is no surprise since the velocity profiles of the simulation agree very well with the experimentally measured profiles. Low rates of axial injection ( $\chi = 5\%$ ) have no significant influence on the local absolute growth rate and frequency. At an injection rate of  $\chi = 7.5\%$ , the local absolute growth rates are already much lower than in the case without injection but still remain clearly positive. Only a small decrease of the local frequencies near the area change is visible for  $\chi = 5$  and  $7.5\%$ . At high rates of axial injection ( $\chi = 10\%$  and  $12.5\%$ ) the local absolute growth rates change significantly. The flow is no longer absolutely unstable near the area change ( $\omega_{0,i} < 0$ ), and the only absolutely unstable domain remains downstream of  $x/D_h > 0.25$  and  $x/D_h > 0.5$  for  $\chi = 10\%$  and  $\chi = 12.5\%$ , respectively.

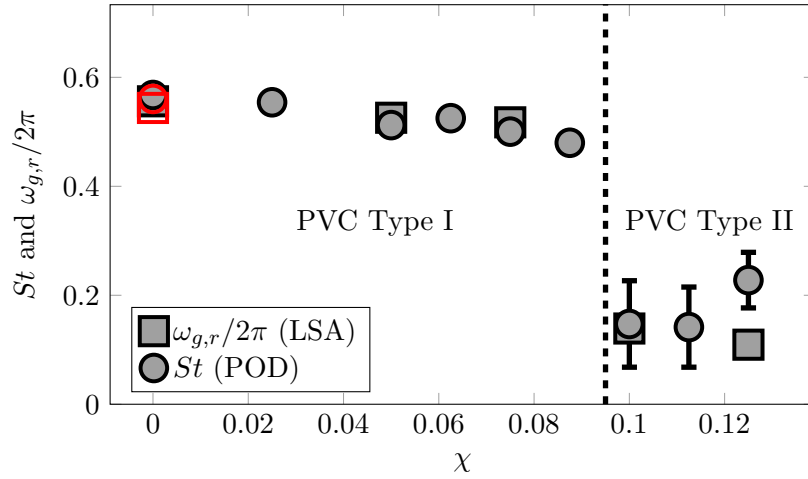
### 6.2.2 Global Stability Properties

Subsequently, the global growth rate ( $\omega_{g,i}$ ), frequency ( $\omega_{g,r}$ ) and the wavemaker location ( $x_s$ ) of the global mode can be calculated from the distribution of the local absolute growth rate and frequency, using the frequency selection criterion provided in Eqn. 2.32. In the local stability framework, also a second frequency selection criterion was proposed (Chomaz et al., 1988; Chomaz, 2005), when the absolutely unstable region appears at the inlet and is a few wavelengths long. In this case, the frequency is not selected at the saddle point, as defined in Eqn. 2.32, but at the flow inlet. It may be argued that the area jump from the mixing tube to the combustion chamber can be regarded as a new flow inlet. However, it will be shown that also the saddle point frequency selection criterion locates the wavemaker in the direct vicinity of the area jump. Therefore, both frequency selection criteria yield very similar frequencies (less than 4% difference). Thus, the presented results are independent of the chosen frequency selection criterion.

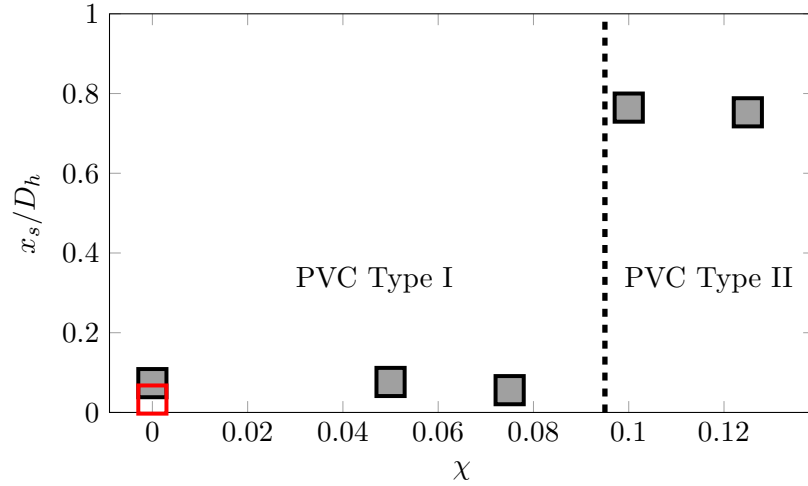
The global frequencies ( $\omega_{g,r}$ ) are compared in terms of a Strouhal number ( $St = \omega_{g,r}/2\pi$ ) to the measured frequencies in Fig. 6.3a. An excellent agreement between the measured and calculated frequencies is evident for the global modes representing a PVC type I. The global frequencies obtained from Eqn. 2.32 differ less than 5% from the measured frequencies. Moreover, the sudden shift of the frequency to much lower values, which is related to the change of the PVC from type I to type II is predicted very well. As it was shown in Fig. 5.12, for the PVC type II, a strong jitter of the frequencies was identified. This is represented with by error bars for the measured frequencies of the PVC type II. The error bars span the range where the spectral peaks of the POD coefficients were found.

The global growth rates ( $\omega_{g,i}$ , not shown) are slightly damped by the axial injection in the PVC type I domain and considerably lower, but still positive, in the PVC type II domain. The associated streamwise wavemaker location ( $x_s$ , Fig. 6.3b) is shifted downstream from  $x_s/D_h \approx 0.05$  (PVC type I) to  $x_s/D_h \approx 0.7$  (PVC type II) by the axial injection. Note that the wavemaker location calculated by the frequency selection criterion (Eqn. 2.32) has no strict physical meaning, and the region of highest structural sensitive is best obtained from an overlap of the direct and adjoint global mode of the flow (Juniper and Pier, 2014). However, the region of highest structural sensitivity is often at least close to the calculated wavemaker (e.g., Juniper and Pier, 2014). Thus, the wavemaker location provides a good idea of the most important region for the excitation of the PVC and the selection of its frequency.

Figure 6.4a shows the time-averaged flame shape of the case without axial injection. The flame foot at  $x/D_h \approx 0.5$  is clearly downstream of the predicted wavemaker location. This explains why the frequency of the PVC type I mode is only weakly affected by combustion. This claim is further supported by considering the flame shown in Fig. 6.4b. Here, due to a slightly higher equivalence ratio, the flame is able to stabilize upstream of the area jump. As a consequence, the oscillation of the PVC is strongly attenuated.



(a) Comparison of the frequencies extracted from the POD coefficients to the frequency of the global mode predicted by the LSA.



(b) Wavemaker location predicted by the LSA

Figure 6.3: Results of the local linear stability analysis. Grey shaded points are based on the experimental data and red hollow points are based on the LES data. Error bars for the PVC type II represent multiple peaks encountered in the spectra

### 6.2.3 Summary

The stability analysis of the isothermal flow fields without or with less than 10% of axial injection rate successfully predicts the excitation of the PVC type I. The local stability analysis yields a large domain of absolute instability with the maximum growth rate close to the combustor inlet. The applied frequency selection criterion yields an excellent agreement of the predicted to the measured frequencies. The predicted wavemaker location is very close to the combustor inlet. This explains why the frequency of the PVC type I is not affected by combustion, as the flame root is located downstream of the wavemaker.

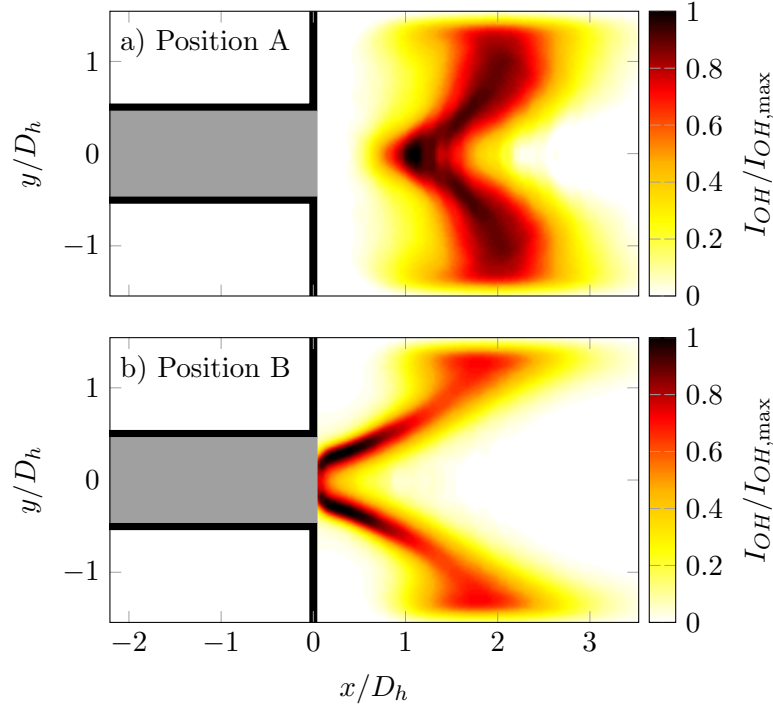


Figure 6.4: Abel-deconvoluted OH\*-chemiluminescence intensity for two different flame positions. Flame position A is the standard flame type without axial injection. Flame position B occurs for a higher equivalence ratio ( $\phi > 0.8$  compared to  $\phi > 0.7$ ) and is prone to flame flashback into the mixing tube. The flame foot is assumed to be located inside the mixing tube, where no measurements were possible. Inlet swirl number is  $S_{\text{prim}} = 0.9$ .

At high rates of axial injection, the stability analyses successfully predict the suppression of the strong and fast PVC type I and the excitation of the slow and weak PVC type II. In the local stability properties, this is manifested by negative absolute growth rates near the area jump. However, an unstable region with positive absolute growth rates remains further downstream. The frequency selection criterion locates the wavemaker of the global mode inside this domain and yields a global frequency and growth rate that are much lower compared to the PVC type I. The shift of the frequency and the streamwise wavemaker location are consistent to the experimentally obtained results.

### 6.3 Analysis of the Effect of Combustion and Different Flame Shapes on the PVC

In Chapter 4 different flame shapes were classified and described. It was found that the flame shape and the corresponding flow fields featured different types of the PVC or it was completely suppressed. This section is fundamentally different from the preceding section in

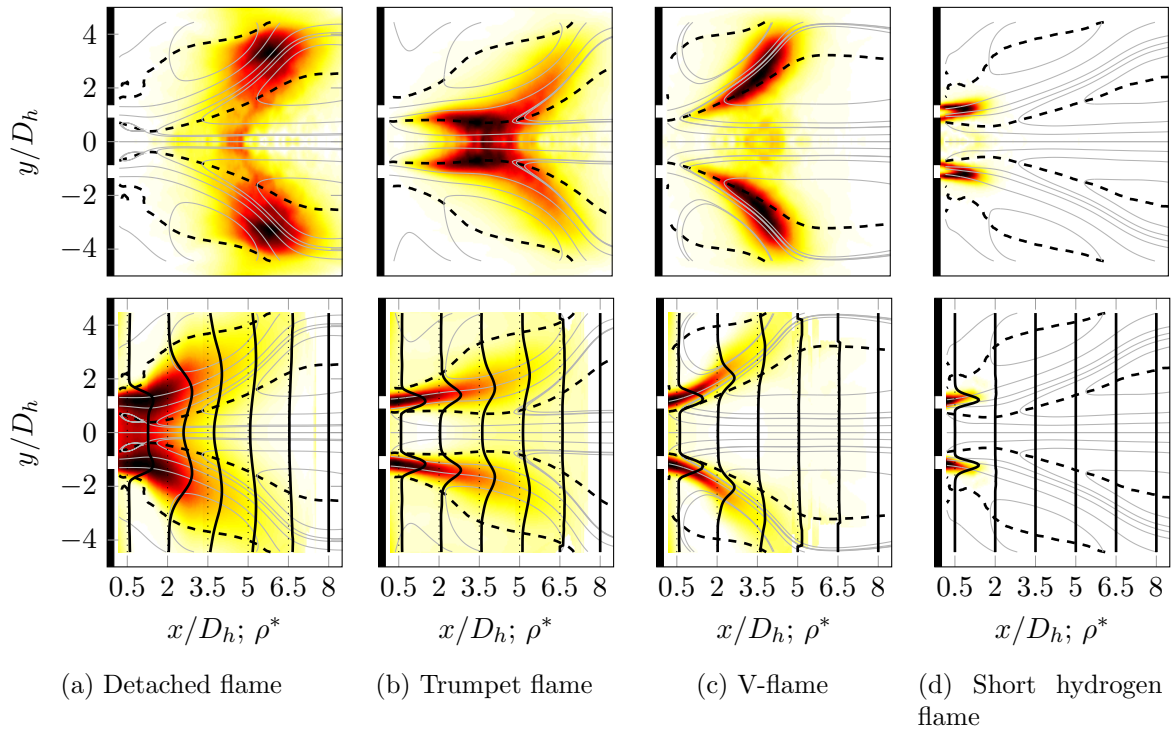


Figure 6.5: Abel-deconvoluted  $\text{OH}^*$ -chemiluminescence intensity (top row) and normalized density distributions (bottom row) of the analyzed flame shapes. Streamlines of the time-averaged flow are superimposed. Dashed lines indicate zero axial velocity. For the color scale, the reader is referred to Fig. 4.4.

a sense that the flow field is not modified on purpose but is the result of the chemical reaction depending on the operating conditions.

For convenience reasons, the investigated flow fields and flame shapes, which were presented in detail in Chapter 4, are repeated in Fig. 6.5. The very different flame shapes lead to very different flow field and, very importantly, also to different density distributions.

In the following, first the local linear stability characteristics of the different flow fields are presented and the role of the density stratification is pointed out. Subsequently, the global stability of the flow fields is deduced from the local characteristics. The analysis provides insight into the regions, where the frequency of the global mode is defined, the wavemaker region, and why a PVC, which was present under isothermal conditions, can be modified or suppressed at reacting conditions. Finally, for selected cases, the global stability deduced from the local stability analysis is compared to results of a Bi-global analysis, where no parallelity assumption had to be made.

### 6.3.1 Local Stability Properties

In the local linear stability concept, the axial evolution of the absolute growth rate  $\omega_{0,i}$  and absolute frequency  $\omega_{0,r}$  are calculated by slicing the flow field into radial profiles and carrying

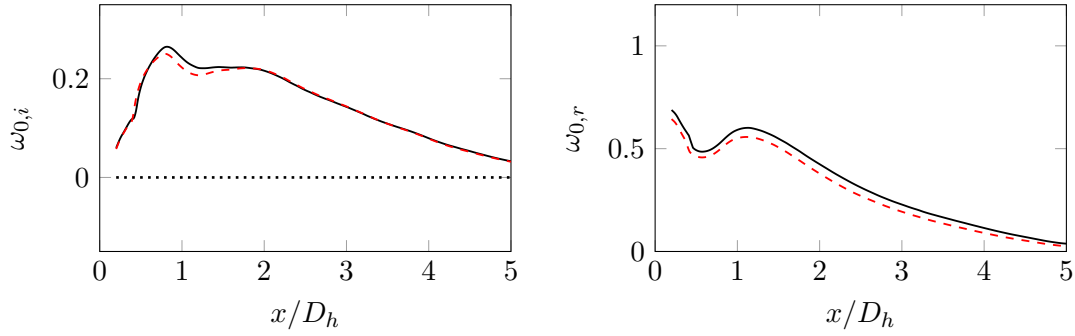


Figure 6.6: Axial distribution of local absolute growth rate ( $\omega_{0,i}$ ) and frequency ( $\omega_{0,r}$ ) for the detached flame. The black line is the stratified analysis and the red dashed line is the analysis of a virtual isothermal flow neglecting the density stratification.

out the analysis separately on each profile. The results of such local stability analyses of the different flame shapes are depicted in Fig. 6.6 to 6.9. To highlight the effect of the density stratification, two analyses were carried out for each case. One incorporates the effect of density stratification and one neglects the density stratification. This analysis of a virtual isothermal flow allows for the analytic isolation of the effect of density on the stability of the flow. Due to the coupling of the flame to the flow field, this is not possible in the experiments.

The analysis of the detached flame (Fig. 6.6) shows increasingly positive absolute growth rates  $\omega_{0,i}$  with increasing axial distance until a maximum growth rate is reached at  $x/D_h = 0.9$ . Further downstream the growth rates slowly decay but remain positive until the downstream end of the analyzed domain. The absolute frequency  $\omega_{0,r}$  initially decreases but subsequently increases and shows a maximum at  $x/D_h = 1.2$ . Interestingly, the effect of the density stratification is very low. This is well in line with the fact that the PVC of the detached flame shows a similar spatial shape and oscillates at the same frequency compared to the isothermal case. The density distribution of the detached flame shows very low gradients along the inner shear layers and significant gradients along the outer shear layers. Thus, it may be concluded that density gradients from the jet to the inner recirculation zone are of major importance, whereas density gradients from the jet to the outer recirculation zone are less crucial.

The analysis of the attached V-flame, see Fig. 6.7, shows considerably lower growth rates compared to the detached flame. The flow remains absolutely stable up to axial location of  $x/D_h = 1$  and the maximum growth rate, which is more than two times lower compared to the detached flame, is reached at  $x/D_h = 2.5$ . Furthermore, the effect of the density stratification is visible up to  $x/D_h = 3.5$ . At this axial location the density gradients along the inner shear layer are becoming less steep and lose their impact on the stability characteristics. The local absolute frequency quickly decreases with the downstream distance.

The case of the trumpet flame (Fig. 6.8), shows similar levels of the absolute growth rates compared to the detached flame and, consequently, much higher growth rates than the V-flame. Similarly to the V-flame, the effect of density is restricted to the zone of steep density

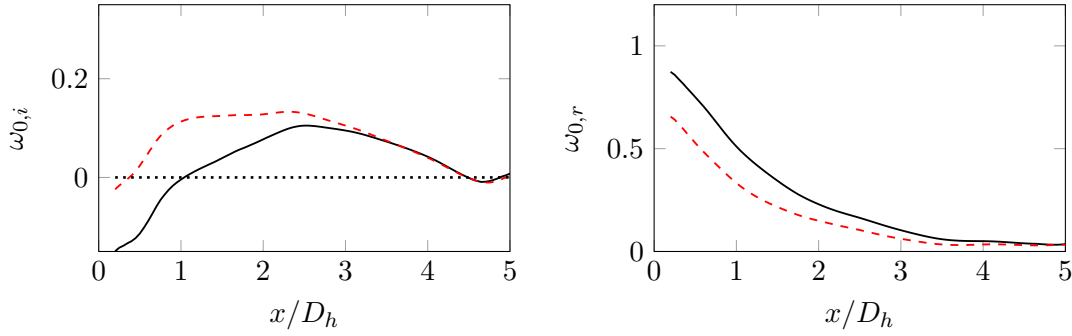


Figure 6.7: Axial distribution of local absolute growth rate ( $\omega_{0,i}$ ) and frequency ( $\omega_{0,r}$ ) for the V-flame. The black line is the stratified analysis and the red dashed line is the analysis of a virtual isothermal flow neglecting the density stratification.

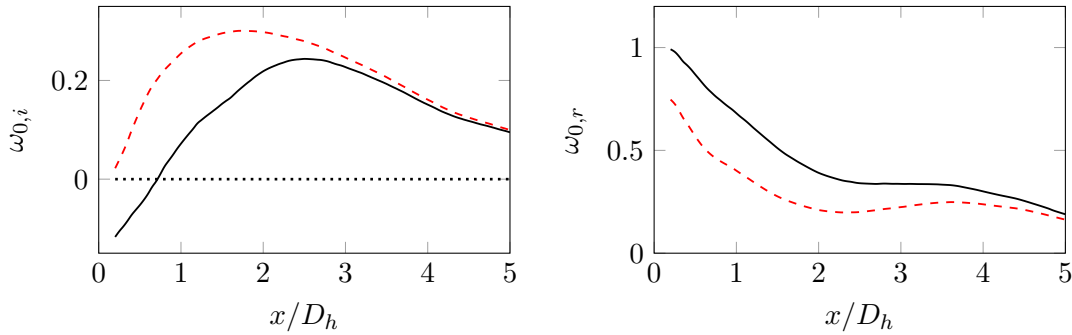


Figure 6.8: Axial distribution of local absolute growth rate ( $\omega_{0,i}$ ) and frequency ( $\omega_{0,r}$ ) for the trumpet flame. The black line is the stratified analysis and the red dashed line is the analysis of a virtual isothermal flow neglecting the density stratification.

gradients along the inner shear layer ( $x/D_h < 3.5$ ). As a result, the axial location of maximum absolute growth rate is shifted downstream from  $x/D_h = 1.8$  for the virtual isothermal analysis to  $x/D_h = 2.5$  for the stratified analysis. Compared to the V-flame, the axial decay of the absolute frequency is considerably lower.

The analysis of the flow field of the short hydrogen flame, as depicted in Fig. 6.9, yields a strong influence of the steep density gradient near the combustor inlet. Further downstream, due to the very short flame, almost no radial density gradients are present and the stratified and the isothermal analysis yield the same results. The local absolute growth rate of the stratified analysis show a peak around  $x/D_h = 1.4$ , which would be located slightly more upstream ( $x/D_h = 1$ ), without density stratification.

### 6.3.2 Global Stability Properties

A region of positive absolute growth rates ( $\omega_{0,i}$ ) is a necessary, but not a sufficient condition for a globally unstable flow. The prediction of the linear global stability of a flow field requires the application of a frequency selection criterion to the results of the local stability analysis.

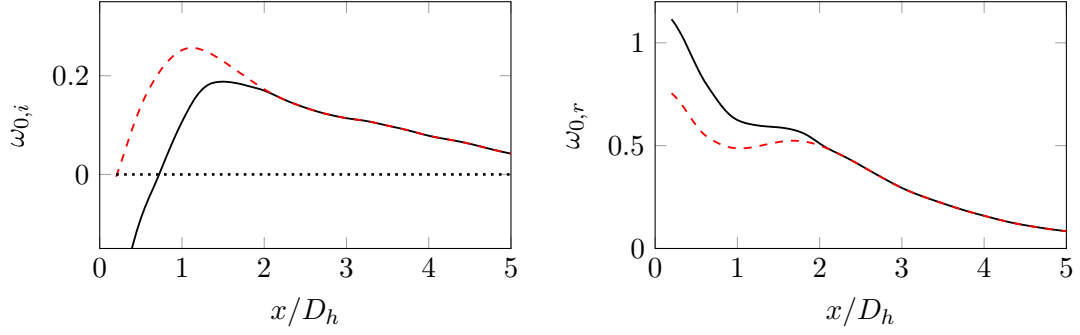


Figure 6.9: Axial distribution of local absolute growth rate ( $\omega_{0,i}$ ) and frequency ( $\omega_{0,r}$ ) for the short hydrogen flame. The black line is the stratified analysis and the red dashed line is the analysis of a virtual isothermal flow neglecting the density stratification.

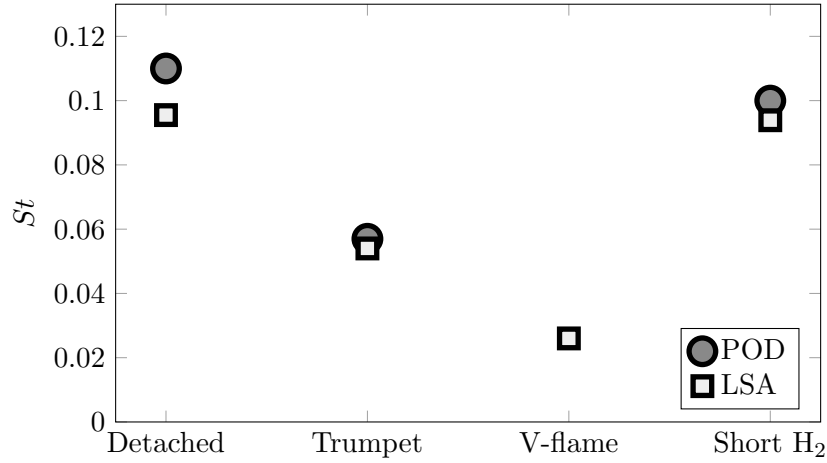


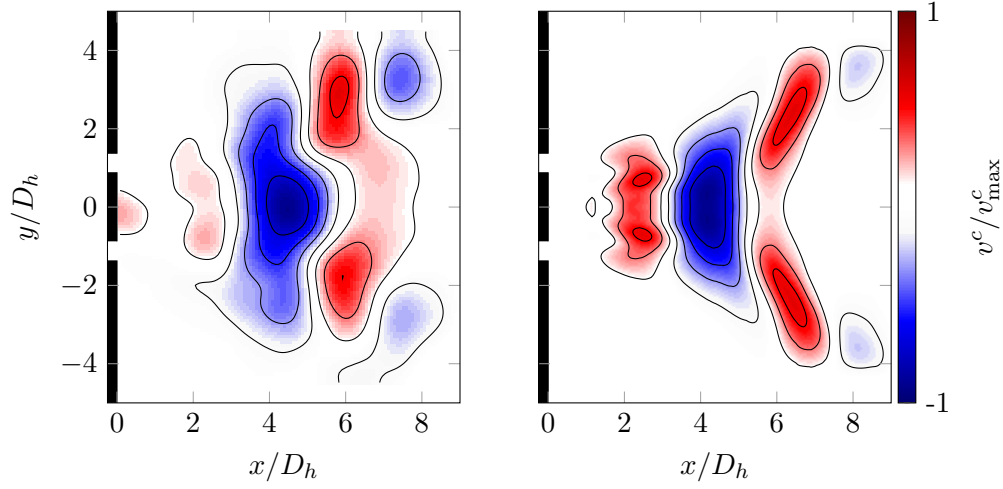
Figure 6.10: Comparison of the frequencies predicted by the stability analysis to measured frequencies. For the V-flame no PVC frequency was observed in the experiments.

Such a criterion, which was very successfully applied to wake-like flows (Pier, 2002), as in the present study, is provided in Eqn. 2.32. This frequency selection criterion yields the global frequency ( $\omega_{g,r}$ ), the global growth rate ( $\omega_{g,i}$ ), and the wavemaker location ( $x_s$ ).

The results of the frequency selection criterion for the four investigated flow fields, corresponding to the four flame shapes, are depicted in Fig. 6.10 and compared, in terms of Strouhal number, to the PVC frequencies obtained from the POD analysis. Overall, a very good agreement is evident. The frequency match for the slow oscillation of the PVC in the case of the trumpet flame is almost perfect, and the increase in the frequency for the detached flame and the short hydrogen flame is predicted correctly. However, the frequency for the detached flame is slightly underestimated.

The local analysis predicts a marginally unstable (the global growth rate is more than two times lower compared to the other cases) slow oscillation for the V-flame, while in the experiments no clear trace of a PVC was found. It cannot be eliminated that this overestimation





(a) Empirical mode reconstruction from the POD.

(b) Physical mode construction from the local stability analysis.

Figure 6.11: Empirical and physical construction of the coherent radial velocity component of the global mode of the trumpet flame at an arbitrary phase angle.

stems from uncertainties in the density estimation and in the incorporation of the damping effect of the small-scale turbulence. However, as it will be shown in the remainder of this section, when the local analysis is compared to a Bi-global stability analysis, it seems very likely that this overestimation of the growth rates stems from the negligence of non-parallelity effects in the local stability concept.

Once the frequency of the global mode is calculated, its spatial shape can be constructed from the eigenfunctions and eigenvalues of the local analysis using Eqn. 2.33, as described in Section 2.4. The results are provided exemplarily for the case of the trumpet flame in Fig. 6.11. For the purpose of comparison, the empirical reconstruction from a POD (Eqn. 2.14) is plotted next to the analytic mode construction. It can be seen that the reconstruction from the analysis and the reconstruction from the POD show a very similar wave pattern of the same axial wavelength. The axial and radial extents of the oscillation agree very well. Minor differences in the appearance of the global mode are assumed to stem from the non-parallelity of the flow, from uncertainties in the density estimation, and from the simplifications made during incorporation of the damping effect of the small-scale turbulence. Nevertheless, the good agreement between the empirically and physically constructed global mode shapes provides further credibility to the results of the local linear stability analysis.

Besides the prediction of the frequency of the global mode  $\omega_{g,r}$ , the frequency selection criterion also provides the axial location  $x_s$  of the so-called wavemaker, as shown in Fig. 6.12. In order to correlate the predicted locations with experimental data, the local phase distribution of the coherent through-plane vorticity is calculated from the two POD modes describing the PVC. This is exemplary shown in Fig. 6.13 for the trumpet flame. A local maximum at the centerline is evident at  $x/D_h = 2.56$ . From this point, the phase decreases in the upstream

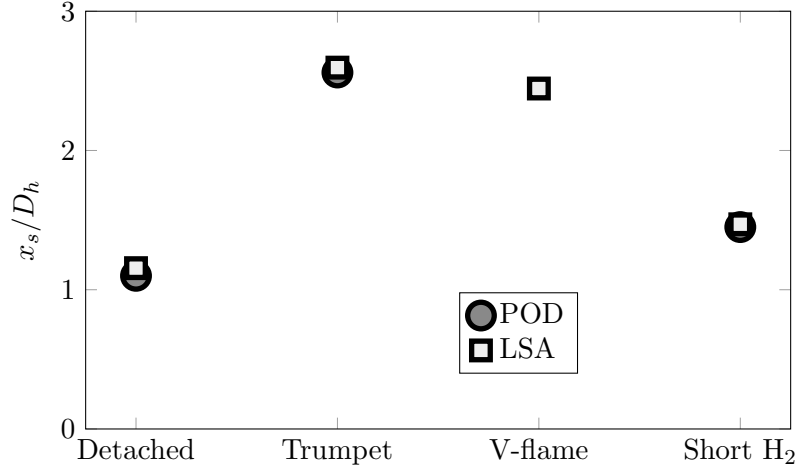


Figure 6.12: Comparison of the predicted wavemaker location to the location of maximum phase of the through-plane vorticity on the centerline. For the V-flame no PVC was observed in the experiments.

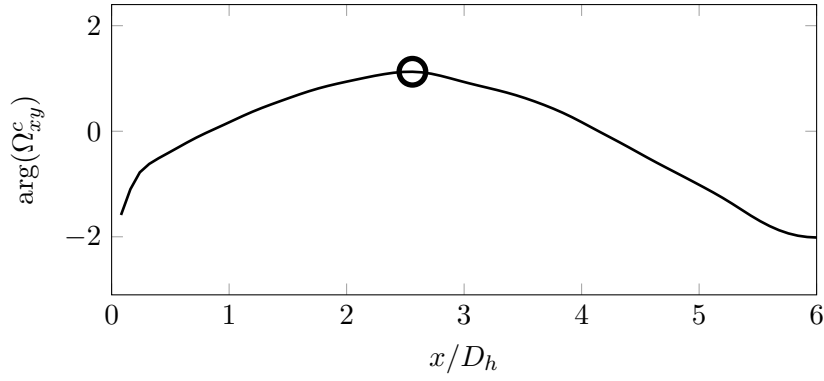


Figure 6.13: Phase of the through-plane vorticity ( $\arg(\Omega_{xy}^c)$ ) along the centerline obtained from the POD of the experimental data of the trumpet flame. At the maximum (indicated by the black circle), the phase velocity changes its sign, indicating that the perturbations propagate away from the wavemaker in upstream and downstream direction.

and downstream direction, indicating that the oscillation is emanating from this region. As it can be observed in Fig. 6.12, the wavemaker location predicted by the stability analysis agrees strikingly well with this point of maximum vorticity phase. This is remarkable since the wavemaker, as obtained through Eqn. 2.32, has no strict physical meaning. However, its location is often close to the intersection of the so-called  $k^+$  and  $k^-$  branches, whose location in contrast to the wavemaker location, is of a strict physical meaning (Juniper and Pier, 2014). Thus, the wavemaker region can often be qualitatively interpreted as the pacemaker for the global oscillation.

Compared to the trumpet flame, the wavemaker is shifted considerably upstream for the short hydrogen flame and is even further shifted upstream for the detached flame. Again, the

predicted wavemaker locations agree extremely well with the locations of maximum vorticity phase, as obtained from the POD analysis. In the case of the V-flame, no PVC was found in the experiments. Hence, no axial location of maximum phase of the through-plane vorticity is obtained from the POD analysis, whereas the analysis predicts a similar wavemaker location for the V-flame as for the trumpet flame.

### 6.3.3 Comparison to Bi-Global Linear Stability Analysis

In the local stability concept, the assumption of a parallel flow was made. However, if one takes a closer look at the measured flow fields (Fig. 6.5), it is evident that, depending on the flame shape, the flow fields feature a significant amount of non-parallelity. In order to assess the effect of the non-parallelity, in the following the results of the local analysis are compared to the results of a Bi-global analysis, where the analysis is carried out on the complete flow field in one step (assuming axisymmetry).

#### Theoretical Method

In the Bi-global analysis, a perturbation of the form

$$\mathbf{v}^c(\mathbf{x}, t) = \Re \left[ \hat{\mathbf{v}}(x, r) e^{i(m\theta - \omega_g t)} \right] \quad (6.2)$$

is used, where  $\hat{\mathbf{v}}(x, r)$  is the vector of the two-dimensional amplitude functions. In the present temporal framework, the complex eigenvalue  $\omega_g$ , and the associated eigenvectors  $\hat{\mathbf{v}}$  are sought. The resulting three-dimensional partial derivative global eigenvalue problem is linear on the eigenvalue  $\omega_g$  and can be written as follows:

$$\mathbf{A}\hat{\mathbf{q}} = \omega_g \mathbf{B}\hat{\mathbf{q}}. \quad (6.3)$$

The elliptic eigenvalue problem (Eqn. 6.3) must be complemented with adequate boundary conditions for the disturbance variables. In streamwise direction, homogeneous Neumann conditions are imposed at the inlet and homogeneous Dirichlet conditions at the walls. The decay of perturbations is imposed through a sponge region at the outlet to avoid spurious reflections. These sponge regions consist of very low local Reynolds numbers, being 80 to 90% lower than the surrounding Reynolds numbers. The same technique has been successfully used by Meliga et al. (2012) for recovering the global modes of swirling jets. At the radial axis  $r = 0$ , the same boundary conditions (Khorrami et al., 1989) are applied, as for the local analysis (see Eqn. 2.28).

Subsequently, the elliptic global problem (Eqn. 6.3) is solved using an Arnoldi algorithm. Details about the employed numerical methods and the discretization scheme can be found in the work of Paredes et al. (2013) and in the literature (e.g., Theofilis, 2003).

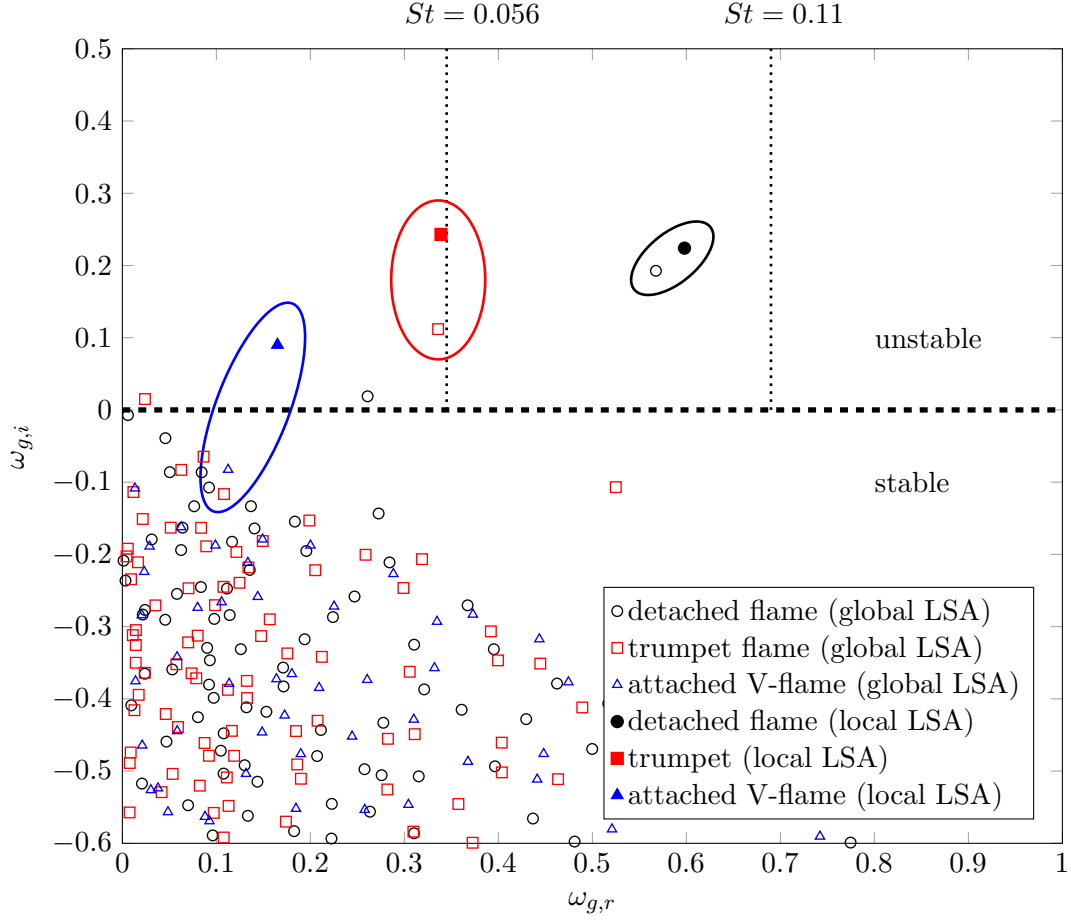


Figure 6.14: Eigenvalue spectrum (global frequency  $\omega_{g,r}$  and global growth rate  $\omega_{g,i}$ ) of the Bi-global stability analysis (hollow symbols) and comparison to the results of the local analysis (filled symbols). Dotted lines indicate the measured frequencies as extracted from the POD analysis.

## Results

The Bi-global analysis was carried out on the measured mean flow field of the detached flame, the trumpet flame, and the attached V-flame. The damping effect of the small-scale turbulence was implemented using the same eddy viscosity approach as for the local analysis (Eqn. 2.22). The resulting eigenvalue spectra of the global analysis are provided in Fig. 6.14 and compared to the global growth rates and global frequencies based on the local analysis (compare Figs. 6.10 and 6.12).

The filled markers correspond to the local analysis, where the global frequency is obtained from the local absolute frequencies by the application of Eqn. 2.32. The vertical dashed lines denote the measured frequencies for the detached flame and the trumpet flame. As already observed in Fig. 6.10, the local analysis reasonably well predicts the frequency of the detached flame and yield an almost perfect frequency match with the measured frequency of

the trumpet flame. In the case of the attached V-flame, the local analysis predicts a positive global growth rate, whereas the experiments suggest that the flow is stable.

The hollow markers represent the eigenvalues of the global analysis (Eqn.6.3). For the attached V-flame, it can be observed that all eigenvalues are stable. Thus, in contrast to the local analysis, the suppression of the PVC in the V-flame case is correctly predicted by the global analysis. For the detached flame, the global analysis predicts the most unstable mode at a very similar growth rate and frequency as the local analysis. Similar to the local analysis, the frequency of the instability is underpredicted. The global analysis of the trumpet flame yields an excellent agreement in terms of the global frequency.

The comparison of the global growth rates and frequencies shows major differences between the results of the local and global analysis of the attached V-flame. These are very likely caused by the very strong non-parallelity of the flow field of the attached V-flame. The local analysis, which assumes a quasi-parallel flow, gets increasingly inaccurate and overpredicts the growth rate, when the flow is strongly non-parallel.

In the case of the detached flame, a reasonable agreement of the local and global analysis to the experimental results is achieved. However, for the global analysis, the results are very sensitive to the selection of the inlet boundary conditions. This is caused by the proximity of the global flow oscillation to the inlet (see Fig. 4.10) and indicates that for a better match of the frequencies, the flow field upstream of the combustor inlet has to be considered. This could not be done in the present work and has to be postponed to future works.

The analysis of the trumpet flame yields excellent results for both the local analysis and the global analysis. The good prediction of the local analysis is presumably related to the very weak non-parallelity of the flow in the region, where the wavemaker is predicted by the local analysis. Furthermore, the structure is sufficiently far away from the inlet, so that the real inlet boundary conditions are approximated sufficiently by the boundary conditions imposed for the global analysis.

In summary, the local analysis works best if, as expected, the flow is only weakly non-parallel. The global analysis implements the effect of the non-parallelity but creates additional challenges regarding appropriate boundary conditions in the flow direction, which are not necessary for the local analysis.

#### 6.3.4 Summary

The stability calculation based on the measured flow fields and estimated density distributions show a strong variation of the local and global stability characteristics for the different flame shapes. The main findings of the local and the Bi-global stability analyses are:

- The occurrence of the PVC in reacting swirl-stabilized combustor flows can be excellently modelled employing local and Bi-global linear stability theory. This shows unambiguously, that the PVC (and the synchronized Kelvin-Helmholtz instabilities) are the cause of a globally unstable flow field.

- Local linear stability theory has advantages over the Bi-global approach when the instability is located close to the boundary conditions, which often cannot be properly modeled.
- Local linear stability theory overpredicts the global growth rate, when the flow is strongly nonparallel.
- Density gradients, as they are typically present in attached swirl-stabilized combustors, stabilize the flow field.
- Only density gradients along the inner shear layer between the jet and the inner recirculation zone are of importance. Density gradients along the outer shear layer have very little influence on the absolute growth rate of the instability.

While density stratification has a significant impact on the global stability of the reacting flow fields, the flame shape not only changes the density distribution but also the complete flow field. Thus, it would be an oversimplification to solely attribute the changes of the stability to the density stratification. As an example, the virtual isothermal analysis of the V-flame features considerably higher growth rates than the stratified analysis but still remains less unstable than the detached flame. Thus, it can be concluded that the combination of different flow field and density field parameters determine the excitation of the PVC. To provide further insight into these parameters, a detailed study is required and will be presented in the following section.

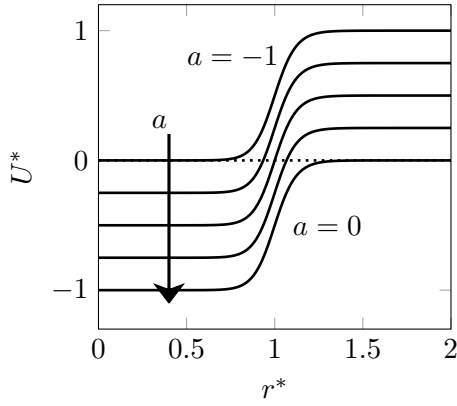
## 6.4 Identification of the Key Parameters Governing the Excitation and Suppression of the PVC

The identification of the most important parameters for the excitation of the PVC based on experimental (or numerical) data is an extremely challenging task. The reason is that it is nearly impossible to change one parameter, while keeping the other parameters constant. For instance, if one aims at investigating the effect of a higher azimuthal velocity, the swirl number has to be increased. However, this leads to a change in the pressure field and usually higher backflow velocities. It is therefore impossible to differentiate between the effect of the increased azimuthal velocity or the higher backflow intensity.

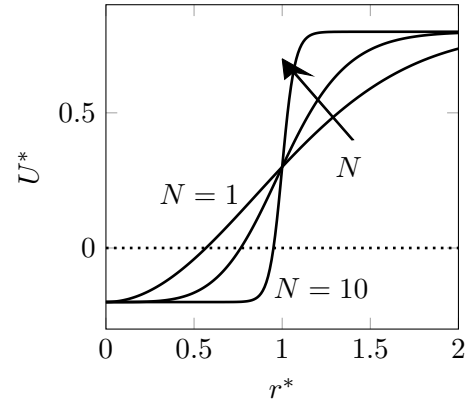
A possible solution for this problem is the use of a reduced model, where the desired isolated variations of single parameters are possible. In the two preceding sections, it was shown that the local linear stability theory is able to accurately predict the occurrence of the PVC, when the analysis is carried out on measured mean flow profiles and mean density profiles. Thus, the local linear stability theory can be excellently employed as the required model to identify the key parameters for the excitation of the PVC.

### 6.4.1 Parametric Model Profiles

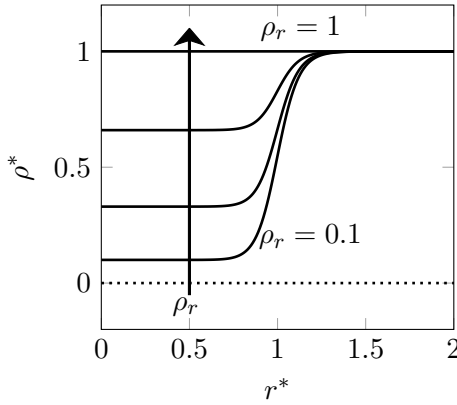
Since global stability is a consequence of the local absolute stability, the approach of the present assessment is to study the stability of a single model velocity and density profile. The



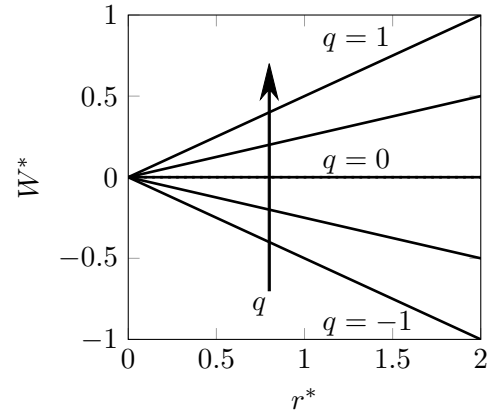
(a) Variation of the axial velocity deficit.



(b) Variation of the shear layer thickness.



(c) Variation of the density deficit in the wake.



(d) Variation of the solid body rotational speed.

Figure 6.15: Model profiles for the axial velocity (a,b), density (c), and tangential velocity (d).

stability analysis is carried out for simple model profiles, given as:

$$U^* = -a - \left[ 1 + \left( e^{r^{*2} \log(2)} - 1 \right)^N \right]^{-1} \quad (6.4)$$

$$\rho^* = 1 - (1 - \rho_r) \left[ 1 + \left( e^{r^{*2} \log(2)} - 1 \right)^N \right]^{-1} \quad (6.5)$$

$$W^* = q \cdot r^*. \quad (6.6)$$

This simplified model, where the axial velocity is modeled with a single shear layer profile, as proposed by Monkewitz and Sohn (1988), includes the basic flow features of a swirling flow. The parameter  $a$  defines the backflow intensity and the type of the profile (see Fig. 6.15a). Values of  $-1 < a < -0.5$  correspond to wake profiles in the positive  $x$  direction, whereas values of  $-0.5 < a < 0$  correspond to jet profiles with counterflow in negative  $x$  direction. The profiles are normalized with the velocity difference between the centerline and the free-

stream velocity and the radius, where the average of both velocities is present. The parameter  $N$  determines the maximum shear layer gradient and correlates with the inverse shear layer thickness, as depicted in Fig. 6.15b.

The density profile (Fig. 6.15c) is modeled similarly to the axial velocity profile with the same parameter  $N$  as the axial velocity profile. Its axial deficit is determined by the density ratio  $\rho_r$  and it is normalized with the free-stream density. The tangential velocities (Fig. 6.15d) are modeled as a simple solid body rotation, where  $q$  determines the rotational speed. All profiles lack the outer shear layer, as it is assumed that the most important mechanisms for the stability are determined by the inner shear layer and the backflow. This is confirmed by the fact that in the case of the detached flame, the analysis of the stratified flow and the analysis of the virtual isothermal flow yield almost the same results, even though a strong density gradient in the outer shear layer is present. Note that no variation of the shear layer thickness is considered, even though it obviously has an important effect on the growth of instabilities. However, the effect of the shear layer thickness can be obtained from dimensional considerations and is, therefore, not included in the model.

#### 6.4.2 Results of the Parametric Study

The results of the model study are presented in Fig. 6.16. The parameters that are not varied remain at the arbitrarily chosen base state of  $(a, N, \rho_r, q) = (-0.8, 6, 0.5, 0.3)$ . Figure 6.16a shows that for wake profiles ( $-1 < a < -0.5$ ) stronger backflow destabilizes the profiles, while density stratification stabilizes the profiles. Hence, in order for the flow to become absolutely unstable, higher backflow intensities are required in the presence of a density deficit. For jet profiles ( $-0.5 < a < 0$ ), the effect is inversed and density stratification destabilizes the profiles. This is expected since a lower fluid density in a jet is known to destabilize the flow (Monkewitz and Sohn, 1988). The effect of the baroclinic torque (see Eqn. 6.1) is to bias the convection speed of an instability towards the velocity of the high-density stream (Soteriou and Ghoniem, 1995). Thus, in the case of a hot jet and a cold wake, the convection speed is decreased, making the flow more prone to an absolute instability. In contrast to that, in the case of a cold jet and a hot wake, the convection speed is increased, making the flow less prone to an absolute instability. Consequently, with density gradients of the cold jet-hot wake type, higher backflow velocities are required for a flow slice to be absolutely unstable.

The frequency of the absolute instability (Fig. 6.16a, lower plot) decreases for higher backflow intensities and changes its sign from co-rotating to counter-rotating when the wake profile change to a jet profile. A density deficit leads to an increase of the absolute frequency for wake profiles and a decrease of the (negative) frequency magnitude for jet profiles.

The highest growth rates are calculated for small positive rotational speeds ( $q \approx 0.3$ ), as depicted in Fig. 6.16b. Furthermore, it is evident that a decay of the tangential velocities from  $q = 0.3$  to 0 has a considerably smaller influence on the growth rate than a variation of the backflow intensity. This shows that no high tangential velocities are required for an absolutely unstable flow. The experimentally and numerically observed influence of the swirl number on the excitation of the PVC (e.g., Oberleithner et al., 2012a) seems to be dominated by the



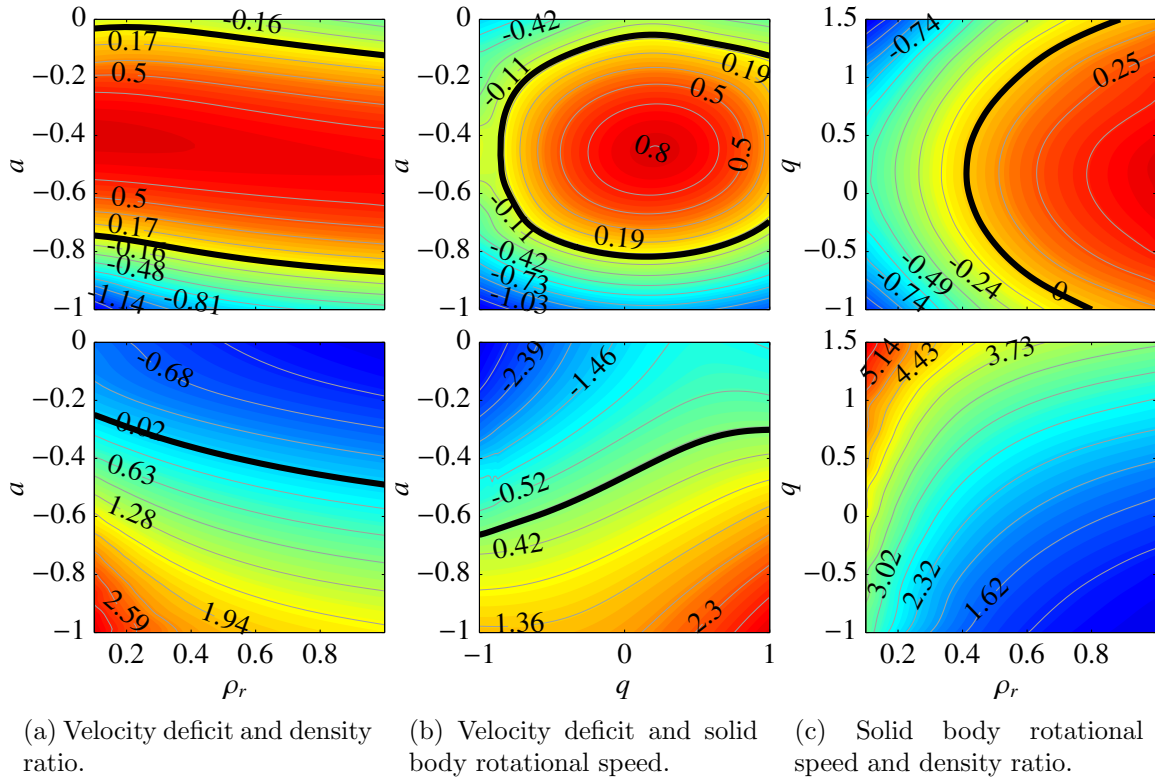


Figure 6.16: Influence of the model parameters on the absolute growth rate ( $\omega_{0,i}$ , top row) and absolute frequency ( $\omega_{0,r}$ , bottom row) of the model profiles. Thick black line separates absolute instability from convective instability (top row) and negative from positive frequencies (bottom row).

coupling of the swirl intensity to the backflow intensity. From Fig. 6.16c, it is evident that the damping effect of the density stratification is almost independent of the swirl intensity. While the absolute growth rate is dominated by the backflow intensity and the density deficit, the influence of the base flow rotation on the absolute frequency, which essentially determines the frequency of the global mode, is very strong (Fig. 6.16b,c).

The results of the model study clearly identify the role of the different flow field and density parameters on the excitation of the PVC. In the following, these correlations will be used to qualitatively explain the different occurrences of the PVC, which were observed in the scope of this thesis. To this end, the model profiles (Eqns. 6.4-6.6) are fitted onto the measured velocity and density fields for the different flame shapes. The fitted backflow parameter  $a$  and the density ratio  $\rho_r$  for the four flame shapes (detached flame, trumpet flame, attached V-flame, and short hydrogen flame) are presented in Fig. 6.17. It is evident that almost no density deficit is present for the detached flame and that the density deficit disappears very fast in the case of the short hydrogen flame. As sufficient backflow is present in both cases, the instabilities arise near the combustor inlet. For the attached V-flame, the density deficit decays considerably slower and the backflow is weaker. This leads to the suppression of the

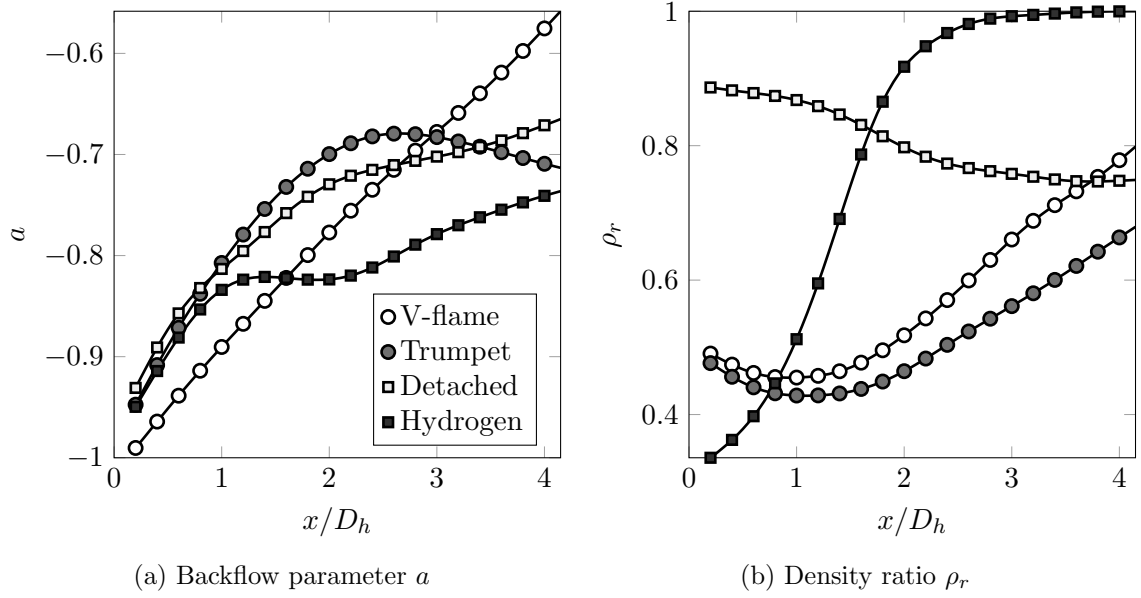


Figure 6.17: Fit of the model parameters to the measured profiles for the different flame shapes.

helical instability in the case of the V-flame. For the trumpet flame, the density difference is similar to the V-flame. However, the backflow is considerably stronger. As a result, the instability is shifted downstream, where the swirl has already significantly decayed, explaining the lower frequency of the PVC. The results of the model study are fully in line with the experimentally observed flow field dynamics.

### 6.4.3 Summary

A model study was carried out to assess the governing parameters for the instability. It was shown that the most important parameters are the backflow intensity and the density stratification. The lower the ratio of the density in the wake, compared to the density in the jet, the more backflow is required for the flow to become absolutely unstable. The reduction of swirl due to dilatation, in contrast to what has been suggested in previous studies, has only minor influence on the growth rate. However, a strong influence on the absolute frequency was observed.

The outcome of the model study explains the findings made for the four different flame shapes. If no density gradient is present at the inlet (detached flames) or if the density deficit decays very fast (very short flames), the instability develops near the combustor inlet. If the decay of the density deficit is slower, the instability depends on the evolution of the velocity deficit. It can either be shifted downstream or be suppressed. If the instability is shifted downstream, the decay of the tangential velocities leads to a lower frequency.

## 6.5 Conclusions

In this chapter local and global linear stability theory were used to understand the excitation and suppression of the PVC at isothermal and reacting conditions. In the first part, the controlled suppression of the PVC by changes to the isothermal mean flow field is assessed. In the second part, the effects of different flame shapes on the velocity field and the density field are assessed regarding the linear stability of the flow field. In these two parts the results of the analysis are compared to experimental results, thereby, validating the approach. In the last part of the present chapter, general relations between the most important flow and density parameters and the stability of a flow profile are derived in a model study.

When the results of the first part are interpreted with the knowledge gained from results of the model study, it is evident that the main effect of the application of the non-swirling central flow is an increase of the axial velocity on the centerline. Thereby, the velocity deficit is decreased. One result of the model study is that this velocity deficit is the most important driver for the PVC at isothermal conditions. Thus, if the non-swirling jet persists far enough downstream, the PVC is suppressed. Only further downstream, the velocity deficit gains enough strength and a PVC is excited. However, due to the decay of the tangential velocities, which strongly influence the PVC frequency, this PVC is very slow.

At non-isothermal conditions, the excitation mainly depends on the velocity deficit and the density gradients along the inner shear layer. When low or no density gradients are present at the inlet, the PVC can develop close to the inlet, provided enough backflow is present. If the flame is very short and the density gradients decay very fast, the PVC is only slightly shifted downstream. For longer flames, the PVC can be either suppressed or significantly shifted downstream, depending on the axial evolution of the backflow intensity. Since the frequency of the PVC significantly depends on the tangential velocity component and this component decays in axial directions, every downstream shift of the PVC is accompanied by a decrease of its frequency.

It is also worth recalling the results of Chapter 4 regarding the increased mixing between the jet and the inner recirculation zone caused by the PVC. This means that a PVC, once it is excited, tends to smooth out density gradients along the inner shear layer. Thus, it creates conditions that are more favorable for its own excitations. On the other hand, once the PVC is suppressed, the reduced mixing even further increases the density gradients, causing an even stronger damping of the PVC. This very interesting mechanism will be further explained and exploited in Chapter 7, where the role of the PVC for the transitions between the different flame shapes is investigated.

The understanding of the PVC phenomenon in reacting flows is significantly extended by the present work. A theoretical explanation of how the excitation, suppression, and shape of the PVC is dominated by the flame length and the backflow intensity is provided for the first time.



## Chapter 7

# The Role of the PVC for Flame Shape Transitions

*In the present chapter the role of the PVC for the transition between different flame shapes is investigated. Transient PIV measurements and  $\text{OH}^*$ -chemiluminescence images are analyzed. The fuel mass flow rate was varied periodically in order to provoke flame shape transitions. The transient measurements reveal that the transitions are not continuous but take place on a very short timescale. Based on the findings of the previous chapters, a new transition and hysteresis mechanism between detached and attached flames is proposed. The key parameter for the hysteresis is the excitation of a PVC and the associated axial-radial eddies. The PVC is excited when the flame is detached and is damped when the flame is attached. The axial-radial eddies, related to the PVC, significantly enhance mixing between the jet and the inner recirculation zone and cause a low temperature region close to the combustor inlet. This cold region hampers the ability of the flame root to sustain the high strain rates near the combustor inlet and impedes a reattachment unless the fuel-air mixture is very reactive. Once the flame root is able to attach, the density gradients along the shear layers damp the PVC and, consequently, the associated axial-radial eddies. As a result, the mixing is reduced, the temperature in the recirculation zone is increased, and the PVC is further damped. Due to the higher temperatures, the flame root is not quenched even if the reactivity of the fuel-air mixture is significantly below the required reactivity threshold for the attachment. Thus, a hysteresis in the flame shape transition is caused. The proposed mechanism is well in line with the presented experimental findings and other results reported in the literature.*

### 7.1 Introduction

In Chapter 4 different flame shapes in the same swirl-stabilized combustor were observed, which depended significantly on the operating conditions. Considering the increased require-

ment for fuel-flexible combustors, possible changes of the flame shape, due to changes of the operating conditions, can become of high relevance for the operation of gas turbine combustors. As motivated in Chapter 4, different flame shapes can have very varying flame responses to the system acoustics and, thus, are closely coupled to the occurrence of thermoacoustic instabilities (Durox et al., 2009; Thumuluru and Lieuwen, 2009). Furthermore, due to different flame locations and mixing lengths, changes in the flame stability and the pollutant emissions are very likely. Moreover, varying flame locations may require different cooling strategies. Therefore, in order to avoid undesired transitions of the flame shape, understanding of the stabilization and transition mechanisms is of utmost importance.

In the literature different flame shapes were observed in a number of studies (e.g., Vanoverberghe et al., 2003a,b; Tummers et al., 2009). Vanoverberghe et al. (2003a,b) experimentally investigated a partially premixed confined swirl-stabilized combustor, similar to the one used in the present study, and observed five different flame states. They continuously varied the swirl number and observed large regions of hysteresis in between the different flame shapes. At high swirl numbers, the flame attaches to the burner nozzle and remains attached even for a subsequent decrease of the swirl number to values 15% lower than that required for the attachment. Tummers et al. (2009) experimentally investigated the hysteresis between two different flame shapes in an unconfined non-premixed swirling flame. The authors reported on one flame shape that was attached to the burner nozzle and one detached flame. The control parameters for the transitions were the amount of swirl and the mass flow rate. They reported on a large hysteresis region and pointed out the importance of large-scale vortical structures for the hysteresis. It is argued that an increase of the mass flow increases the strength of the shear between the jet and the ambient air. Once the vortices have grown to a sufficient size, they are able to penetrate into the inner recirculation zone, where they cause the premixing of air and fuel, leading to the transition to the detached blue flame. After a successful transition, the mass flow can be reduced and the flame remains in its detached state. However, they state that their measurements do not allow for an accurate physical explanation of the observed hysteresis. Even though Tummers et al. (2009) did not provide evidence of a single-tone global mode, it seems very likely that the vortices they observed are indeed traces of the PVC. Similar as in the present thesis (see Chapter 4), the PVC is suppressed when the flame is attached and is excited when the flame is detached.

In this chapter the results of transient measurements varying the fuel mass flow rate are presented to investigate the transition process between three flame shapes. Time series of the detachment, attachment, and the transition from the trumpet flame to the V flame are presented. The discussion of the results indicates an important role of the PVC for the transitions and the encountered hysteresis.

## 7.2 Experimental Procedure

The results presented in this chapter are based on transient measurements, where the equivalence ratio of the natural gas fuel was varied continuously between  $\phi \approx 0.5$  and  $\phi \approx 0.7$  in

periods of 5 s length to provoke flame shape transitions. All other operating conditions were kept constant at an inlet temperature of  $T_{\text{in}} = 600$  K, a steam dilution rate of  $\Omega = 0.1$ , a total mass flow rate of 180 kg/h, and a swirl number of  $S = 0.7$ . During the transient measurement, 27 000 simultaneously recorded samples of the flow field and the spatial distribution of the OH\*-chemiluminescence intensity were taken at a sampling frequency of 1500 Hz. Hence, one measurement included almost four periods of the equivalence ratio variation.

For the presentation of the instantaneous flow fields shown in this chapter, the data was filtered employing the POD filtering approach as introduced in Section 2.5.4. The instantaneous flow fields are reconstructed using the first 150 POD modes. Thereby, the small scale fluctuations are filtered out of the data and the perceptibility of the large-scale flow field structures that dominate the vortex-flame interactions (Stöhr et al., 2012) is enhanced. The number of 150 modes has no physical meaning and was chosen to agree with the filtering approach used by Boxx et al. (2010b).

### 7.3 Extraction of the Instantaneous Flame Shape and the Coherent Structures

During the transient measurements three different flame shapes - the same that are presented in detail in Chapter 4 - occurred in the combustor. In the following, a set of parameters will be introduced that are used to extract the instantaneous flow field shape, the occurrence and type of the PVC, the flame shape, and the characteristics of the density field. To characterize the flame shape in terms of being attached or detached, the mean OH\*-chemiluminescence intensity in the vicinity of the centerbody ( $0 < x/D_h < 2$  and  $-0.8 < y/D_h < 0.8$ ) is calculated as:

$$R_{OH}(\mathbf{x}, t) = \frac{\iint_A I_{OH}(\mathbf{x}, t) dA}{\iint_A \bar{I}_{OH}(\mathbf{x}) dA}. \quad (7.1)$$

This parameter indicates if the flame is detached or attached (either as a V-flame or as a trumpet flame). The second parameter describes the estimated density in the upstream part of the IRZ. Its definition is analog to  $R_{OH}$ :

$$R_\rho(\mathbf{x}, t) = \frac{\iint_A \rho^*(\mathbf{x}, t) dA}{\iint_A \bar{\rho}^*(\mathbf{x}) dA}. \quad (7.2)$$

The third measure is the instantaneous opening angle  $\alpha$  of the jet as defined in Eqn. 4.2. It shows very low values for the narrow trumpet flame, high values for the strongly divergent V-flame, and intermediate values for the detached flame.

In Chapter 4 it was demonstrated that the flow field of the detached flame and the flow field of the trumpet flame feature strong self-excited helical coherent structures, which manifest as a PVC. Their occurrence and shape were extracted from the flow fields by means of a POD. However, for the transient measurement, the POD cannot be used since in the transient phase, the PVC changes its appearance and frequency. Thus, the POD fails to represent the PVC during the transition in two well-defined POD modes. Instead of the POD, a simple approach

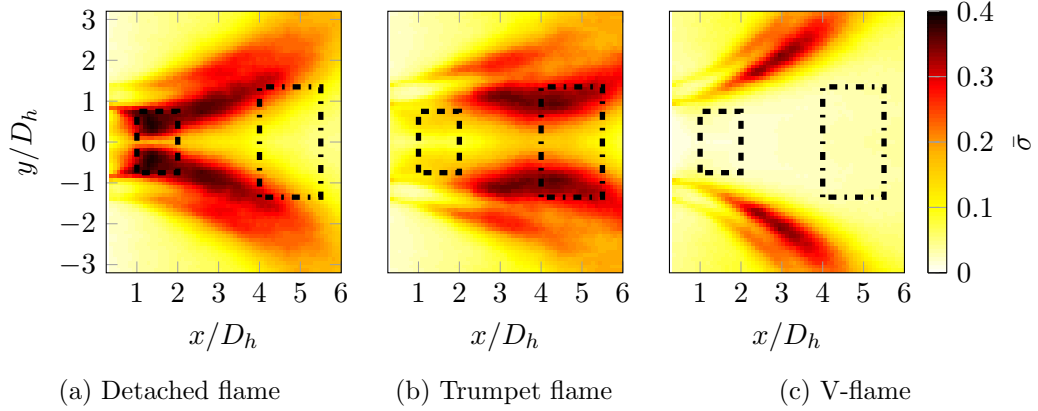


Figure 7.1: Distribution of the time-averaged normalized antisymmetric velocity fluctuation intensity  $\bar{\sigma}$ . Dashed square indicates integration zone for  $\Sigma_{us}$  and dash-dotted square is the integration zone for  $\Sigma_{ds}$ .

is employed here, which makes use of the fact that the velocity perturbations induced by the PVC are antisymmetric and occur in well-defined regions. To assess this antisymmetry, a measure for its spatial distribution is introduced as:

$$\sigma(x, y, t) = \frac{1}{U_0^2} \left[ [u(x, y, t) - u(x, -y, t)]^2 + [v(x, y, t) + v(x, -y, t)]^2 \right]. \quad (7.3)$$

The time-averaged spatial distribution of  $\sigma$  is depicted in Fig. 7.1 for the steady state flow field of a detached flame, a trumpet flame, and a V-flame. It is evident that the asymmetry in the flow field reaches the highest levels in very different regions depending on the flame shape. These regions are closely coupled to the antisymmetric structure of the PVC. Consequently, for the detached flame, strong antisymmetric fluctuations prevail close to the combustor inlet, where also the PVC is strong. For the trumpet flame, the PVC is shifted downstream, leading to a downstream shift of the region of maximum antisymmetric fluctuations. In the case of the V-flame (where the PVC is suppressed), the region in the jet, where the overall turbulence intensity is high, is the only region with considerable levels of antisymmetric fluctuation intensity.

To exploit the different spatial distribution for the identification of the occurrence of the two PVC types, two integration regions are defined, as indicated by the dashed boxes in Fig. 7.1. An integration over these areas yields a measure for the instantaneous magnitude of the flow asymmetry. The integration close to the combustor inlet yields the upstream asymmetry  $\Sigma_{us}$  and shows the highest value for the detached flame. For the V-flame,  $\Sigma_{us}$  is very low, due to the suppression of the PVC. For the trumpet flame, the integration further downstream ( $\Sigma_{ds}$ ) yields the highest values, since the PVC is also shifted more downstream. In the case of the detached flame, a small contribution of the PVC is found to  $\Sigma_{ds}$ , and for the V-flame, again, the level of asymmetry is very low. A summary of the introduced parameters and their expected values for the three flame shapes is provided in Tab. 7.1.



Table 7.1: Compilation of the parameters for the identification of the flame shapes.

Parameter	Symbol	V-flame	Detached flame	Trumpet flame
Upstream OH* intensity ratio	$R_{OH}$	High	Low	High
Upstream density ratio	$R_\rho$	Low	High	Low
Initial jet opening angle	$\alpha$	High	Medium	Low
Upstream antisymmetry	$\Sigma_{us}$	Low	High	Medium
Downstream antisymmetry	$\Sigma_{ds}$	Low	Medium	High

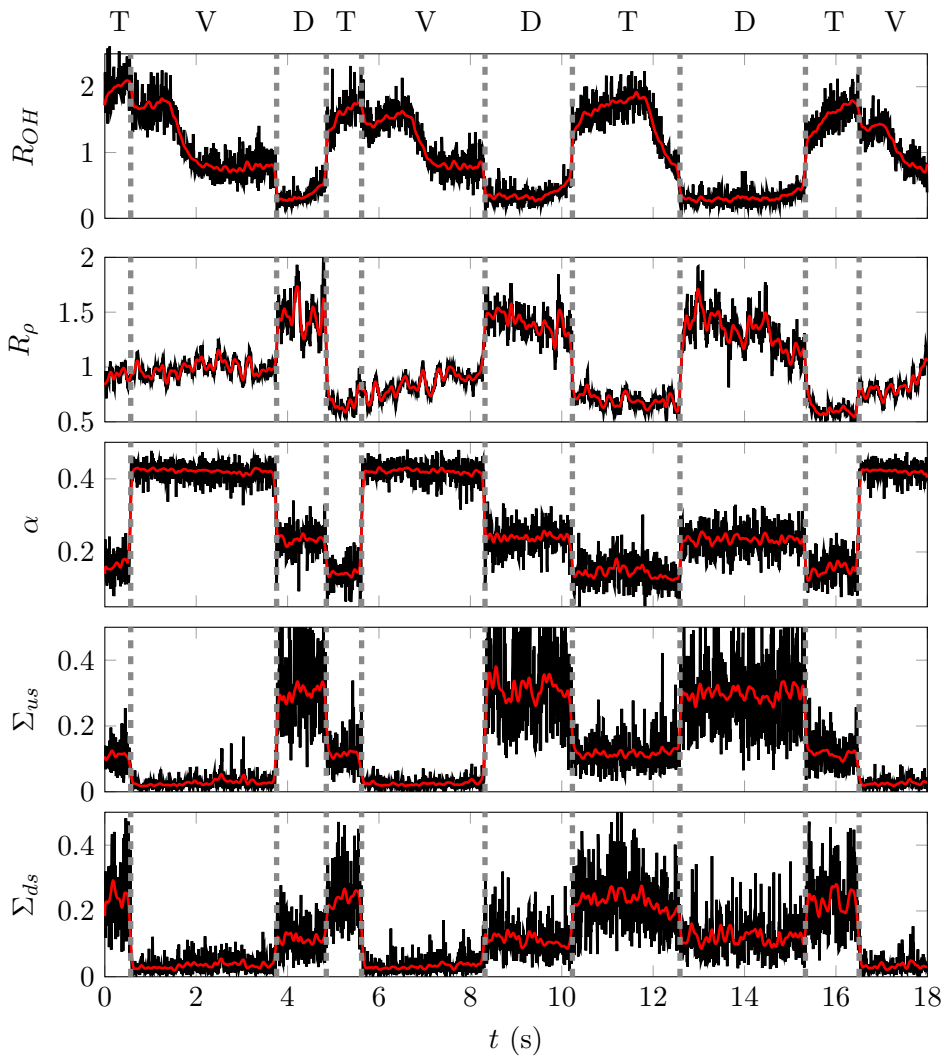


Figure 7.2: Flow field and flame parameters for the transient measurement. The dashed lines indicate changes of the flame shape. **V**: attached V-flame, **T**: trumpet flame, **D**: detached flame.

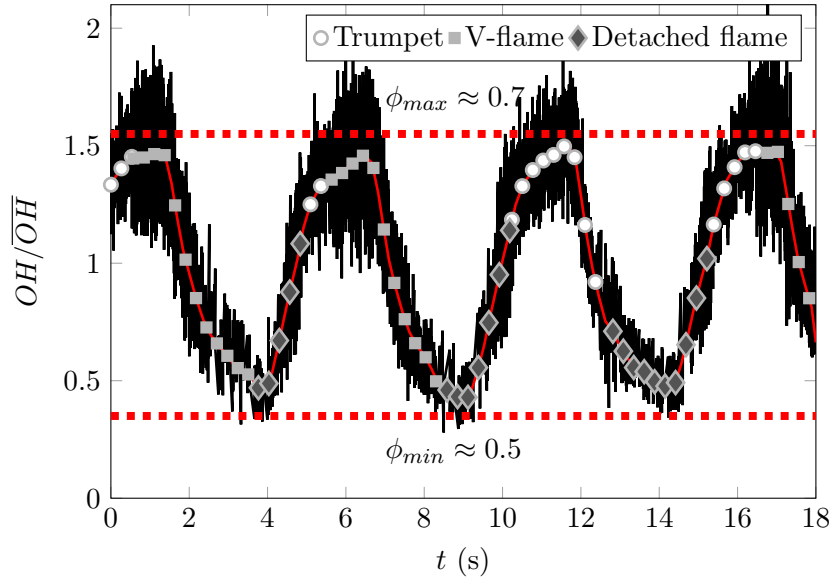


Figure 7.3: Time trace of the normalized integral OH\*-chemiluminescence intensity during the periodic variation of the equivalence ratio  $\phi$ . Solid red line is the low pass filtered normalized integral OH\*-chemiluminescence intensity. Symbols indicate the flame shape. Red dashed lines represent the mean OH\*-chemiluminescence intensity for the minimum and maximum equivalence ratio, respectively.

The temporal evolution of all five calculated parameters during the complete measurement time is depicted in Fig. 7.2. The instantaneous flame shapes can be deduced from the parameters. The time traces of  $\Sigma_{us}$  and  $\Sigma_{ds}$  show the expected trends, with high values of  $\Sigma_{us}$  for the detached flame and high values of  $\Sigma_{ds}$  for the trumpet flame. However, the signals are overlaid by a considerable amount of noise, which is caused by the strong turbulence.

The introduced parameters enable to conveniently extract the interesting flame shape transitions from the transient data. Furthermore, they will be used in the following to assess the role of the PVC for the transition processes.

Figure 7.3 shows the integrated OH\*-chemiluminescence intensity of the 27,000 samples measured with an intensified camera. The variation of the equivalence ratio between a minimum value of  $\phi \approx 0.5$  and a maximum value of  $\phi \approx 0.7$  is evident, even though the signal is very noisy because of the intense turbulence. Due to the nonlinear relation of the OH\*-chemiluminescence intensity for partially premixed flames, however, the exact temporal evolution of the equivalence ratio cannot be deduced from the OH\*-chemiluminescence intensity without an extensive calibration. Nevertheless, Fig. 7.3 provides a very good qualitative idea of the instantaneous equivalence ratio. The instantaneous flame shapes, extracted from Fig. 7.2, are indicated by the overlaid symbols.

## 7.4 Time-Series Investigation of the Flame Shape Transitions

In the following the flame shape transitions are investigated in detail by the inspection of time-series of instantaneous flow fields, OH\*-chemiluminescence images, and density estimations taken during the transitions.

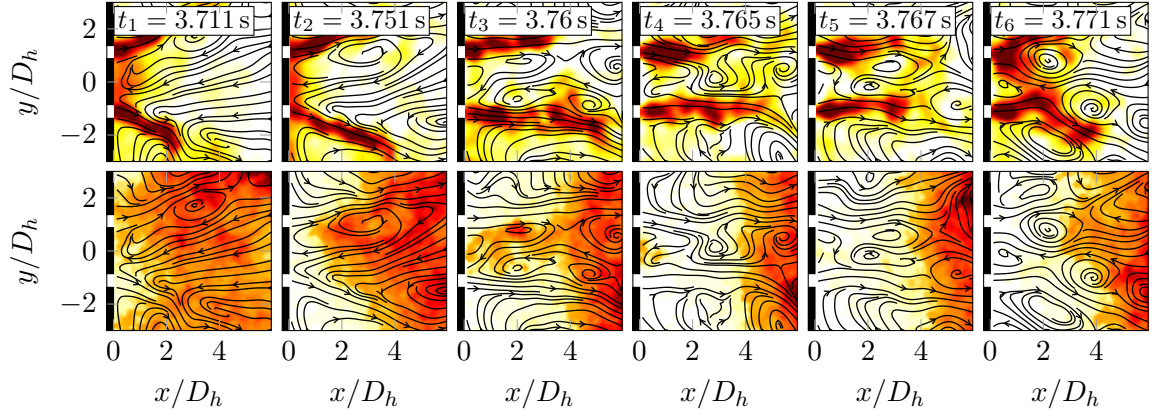
### 7.4.1 Detachment of the Flame

Figure 7.4 depicts the detachment process from the attached V-flame to the detached flame. The top row shows the instantaneous velocity fields superimposed on the instantaneous normalized density distribution and the bottom row shows the velocity field and the instantaneous OH\*-chemiluminescence intensity. At  $t_1 = 3.711$  s, the flame is already very lean (see Fig. 7.3). Therefore, it is spatially much wider distributed compared to the standard V-flame (compare Fig. 4.4). However, the wide opening angle and the density distribution clearly show that the flow field is typical for the V-flame shape. Starting from this point ( $t_1$  in Fig. 7.4), the opening angle of the flame slightly decreases and the downstream asymmetry  $\Sigma_{ds}$  is increased until  $t_3 = 3.76$  s. Subsequently, the flame and the corresponding flow field are very similar to the trumpet shape flame. The increase of the downstream asymmetry is assumed to be caused by the excitation of the PVC of the trumpet flame type.

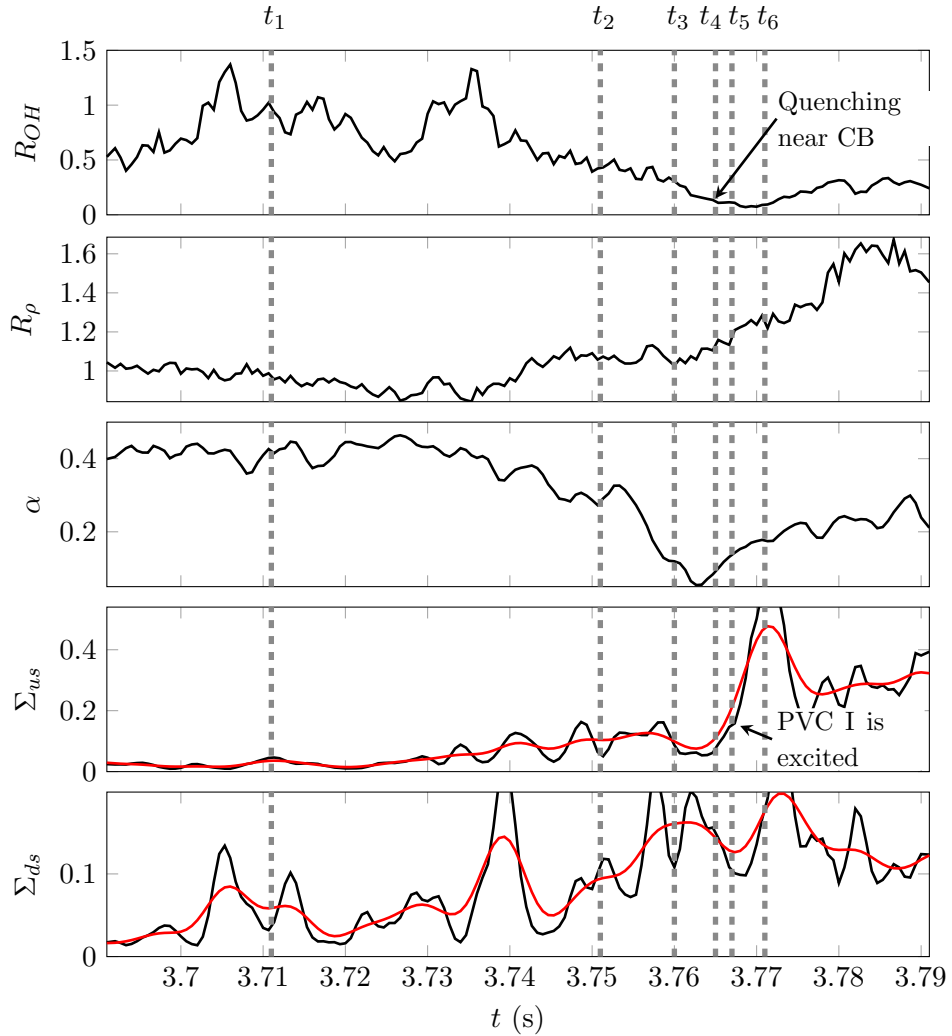
The flame is still attached, but the amount of reaction near the combustor inlet, as indicated by  $R_{OH}$ , is considerably decreased and the density ( $R_\rho$ ) is slightly increased. At  $t_4 = 3.765$  s, the reaction in the wake of the centerbody is quenched and the asymmetry in the upstream section ( $\Sigma_{us}$ ) grows rapidly. In the instantaneous velocity field at  $t = 3.771$  s, vortices in the inner shear layer are evident, as a result of the onset of the PVC of the detached flame type. At the same time, the density in the IRZ rises significantly. This is in line with the findings of Chapter 4, that the PVC of the detached flame type increases the mixing between the jet and the IRZ. In summary, the identified course of actions involved into the detachment process of the V-flame is the following:

1. The reaction in the upstream part of the IRZ gets weaker due to the lower equivalence ratio ( $t_1$  to  $t_6$ ).
2. The flow field and the flame shape gradually change from the V-flame type to the trumpet flame type ( $t_1$  to  $t_3$ ).
3. The PVC of the trumpet flame type is excited intermediately ( $t_2$  to  $t_6$ ).
4. The flame root is quenched ( $t_4$ ).
5. The PVC of the detached flame type is excited ( $t > t_4$ ).
6. The PVC leads to increased mixing and cools down the IRZ ( $t > t_4$ ).

Figure 7.5 shows the detachment of the trumpet flame. As it was described above, the detachment of the V-flame is a two-step process consisting of the transition from the V-shape to the trumpet shape and the subsequent detachment. Consequently, the detachment of the trumpet flame (without preceding V-flame) follows essentially the same pattern as the second part of the detachment process of the V-flame. First, the reaction rate in the inner

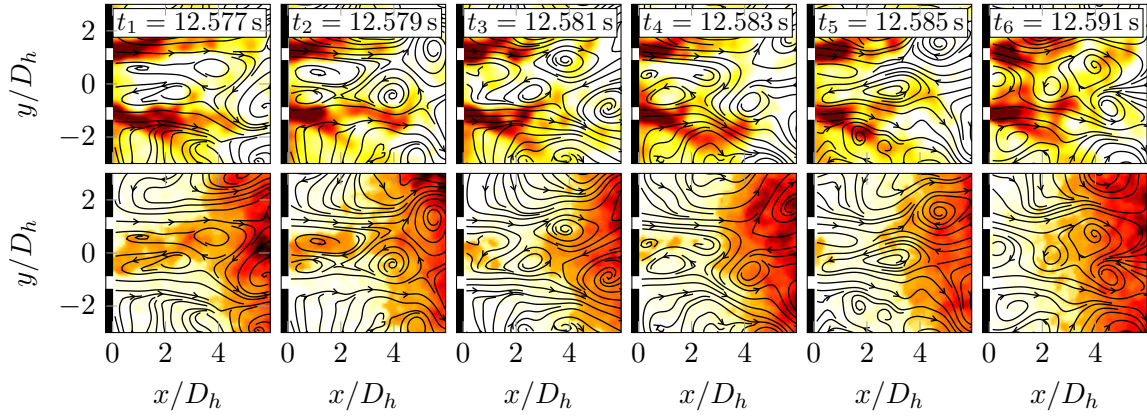


(a) Instantaneous images. Flow field is superposed on the estimated density distribution (top) and the OH\*-chemiluminescence intensity (bottom).

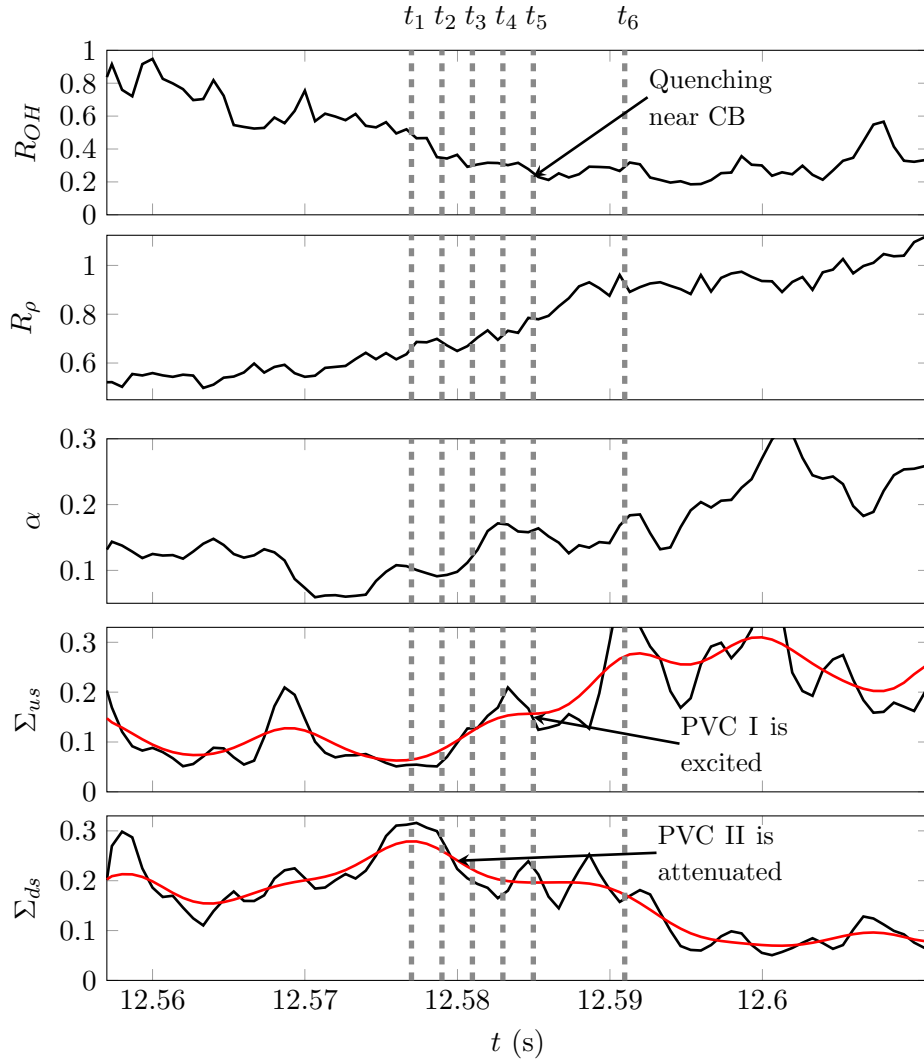


(b) Flow field and flame parameters. The dashed lines indicate the times, when the instantaneous images were extracted. Red lines are lowpass filtered trends. PVC I refers to the PVC of the detached flame.

Figure 7.4: Flow field and flame parameters for the detachment process of the V-flame.



(a) Instantaneous images. Flow field is superimposed on the estimated density distribution (top) and the OH\*-chemiluminescence intensity (bottom).



(b) Flow field and flame parameters. The dashed lines indicate the times, when the instantaneous images were extracted. Red lines are lowpass filtered trends. PVC I refers to the PVC of the detached flame, and PVC II refers to the PVC of the trumpet flame.

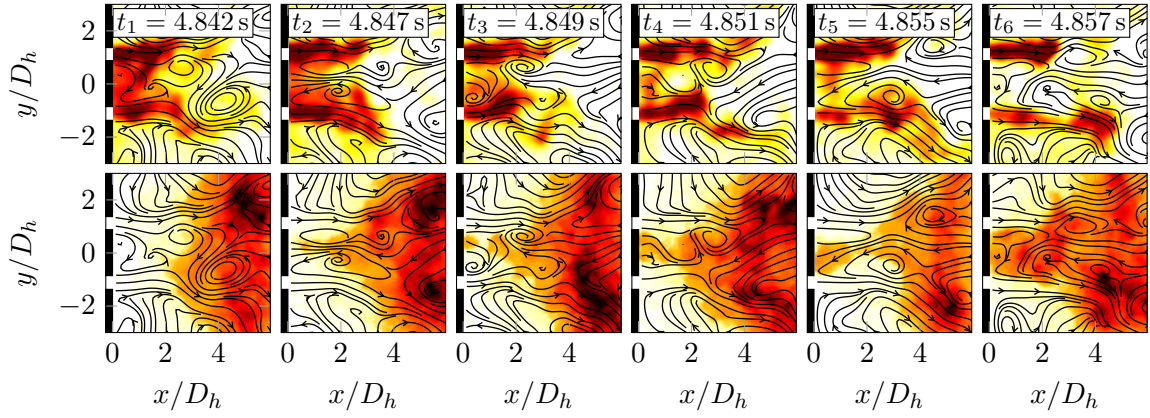
Figure 7.5: Flow field and flame parameters for the detachment process of the trumpet flame.

recirculation zone is decreased, leading to lower  $\text{OH}^*$  intensities and a higher density close to the inlet ( $t_1$  to  $t_5$ ). Simultaneously, the PVC of the trumpet flame type is attenuated, as indicated by  $\Sigma_{ds}$ , and the PVC of the detached flame type ( $\Sigma_{us}$ ) is slightly excited. When the flame in the wake of the centerbody is quenched ( $t_5 = 12.585$  s),  $\Sigma_{us}$  increases significantly, indicating a strong increase of the oscillation amplitude of the PVC of the detached flame type. From Fig. 7.3 it can be observed that the flame detaches at a much higher equivalence ratio when the flame was in its trumpet shape, compared to when the flame was in its V shape. One reason is assumed to be the narrower inner recirculation zone, which goes along with higher strain rates. Another possible explanation is the much higher backflow intensity. Therefore, the excitation of the upstream PVC of the detached flame type is facilitated (see Chapter 6). In the subsequent sections, more arguments will be found to manifest that the excitation of the upstream PVC is assumed to play an important role for the flame shape transition process.

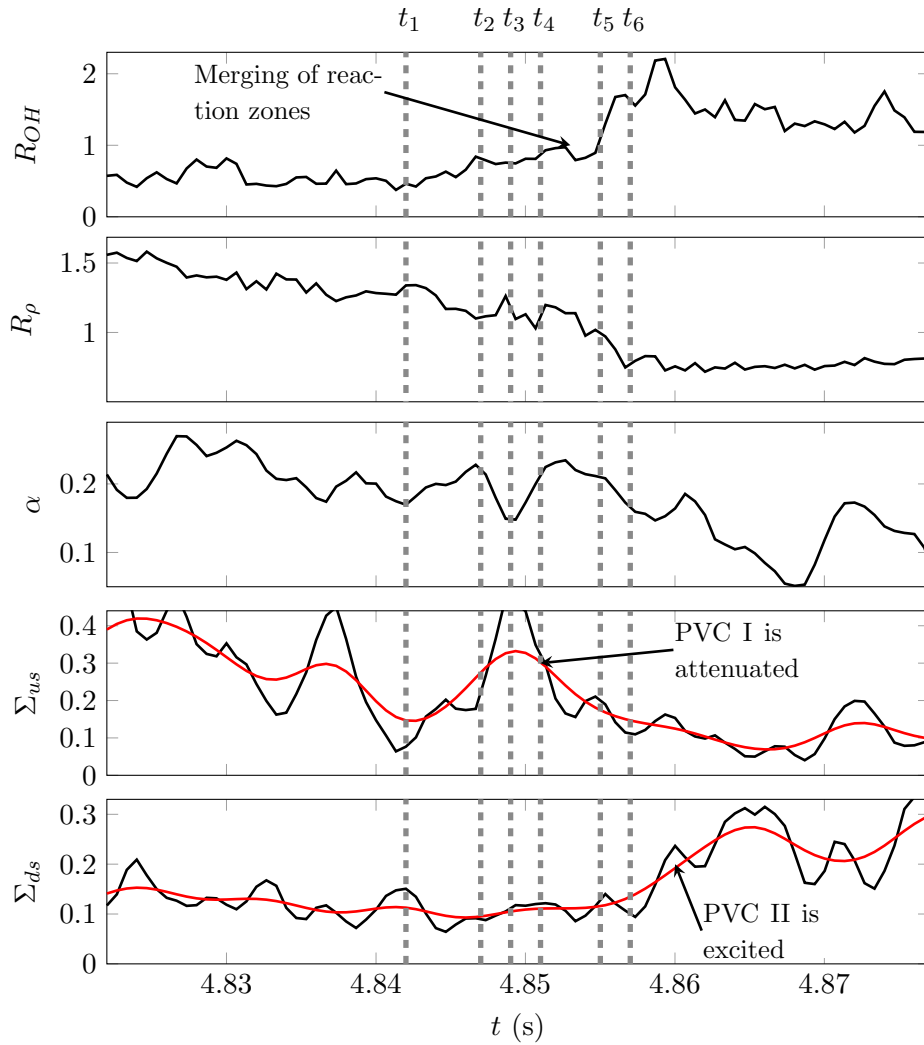
#### 7.4.2 Attachment of the Flame

The attachment of the flame is presented in Fig. 7.6. At  $t_1 = 4.842$  s, the strong PVC of the detached flame type is intermediately weakened, leading to lower values of  $\Sigma_{us}$  compared to  $t < t_1$ . Nevertheless, the density distribution in the vicinity of the inlet is still homogeneous, and the flame is detached from the centerbody. However, starting from this point in time, the density, indicated by  $R_\rho$ , is decreasing, whereas the strength of the PVC, indicated by  $\Sigma_{us}$ , intermediately rises. In the subsequent time step at  $t_2 = 4.847$  s, the very reactive fuel-air mixture at a high equivalence ratio is able to propagate into the cold region of the inner recirculation zone. This new flame root stabilizes in the wake of the centerbody and finally merges with the main reaction zone ( $t_4$  to  $t_5$ ). During the merging process, the density in the recirculation zone is considerably decreased. At the same time, the PVC of the detached flame type is strongly attenuated ( $t > t_4$ ). Its lower amplitude is assumed to be a direct result of the density gradients along the jet (see Chapter 6) and at the same time it causes steeper density gradients (see Chapter 4) due to weaker mixing. At the end of the transition, the flame and flow field show the trumpet shape and the PVC type has changed from the detached flame type to the trumpet flame type.

After the reattachment process, the flame remains first in the trumpet shape with weak variations of the flame and flow field parameters. A further increase of the reactivity leads to the final transition to the V-flame (Fig. 7.7). In contrast to the detachment and attachment, this process is continuous and no determining point can be identified. Figure 7.7 shows that the amplitude of the PVC of the trumpet flame type is reduced during the transition process. One may speculate that the PVC of the trumpet flame type is damped by the stronger density gradients due to the higher flame temperatures and its suppression facilitates the transition to the V-flame. However, it also seems possible that during the continuous change of the flow, as indicated by the gradual change of the flame opening angle  $\alpha$ , the backflow intensity is reduced, and the PVC is stabilized by this mean flow field modification.



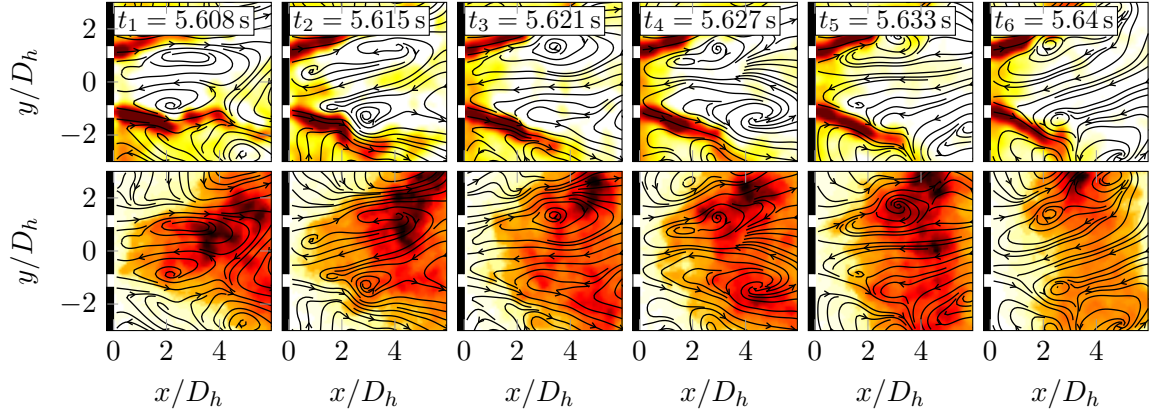
(a) Instantaneous images. Flow field is superimposed on the estimated density distribution (top) and the OH\*-chemiluminescence intensity (bottom).



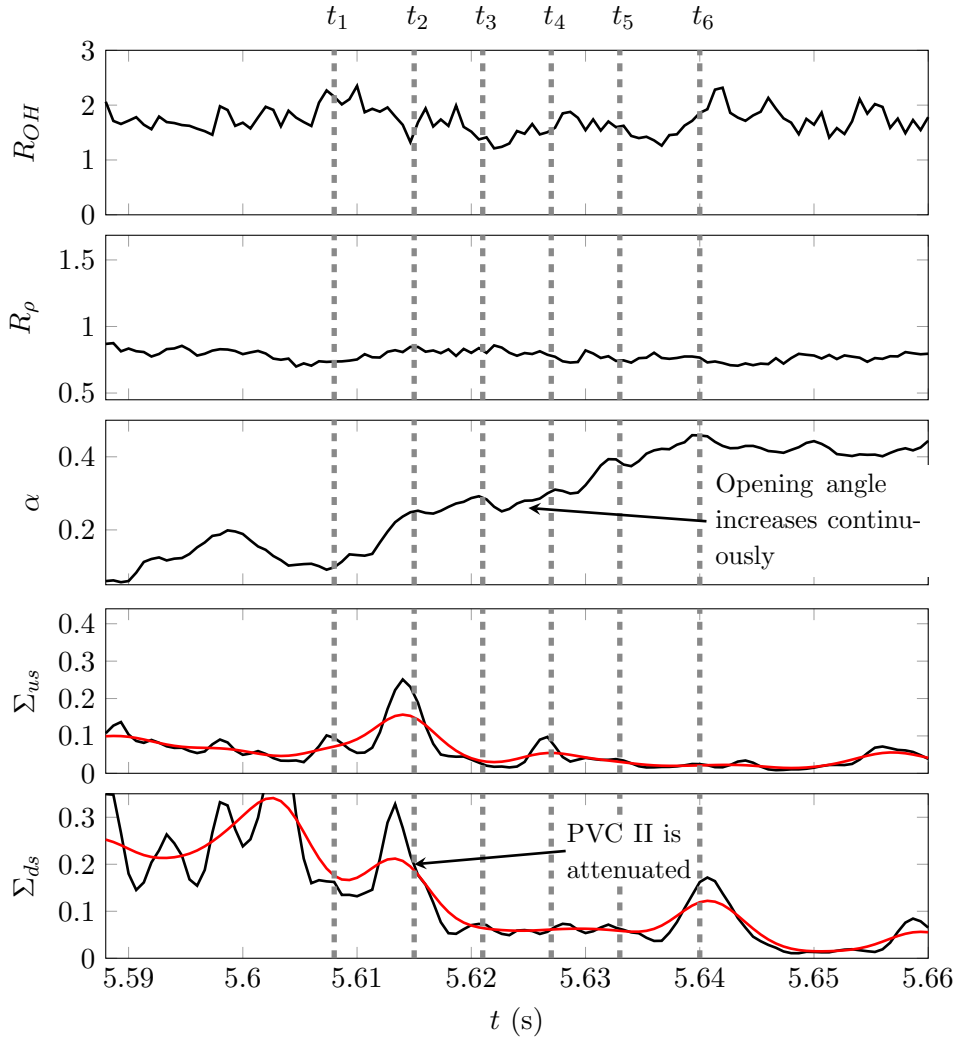
(b) Flow field and flame parameters. The dashed lines indicate the times, when the instantaneous images were extracted. Red lines are lowpass filtered trends. PVC I refers to the PVC of the detached flame, and PVC II refers to the PVC of the trumpet flame.

Figure 7.6: Flow field and flame parameters for the attachment process of the flame.





(a) Instantaneous images. Flow field is superimposed on the estimated density distribution (top) and the OH\*-chemiluminescence intensity (bottom).



(b) Flow field and flame parameters. The dashed lines indicate the times, when the instantaneous images were extracted. Red lines are lowpass filtered trends. PVC II refers to the PVC of the trumpet flame.

Figure 7.7: Flow field and flame parameters for the transition from the trumpet flame to the V-flame.



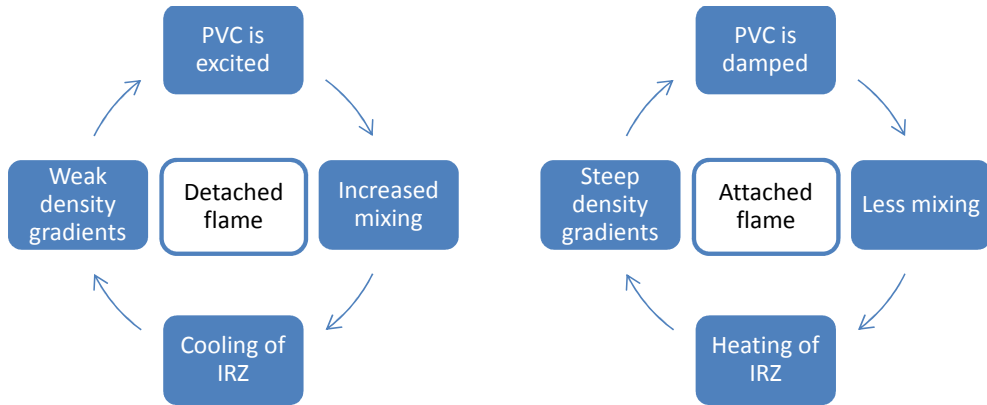


Figure 7.8: Schematic of the proposed stabilization mechanism for detached and attached flames.

## 7.5 Transition and Hysteresis Mechanism

A large region where different flame types for the same equivalence ratio are possible (e.g.,  $\overline{OH}/\overline{OH} = 1$ ) is evident from Fig. 7.3. The flame type strongly depends on the direction of the equivalence ratio variation from lean to rich or from rich to lean. The flame detaches from the V-shape near the minimum of the integral  $\text{OH}^*$ -chemiluminescence intensity, which correlates to the minimum global equivalence ratio. When increasing the equivalence ratio, it reattaches only when the integral  $\text{OH}^*$ -chemiluminescence intensity is above its average value and requires almost its maximum value to recover to the V-shape. In the following, a flame stabilization and transition mechanism, including the PVC, will be described, which explains the findings of the present work and is well in line with the findings of Tummers et al. (2009).

A schematic representation of the proposed mechanism for the detachment of the flame is provided in Fig. 7.8. One of the key findings of Chapter 4 is that in case of a detached flame, a strong PVC is excited. This PVC and the associated axial-radial eddies (Kelvin-Helmholtz instabilities) cause an increased mixing of unburnt gases with the hot product gases of the inner recirculation zone at the combustor inlet. As a result, in the vicinity of the combustor inlet, low temperatures are present in the jet and in inner recirculation zone (see Chapter 4). These low temperatures reduce the local reactivity of the fuel-steam-air mixture and, thereby, inhibit the reattachment of the flame. This effect is evident in Fig. 7.9, where the dependence of the laminar burning velocity on the temperature is depicted for different inlet temperatures. At lower temperatures, the laminar burning velocity, which is the critical parameter for the ability of the flame not to be quenched (Williams, 2000), is strongly reduced. The low density gradients along the inner shear layer facilitate the occurrence of the PVC (see Chapter 6), thus, closing the loop for the stabilization of the flame in a detached shape.

In the case of an attached flame, the PVC is suppressed, resulting in a very low mixing intensity from the jet to the IRZ. Consequently, the IRZ remains very hot up to the centerbody and facilitates the stabilization of the flame in its vicinity, due to the considerably higher

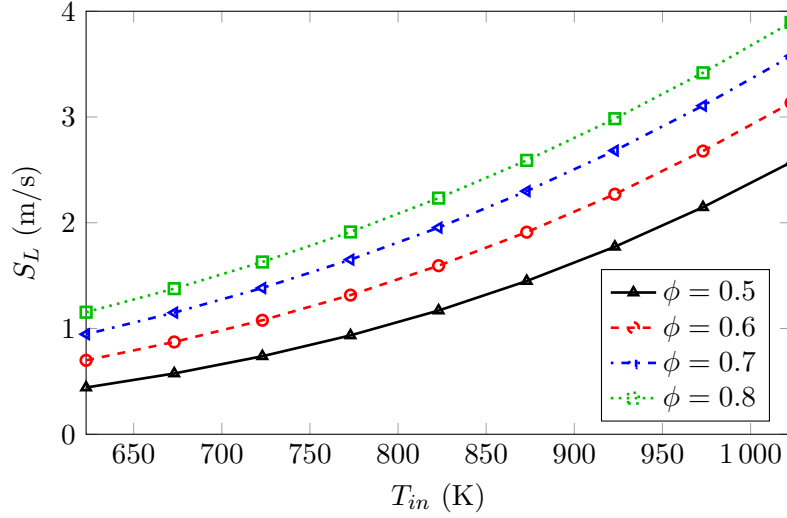


Figure 7.9: Laminar burning velocities for methane flames at different equivalence ratios and at increasing inlet temperatures. For the calculation the GRI3.0 reaction mechanism (Smith et al., 2000) was employed.

reactivity of the mixture at higher temperatures. The strong density gradients inhibit the excitation of the PVC and, thus, stabilize the attached flame.

One of the most important features of the proposed stabilization mechanism is the self-strengthening effect of the PVC on the flame stabilization. To better understand the implications of this mechanism, one has to consider an attached flame, where the reactivity of the mixture is reduced by leaning out the mixture or increasing the rate of steam dilution. At a critical value of the reactivity, the flame root is not able to sustain the high strain rates near the combustor inlet and quenches (Williams, 2000; Wicksall et al., 2005a), leading to a detachment of the flame root. Subsequently, the flame can be either blown out, as observed by Stöhr et al. (2011a), or stabilized as a detached flame at a more downstream location, as in the present study. In this case the density field inside the combustor changes and the density gradients along the inner shear layers get weaker. As a result of the lower density gradients, the excitation of the PVC is facilitated and further increases the mixing, leading to even lower density gradients. The transition from the attached to the detached flame is complete. If the PVC fails to set in, however, the temperatures in the IRZ remain higher and the flame may reattach.

The process of a reattachment follows the same train of thoughts as the detachment. Consider a detached flame, where the reactivity of the fuel-air-steam mixture is increased. Once the flame is able to propagate upstream, the density gradients in the shear layers get steeper. This leads to a damping of the PVC and the corresponding axial-radial eddies. Consequently, the mixing between the jet and the recirculation zone is reduced and the temperature in the recirculation zone increases. This further attenuates the PVC and also increases the ability

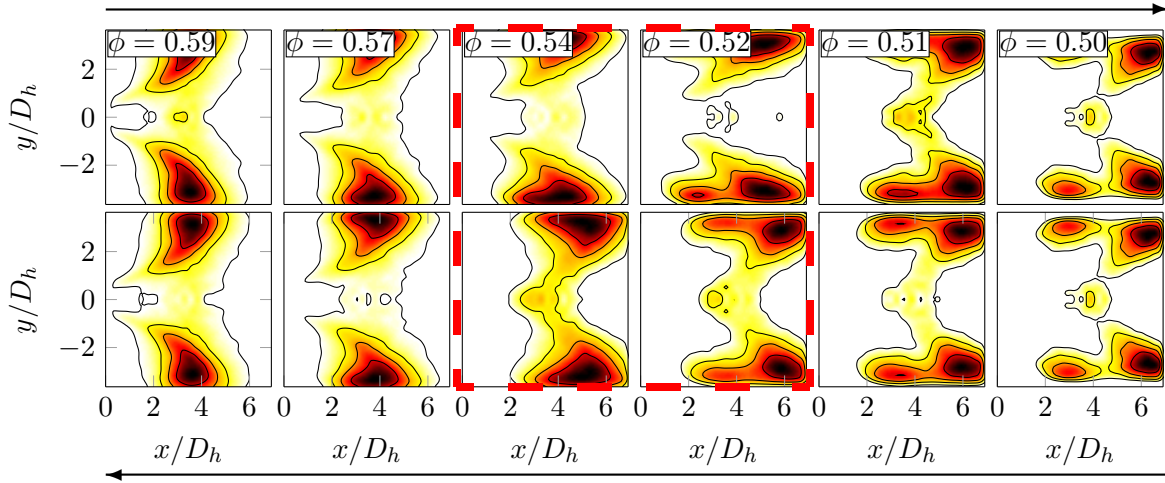


Figure 7.10: Abel-deconvoluted  $\text{OH}^*$ -chemiluminescence images at decreasing (top row) and increasing (bottom row) equivalence ratios. Red dashed rectangle indicates the hysteresis region between detached and attached flames. The combustor has a smaller centerbody diameter of  $D_{cb} = 27.5$  mm (compared to  $D_{cb} = 35$  mm in the previous measurements presented in this chapter). The smaller centerbody inhibits the stable occurrence of the trumpet flame.

of the flame root to sustain high strain rates, as they are typically present in the vicinity of the centerbody (Wicksall et al., 2005b).

One consequence of the self-strengthening stabilization mechanism is a hysteresis for the flame shape transition. This is evident in the steady measurements shown in Fig. 7.10. In a slightly different combustor configuration (smaller centerbody), where no trumpet flame was possible, the equivalence ratio was varied stepwise ( $\Delta\phi = 0.01$ ) between  $\phi = 0.5$  and  $\phi = 0.59$ . Starting from an attached flame, the equivalence ratio is reduced. At  $\phi = 0.51$  the flame detaches and remains in its detached state even for a further reduction of the equivalence ratio. When starting from the detached flame, the equivalence ratio is increased, an equivalence ratio of  $\phi > 0.54$  is required for the reattachment. This is considerably richer than the equivalence ratio, where the flame detaches. In the hysteresis region, indicated by the red dashed rectangle, differences between the two flames at the same equivalence ratio are obvious. The attached flame (upper row) is located more upstream and the flame root is located in the shear layers, whereas the detached flame is located more downstream.

One may argue that the observed hysteresis can also be caused by thermal effects, such as heating of the burner plate or the combustion chamber. However, during the measurement campaign of the transient equivalence ratio variations, no incident of an instantaneous reattachment was observed. This allows suggesting that the investigated hysteresis is not dominated by thermal effects since the typical timescales of the heating process are considerably longer than the flow timescales. Thus, theoretically allowing for an instantaneous reattachment, which was never observed during the experiments.

## 7.6 Conclusions

In the present chapter, transitions between the different flame shapes were studied in detail. Experiments were carried out, where the transitions were provoked by periodic variations of the equivalence ratio. A set of parameters was introduced to identify the instantaneous flame shape and the occurrence and type of the PVC. Subsequently, examples of each transition process were assessed by means of the inspection of instantaneous flow fields, OH\*-chemiluminescence distributions, and density fields. The main findings for the detachment of flame are summarized in the following:

- The detachment of the flame is a two-step process. First, the flame transits from the V-flame to the trumpet flame and subsequently, detaches.
- Once the reaction in the wake of the centerbody is quenched, the PVC of the detached flame type is excited, increases the mixing, and cools down the IRZ.

For the reattachment of flame, the opposite train of actions was observed:

- Once the reactivity is high enough for the flame to propagate into the upstream part of the IRZ, it stabilizes in the wake of the centerbody.
- The reaction in the IRZ decreases the density and, thereby, attenuates the PVC and consequently the mixing caused by the PVC. Thus, the density in the IRZ decreases even more strongly.

The strong influence of the PVC on the mixing was demonstrated in Chapter 4 and the influence of the density field on the excitation of the PVC was shown analytically in Chapter 6. The combination of these results with the results from the present chapter allows for the formulation of a transition mechanism. One important implication of this mechanism is that the transitions between the detached and the attached flames are self-strengthening processes. In other words, once the flame detaches *a little bit*, its detachment is boosted by the excitation of the PVC. The other way around, the attachment of the flame with a corresponding suppression of the PVC is also strengthened. In terms of stability, the detachment and attachment must, therefore, be of a subcritical nature. This is well in line with the hysteresis in the flame shape transitions found in steady measurements, in the transient measurements, and in cases presented in the literature.

## Chapter 8

# Axisymmetric Coherent Structures and their Impact on the Flame Response

*<sup>4</sup>In contrast to the previous chapters, the present chapter places the focus on acoustically forced axisymmetric coherent structures, as they are typically present at thermoacoustically unstable conditions. It is shown that the flame response to acoustic forcing at perfectly premixed conditions is strongly influenced by the growth of axisymmetric vortical structures in the shear layers. An experimental study is conducted in order to measure the amplitude-dependent flame transfer function and the corresponding flow fields subjected to acoustic forcing. Measurements are taken for three different swirl numbers and different acoustic forcing amplitudes. The results show that forcing leads to significant changes in the time-averaged reacting flow fields and flame shapes. Coherent velocity fluctuations at the forcing frequency are amplified considerably stronger in the shear layers at low forcing amplitudes than at high amplitudes. This is an indicator for a nonlinear saturation process. The strongest saturation is found for the lowest swirl number, where the forcing additionally detached the flame. For the highest swirl number, the saturation of the vortex amplitude is weaker. Overall, the amplitude-dependent vortex amplification resembles the flame response reasonably well. An application of a linear stability analysis to the time-averaged flow fields at increasing forcing amplitudes yields the decreasing growth rates of shear flow instabilities at the forcing frequency. It therefore successfully predicts a saturation at high forcing amplitudes and demonstrates that the mean flow field and its modifications are of utmost importance for the growth of vortices in the shear layers. Moreover, the results clearly show that the amplification of vortices in the shear layers is an important driving factor for heat release fluctuations and their saturation.*

---

<sup>4</sup>The results presented in the present chapter were previously published in Terhaar et al. (2014a). Bernhard Ćosić assisted with the acoustic measurements and did the post processing of the microphone data. Kilian Oberleithner provided the original version of the stability solver and assisted with the interpretation of the results of the stability analysis. All other tasks were carried out by the author.

## 8.1 Introduction

In the previous chapters the occurrence of self-excited helical instabilities was assessed. The reason for these instabilities is a hydrodynamic resonance in the flow field. In the present chapter axisymmetric coherent structures are investigated, whose origins are not purely in the hydrodynamic field. In contrast to the self-excited helical instabilities, they are excited by acoustic forcing.

Acoustics become increasingly important at lean premixed combustion, which is widely applied in modern gas turbines to reduce toxic  $\text{NO}_x$  emissions. Unfortunately, at these lean conditions, combustors are very prone to thermoacoustic instabilities. The resulting heat release oscillations can lead to increased emissions and very high pressure amplitudes, which can cause severe damages to the combustion chamber or even to the entire gas turbine. These mostly self-excited thermoacoustic instabilities are caused by a feedback cycle between heat and pressure oscillations (Rayleigh, 1878). A comprehensive review on combustion instabilities is available by Lieuwen and Yang (2005).

In industrially used combustors, fuel and air are usually partially premixed prior to the combustion. The aim is to achieve a sufficient amount of mixing required for the emission reduction with the shortest possible premixing length since long premixing sections increase the danger of undesired autoignition. In these partially premixed systems, heat release fluctuations of the flame are caused by two mechanisms: Flow field perturbations and equivalence ratio fluctuations. If the fuel mass flow is considered as constant, a fluctuation of the air mass flow, as it is typical for a thermoacoustic oscillation, causes oscillating equivalence ratios.

The complex interaction of heat release fluctuations caused by equivalence ratio fluctuations and heat release fluctuations caused by the velocity fluctuations render the prediction or modeling of the flame response a very challenging task. However, in a recent work Ćosić et al. (2014) showed that it is generally possible to linearly decompose the flame response at low and high oscillation amplitudes into contributions of both mechanisms. Therefore, understanding the role of coherent structures for the flame response is an important step towards a better modeling of the flame response. In the present chapter, the focus is placed on the role of the velocity fluctuations. For laboratory-scale combustors, the equivalence ratio fluctuations can be eliminated by perfectly premixing air and fuel well upstream of the combustor. This is done in the present work.

Schadow and Gutmark (1992) investigated the role of shear layer instabilities for the growth of coherent structures and the resulting heat release fluctuations in dump combustors. The vortices are amplified if the shear layers are convectively unstable at the frequency of the instability. Paschereit et al. (1999, 2000) emphasized the pronounced vortex-flame interactions associated with these large-scale structures. They found that the fluctuation of heat release caused by the vortices acts as a feedback loop between the flame, the acoustics, and the hydrodynamic field. The acoustic field acts as a pacemaker for the coherent structures (Keller, 1995). The self-excited helical structure of the PVC, however, plays only a secondary role for thermoacoustic oscillations. Moeck et al. (2012) showed that the asymmetric flow structures

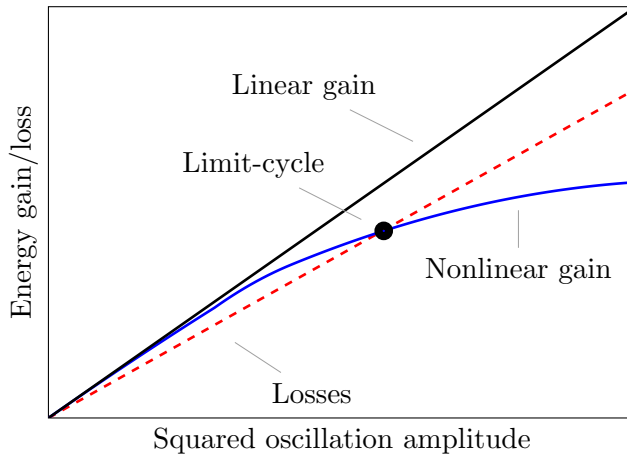


Figure 8.1: Schematic representation of the determination of the limit-cycle amplitude.

do not cause integral heat release oscillations, which is also confirmed in Chapter 4 of this thesis. Therefore, the focus is placed on axisymmetric vortical structures in the present investigation.

The limit-cycle amplitude of thermoacoustic oscillations is determined by an equilibrium of acoustic energy added by the flame and acoustic dissipation, as it is depicted schematically in Fig. 8.1. The losses are often assumed to increase linearly with the squared oscillation amplitude. In contrast to that, the rate of acoustic energy addition is essentially non-linear and, therefore, determines the limit-cycle amplitude. The energy gain is frequently characterized by the amplitude-dependent flame response, which has been successfully used to predict limit-cycle amplitudes (Dowling, 1997; Palies et al., 2011; Ćosić et al., 2013).

An important saturation mechanism of the flame response was found by Schimek et al. (2012b), who showed that axial velocity fluctuations introduced by loudspeakers lead to changes in the mean flow field. Similar trends were observed in several studies (Bellows et al., 2007; Thumuluru and Lieuwen, 2009), which reported changes in the time-averaged flame shape. Oberleithner et al. (2012b) performed linear hydrodynamic stability analysis on mean flow fields measured for increasing forcing amplitudes and showed that the growth rate of the vortices in the shear layers is considerably decreased at high forcing amplitudes. With their findings, they explained an intermediate saturation of the flame describing function and emphasized the importance of the mean flow field.

A simplified scheme of the investigated mechanisms that are involved in the transfer function of velocity fluctuations (e.g., acoustic forcing) into heat release fluctuations is shown in Fig. 8.2. The acoustic forcing at the combustor inlet causes velocity fluctuations. These fluctuations are amplified in the shear layers and result in large-scale vortical structures that eventually cause heat release fluctuations. The damping mechanism of these vortices, which is investigated in the present study, is shown in Fig. 8.2 via the mean flow field correction, where the large-scale structures change the time-averaged flow field. This *new* flow field results in a different (lower) shear layer amplification. An equilibrium of shear layer amplification and mean flow field changes is reached in the steady-state. Moreover, the flame shape and position strongly influence the mean flow field and vice versa.

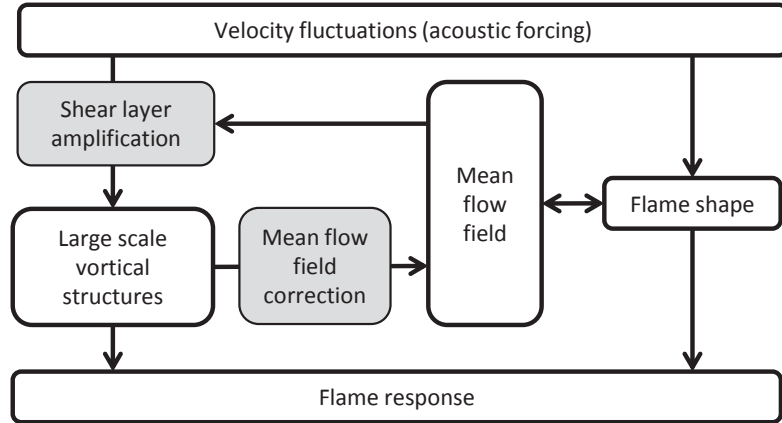


Figure 8.2: Schematic of the mechanisms that are involved in the transfer function of velocity fluctuations at the combustor inlet to the flame response. Investigated mechanisms are shaded gray.

In the presented work, first the amplitude-dependent flame response to velocity fluctuations at 196 Hz forcing frequency is investigated for three swirl numbers. At the selected forcing frequency, all investigated flames show a well-defined flame response and different saturation behaviors. Additionally, modifications to the mean velocity field caused by the large-scale vortical structures and the resulting flame shapes are assessed. To obtain insight into the growth of vortical structures and changes of the shear layer amplification, a combined empirical and analytical approach is used. First, the concept of a triple decomposition of the experimental data, as presented in Section 2.2, is employed to derive the coherent velocity fluctuations at the forcing frequency. Next, the influence of the mean flow field on the growth of vortical structures is shown, employing linear hydrodynamic stability theory. The results are well in line with the empirically derived results. Both show the crucial importance of the shear layer saturation mechanisms related to mean flow field changes for the growth of vortices. Furthermore, the resulting amplitudes of the large-scale coherent structures, which are assumed to play an important role for the heat release fluctuations, show similar characteristics to the flame response at the same forcing frequency and amplitude.

The presented work significantly extends previous studies, in particular the work by Oberleithner et al. (2012b), as the strength of the coherent vortices is quantitatively measured. This data is compared directly to the heat release fluctuations and is used to validate the linear stability analysis. The validity of this approach is proven by the investigation of three different swirl numbers.

The present chapter is structured as follows: First, the experimental and analytical procedure is described. Subsequently, the results of the flame response at the investigated forcing frequency are provided and the amplitude-dependent influence of the acoustic forcing on the mean flow fields and flame shapes is investigated. Next, the results from the empirical triple decomposition method are presented and compared with the measured flame describing func-



tions. In the final step, the coherent velocity fluctuations are predicted from the measured mean flow fields employing linear stability theory and compared to the experimental results.

## 8.2 Experimental and Analytical Procedure

The experiments are carried out in the atmospheric high forcing amplitude combustor test rig as shown in Fig. 3.4b, where the flow can be excited with axisymmetric forcing using four loudspeakers. The combustor, as shown in Fig. 3.2a, consisted of a swirl generator, a silica glass combustion chamber, and an annular duct. The combustor inlet diameter of 55 mm and the centerbody diameter of  $D_{cb} = 27.5$  mm result in a hydraulic diameter  $D_h$  of 27.5 mm. The theoretical swirl number (Leuckel, 1967), was varied during the experiments between  $S=0.6$  and  $S=1$ . The fuel (natural gas) was mixed with the air flow well upstream of the combustor and the loudspeakers to assure a homogeneous fuel–air mixture, even at strong forcing amplitudes.

The acoustic field inside the combustor was measured using the Multi-Microphone-Method (MMM) (Paschereit et al., 2002), and global heat release fluctuations were captured using a narrow bandpass-filtered (308 nm) photomultiplier that measured the chemiluminescence of the OH\*-radical. The flame response at increasing forcing amplitudes, also denoted as flame describing function, is defined as the amplitude of the integral coherent heat release fluctuations  $|Q^c|$  at the forcing frequency divided by the average heat release rate  $\bar{Q}$ . Since no equivalence ratio fluctuations are present, the normalized OH\*-chemiluminescence fluctuations  $|OH^c|/\overline{OH}$  is taken as a measure for the normalized heat release fluctuations  $|Q^c|/\bar{Q}$ . Previous measurements in the same combustor (Ćosić et al., 2013) showed a very good agreement between the flame response measured using the OH\*-chemiluminescence fluctuations and measured with the very precise MMM (Schuermans et al., 2010) at perfectly premixed conditions. The application of the MMM for the measurement of the heat release fluctuations was precluded due to possible malfunction of the microphones caused by residuals of the seeding powder used for the velocity measurements. However, microphones upstream of the seeding injection were used to exactly measure the excitation amplitude. This is regarded as sufficient since the burner transfer function can be assumed to be independent of the excitation amplitude (Schimek et al., 2012b).

Time-resolved spatial distributions of the heat release rate were obtained using a high-speed camera coupled to a high-speed capable bandpass filtered image intensifier, as described in Section 3.3.3. The two-dimensional velocity field in the streamwise plane aligned with the combustor axis was measured using high-speed PIV, as described in Section 3.3.1, in its monoscopic form. For the present study, the PIV system and the OH\*-chemiluminescence imaging operated at a frequency of 1 kHz. During the measurements, over a time span of 17 s, the forcing amplitude was gradually increased from very low forcing amplitudes to the maximum forcing amplitude. The 17 000 instantaneous velocity and OH\*-chemiluminescence distributions were averaged over a time span of 0.5 s, yielding 34 bins containing 500 samples, respectively. These data describe a nearly continuous increase of the forcing amplitude. The

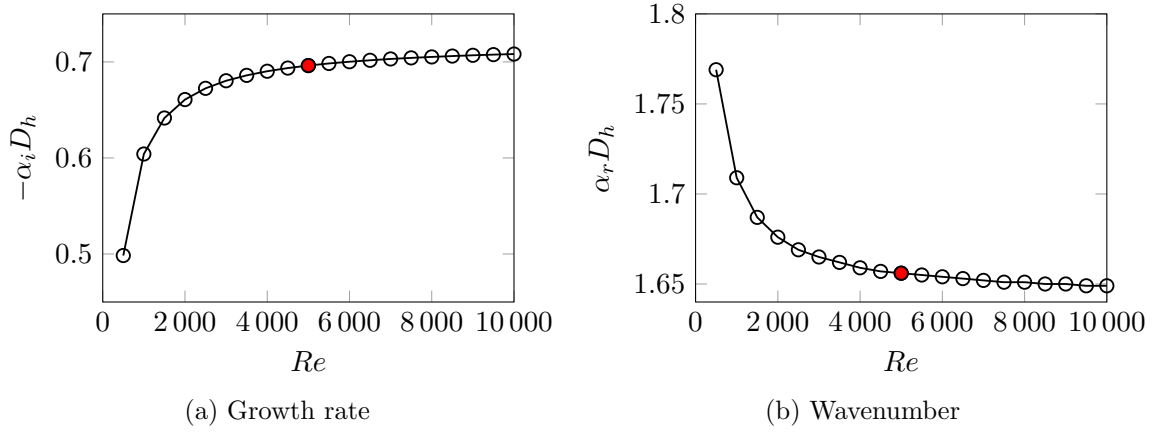


Figure 8.3: Preliminary investigation of the influence of the Reynolds number on the eigenvalue  $\alpha$  of the axisymmetric  $m = 0$  mode at  $x/D_h = 0.25$ . Filled marker indicates the selected value of  $Re = 5000$ .

forcing amplitude at the combustor inlet was measured using the MMM and was also derived from the PIV measurements. Both measurement techniques show similar results. However, since the MMM was shown to be very well suited for the determination of the velocity fluctuations (Paschereit et al., 2002), the more precise results from the MMM are used for the determination of the forcing amplitude in the remainder of this chapter.

In this chapter the triple decomposition, as described in Section 2.2, is employed to extract the coherent from the turbulent, stochastic heat release and velocity fluctuations. For the empirical mode construction, in contrast to the previous chapters, where a POD analysis was required for the phase averaging, in the present chapter an external forcing signal (loudspeaker voltage) is present and conveniently delivers the phase information.

The physical mode construction follows the scheme presented in Section 2.4. However, since the structures are forced at a discrete frequency and are not self-excited, obviously no calculation of the global mode frequency is required. Instead, the spatial distribution of the global mode can be calculated with the spatial stability analysis and the application of Eqn. 2.33. In the present chapter, the focus of the stability analysis is placed on the effect of mean flow field changes on the growth of vortical structures. In contrast to Chapter 6, the stability analyses of the present chapter are carried out in the inviscid limit. Therefore, preliminary measurements, shown in Fig. 8.3, were carried out to yield the Reynolds number, where the analysis can be regarded as inviscid. It is evident that for  $Re > 5000$  the growth rate and wavenumber only weakly depend on the Reynolds number. Therefore, a fixed Reynolds number of  $Re = 5000$  was chosen for all analyses.

For most of the measurement points, only monographic PIV data containing the axial and radial velocity components are available. For a reference measurement, tangential velocities were also measured using LDV. With this set of data, the influence of tangential velocities on the complex wave number ( $\alpha$ ) of the axisymmetric mode ( $m = 0$ ) was assessed. Two preliminary linear stability analyses were carried out, one incorporating the measured tan-

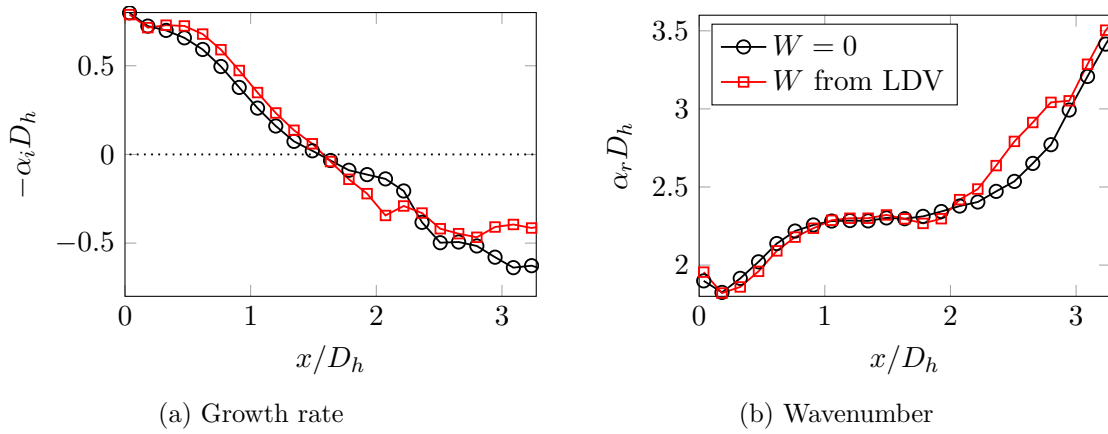


Figure 8.4: Preliminary investigation of the influence of the tangential velocity ( $S = 0.8$ ) on the eigenvalues of the axisymmetric ( $m = 0$ ) mode.

Table 8.1: Operating conditions of the acoustically forced measurements.

Inlet temperature	$T_{\text{in}}$	300 K
Air massflow	$\dot{m}$	150 kg/h
Equivalence ratio	$\phi$	0.7
Reynolds number	Re	35 000
Swirl number	$S$	0.6, 0.8, 1
Forcing frequency	$f_a$	196 Hz
Norm. forcing amplitude	$ u^c /U_0$	0 - 0.7

gential velocities for a swirl number of  $S = 0.8$  and another assuming zero tangential velocity. The results, which are depicted in Fig. 8.4, show that the tangential velocities have very little influence on the growth rate ( $-\alpha_i$ ) and real wave number ( $\alpha_r$ ) of the axisymmetric mode. This confirms the findings of Oberleithner et al. (2014), who found that the axial shear layer dominates the streamwise growth of the axisymmetric ( $m = 0$ ) instability. Thus, for the remainder of this study, the linear stability analyses are carried out omitting the tangential velocity profiles.

Another important simplification in the present calculations is the negligence of the inhomogeneous density field. As it was shown in Chapter 6, the density gradients encountered in swirl-stabilized combustor flows (cold jet – hot wake) should generally have a stabilizing effect on the shear layers. While this affects the appearance of self-excited hydrodynamic instabilities, it can be assumed that the principal relation between shear layer saturation and mean flow correction is still captured by neglecting the density variations. This assumption is supported by the good agreement between the predicted growth rates and the measured flow responses, as will be shown later.

A summary of the investigated operating conditions is provided in Tab. 8.1.

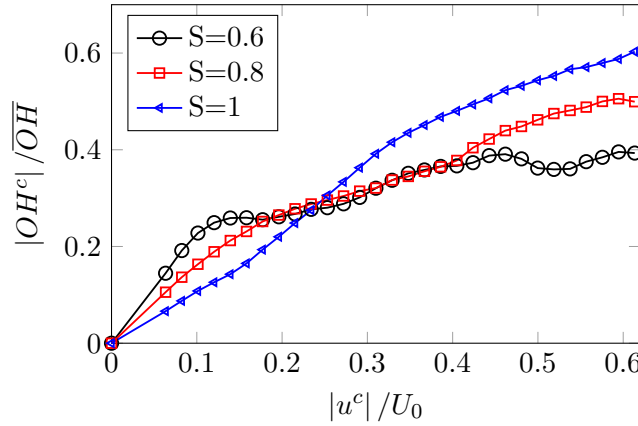


Figure 8.5: Flame response for acoustic forcing at  $f_a = 196$  Hz for three swirl numbers.

### 8.3 Results

In the following, the experimental observations and the results of the analytical modeling are presented. Firstly, the measurements of the flame response to acoustic forcing are shown for three different swirl numbers. Subsequently, the effect of acoustic forcing on the time-averaged flow fields and the flow field dynamics is investigated. Finally, the empirically obtained flow structures are compared to analytical predictions based on linear stability analyses.

#### 8.3.1 Flame Response

Figure 8.5 shows the flame response measured at 196 Hz for the three investigated swirl numbers. All cases reveal a saturation of the flame response at high forcing amplitudes. However, significant differences between the three configurations are visible. For the lowest swirl ( $S = 0.6$ ), the initial gain is the highest, but the gain decreases quickly at moderate forcing intensities ( $|u^c|/U_0 = 0.15$ ), and, as a consequence, the flame response almost stagnates for high forcing amplitudes. At a forcing amplitude of  $|u^c|/U_0 = 0.45$ , the flame response even slightly decreases. This is related to a detachment of the flame due to the strong forcing, as will be shown in the next section.

At the medium swirl number ( $S = 0.8$ ), the initial gain is smaller than for the case of the lower swirl. At intermediate forcing amplitudes ( $|u^c|/U_0 = 0.15$ ), the flame describing function shows a saturation similar to the lowest swirl number. In contrast to the lowest swirl, at higher forcing amplitudes the amplitude of the flame response starts to increase again. This behavior of an intermediate saturation at moderate forcing amplitude has been reported in a number of previous studies (e.g., Balachandran et al., 2005; Schimek et al., 2012b).

For the highest swirl ( $S = 1$ ), the initial gain is the lowest of the three cases. No saturation is encountered at intermediate forcing amplitudes, in contrast to the cases of the lower swirl

numbers. In fact, even a small increase of the gain is observed. A weak saturation can be observed only at very high forcing amplitudes.

### 8.3.2 Time-Averaged Flow Fields and Flame Positions

The time-averaged flow fields and the OH\*-chemiluminescence distributions are presented in Fig. 8.6. The rows correspond to the investigated swirl numbers and the columns correspond to forcing amplitudes, increasing from left to right. All flow fields resemble the typical shape encountered in swirl stabilized combustors, as the swirl number in all cases is high enough to ensure a stable vortex breakdown. Without forcing, the flame stabilizes for all swirl numbers along the inner shear layer between the jet and the IRZ showing a typical V-shape. The isothermal flow field is considerably different to the reacting flow fields. In particular, combustion leads to a wider IRZ and more uniform backflow velocities (for details see Chapter 4).

The basic effects of forcing are similar for all three swirl numbers. The opening angle of the jet is decreased and the region of highest heat release rates is shifted upstream and to smaller radii. Additionally, for the lowest swirl number at a forcing amplitude of  $|u^c|/U_0 = 0.45$ , a sudden change in the flame shape and flow field is observed when the flame, due to the strong forcing, is lifted off and stabilizes further downstream as a detached flame. With increasing swirl, the effect of the forcing on the jet divergence and the heat release distribution is weaker but still remains significant. For comparison purposes, the isothermal flow field at the intermediate swirl number is also shown. It is evident that the influence of the forcing on the isothermal flow field is considerably smaller than for the three reacting flow fields, indicating the importance of the flame on the flow field dynamics.

### 8.3.3 Coherent Structures in the Forced Flow Fields

The acoustic forcing induces fluctuations of the velocity at the combustor inlet, which cause vortical structures in the shear layers. These vortices originate from the area jump from the mixing tube to the combustion chamber and are convected downstream. They can be further amplified or damped in the shear layers. Figure 8.7 shows streamlines of the coherent velocity fluctuations superimposed on the coherent through-plane vorticity fluctuations of the intermediate swirl number ( $S = 0.8$ ) at a forcing amplitude of  $|u^c|/U_0 = 0.3$  for four equidistant phases. The bottom row shows the phase-averaged flow fields superimposed on the phase-averaged OH\*-chemiluminescence images for the same phases. Strong vortices are formed near the combustor inlet in the first phase due to the forcing. These vortices are convected downstream in the shear layers of the jet and are further amplified. The maximum value of the vorticity is reached at an axial position of  $x/D_h \approx 2$ . Further downstream, the vortices are gradually damped. The phase-averaged OH\*-chemiluminescence images show large-scale fluctuations of the heat release.

In order to quantitatively assess the strength of the vortices, the coherent fluctuation amplitude for every point in the measured flow field plane is obtained from the phase-averaged

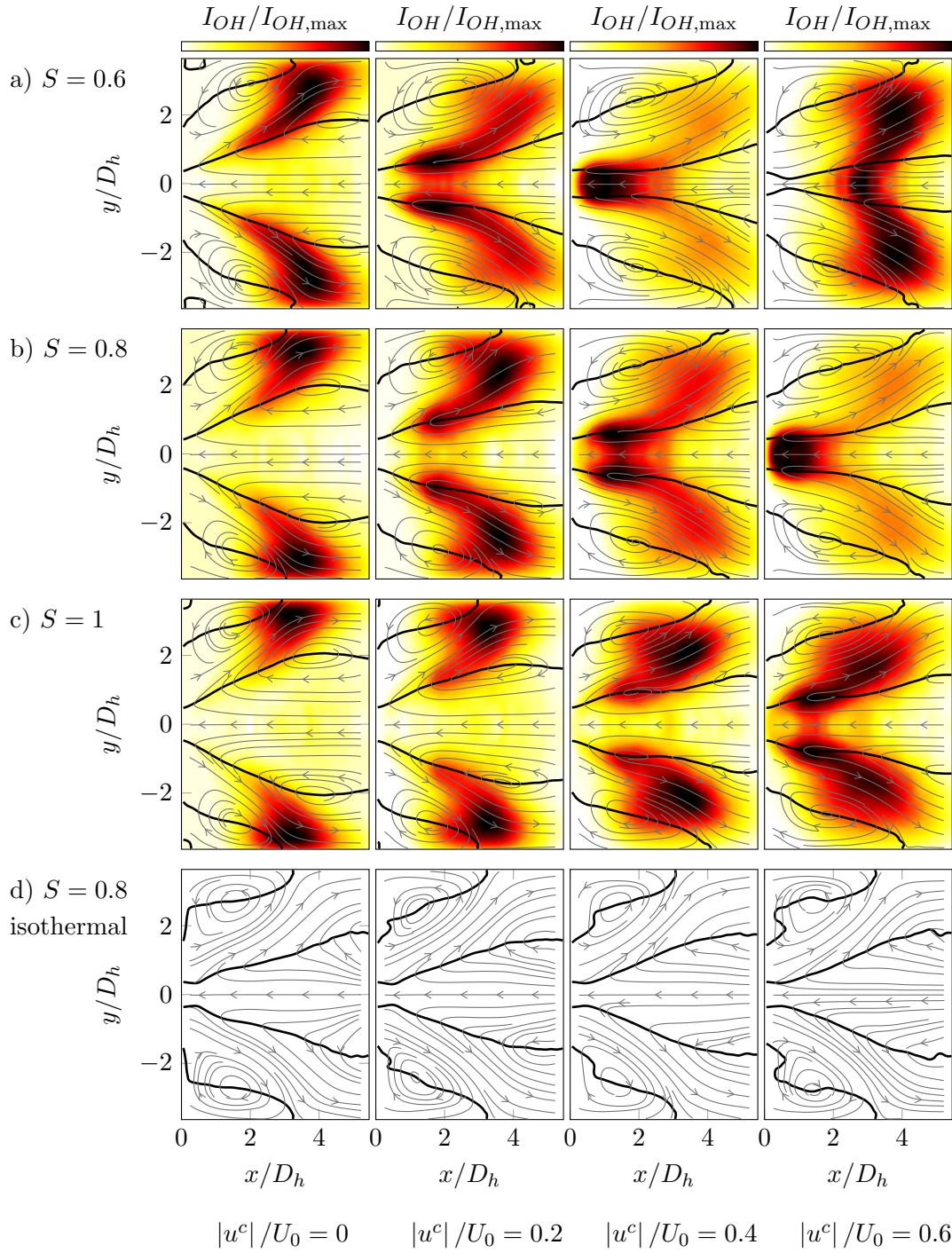


Figure 8.6: Time-averaged flow field superimposed on the normalized OH\*-chemiluminescence distribution at increasing forcing amplitude. Thick lines indicate zero axial velocity. a)  $S = 0.6$ , b)  $S = 0.8$ , c)  $S = 1$ , d)  $S = 0.8$  isothermal.

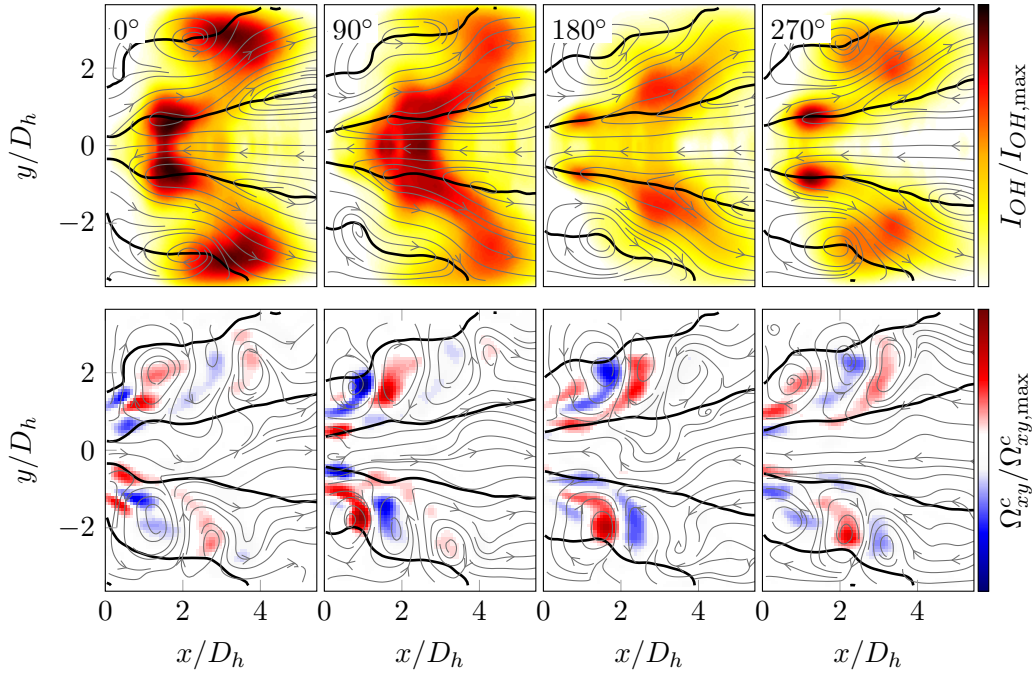


Figure 8.7: Phase-averaged flow fields and flame positions at four equidistant phase angles ( $S = 0.8$ ,  $|u^c|/U_0 = 0.3$ ). First row: Normalized phase-averaged Abel-deconvoluted OH\*-chemiluminescence distribution ( $I_{OH}/I_{OH,max}$ ) and superimposed phase-averaged velocity streamlines. Second row: Streamlines of the coherent velocity fluctuations superimposed on the normalized coherent through-plane vorticity ( $\Omega_{xy}^c$ ). Thick lines indicate zero phase-averaged axial velocity.

measurements. Subsequently, the coherent fluctuation intensity is integrated along radial profiles for all axial positions and normalized with respect to the volume flow at the combustor inlet  $\dot{V}$ .

$$K(x) = \frac{1}{\dot{V}} \int_0^{D/2} \sqrt{0.5 (\hat{u}^c(x, r)^2 + \hat{v}^c(x, r)^2)} 2\pi r dr \quad (8.1)$$

The streamwise development of the coherent fluctuation intensity  $K$  is shown for exemplarily chosen forcing amplitudes in Fig. 8.8. Up to a certain streamwise location,  $K$  is considerably amplified and subsequently decays. It is evident that for higher forcing amplitudes, the maximum coherent fluctuation intensity  $K_{max}$  is reached further upstream and the maximum amplification ( $K_{max}/K(x=0)$ ) is considerably reduced, thus, indicating a saturation of the amplification of the vortices in the shear layers.

This saturation becomes evident when the maximum coherent fluctuation intensity  $K_{max}$  is plotted over the forcing amplitude, as shown in Fig. 8.9 for the three measured swirl numbers. After an initial linear increase, all curves show a considerably flattening that corresponds to the saturation.

A comparison of the maximum coherent fluctuation intensity (Fig. 8.9) to the measured integral heat release fluctuation (Fig. 8.5) shows that both quantities show very similar trends.



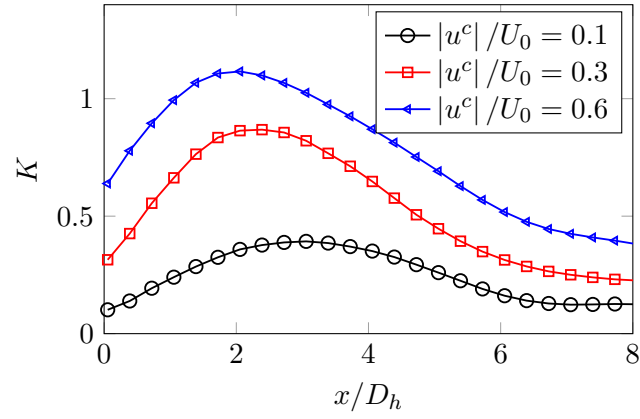


Figure 8.8: Streamwise development of the coherent fluctuation intensity  $K(x)$  at  $S = 0.8$  for three acoustic forcing amplitudes.

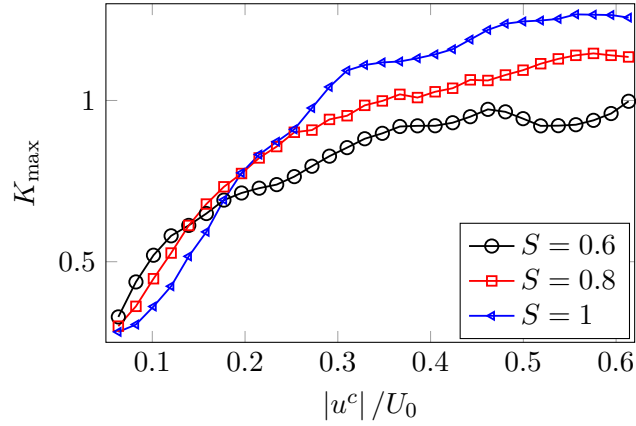
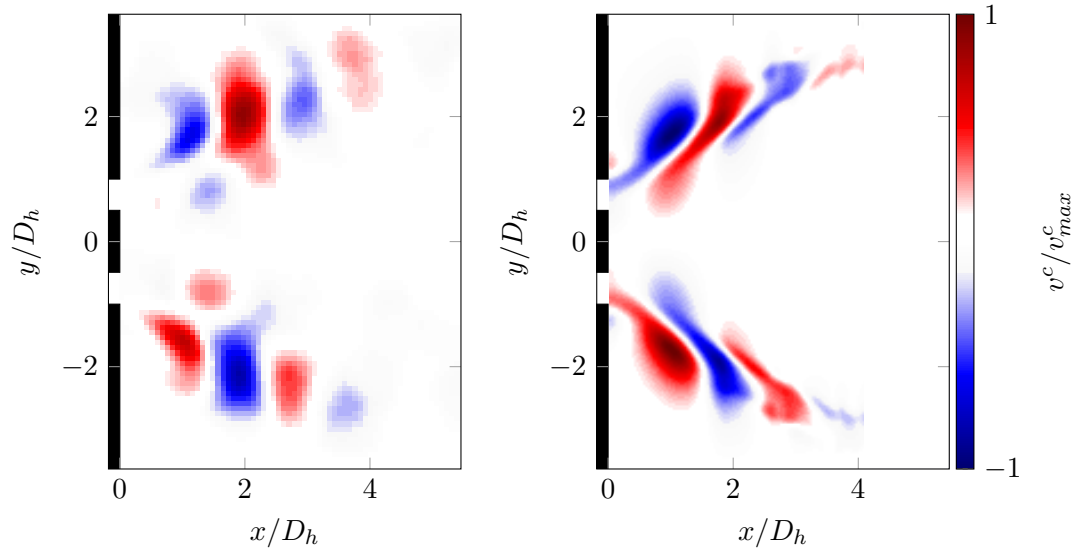


Figure 8.9: Maximum coherent fluctuation intensity  $K_{\max}$  at increasing forcing amplitudes for three different swirl numbers.

A comparison of the different swirl numbers yields the highest linear amplification of the coherent fluctuation intensity for the lowest swirl number and the strongest saturation at higher forcing amplitudes. This trend holds for the coherent fluctuation intensity and for the heat release fluctuations. The good similarity between both quantities demonstrates that the velocity fluctuations are an important mechanism for heat release fluctuations in perfectly premixed flames. Furthermore, the maximum coherent fluctuation intensity and the flame response show a slight decrease for the lowest swirl number at  $u'/u_0 = 0.45$ . This is the amplitude where the flame detaches (see Fig. 8.6). A transfer function from the hydrodynamic fluctuations to the heat release fluctuations would be necessary in order to quantitatively relate the saturation of the vortices to the saturation of the flame describing function. However, this is beyond the scope of this thesis.





(a) Empirical mode construction from phase averaging

(b) Physical mod constructions from LSA

Figure 8.10: Empirical and physical construction of the coherent radial velocity component ( $S = 0.8$  and  $|u^c|/U_0 = 0.1$ ).

### 8.3.4 Linear Stability Analysis

The vortex amplification saturates stronger for the cases, where also the mean flow field modifications due to the forcing are more pronounced. This empirically indicates the important role of the saturation mechanism via the mean flow correction as shown in Fig. 8.2. In order to further investigate this mechanism, the influence of the mean flow field on the growth rate of shear flow instabilities is investigated analytically by the application of linear hydrodynamic stability analysis on the time-averaged forced flow fields. The flow field is sliced into radial profiles, which are assumed to represent a fictitious parallel flow. For every profile the spatial analysis yields a complex wavenumber  $\alpha$  and an eigenmode for a given real (forcing) frequency  $\omega$ . The coherent velocity fluctuations are constructed subsequently, using Eqn. 2.33. In Fig. 8.10, the constructed coherent radial velocity fluctuations from the stability analysis are compared to the empirically obtained coherent fluctuations from the triple decomposition. Both velocity fields show the same wave pattern with similar wavelengths, but the stability analysis slightly overestimates the radial velocities in the inner shear layer. In particular, the differences close to the inlet can be attributed to the inlet conditions. In the experiments, the jet bulk velocity is actuated. The analysis, in contrast to that, predicts the most amplified eigenmode. Another reason for the difference between the analysis and the experiment is assumed to be the strong non-parallelity of the flow field. Nevertheless, the stability analysis seems to reasonably capture the essential structure of the coherent velocity fluctuations and, most importantly, the streamwise growth rates and decay.

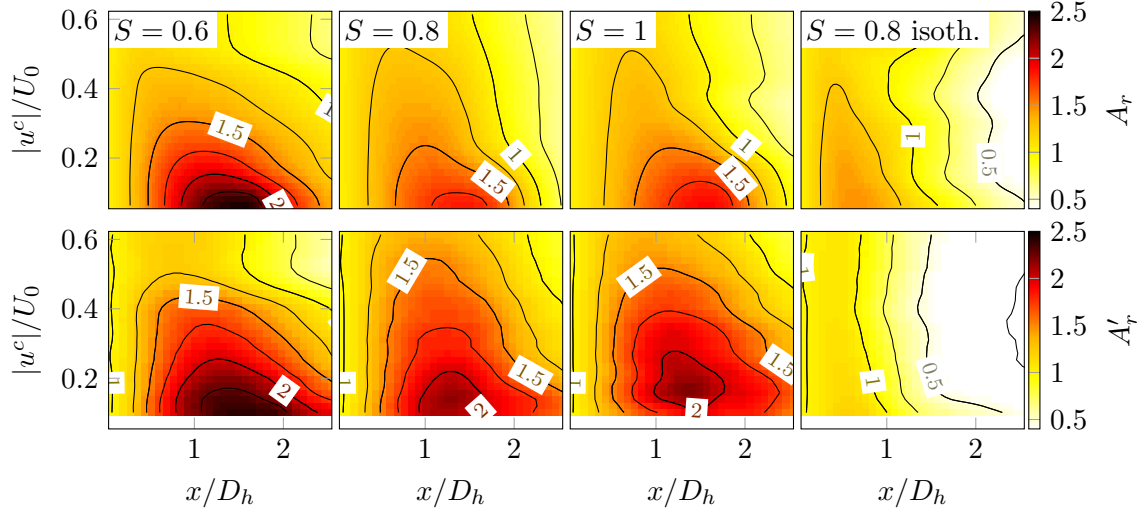


Figure 8.11: Comparison of predicted to empirically obtained amplitude ratios. First row: Amplitude ratio  $A_r(x)$  of the  $m = 0$  mode from stability analysis. Second row: Modified amplitude ratio  $A'_r(x)$  from the triple decomposition.

The application of the linear stability theory to the time-averaged flow fields at increasing forcing amplitudes yields the axial distributions of the complex axial wave numbers  $(-\alpha D_h)$ . An integration of  $\alpha$  in the streamwise direction yields the amplitude ratio

$$A_r(x) = \Re \left[ e^{i \left( \int_0^x \alpha(\xi) d\xi \right)} \right], \quad (8.2)$$

which is defined as the ratio of the amplitude of the instability at an axial location  $x$  to the amplitude at the combustor inlet ( $x = 0$ ). It is shown in the top row of Fig. 8.11 for the three measured reacting cases and the isothermal case. By definition, the amplitude ratio at the combustor inlet is  $A_r(x = 0) = 1$ . The amplification of the vortices in the shear layers leads to increasing amplitude ratios  $A_r(x)$  with downstream locations up to the maximum amplification, downstream of which the vortices are damped and  $A_r(x)$  decreases again.

The damping related to the changes in the mean flow field is evident for all three reacting cases. At higher forcing amplitudes ( $|u^c|/U_0$ ), the maximum amplitude ratio is significantly lower and the axial location, where it is reached, is shifted upstream. Furthermore, differences between the different swirl numbers can be observed. The lowest swirl number shows the highest amplification at low forcing amplitudes and the strongest saturation. The higher swirl numbers show a weaker initial amplification but also a weaker saturation. This is in line with the findings that the mean flow field changes more drastically for the low swirl number than for the higher swirl numbers, as shown in Fig. 8.6. In contrast to the reacting cases, the analysis predicts very low amplitude ratios and a very weak saturation for the isothermal case.

For the comparison of the calculated amplitude ratio  $A_r(x)$  with the empirically obtained growth of the coherent velocity fluctuations, a slightly different definition to Eqn. 8.1 is used.

The growth rate  $-\alpha_i D_h$ , as obtained from the linear stability analysis, does not account for the displacement of the vortices to higher radii for higher axial positions due to the divergence of the jet. For the comparison of the measured flow response to the analytic results, this effect is removed by using a modified normalized coherent fluctuation intensity  $K'(x)$ . It accounts for the spreading of the jet by dividing  $K(x)$  by the radius  $r_p(x)$  of the peak axial velocity

$$K'(x) = \frac{1}{r_p(x)U_0 D_h} \int_0^{D/2} \sqrt{0.5(\hat{u}^c(x, r)^2 + \hat{v}^c(x, r)^2)} 2\pi r dr. \quad (8.3)$$

An empirical equivalent to the amplitude ratio  $A_r(x)$  from the stability analysis is obtained from the modified normalized coherent fluctuation intensity  $K'(x)$ . It is defined as the ratio of the modified normalized coherent fluctuation intensity  $K'(x)$  at an axial position to the modified normalized coherent fluctuation intensity  $K'(0)$  at the combustor inlet, yielding

$$A'_r(x) = \frac{K'(x)}{K'(x=0)}. \quad (8.4)$$

For comparison purposes, the distribution of the empirical amplitude ratio  $A'_r(x)$  is shown for the three reacting cases and the isothermal case in the bottom row of Fig. 8.11. The empirical amplitude ratio  $A'_r(x)$  shows essentially the same trends as the theoretically obtained amplitude ratio  $A_r(x)$ . The axial location of the maximum amplification and the maximal amplitude ratio are very similar. The significantly lower amplification and weaker saturation of the isothermal case predicted by the stability analysis is confirmed by the empirically obtained amplitude ratio.

Overall, a very good agreement between the theoretically obtained amplitude ratio  $A_r(x)$  and the empirically obtained amplitude ratio  $A'_r(x)$  is evident. This shows that the stability analysis carried out on the time-averaged forced flow fields is able to capture the most important saturation mechanisms. Since the stability analysis is carried out using solely the time-averaged flow fields, this is a strong indication that the saturation of the vortices is caused by the mean flow field correction. The deviations of the experimental results to the predictions from the stability analysis can be mainly attributed to the simplifications made for the linear stability analysis (e.g., small amplitude fluctuations and parallel flow).

## 8.4 Conclusions

Measurements of the amplitude dependent flame response of a perfectly premixed swirl-stabilized combustor at 196 Hz have been carried out using the multi-microphone-method and OH\*-chemiluminescence imaging for three different swirl numbers. All cases showed a saturation of the flame response at high forcing amplitudes. However, the linear gain, the onset of the saturation, and the flame response at high forcing amplitudes differ significantly. The effect of the swirl number on the flame response was found to be different for low and high forcing amplitudes. The lowest swirl number showed the highest initial gain but the strongest saturation and, consequently, the lowest flame response at high forcing amplitudes.

The highest swirl number showed the lowest gain at low forcing amplitudes, but the saturation at high forcing amplitudes was much weaker.

The amplitude-dependent flow fields of the three reacting cases and an isothermal case were measured using high-speed particle image velocimetry. The measurements revealed that for the reacting cases, the forcing led to significant changes in the flow field, which came along with changes in the flame shape. Forcing generally led to smaller jet opening angles with the zone of maximum heat release located more upstream and closer to the centerline. The effects are more pronounced for the smaller swirl numbers. Furthermore, for the smallest swirl number, the flame is lifted off at high forcing amplitudes and stabilized farther downstream. The detachment of the flame causes a decrease of the flame response and, thus, acts as an additional saturation mechanism. The isothermal case did not show a significant influence of the forcing on the time-averaged flow fields, in contrast to the reacting flow fields.

The distribution of the coherent fluctuation intensity for the three cases at increasing forcing amplitudes was obtained from phase-averaged measurement data and compared to the flame response. A good qualitative agreement could be observed. In particular, the different saturation types of the three reacting cases were captured very well in the amplitude dependent coherent fluctuation intensity distribution. The results clearly demonstrate that the saturation mechanism of the hydrodynamic field is an important driver for the saturation of the flame response.

The saturation of the coherent fluctuation intensity is strongly connected to changes in the time-averaged flow field, as demonstrated employing hydrodynamic linear stability analysis to the time-averaged flow fields at the different forcing amplitudes. The results of the stability analysis successfully predict the saturation of the shear layers at intermediate and high forcing amplitudes. Also, the different saturation characteristics of the reacting flow fields and the isothermal flow field could be reconstructed using solely the time-averaged flow fields.

The results of this chapter emphasize the role of the shear layer amplification and saturation for the flame response at low, intermediate, and high forcing amplitudes. With the application of linear stability theory on the mean flow fields, it was shown that changes in the mean flow field are of utmost importance for the saturation of the shear layers, and thus, for the saturation of the flame describing function.

The established link between the hydrodynamic field and the flame response can be used in future works for the prediction of limit-cycle amplitudes of thermoacoustic instabilities in gas turbine engines. For now, the stability analysis provides analytic insights into the flow dynamics at limit-cycle conditions. Once the link between the saturation of coherent structures, mean flow field correction, and the nonlinear flame dynamics is understood and modeled, one will be able to predict the limit-cycle amplitude based on the stable non-oscillating mean flow.

## Chapter 9

# Interaction of Axisymmetric Coherent Structures with the PVC

*In the present chapter the excitation and suppression of the PVC by acoustically forced axisymmetric coherent structures is investigated in a swirl-stabilized combustor. Two flow fields with a naturally excited PVC (isothermal case and detached flame) and one flow field with no naturally excited PVC (attached V-flame) were considered. With acoustic forcing, the natural PVC is gradually attenuated and finally suppressed. In contrast to this, the initially stable flow field of the attached V-flame is destabilized by the acoustic forcing and features a PVC at high forcing amplitudes. A spectral analysis yields antisymmetric velocity fluctuations at various interaction frequencies of the self-excited PVC and the acoustic forcing frequencies. It is shown that the basic behavior of the PVC can be modeled by a parametrically excited nonlinear Van der Pol oscillator. Both the damping of the PVC and the occurrence of the spectral peaks are reproduced with this simple model. The modeling assumptions are further supported employing linear hydrodynamic stability analysis. Furthermore, the analysis reveals that the excitation of the PVC in a previously stable flow is caused by mean flow field changes induced by the acoustic forcing. The applied models allow for the explanation of the frequently observed suppression of the PVC and the newly observed excitation of the PVC.*

### 9.1 Introduction

In the present chapter, the interaction of the self-excited helical coherent structure, the PVC, and forced axisymmetric coherent structures is investigated. In gas turbine combustors, both types of coherent structures occur at the same time when the flow field is hydrodynamically unstable (helical mode) and the combustion system is thermoacoustically unstable (axisymmetric mode). Despite the large importance of both flow instabilities, only limited knowledge is available about the interaction of both structures. In previous studies, the focus was placed

on the suppression of the helical mode by the symmetric mode. Paschereit et al. (2000) found that low amplitude acoustic forcing at the frequency of the helical instability leads to a suppression of the helical mode in a reacting swirl-stabilized combustor. Iudiciani and Duwig (2011) conducted reacting LES simulations and found the acoustic forcing to damp or suppress the PVC (depending on the forcing amplitude), when the forcing was applied at lower frequencies than the natural helical frequency. In contrast to this, forcing at higher frequencies led to an increase of the amplitude of the helical instability. The higher damping efficiency of low frequency forcing has been observed already in earlier experimental isothermal studies by Khalil et al. (2006) and Lacarelle et al. (2009). Khalil et al. (2006) found that the natural instability (PVC) was only suppressed if the forcing frequency was lower than half the natural frequency. In a recent reacting experimental study, Moeck et al. (2012) successfully suppressed the natural helical instability with acoustic forcing at a lower frequency than the natural frequency. However, they did not report of results of forcing at a higher frequency and at similar excitation amplitudes.

Different mechanisms for the damping of the helical instability due to acoustic forcing have been proposed. Iudiciani and Duwig (2011) suggested that the low frequency forcing leads to a periodic variation of the frequency of the helical mode and, thus, to a broadening and lowering of the peak. The damping was also suggested to depend on a sufficient growth of the acoustically induced perturbation upstream of the wavemaker of the helical mode and to nonlinear interference of both modes (Moeck et al., 2012). This general mode interaction mechanism was described analytically by Pier (2003). Lastly, the damping may also be related to changes of the mean flow field by the forcing, as observed by Khalil et al. (2006); Lacarelle et al. (2009); Iudiciani and Duwig (2011) and also in Chapter 8 of this thesis. This assumption can be made plausible by recalling the results of Chapter 6. The excitation of the PVC could be predicted considering solely the time-averaged flow field and density field. Acoustic forcing can change the time-averaged flow field, and this *new* flow field is then suggested to be no longer globally unstable to the first helical mode. Oberleithner et al. (2012b) showed the suppression of the PVC via this mechanism for an isothermal unconfined swirling jet. They acoustically forced the jet with a double helical structure and observed a reduction of the recirculation zone size. Employing linear stability theory, they showed that the forced flow field was no longer globally unstable and no PVC was self-excited. An excellent agreement between the analytical predictions and the experiments was found.

Besides the suppression of the PVC by acoustic forcing, also signs of the dynamic interaction of the PVC and the forced coherent structures were observed. Steinberg et al. (2010) observed flow field fluctuations at exactly the difference of the PVC frequency and the frequency of a self-excited thermoacoustic oscillation. They also found a periodic deformation of the PVC structure at the acoustic frequency (Steinberg et al., 2011). Moeck et al. (2012) confirmed the occurrence of flame and flow field oscillations at linear combinations of the PVC frequency and the frequency of acoustic forcing. In the reacting cases, the oscillation amplitude associated with the interaction frequency was reported to be larger for the heat release rate than for the flow field. They explained this findings with a second-order analysis of the G-equation and

showed a nonlinear coupling between flow field and heat release. However, they also found strong oscillations at the interaction frequencies at non-reacting conditions, which cannot be explained by the flow field-flame coupling.

All previously mentioned studies reported of flows, where a PVC was present in the unforced case. This naturally excited helical instability could be damped or suppressed by the forcing. In strong contrast to that, Giauque et al. (2005) observed in their LES simulation an excitation of the PVC in a naturally stable flow by axial forcing. However, the excitation of the PVC was not validated by experiments and no explanation of the excitation was provided.

In the remainder of this chapter, both the damping and the excitation of the helical structure by acoustic forcing are experimentally and analytically investigated. Two flow fields with a naturally excited helical instability (isothermal case and detached flame) and one flow field with no naturally excited helical instability (attached V-flame) were acoustically forced at two different frequencies and various forcing amplitudes. The structure of the PVC at forced and unforced conditions is subsequently analyzed using frequency spectra and POD. The application of linear hydrodynamic stability theory on the measured mean flow fields provides evidence that the excitation of a PVC due to axial forcing is caused by mean flow field changes induced by the forcing, whereas the suppression of the PVC is not caused solely by changes to the mean flow field. In the next step, it is shown that the oscillation of the PVC at axially forced conditions features a significant analogy to a parametrically forced nonlinear oscillator. Finally, the dynamics of this oscillator are exploited to further explain the experimental findings of this chapter and to provide a generalized explanation for the findings of previous studies.

## 9.2 Experimental and Analytical Procedure

The experiments were carried out in the atmospheric combustor test rig for high-amplitude acoustic forcing, as shown in Fig. 3.4b. The swirl-stabilized combustor, as shown in Figs. 3.1 and 3.2a was used with a centerbody size of  $D_{cb} = 27.5$  mm, resulting in a hydraulic diameter  $D_h = 27.5$  mm. The swirl number was set to a fixed theoretical value of  $S = 0.6$ . In order to suppress self-excited thermoacoustic instabilities, an area contraction with a ratio of 8:1 was applied downstream of the exhaust tube. At the investigated reacting conditions, no upstream effect of the orifice on the combustor flow field was present, whereas at non-reacting conditions the constriction had to be removed (see Appendix A). The combustor was operated in premixed mode, where the fuel (natural gas) was mixed with the air flow well upstream of the combustor and the loudspeakers to assure a homogeneous fuel-air mixture, even at strong forcing amplitudes.

The two-dimensional velocity field in the streamwise plane aligned with the combustor axis was measured using high-speed PIV, as described in Section 3.3.1. Spatial heat release distributions were measured by the OH\*-chemiluminescence distributions, as described in Section 3.3.3. For the present study, the PIV system and the OH\*-chemiluminescence imaging operated at a frequency of 1.01 kHz. During the measurements, over a time span of 15 s,

Table 9.1: Operating conditions of the combustor and the forcing apparatus.

Inlet temperature	$T_{\text{in}}$	300 K
Air mass flow	$\dot{m}$	150 kg/h
Equivalence ratio	$\phi$	0; 0.6; 0.7
Reynolds number	Re	35 000
Swirl number	$S$	0.6
Forcing frequency	$f_a$	110 and 158 Hz
Norm. forcing amplitude	$ u^c /U_0$	0 - 1.23

the forcing amplitude was increased in 15 steps from no forcing to the maximum forcing amplitude. At each forcing amplitude, 1000 samples were recorded. These data describe a nearly continuous increase of the forcing amplitude. The forcing amplitude derived from the PIV results. A summary of the investigated operating conditions can be found in Tab. 9.1.

For the analysis of the experimental results, the concept of symmetric and antisymmetric spectra, as described in Section 2.5, is employed. The symmetric spectra are obtained by spatially averaging the instantaneous velocity field with respect to the combustor axis prior to the calculation of the spectra. Analogously, the antisymmetric spectra were obtained by calculating the spectra of the instantaneous flow fields, where the top half is subtracted from the lower half, thereby, eliminating all symmetric fluctuations.

The spatial shapes of the coherent structures related to the peaks in the spectra are obtained by means of POD, as described in Section 2.3. Similar to the spectra, the POD is carried out on the antisymmetric and symmetric fluctuations only, yielding the antisymmetric (self-excited) and symmetric (forced) structures, respectively.

Lastly, the impact of changes to the flow field on the excitation of the PVC is investigated employing linear stability analysis, as described in Section 2.4 and demonstrated in Chapter 6. An additional challenge in the present chapter is that for the PIV measurements only one high-speed camera was available. Thus, only the axial and radial velocity components were resolved. In order to carry out stability analyses, some assumptions regarding the tangential component have to be made. For the unforced isothermal case, a velocity profile from non-reacting water tunnel measurements (Strangfeld et al., 2011) is used. This is valid since the similarity between the flow field in water and in air is very high (Terhaar et al., 2011). As it is depicted in Fig. 9.1 for a slightly larger centerbody size ( $D_{cb} = 35$  mm), the tangential velocity component is only weakly influenced by combustion, as long as the flame remains detached. If the reacting flow features the shape corresponding to the attached V-flame, the influence of combustion on the tangential velocity profile is very large. Thus, for the detached flame case, the same tangential velocity profile measured at isothermal conditions is used for the stability analysis, whereas for the analysis of the attached V-flame, tangential velocities measured at reacting conditions, but without forcing, are employed.

In the previous chapters either self-excited or forced coherent structures were investigated. Therefore, the classical triple decomposition into the time-averaged mean, the coherent fluctuations, and the stochastic fluctuations was sufficient. Here, the coherent part  $\mathbf{v}^{c,ha}$  depends



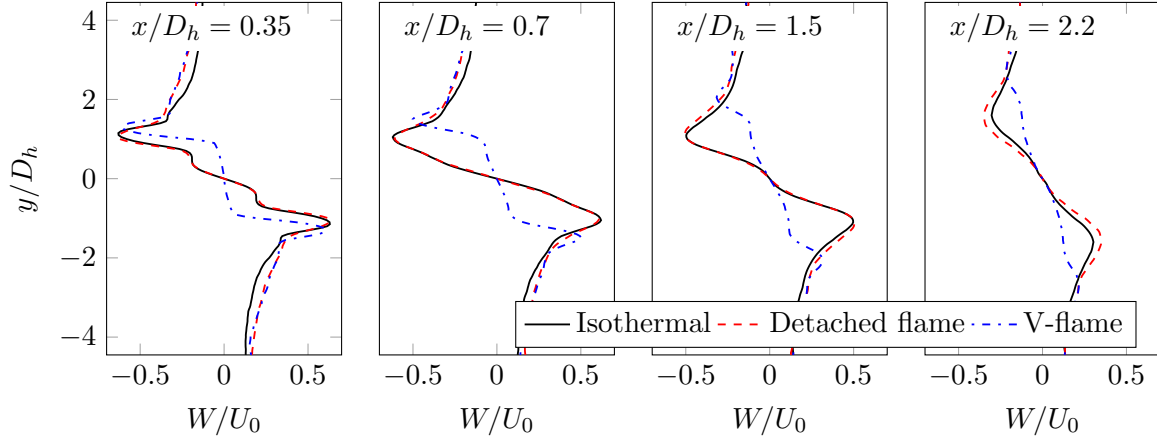


Figure 9.1: Comparison of the tangential velocity component for the isothermal case, the detached flame, and the V-flame. Operating conditions are provided in Tab.4.2.

on the phase of the PVC ( $\theta$ ) and on the forcing phase ( $\Psi$ )

$$\mathbf{v}(\mathbf{x}, t) = \mathbf{V}(\mathbf{x}) + \mathbf{v}^{c,ha}(\mathbf{x}, \theta(t), \Psi(t)) + \mathbf{v}^s(\mathbf{x}, t). \quad (9.1)$$

The phase with respect to the PVC oscillation ( $\theta$ ) is obtained from a POD analysis using Eqn.2.38 and the phase with respect to the forcing cycle ( $\Psi$ ) is extracted from the time traces of the excitation signal. Subsequently, the doubly phase-resolved velocity fluctuations are obtained as

$$\mathbf{v}^{c,ha}(\mathbf{x}, \theta, \Psi) = \frac{1}{N_1 \cdot N_2} \sum_{n_1=0}^{N_1-1} \sum_{n_2=0}^{N_2-1} \mathbf{v}(\mathbf{x}, \theta + 2\pi n_1, \Psi + 2\pi n_2) - \mathbf{V}(\mathbf{x}). \quad (9.2)$$

The coherent fluctuations, resolved with respect to the acoustic forcing phase only, are defined as

$$\mathbf{v}^{c,a}(\mathbf{x}, \Psi) = \frac{1}{2\pi} \int_0^{2\pi} \mathbf{v}^{c,ha}(\mathbf{x}, \theta, \Psi) d\theta. \quad (9.3)$$

Analog to this, the coherent fluctuations, resolved with respect to the helical PVC phase only, are defined as

$$\mathbf{v}^{c,h}(\mathbf{x}, \theta) = \frac{1}{2\pi} \int_0^{2\pi} \mathbf{v}^{c,ha}(\mathbf{x}, \theta, \Psi) d\Psi. \quad (9.4)$$

## 9.3 Experimental Observations

The results of the unforced and forced flow fields will be presented in the following for the three investigated combustor operating conditions.

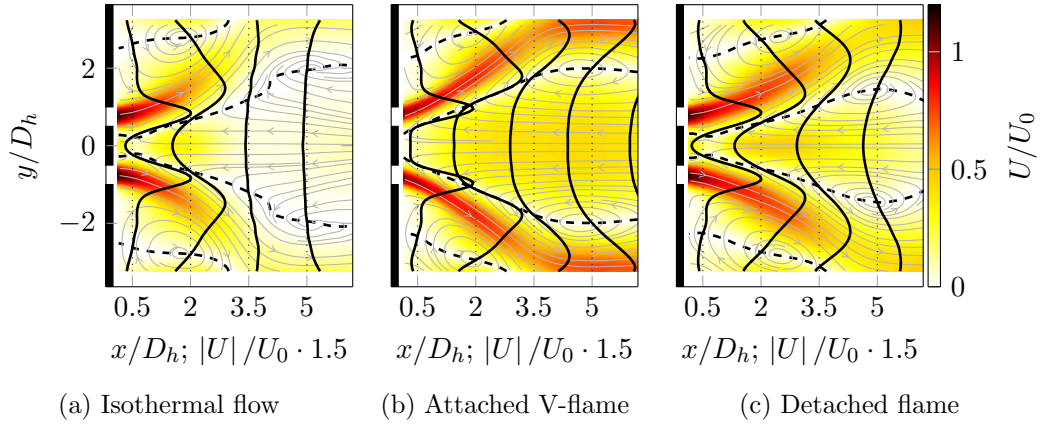


Figure 9.2: Streamlines of the time-averaged flow fields without forcing are superimposed on the normalized axial velocity magnitude. At four axial locations, radial profiles of the normalized axial velocity are extracted. Dashed lines indicate zero axial velocity.

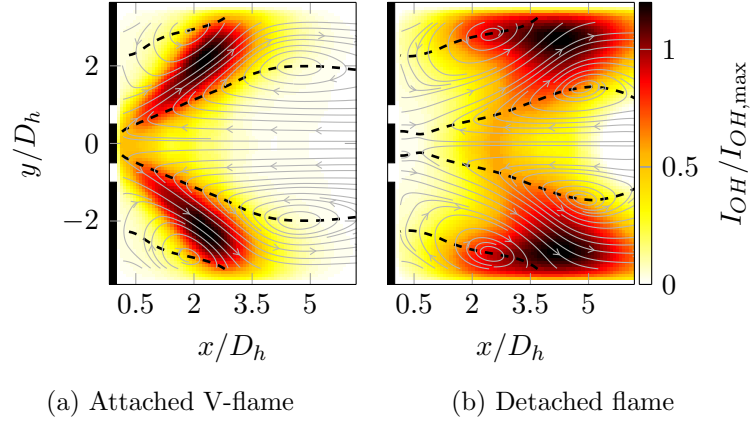


Figure 9.3: Streamlines of the unforced time-averaged flow field are superimposed on the normalized Abel-deconvoluted OH\*-chemiluminescence intensity. Dashed lines indicate zero axial velocity.

### 9.3.1 Time-Averaged Flow Fields and Flow Field Dynamics without Acoustic Forcing

Figures 9.2 and 9.3 show the time-averaged flow fields encountered in the absence of acoustic forcing for the isothermal case, the detached flame, and the attached V-flame. The flow fields resemble very well the features observed in Chapter 4 for the different flame shapes. Despite the higher velocities caused by the dilatation in the reacting case, the isothermal flow field and the flow field of the detached flame correspond well. The strong increase of the jet divergence is the most remarkable difference between the attached flame and the detached and isothermal case. In Chapter 4 it was shown for the same combustor geometry with a slightly larger centerbody that the isothermal flow field features a strong PVC. In the case of detached flames, the PVC remained very similar to the isothermal case, and in attached

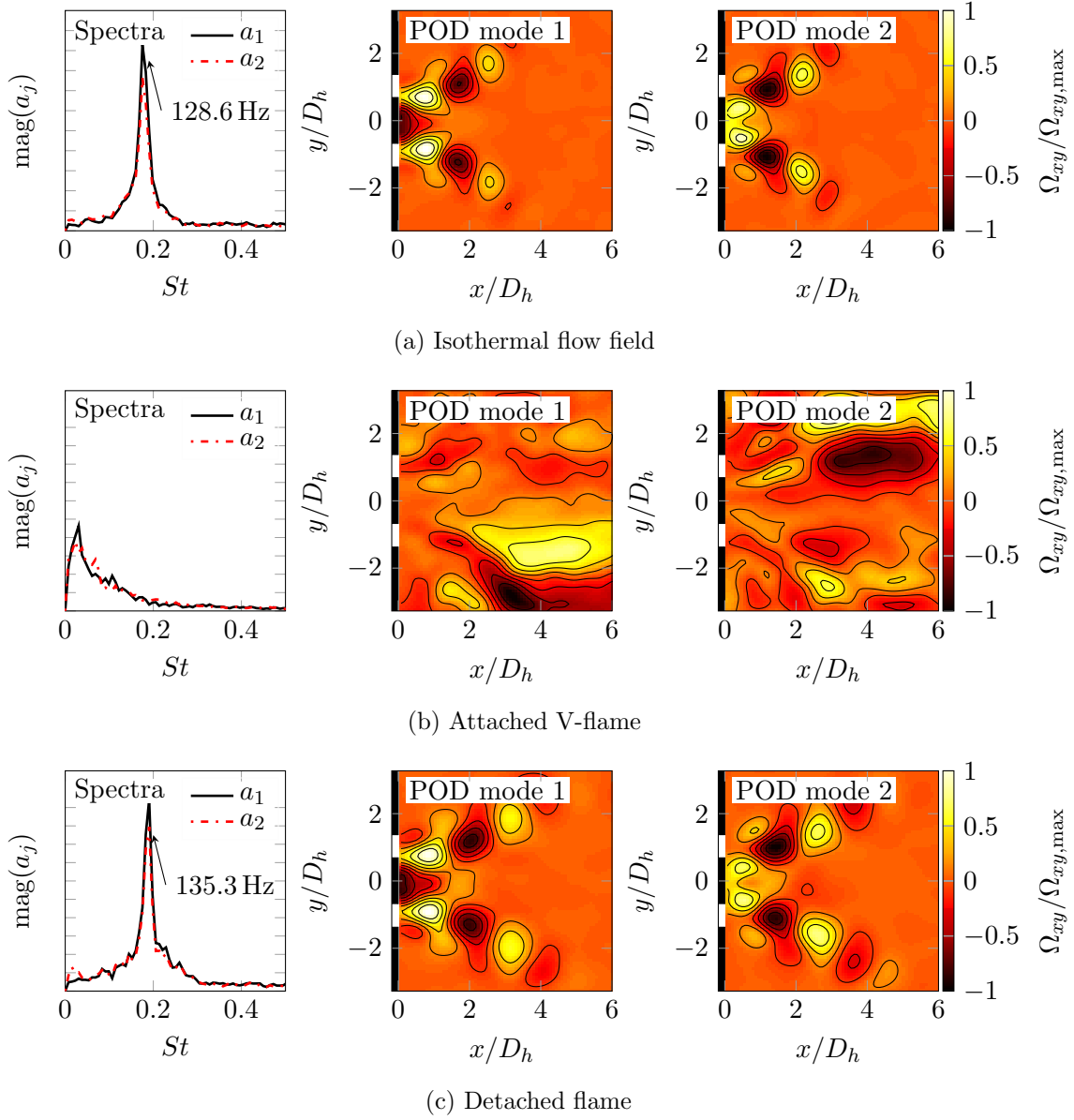


Figure 9.4: Results of the POD analysis of the isothermal flow, the detached flame, and the attached V-flame without acoustic forcing. Left column: Power spectra of the first two temporal POD coefficients. Middle and right columns: Normalized through-plane vorticity  $\Omega_{xy}$  of the first two spatial POD modes.

V-flame cases, it was completely suppressed. The same results are obtained from a POD analysis of the presently investigated unforced flow fields and are briefly presented here for the sake of completeness.

The two most energetic modes of the isothermal flow field in the absence of forcing, as can be seen in Fig 9.4a, show the same pattern of alternating vortices in the shear layers, as depicted in Fig. 4.6, and the spectra show a clear peak at a Strouhal number of  $St = 0.177$ ,

corresponding to a frequency of 128.6 Hz. Hence, it is concluded that the isothermal flow field without forcing features a strong PVC. Its Strouhal number is considerably higher compared to the results presented in Chapter 4. This stems mostly from the definition of the Strouhal number, including the larger hydraulic diameter  $D_h$  and the lower combustor inlet bulk velocity  $U_0$  at the same mass flow rate.

For the attached V-flame case (Fig 9.4b), the POD analysis shows no signs of the PVC. The two most energetic modes indicate slow large-scale movements of the shear layers that are neither axisymmetric nor antisymmetric. In agreement with Chapter 4, the analysis suggests that in the V-flame case no PVC is present.

The results of the detached flame (Fig 9.4c) resemble very well the findings of Chapter 4. The PVC is similar to the isothermal case in terms of frequency and spatial shape. Solely, the axial extent is slightly increased.

### 9.3.2 Time-Averaged Flow Fields with Acoustic Forcing

In Fig. 9.5 the time-averaged flow fields of the isothermal flow, the V-flame, and the detached flame are shown for forcing at a frequency of  $f_a = 110$  Hz and at forcing amplitudes ranging from  $|u^c|/U_0 = 0$  to 1.25. Even though the focus of this chapter is placed on the flow field dynamics and the influence of acoustic forcing on the PVC, the time-averaged flow fields were identified as the determining factor for the self-excitation of the PVC (Chapter 4) and the amplification of the forced structures (Chapter 8). Thus, a close inspection of the time-averaged flow field is vital for the conclusions drawn in the remainder of this chapter.

The effect of forcing on the attached V-flame (Fig. 9.5b) is very similar to the cases presented in Chapter 8. The most striking effect of acoustic forcing on the flow field is a significant reduction of the width of the IRZ. The flame angle follows the opening angle of the jet and the flame is shifted upstream until the maximum heat release is located directly downstream of the centerbody. At high forcing amplitudes, the flow field and the flame shape show a remarkable similarity to the flow field of the trumpet flame in the unforced, steam-diluted case (compare Fig. 4.4b). Furthermore, the profiles of the normalized axial velocity clearly show that the backflow velocities close to the combustor inlet in the IRZ are significantly increased by the forcing.

The time-averaged isothermal flow field, as shown in Fig. 9.5a, is less affected by the acoustic forcing, than the flow field of the V-flame. The jet opening angle remains very similar even for very strong forcing. An increase of the back flow velocities can be observed in the axial velocity profiles, but it is much smaller compared to the attached V-flame. The influence of acoustic forcing on the flow field of the detached flame is comparable to the isothermal case. The jet divergence remains constant and the backflow intensity is slightly increased. The heat release distribution of the detached flame is only weakly affected by the forcing.

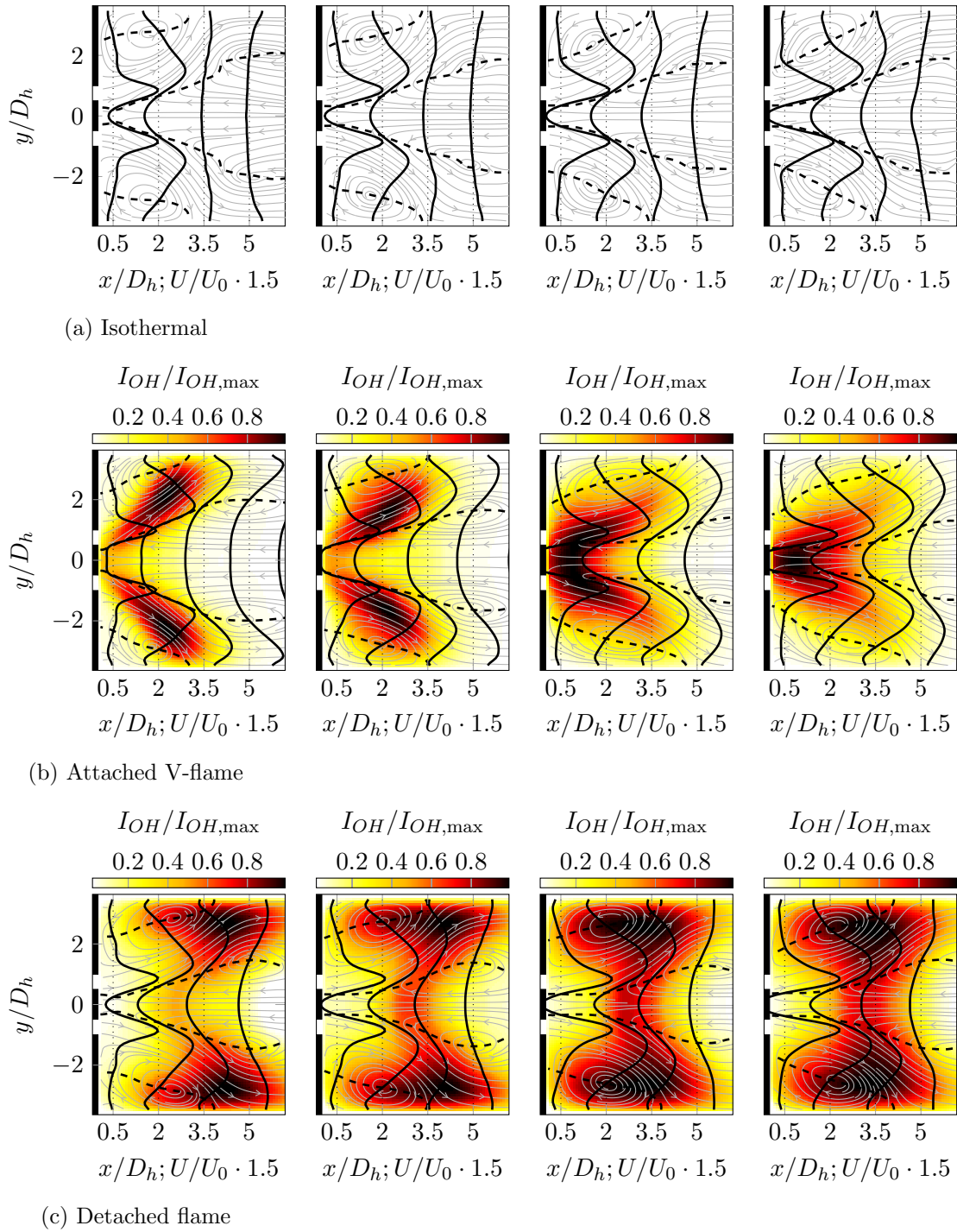


Figure 9.5: Flow fields (a-c) and normalized Abel-deconvoluted OH\*-chemiluminescence intensity distribution (b,c) of the encountered flow field and flame shapes at increasing forcing amplitudes. Forcing is increased from left to right from  $|u^c|/U_0 = 0$  to  $|u^c|/U_0 \approx 1.2$  at a forcing frequency of  $f_a = 110$  Hz. The solid black lines are radial profiles of the normalized axial velocity and the dashed black lines represent isolines of zero axial velocity.

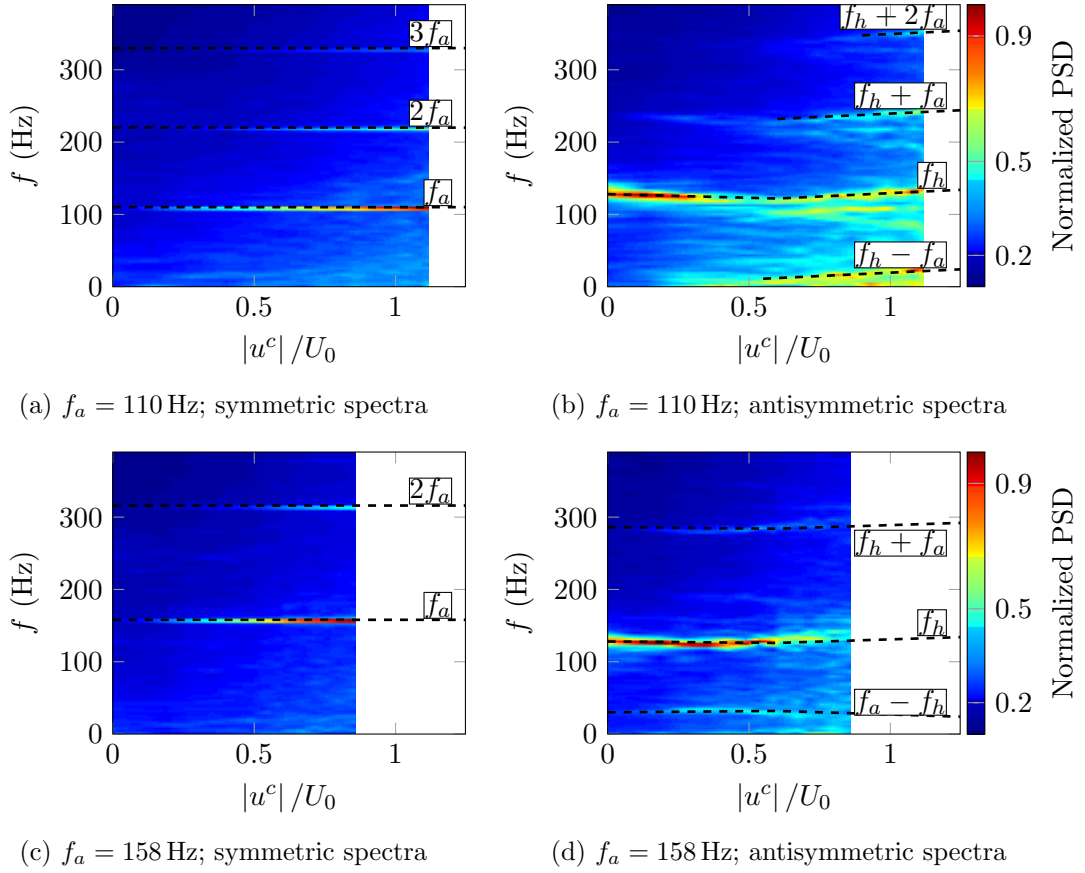


Figure 9.6: Spectra of the isothermal flow field dynamics at increasing forcing amplitudes. Left: Symmetric spectra showing peaks at the forcing frequency. Right: Antisymmetric spectra.

### 9.3.3 Flow Field Dynamics with Acoustic Forcing

In the following, the flow field dynamics of the detached flame, the isothermal case, and the attached V-flame are analyzed at increasing forcing amplitudes and at two acoustic forcing frequencies. In order to obtain an overview of the frequency content in the flow field, the concept of symmetric and antisymmetric spectra, as described in Section 2.5, is employed. The spectra are calculated for all measured spatial locations and are subsequently averaged to increase the signal-to-noise ratio.

#### Isothermal Flow Field

The results of the spectral analysis are provided for the isothermal case in Fig. 9.6. The left side shows the spectra of the symmetric velocity fluctuations, whereas the right side shows the spectra of the antisymmetric fluctuations. It can be observed that, in the absence of forcing ( $|u^c|/U_0 = 0$ ), the only spectral peak can be found in the antisymmetric spectra at  $f \approx 128.6$  Hz. This frequency corresponds to a Strouhal number of  $St \approx 0.177$  and is caused

by the PVC, depicted in Fig. 9.4a. At increasing acoustic forcing amplitude, the peak at the forcing frequency, and its harmonics, get more pronounced in the symmetric spectra. In the antisymmetric spectra, in contrast to this, only very weak traces of the forcing frequencies are visible, since the forced structures are essentially axisymmetric. The small contribution to the antisymmetric spectra is assumed to stem from the lack of perfect axisymmetry of the mean flow field, which are assumed to cause a deviation from perfect axisymmetry of the forced structures.

When the forcing frequency is higher than the frequency of the PVC ( $f_a = 158$  Hz, Fig. 9.6c,d), the effect of low amplitude acoustic forcing on the PVC is quite weak. The PVC is only slightly damped up to forcing amplitudes of  $|u^c|/U_0 = 0.6$  and its frequency is slightly reduced. For higher forcing amplitudes, the damping of the PVC gets considerably stronger. Beside the peak corresponding to the PVC, two additional peaks can be clearly observed in the antisymmetric spectra for almost all forcing amplitudes. These peaks occur at the difference frequency of the forcing frequency and the PVC frequency ( $f_a - f_h$ ) and at the sum of both frequencies ( $f_h + f_a$ ).

In order to get a better insight into the flow dynamics, a POD analysis is carried out at a forcing amplitude of  $|u_c|/U_0 = 0.71$  and a forcing frequency of  $f_a = 158$  Hz. Analog to the symmetric and antisymmetric spectra, the POD analysis is carried out first on the symmetric fluctuations and subsequently on the antisymmetric fluctuations. The results of the symmetric POD, depicted in the top row of Fig. 9.7, show two spatial modes describing the convection of the forced vortices in the shear layers. These forced structures are essentially the same structures that were observed in Chapter 8 and cause integral heat release fluctuations. The spectra of the corresponding time coefficients reveal the forcing frequency and higher harmonics.

The antisymmetric POD at forced conditions (bottom row of Fig. 9.7) yields two modes describing the PVC. In comparison to the unforced case (Fig. 9.4a), the axial extent of the PVC is slightly reduced. The spectra of the two modes representing the PVC show the same peaks as the averaged antisymmetric spectra (Fig. 9.6) at the frequency of the PVC and at the sum and the difference of the forced frequency and the PVC frequency ( $f_a - f_h$  and  $f_h + f_a$ ).

The dynamics of the flow field forced at  $f_a = 110$  Hz (Fig. 9.6a,b) show a qualitatively similar behavior as the flow field forced at  $f_a = 158$  Hz. However, the peak corresponding to the PVC dynamics only remains unaltered up to forcing amplitudes of  $|u^c|/U_0 = 0.3$ . At higher forcing amplitudes, the peak is notably damped and several peaks at the difference frequency of the PVC frequency and the forcing frequency ( $f_h - f_a$ ) and at sums of both frequencies ( $f_h + f_a$  and  $f_h + 2f_a$ ) occur.

Since the spectral peak related to the PVC is strongly attenuated by the forcing, it is of interest how the spatial shape of the PVC is affected by the forcing. The evolution of the PVC is determined through the application of antisymmetric POD. At each forcing amplitude, it was visually checked that the two most energetic antisymmetric modes describe the same dynamic feature and correspond to the PVC. As it was described in Section 2.3, in this case



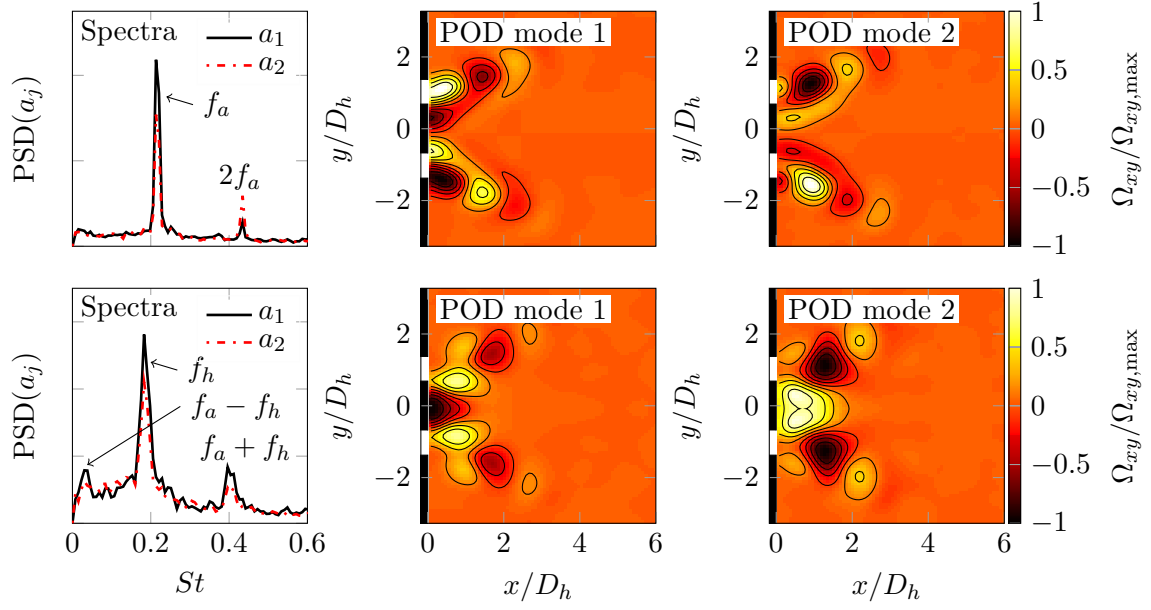


Figure 9.7: Results of the symmetric (top) and antisymmetric (bottom) POD analysis of the isothermal flow with forcing at  $f_a = 158\text{ Hz}$  and  $|u_c|/U_0 = 0.71$ . Left column: Power spectra of the first two temporal POD coefficients. Middle and right columns: Normalized through-plane vorticity  $\Omega_{xy}$  of the first two spatial POD modes.

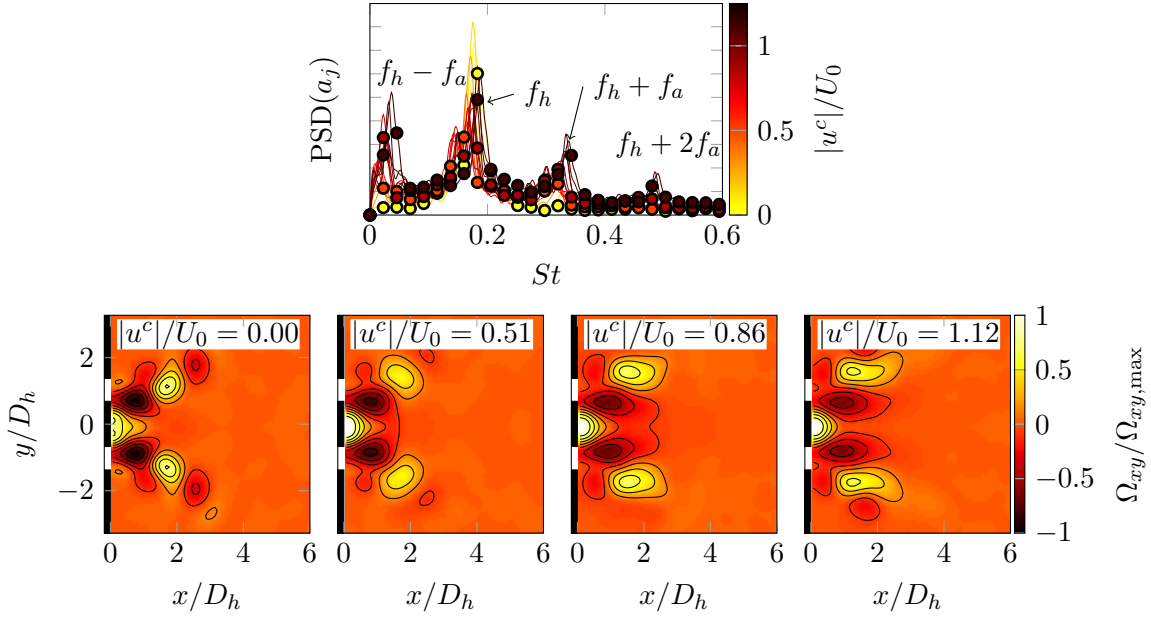


Figure 9.8: Results of the antisymmetric POD analysis of the isothermal flow with forcing at  $f_a = 110\text{ Hz}$  and  $|u_c|/U_0 = 0$  to  $1.12$ . Top: spectra of the first time coefficient. Bottom: normalized through-plane vorticity  $\Omega_{xy}$  of the antisymmetric structure described by the first two spatial POD modes. Phase is adjusted to increase the comparability between the forcing amplitudes.



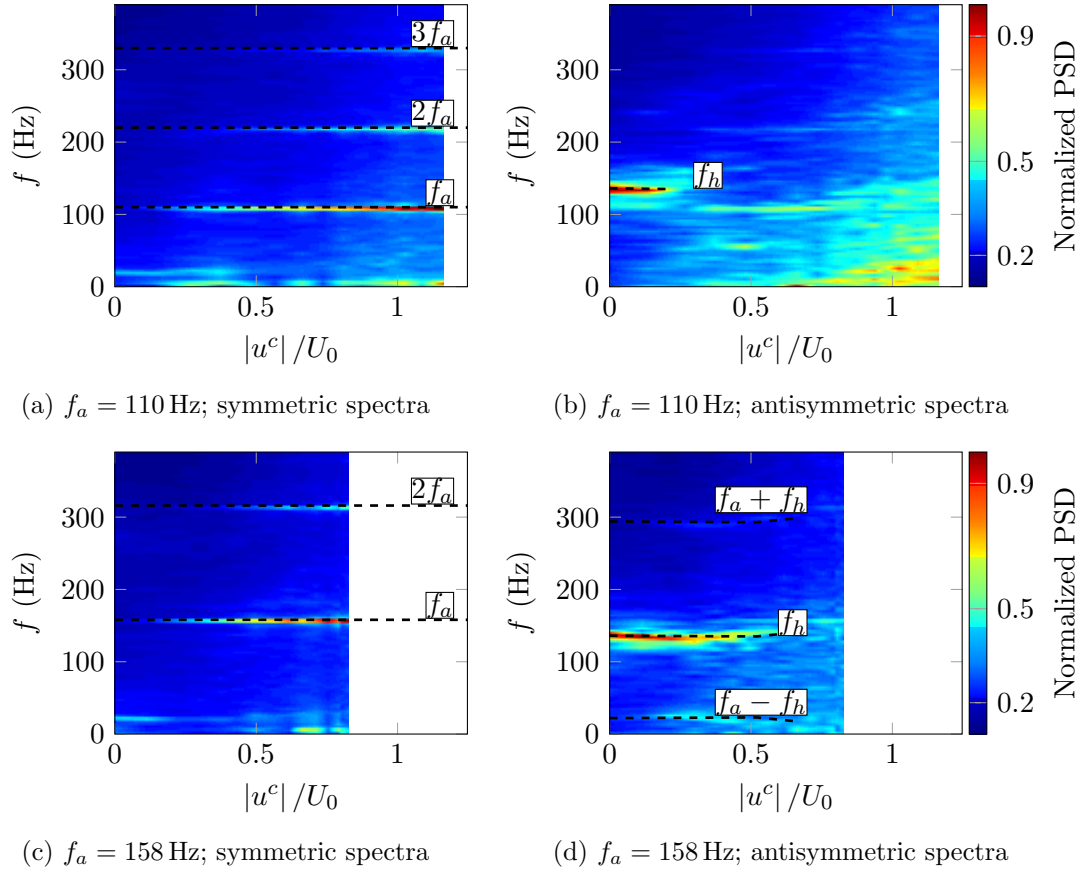


Figure 9.9: Spectral analysis of the detached flame. Left: Symmetric spectra showing peaks at the forcing frequency. Right: Antisymmetric spectra.

the PVC can be reconstructed by a linear superposition of the first two POD modes.

$$\mathbf{v}^{c,h}(\mathbf{x}, \theta) = \Re \left[ \sqrt{a_1^2 + a_2^2} (\Phi_1(\mathbf{x}) + i\Phi_2(\mathbf{x})) e^{-i\theta} \right] \quad (9.5)$$

The shape of the PVC at increasing forcing amplitudes is shown in Fig. 9.8. To increase the comparability of the spatial shape of the PVC, the phase  $\theta$  is adjusted in Fig. 9.8 to achieve a maximum correlation between the different forcing amplitudes. It is evident that the PVC changes its shape with increasing forcing amplitude but still remains similar. Simultaneously, the fluctuating energy content captured by the first two modes is reduced by approximately 40% (not shown). The spectra of the temporal coefficients of the first POD modes show very well the peaks at the PVC frequency and at the interaction frequencies, similar to the antisymmetric spectra showed in Fig. 9.6b.

### Detached Flame

The results of the spectral analysis for the detached flame are presented in Fig. 9.9. Very similar to the isothermal case, the peak at the frequency of the PVC is damped by the acoustic forcing. However, it can be observed that the damping is considerably stronger for the reacting cases. Only for very low forcing amplitudes ( $|u_c|/U_0 < 0.25$ ), the effect of the forcing is comparably low. For increasing forcing amplitudes the spectral peak corresponding to the PVC is strongly damped and finally gets completely suppressed. This suppression is considerably stronger for forcing at 110 Hz compared to 158 Hz forcing. The POD analysis of the  $f_a = 158$  Hz and  $|u_c|/U_0 = 0.5$  case (Fig. 9.10) shows similar results as in the isothermal case. The forcing excites axisymmetric structures, but the two POD modes representing the PVC remain very similar to the unforced case (compare Fig. 9.4c).

The effect of forcing on the spatial shape of the PVC is investigated using antisymmetric POD, similar as it was done in the isothermal case. The results are presented in Fig. 9.11 for forcing at  $f_a = 110$  Hz. It is evident that the spatial shape of the PVC is significantly affected by the forcing. However, even at the highest forcing amplitude ( $|u_c|/U_0 = 1.16$ ), it still shows some similarity to the unforced case. This is particularly interesting, since already at forcing amplitudes  $|u_c|/U_0 > 0.4$ , no spectral peak of the PVC could be observed, whereas the POD still identifies similar coherent structures as in the unforced case. The explanation for this can be found considering the spectra corresponding to the POD modes describing the PVC. The temporal coefficients do not describe an oscillation at a well-defined frequency anymore, whereas the spatial structure seems to persist in the forced flow field.

### Attached V-Flame

The spectra of the attached V-flame (Fig. 9.12) show very different characteristics compared to the isothermal case and the detached flame case. In the absence of forcing, no self-excited antisymmetric structure is present, thus, no peak in the antisymmetric spectra is evident. However, when the forcing amplitude, both at  $f_a = 110$  Hz and 158 Hz, reaches a certain value, the spectra of the antisymmetric fluctuations show distinct peaks at  $f_h = 50$  Hz. An increase of the forcing amplitude leads to an increase of the frequency to almost  $f_h = 100$  Hz. This frequency range is not related to the forcing frequency and gives rise to the assumption that the spectral peak is caused by a self-excited antisymmetric instability, such as the PVC. Furthermore, also peaks at the difference of the acoustic frequency and the frequency of the self-excited structure are evident.

The POD analysis of the antisymmetric fluctuations (Fig. 9.13) yields the dynamic feature that is related to the peak in the antisymmetric spectra. Similar to the unforced isothermal case and the unforced detached flame, the POD modes show a pattern of alternating vortices, and the second POD mode is shifted by a quarter wavelength relative to the first POD mode. Compared to the isothermal and detached case, the POD modes describe a coherent structure that is considerably shifted downstream. When the POD modes are compared to the POD modes representing the PVC of the trumpet flame (Fig. 4.9), a reasonable similarity is evident. This similarity is fully in line with the finding that the time-averaged flow field of the strongly

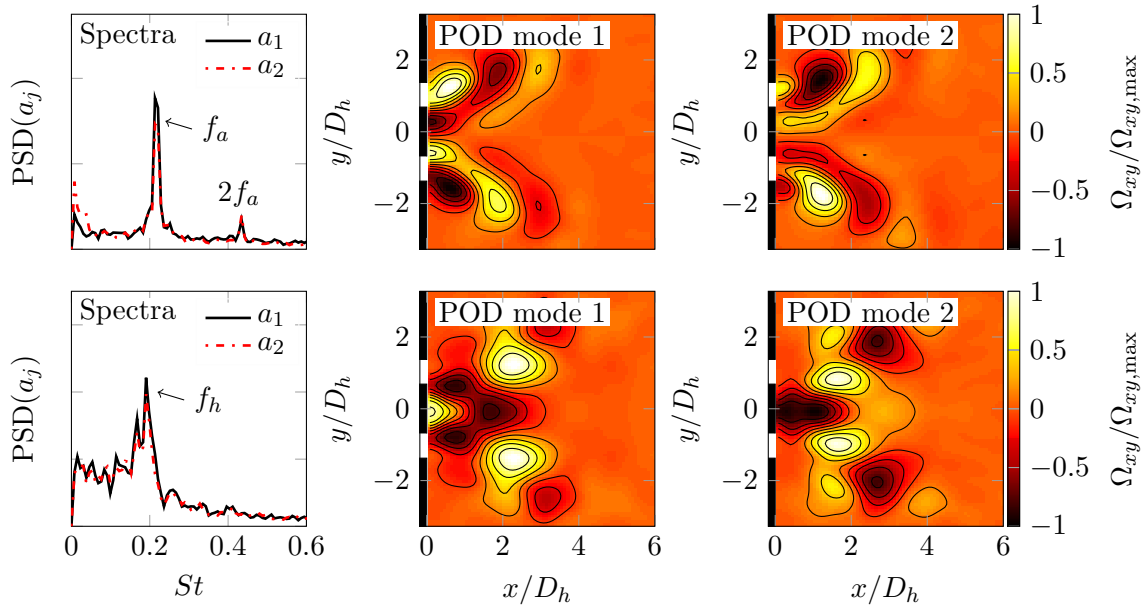


Figure 9.10: Results of the symmetric (top) and antisymmetric (bottom) POD analysis of the detached flame with forcing at  $f_a = 158\text{Hz}$  and  $|u_c|/U_0 = 0.5$ . Left column: Power spectra of the first two temporal POD coefficients. Middle and right columns: Normalized through-plane vorticity  $\Omega_{xy}$  of the first two spatial POD modes.

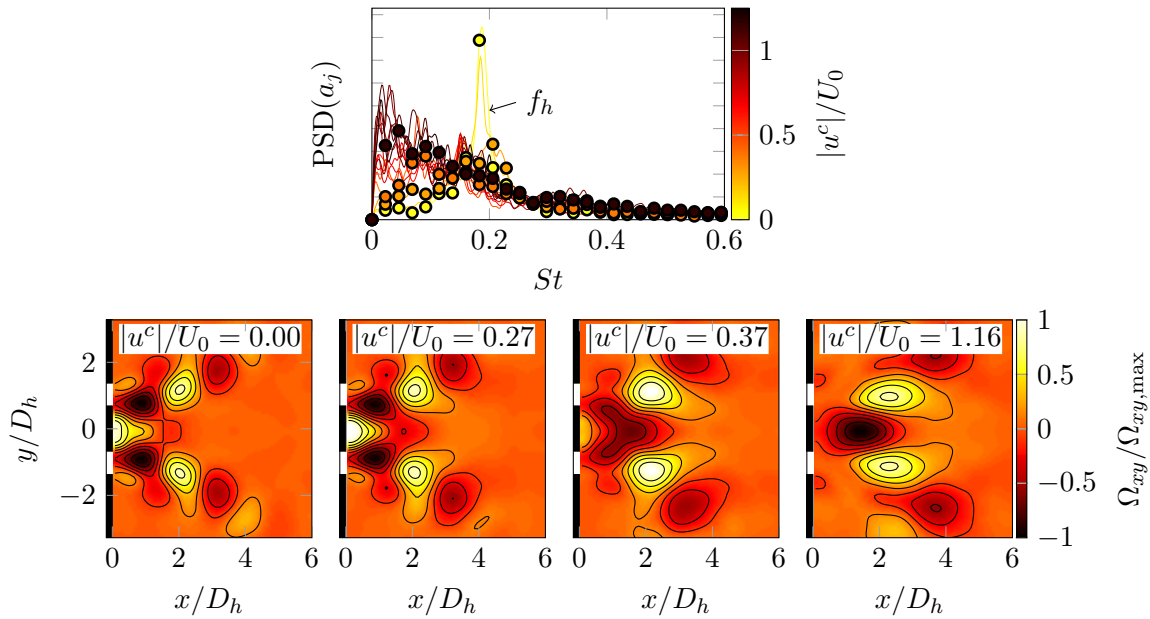


Figure 9.11: Results of the antisymmetric POD analysis of the detached flame with forcing at  $f_a = 110\text{Hz}$  and  $|u_c|/U_0 = 0$  to  $1.16$ . Top: spectra of the first time coefficient. Bottom: normalized through-plane vorticity  $\Omega_{xy}$  of the antisymmetric structure described by the first two spatial POD modes. Phase is adjusted to increase the comparability between the forcing amplitudes.

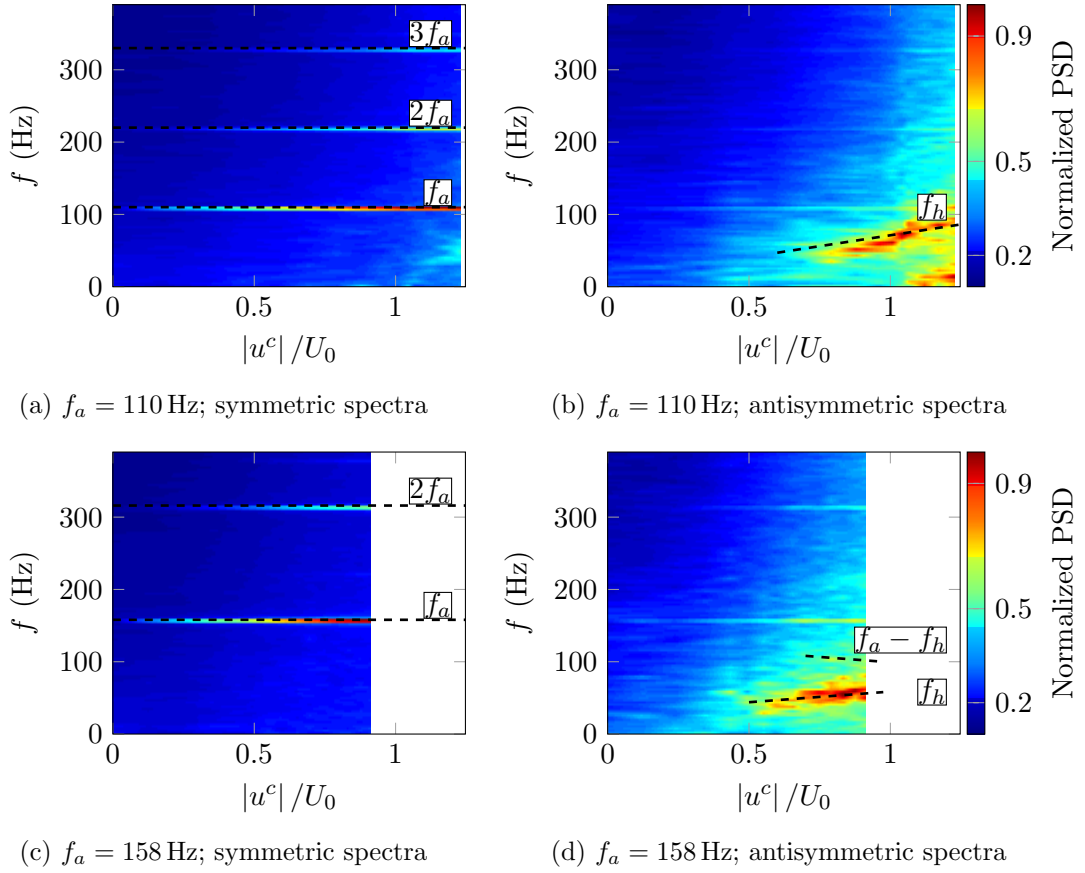


Figure 9.12: Spectral analysis of the attached V-flame. Left: Symmetric spectra showing peaks at the forcing frequency. Right: Antisymmetric spectra.

forced V-flame is similar to the time-averaged flow field of the trumpet flame. Thus, it seems very likely that the structure at  $f_h = 50$  to  $100$  Hz (depending on the forcing amplitude) is the PVC of the same type that occurs in the flow field of the trumpet flame. So far, the excitation of a PVC by axial acoustic forcing, in a case where no PVC is present without forcing, has not been reported in experiments and only in a numerical study by Giauque et al. (2005).

## 9.4 Influence of Axial Forcing on the Stability of the Flow Fields

Both at isothermal conditions and for the detached flame case, the spectral peak corresponding to the PVC can be considerably decreased or even completely suppressed by the acoustic forcing. In contrast to that, in the attached flame case, the PVC only appears at high forcing amplitudes. From Fig. 9.5 it is evident that axial forcing has an effect on the time-averaged flow field. It is to be reminded that in Chapter 6 it is demonstrated that the PVC is the result of a globally unstable flow field, and the excitation and suppression of the PVC at different flame shapes is associated with changes in the time-averaged flow field and density

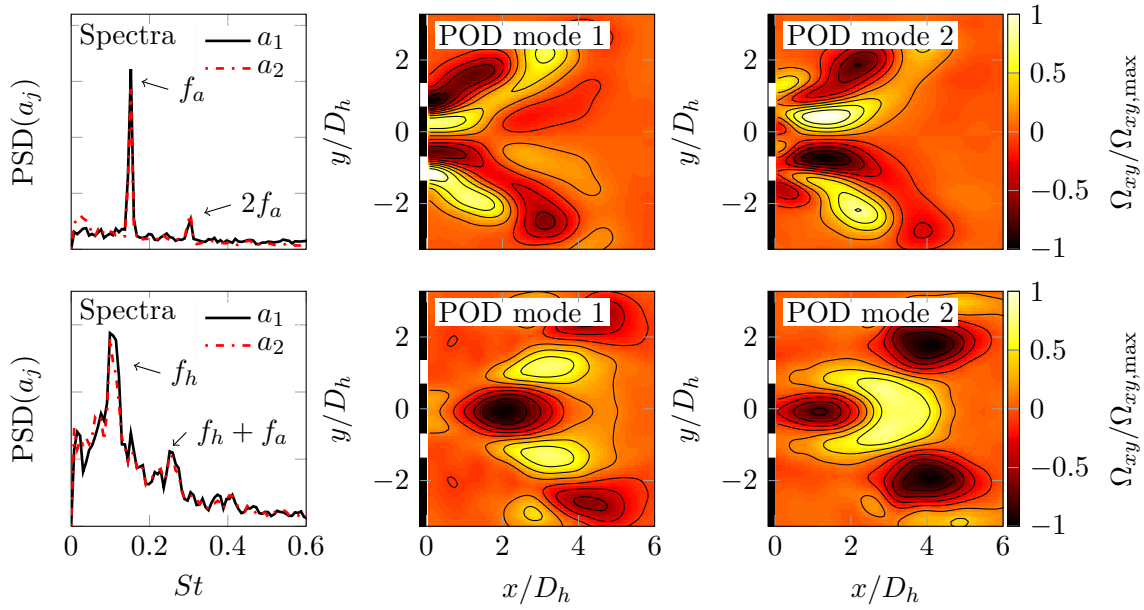


Figure 9.13: Results of the symmetric (top) and antisymmetric (bottom) POD analysis of the attached V-flame with forcing at  $f_a = 110$  Hz and  $|u_c|/U_0 = 1.23$ . Left column: Power spectra of the first two temporal POD coefficients. Middle and right columns: Normalized through-plane vorticity  $\Omega_{xy}$  of the first two spatial POD modes.

field. Thus, it seems plausible that the suppression and/or excitation of the PVC is caused by changes to the time-averaged flow field induced by the axial forcing.

In the following, this assumption will be further investigated by the application of linear hydrodynamic stability theory on the time-averaged velocity and density fields at different forcing amplitudes, similar as it was done in Chapter 6.

#### 9.4.1 Suppression of the PVC in the Isothermal Cases and the Detached Flame Cases

In the cases where the PVC is damped or suppressed by the forcing, a possible assumption is that axial forcing has such an effect on the time-averaged flow field and density field that it is no longer globally unstable, and the PVC is no longer excited. This assumption is investigated in the following by calculating the linear stability of the isothermal case and the detached flame at unforced and forced conditions.

Figures 9.14a,b show the results of the stability analysis of the isothermal flow field forced at  $f_a = 110$  Hz and  $f_a = 158$  Hz at increasing forcing amplitudes. During the measurement of the forced flow fields, monoscopic PIV was used. Therefore, no tangential velocity component of the forced cases was available, and the unforced velocity profile from a different measurement in the same combustor had to be used, as it was described in the analytical procedure section of this chapter. The validity of this approach is supported by the findings of Chapter 6,

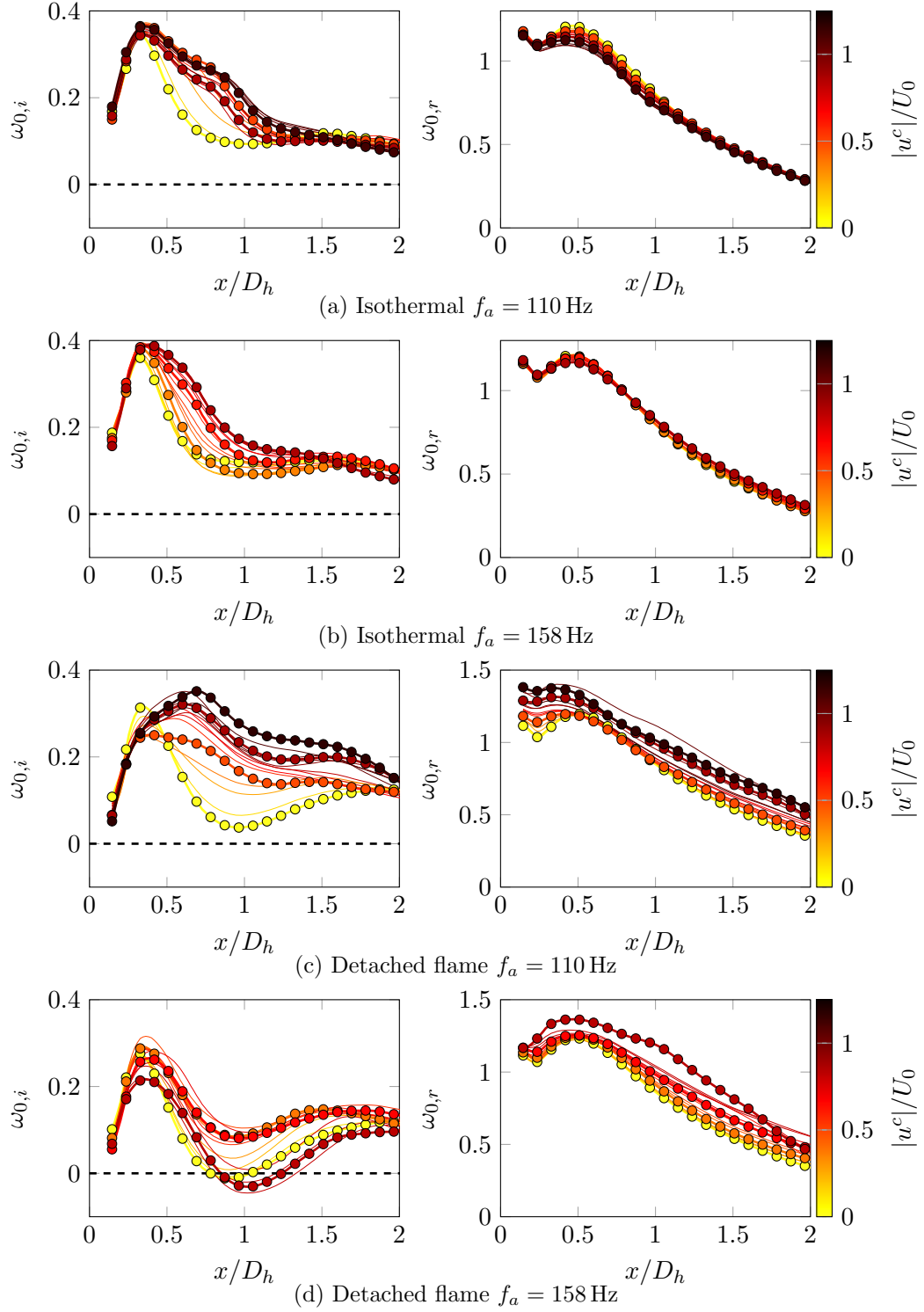


Figure 9.14: Results of the stability analysis on the time-averaged forced flow fields. Left: absolute growth rate  $\omega_{0,i}$ . Right: absolute frequency  $\omega_{r,i}$ .

where it is shown that reasonable changes to the tangential flow component only have a minor impact on the absolute growth rates.

In Figs. 9.14a,b it can be observed that in the isothermal case, forcing has very little influence on the local absolute growth rate  $\omega_{0,i}$  upstream of the location of maximum growth rate. Further downstream, the decay of the growth rate is increasingly attenuated by the forcing. This is correlated to the higher recirculating velocities in the forced cases. The local absolute frequencies  $\omega_{0,r}$  are slightly decreased by the forcing at  $f_a = 110$  Hz and hardly influenced by the forcing at  $f_a = 158$  Hz. However, since the effect of forcing on the tangential velocity component is not accounted for in the analysis, the predicted absolute frequencies should not be over-interpreted.

The application of the frequency selection criteria (Eqn. 2.32) to the local analysis yields a global frequency of 132.9 Hz and a wavemaker location of  $x_s = 0.32D_h$  for both unforced cases. Despite the uncertainty in the tangential velocities, this frequency is close to the measured frequency of  $f_h = 128.6$  Hz. In the cases forced at  $f_a = 110$  Hz, the stability analysis yields a slight decrease of the instability frequencies to  $f_h = 125$  Hz, while the global growth rate and the wavemaker location remain almost unchanged. A similar trend of slightly lower frequency of the PVC caused by the forcing is also evident in the experiments (Fig. 9.6b). Hence, the mean flow field modifications induced by the acoustic forcing have only limited influence on the linear stability of the isothermal flow field and are not likely to cause the strong attenuation of the PVC, which was observed in the experiments.

In the case of the detached flame, a considerable influence of forcing at  $f_a = 110$  Hz on the local absolute growth rate is visible in Fig. 9.14c. In the unforced case, the application of the frequency selection criterion yields a wavemaker location of  $x_s = 0.36D_h$  and a global frequency of 131.1 Hz, which is close to the measured frequency of  $f_h = 135.3$  Hz. At forced conditions, the peak of  $\omega_{0,i}$  at  $x \approx 0.3D_h$  is slightly damped with increasing forcing amplitudes. For high forcing amplitudes ( $|u_c|/U_0 > 0.5$ ), the peak vanishes and a downstream shifted peak is established at  $x \approx 0.7D_h$ . Simultaneously, the absolute frequency  $\omega_{0,r}$  is increased. Consequently, the frequency selection criterion yields a downstream shift of the wavemaker location to  $x_s = 0.73D_h$  for the highest forcing amplitude, while the global frequency and the global growth rate remain similar. This downstream shift of the wavemaker is qualitatively in line with the downstream shift observed in the antisymmetric POD analysis presented in Fig. 9.11.

The stability analysis for the forcing at  $f_a = 158$  Hz yields a smaller influence of the forcing compared to the 110 Hz case. With increasing forcing amplitudes, the maximum absolute growth rate is slightly reduced and the absolute frequency is slightly increased. The frequency selection criterion yields a downstream shift of the wavemaker from  $x_s = 0.34D_h$  to  $x_s = 0.44D_h$ .

The linear stability analysis of the detached flame indicates that the mean flow field changes induced by the forcing have a considerable influence on the stability of the flow field. Some findings of the spectral and POD analysis, such as the downstream shift of the PVC structure (compare Fig. 9.11) seem to depend on these changes (downstream shift of the wavemaker).

However, the flow fields remain still clearly globally unstable even at very high forcing amplitudes, where the experiments showed a complete suppression of the spectral peaks of the PVC (Fig. 9.9). This is in line with the results of the antisymmetric POD analysis, where a spatial structure, similar to the unforced PVC, was still found up to the highest forcing amplitudes, even though the spectral peak corresponding to this structure was completely suppressed. These findings, which seem counterintuitive at the first glance, will be further investigated in Section 9.5.

#### 9.4.2 Excitation of the PVC in the Attached V-Flame Cases

Acoustic forcing of the V-flame caused significant modification of the mean flow field (see Fig. 9.5). In the following, linear stability analysis is carried out to assess the stability of the flow field of the attached V-flame at forced and unforced conditions. The analysis is conducted using tangential velocities taken from the unforced measurements presented in Chapter 4. This is justified by considering the comparison of the flow fields presented in Fig. 9.15. Without forcing, the flow field shows a reasonable similarity to the flow field of the attached V-flame presented in Chapter 4. The difference in the magnitude of the axial velocities at the downstream positions stems from different density ratios of the two flow fields. The density ratio has, however, only very little influence on the tangential velocities (Weber and Dugué, 1992; Terhaar et al., 2012).

In contrast to the unforced case, the flow field of the strongly forced attached V-flame is very similar to the trumpet flame featuring a similarly low jet divergence. Consequently, for the analysis of the unforced case, the tangential velocities of the attached V-flame are used and for the analysis of the strongly forced cases, the tangential velocities of the trumpet flame are employed. The analyses are carried out in the absence of forcing and for three high forcing amplitudes. At moderate forcing amplitudes the flow field shapes do not feature a good similarity to neither the unforced attached V-flame nor the unforced trumpet flame. Thus, no adequate tangential velocity distribution is available and no stability analysis can be carried out for the moderately forced cases. It is to be emphasized here that the calculations based on the substitute tangential velocities only provide an estimation of the stability characteristics. However, the model study presented in Chapter 6 yielded that the predicted growth rate of the PVC is only weakly depended on the tangential velocities, whereas its frequency strongly depends on the tangential velocities.

The results of the stability analyses of the forced flow fields of the V-flame are shown in Fig. 9.16. In the absence of forcing, the flow remains absolutely stable up to  $x/D_h = 1.1$  and the maximum growth rate of  $\omega_{0,i} = 0.1$  is reached at  $x/D_h = 2.5$ . At positions that far downstream, the absolute frequency has already considerably decayed. In the experiments it is evident that the flow field without forcing does not feature a hydrodynamic instability. The global stability criterion (Chomaz et al., 1991), however, indicates a small positive global growth rate. This overprediction of the growth rate was already observed for the V-flame in Chapter 6 and was shown to stem from the negligence of the considerable non-parallelity of the flow field of the attached V-flame.



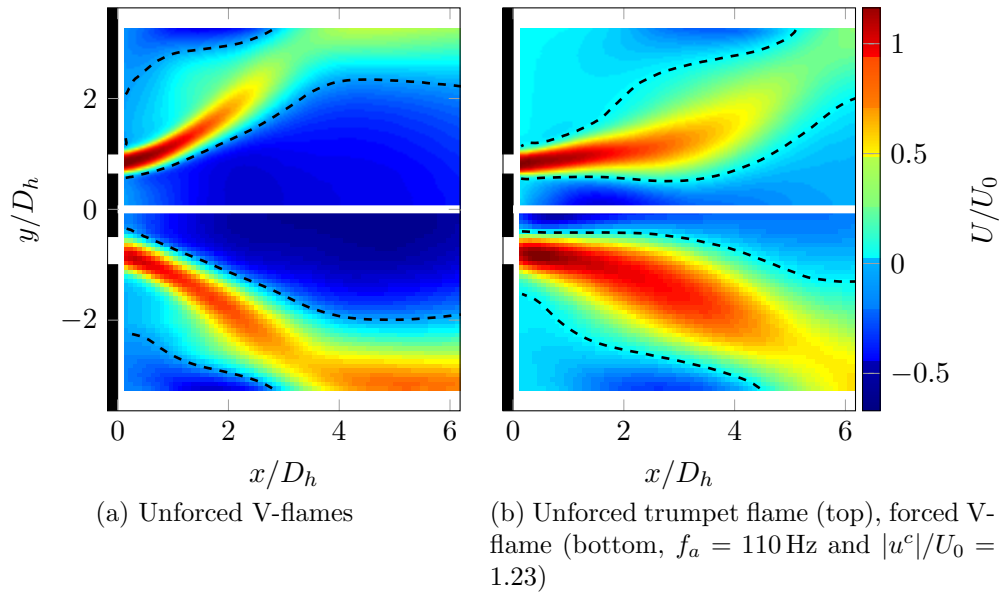


Figure 9.15: Comparison of the normalized axial velocity distribution of the unforced V-flame and trumpet flame (top halves) to the unforced and forced V-flame (bottom halves). Black dashed lines indicate zero axial velocity. For the operating conditions of the unforced cases see Tab. 4.2.

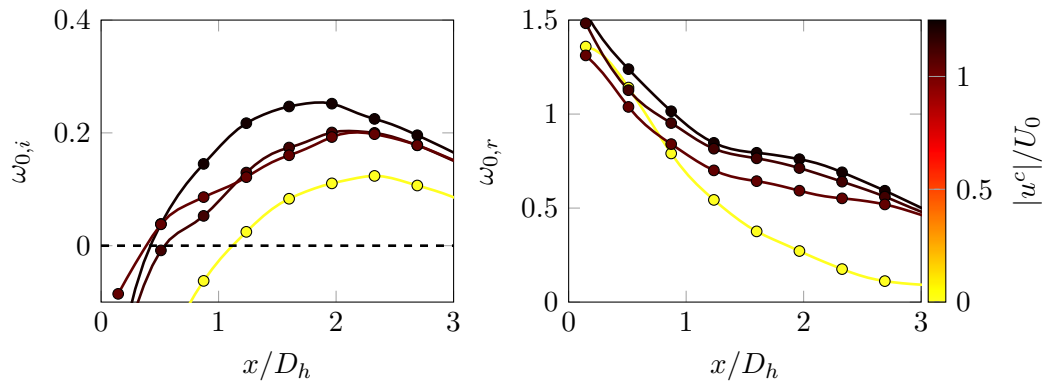


Figure 9.16: Results of the stability analysis on the time-averaged forced flow fields ( $f_a = 110$  Hz) of the attached V-flame. Left: Absolute growth rate  $\omega_{0,i}$  and right: Absolute frequency  $\omega_{0,r}$ .

In Fig. 9.16 the destabilizing effect of the forcing on the flow field is clearly visible. For the investigated cases with high forcing amplitudes ( $|u^c|/U_0 = 1.04; 1.11; 1.23$ ), the onset of absolute instability is shifted upstream and the absolute growth rates considerably increase. Consequently, the global stability criterion yields considerably higher global growth rates and frequencies. The predicted frequencies rise from 73.8 Hz at  $|u^c|/U_0 = 1.04$ , to 87.6 Hz at  $|u^c|/U_0 = 1.11$ , and to 91.67 Hz at  $|u^c|/U_0 = 1.23$ . This compares reasonably well with the measured frequencies of 68.1 Hz, 77.1 Hz, and 89.1 Hz, respectively. Since the effect of the forcing on the angular velocity, which is very important for the frequency but less important for the growth rate, was not measured, the achieved frequency match is rather remarkable and provides further credibility to the stability calculations based on the substitute profiles for the tangential velocities.

The results of the stability analysis clearly demonstrate that the excitation of the PVC in the attached flame case is caused by changes of the mean flow field induced by axial acoustic forcing. The spatial shape of the PVC, shown in Fig. 9.11, indicates that the PVC is considerably shifted downstream compared to the isothermal case and the detached flame. This is qualitatively in line with the wavemaker location predicted by the stability analysis of  $x_s = 1.62D_h$  for the highest forcing amplitude compared to  $x_s = 0.34D_h$  in the detached flame case.

## 9.5 Analogy of the Acoustically Forced PVC to a Parametric Oscillator

In this section it is aimed to show that basic features of the PVC at axially forced conditions are captured by a simple nonlinear parametric model oscillator. The model oscillator is considered as a parametric nonlinear Van der Pol (VdP) oscillator, which is described by the following second order nonlinear differential equation:

$$\ddot{q} + \mu(1 - q^2)\dot{q} - \gamma(t)\dot{q} + \beta(t)q = 0. \quad (9.6)$$

Here, the time-dependent coefficients  $\gamma(t)$  and  $\beta(t)$  are introduced to vary the linear damping and the eigenfrequency of the oscillator. The damping coefficient  $\gamma(t)$  and the coefficient  $\beta(t)$  are assumed to be periodically oscillating at a frequency  $f_a^*$

$$\beta(t) = 1 + \hat{\zeta} \sin(2\pi f_a^* t) \quad (9.7)$$

$$\gamma(t) = \hat{\zeta} \sin(2\pi f_a^* t), \quad (9.8)$$

whereas the eigenfrequency of the unforced system ( $\hat{\zeta} = 0$ ) is  $f_h^* \approx 1$ .

### 9.5.1 Motivation by Phase-Averaged Stability Calculations

The periodic variation of the linear damping and the eigenfrequency of the oscillator will be motivated in the following with results from the linear stability analysis. During one axial

forcing cycle, the flow field undergoes very strong changes. It seems plausible that during this forcing cycle, both the eigenfrequency of the helical mode (PVC) and its growth rate vary. If one considers a very low acoustic forcing frequency, where the forcing frequency is an order of magnitude lower than the frequency of the PVC, the PVC can fully develop during the different phases of the forcing. It will adapt to the new phase-averaged flow field with changes of its shape, frequency, and amplitude. In this case, a linear stability analysis of the phase-averaged flow fields (with respect to the forcing)

$$\mathbf{v}(\mathbf{x}, \Psi) = \mathbf{V}(\mathbf{x}) + \mathbf{v}^{c,a}(\mathbf{x}, \Psi) \quad (9.9)$$

could accurately predict the modulation of the PVC.

Similar studies have been carried out successfully for slowly varying base flows (e.g., Thiria et al., 2007). In the present case, however, the forcing frequency and the frequency of the PVC are of the same order. Thus, for an exact study, the framework of a Floquet analysis would be necessary. Since the main interest in this chapter is placed on the qualitative effect of the oscillating flow on the PVC, the implementation of the Floquet analysis into the local stability analysis is beyond the scope of this work. Instead, it is assumed that a strictly qualitative idea of the modulation of the PVC can be obtained from the calculation of the stability characteristics of the flow field at different phases of the forced oscillation. This assumption is based on the idea that the mechanisms remain the same, even though the PVC cannot be expected to fully develop into its theoretical limit-cycle at every phase of the forcing cycle.

The results of the stability analysis on the phase-averaged flow fields are presented in Fig. 9.17 for an axial location of  $x/D_h = 0.4$ , which is close to the predicted wavemaker location. It is evident that the absolute growth rate  $\omega_{0,i}$ , from which also the global growth rate  $\omega_{g,i}$  is deduced, strongly oscillates along the forcing cycle. Since the tangential velocity was not measured for the stability analyses presented in Fig. 9.17, only the forced oscillations of the axial velocity and the density field are considered. Thus, no valid information about the oscillation of the absolute frequency  $\omega_{0,r}$  can be obtained. In contrast to the growth rates, the absolute frequency strongly depends on the tangential velocities (see Chapter 6). Nevertheless, since the tangential velocity component oscillates at the forcing frequency, the same is expected from the absolute frequency  $\omega_{0,r}$ .

The validity of the presented phase-averaged stability calculations can be assessed by considering the amplitude modulation of the PVC from the experiments. To obtain the amplitude of the helical oscillation at different forcing phases, first the phase-averaged fluctuations with respect to the forcing phase ( $\Psi$ ) and the PVC phase ( $\theta$ ) are calculated. Subsequently, the difference of these doubly phase-resolved fluctuations ( $\mathbf{v}^{c,ha}(\mathbf{x}, \theta, \Psi)$ ) and the coherent fluctuations, phase-averaged with respect only to the forcing ( $\mathbf{v}^{c,a}(\mathbf{x}, \Psi)$ ) are calculated. Thereby, the virtual oscillation of the PVC at a fixed forcing phase  $\Psi$  is obtained as  $\mathbf{v}^{c,ha}(\mathbf{x}, \theta, \Psi) - \mathbf{v}^{c,a}(\mathbf{x}, \Psi)$ . Next, the modulation of the amplitude of the helical oscillation is

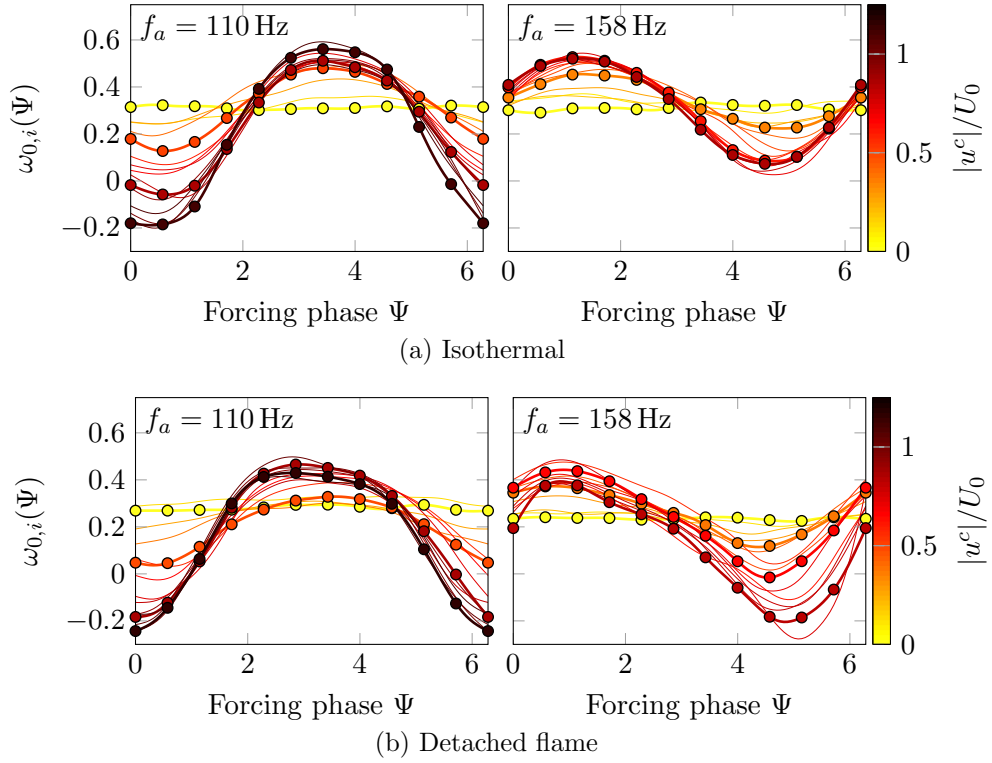


Figure 9.17: Results of the phase-resolved stability analysis at  $x/D_h = 0.4$  of the isothermal flow and the detached flame forced at  $f_a = 110$  Hz (left) and  $f_a = 158$  Hz (right).

obtained as the magnitude of the Fourier transform of this difference.

$$\hat{\mathbf{v}}^{c,h}(\mathbf{x}, \Psi) = \left| \mathcal{F} \left( \mathbf{v}^{c,ha}(\mathbf{x}, \theta, \Psi) - \mathbf{v}^{c,a}(\mathbf{x}, \Psi) \right) \right| \quad (9.10)$$

Finally,  $\hat{\mathbf{v}}^{c,h}(\mathbf{x}, \Psi)$  is integrated over the region of interest ( $-2.5 < y/D_h < 2.5$  and  $0 < x/D_h < 4$ ) and yields the integral amplitude of the PVC, phase-averaged with respect to the forcing.

$$A_{\text{PVC}}(\Psi) = \frac{1}{D_h \dot{V}} \int 2\pi r \sqrt{0.5 (\hat{u}^{c,h}(\mathbf{x}, \Psi)^2 + \hat{v}(\mathbf{x}, \Psi)^2)} dA \quad (9.11)$$

This integral PVC amplitude oscillates during the forcing cycle at a specific phase with respect to the forcing signal. In Fig. 9.18, the phase-lag of the integral PVC amplitude to the forcing signal is shown for various forcing amplitudes. Additionally, the phase-lag of the calculated phase-dependent linear absolute growth rate  $\omega_{0,i}$  to the forcing signal is provided. For forcing at 110 Hz, the average difference of the phase of the PVC amplitude oscillation to the phase of the growth rate oscillation is  $101^\circ$ . In the 158 Hz case, the mean phase difference is  $115^\circ$ .

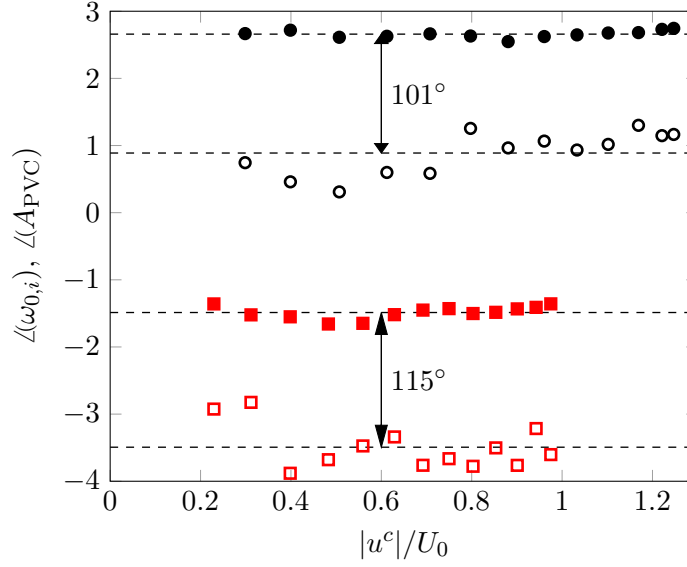


Figure 9.18: Phase of the absolute growth rate predicted by the stability analysis in the wavemaker region ( $\omega_{0,i}$ , filled symbols) and phase of the amplitude fluctuation of the PVC ( $A_{PVC}$ , hollow symbols). Forcing at 110 Hz (black circles) and 158 Hz (red squares). Dashed lines are the average phases and arrows indicate the average phase differences between  $A_{PVC}$  and  $\omega_{0,i}$ .

In the linear framework, the amplitude  $A$  of an oscillation is determined by the linear global growth rate as

$$\omega_i = \frac{\partial A}{\partial t}. \quad (9.12)$$

That is, the amplitude  $A$  is increased as long as the growth rate  $\omega_i$  is positive. If  $\omega_i$  oscillates around zero at a fixed frequency, it follows from Eqn. 9.12 that the phase-lag between  $A$  and  $\omega_i$  is exactly  $90^\circ$ . In the present investigation of the amplitude of the PVC  $A_{PVC}$ , it is assumed that the phase of the global growth rate  $\omega_{g,i}$  is qualitatively similar to the phase of the absolute growth rate  $\omega_{0,i}$  in the vicinity of the wavemaker. Thus, the phase of  $\omega_{0,i}$  can be used as a substitute to the phase of  $\omega_{g,i}$  in order to avoid the cumbersome and fault-prone task of identifying the wavemaker at each forcing phase (see Section 2.4.2). The reasonable proximity of the observed phase-difference between the PVC amplitude  $A_{PVC}$  and the predicted absolute growth rate  $\omega_{0,i}$  to the theoretical value of  $90^\circ$  indicates that the results of the linear stability analysis capture the effect of the oscillating flow on the excitation of the PVC at least qualitatively. The linear growth rate (and eigenfrequency) seem to oscillate at the forcing frequency.

### 9.5.2 Dynamics of the Parametric Van der Pol Oscillator

The consideration of the phase-averaged linear stability analysis suggests that the parametric oscillator with an oscillating linear damping and eigenfrequency is a viable model to describe

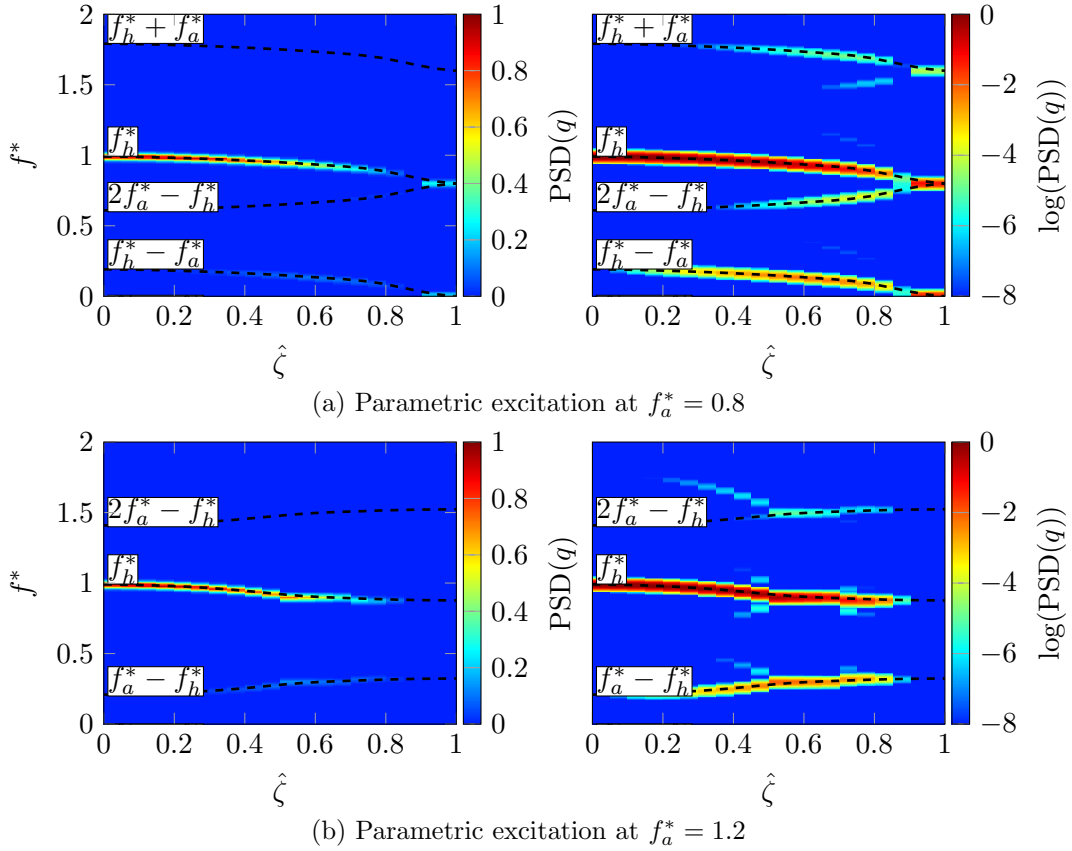


Figure 9.19: Spectra of the parametrically forced VdP oscillator.

the PVC dynamics at axially forced conditions. The dynamics of the parametrically forced oscillator are obtained by the numerical integration of Eqn. 9.6 and are presented in Fig. 9.19 for a nonlinearity of  $\mu = 0.4$ . Note that the value of  $\mu = 0.4$  is exemplarily chosen and the results presented in the following remain similar for reasonable variations of  $\mu$ . The oscillator is parametrically excited with amplitudes from  $\hat{\zeta} = 0$  to  $\hat{\zeta} = 1$  at one frequency lower than the eigenfrequency ( $f_a^* = 0.8$ ) and one frequency higher than the eigenfrequency ( $f_a^* = 1.2$ ).

At increasing amplitudes of the parametric excitation  $\hat{\zeta}$ , the peak amplitude is considerably decreased and almost completely vanishes for high parametric forcing amplitudes. Furthermore, the peak frequency is slightly reduced and peaks at the difference and sum of the self-excited and the modulation frequency occur. No peak at the modulation frequency itself can be observed, what is in strong contrast to a (non-parametrically) forced oscillator, where a peak at the forcing frequency is always present, which may be accompanied by the natural peak and several interaction frequencies. The observed spectral behavior of the parametric VdP oscillator resembles very well the antisymmetric spectra observed in Figs. 9.6b and 9.9b.

It may be concluded that the PVC at axially forced conditions shows a similar dynamical behavior as a parametric nonlinear oscillator. This analogy to a parametric oscillator allows for the explanation of the pronounced frequency sensitivity of the damping of the PVC due

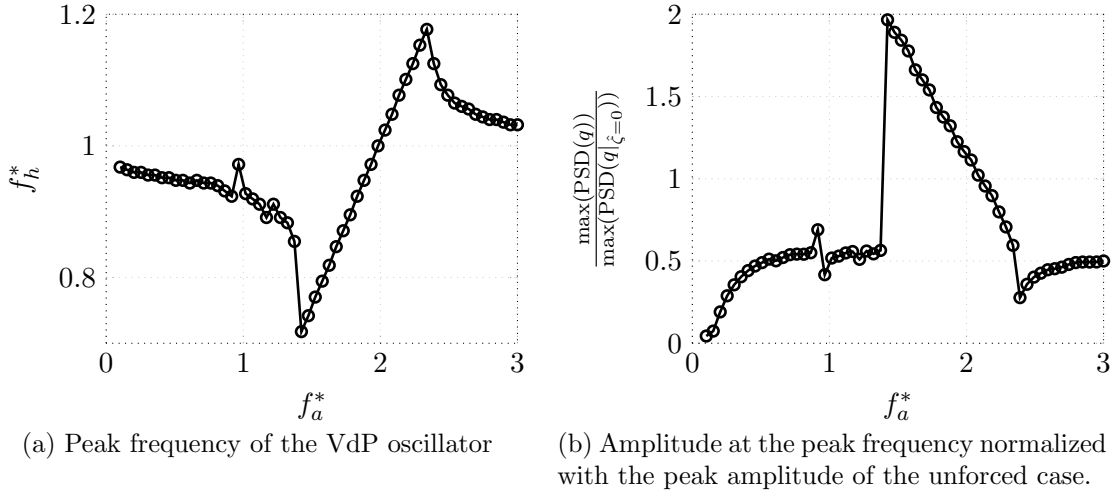


Figure 9.20: Frequency dependence of the parametric VdP oscillator forced at  $f_a^* = 0 - 3$  and a forcing amplitude of  $\hat{\zeta} = 0.6$ .

to axial forcing. An example of this dependency is presented in Fig. 9.20. The peak frequency and the peak amplitude are extracted from the numerical integration of the parametrically forced VdP oscillator at different parametric forcing frequencies. It can be clearly observed that the lowest amplitudes are present for low frequency parametric forcing. This is in line with the findings of Lacarelle et al. (2009) and Khalil et al. (2006), who observed a much higher damping efficiency for lower forcing frequencies. Paschereit et al. (2000) found that the PVC is very efficiently suppressed by acoustic forcing, when the flow is forced at exactly the PVC frequency. This is also evident from Fig. 9.20. At  $f_a^* = 1$ , the amplitude shows a distinct local minimum. If the parametric forcing frequency approaches  $f_a^* = 1.6$ , which is twice the peak frequency of  $f_h^* = 0.8$  at this forcing frequency, the amplitude rises quickly. This phenomenon is known as parametric resonance and is likely to be the reason for the observations made by Iudiciani and Duwig (2011), who found that axial forcing at twice the PVC frequency increased the amplitude of the PVC.

## 9.6 Conclusions

In the present chapter the influence of axisymmetric acoustic forcing on the PVC is investigated experimentally and analytically. Three different cases are considered. Two of them, the isothermal case and the detached flame case feature a self-excited PVC. In the third case of an attached V-flame, the flow field is hydrodynamically stable and no PVC is self-excited. Experimental data is presented, where the flow fields are acoustically forced at two forcing frequencies, one below and one above the PVC frequency, and at various forcing amplitudes. The spectral analysis of the velocity fluctuations show that for the cases with a self-excited PVC, the PVC is damped and can subsequently be suppressed by acoustic forcing. In contrast to this, in the attached flame case, where no PVC was present at unforced conditions, a

PVC appears only at high axial forcing amplitudes. In all cases, the damping or excitation of the PVC is accompanied by spectral peaks at several interaction frequencies (integer linear combinations of the forcing frequency and the PVC frequency).

The application of linear hydrodynamic stability theory clearly indicates that the excitation of the PVC in the attached flame case, which was stable at unforced conditions, is caused by changes to the mean flow field. These mean flow field changes are induced by the acoustic forcing. To the author's knowledge, this is the first experimentally validated explanation of this phenomenon in a swirling combustor flow.

The linear stability analysis of the cases where the PVC is damped or suppressed by the acoustic forcing reveals that mean flow field changes may be responsible for the observed changes to the PVC in terms of frequency and shape. However, the calculated growth rates indicate that the mean flow field changes induced by the acoustic forcing are not exclusively causing the observed damping of the PVC.

Furthermore, the results of the stability calculation suggest that the dynamics of the PVC at acoustically forced conditions can be qualitatively modeled with a parametric Van der Pol oscillator. The dynamics of this oscillator are numerically calculated and resemble the dynamics of the forced PVC reasonably well in terms of the attenuation of the self-excited oscillation and the occurrence of the spectral peaks at the interaction frequencies. Furthermore, the strong frequency dependence of the damping, which was observed in this work and also in previous studies (Khalil et al., 2006; Lacarelle et al., 2009; Paschereit et al., 2000; Iudiciani and Duwig, 2011), is captured by the simple model.

The presented experimental and analytical results show the complex interaction of forced axisymmetric structures, as they are caused by thermoacoustic oscillation, and the hydrodynamically excited PVC. It is shown that the effect of axial forcing on the PVC is dominated by two mechanisms: Firstly, changes to the mean flow field alter the linear stability of the flow field and, thereby, influence the excitation of the PVC. Secondly, the forced oscillation of the flow field leads to oscillations of the eigenfrequency and the damping of the unstable flow field. The first effect was shown to cause the excitation of the PVC in the attached flame case. The second effect is assumed to be responsible for the damping and suppression of the PVC. Both mechanisms can be modeled with the tools presented in the present work. Furthermore, the analogy of the forced PVC to a simple parametric nonlinear oscillator significantly enhances the understanding of the observed phenomena and provides a valuable tool for physics-based flow control.



# Summary and Concluding Remarks

Swirling combustor flows are used in the majority of gas turbine combustors. The induced swirling flow field is very beneficial for flame stabilization, but on the other hand, it is very complex and prone to flow instabilities. The increased need for fuel flexibility and the introduction of new cycle concepts impose further challenges on the combustor design. At varying operating conditions, different flame shapes occur that are accompanied by strong changes of the flow field. Large-scale coherent flow structures, dominated by the flow field dynamics, can interact with the flame and lead to high-amplitude heat release fluctuations.

In the present thesis, the occurrence and role of coherent structures in swirl-stabilized combustors was experimentally and analytically investigated. A distinction was made between two types of coherent structures. Structures of the first type are intrinsically excited by the hydrodynamic field, whereas structures of the second type are extrinsically excited by the acoustics of the combustion system. The dominant flow-intrinsic coherent structure describes a precession of the vortex core around the geometrical centerline (precessing vortex core, PVC) and synchronized helical vortex structures. The dominant extrinsically excited coherent structures are axisymmetric, ring-shaped vortices.

In the present thesis, state-of-the-art optical measurement techniques and advanced analytical tools were employed. This combination allowed for a significantly improved insight into the mechanisms that cause the excitation and suppression of the PVC in reacting swirling combustor flows. Prior to the work of this thesis, only empirical correlations for the effect of combustion and axisymmetric structures on the PVC were reported. The developed analytical modeling allows for a fundamental understanding of the occurrence of the PVC. Moreover, it provides hints to improve the combustor design for increased flow stability and offers a means for physics-based flow control. The same applies to the presented modeling of the growth of axisymmetric structures in the swirling flow field. The advanced analytical tools can be employed in the combustor design process to predict the growth of axisymmetric vortices and choose the design that features the lowest amplification rates.

In the introduction, a series of questions (see Fig. 1.11) was presented. In the following, the main findings of the present thesis are summarized by briefly providing answers to these questions.

- *When does the PVC occur and why is it excited?*

The PVC is the manifestation of a globally unstable swirling flow field, and the global stability of the flow at reacting conditions is dominated by the flame shape, which de-

depends on the reactivity of the fuel-air(-steam) mixture. The most important properties of the flame were found to be its length and axial location. The influence of the flame on the global stability is via its influence on the time-averaged flow field and density field. In particular, the density field, caused by the heat release, can have a stabilizing effect on the flow field. The theoretical analysis of a globally unstable flow field yields a so-called wavemaker, which can be qualitatively interpreted as the pacemaker for the PVC. If the flame stabilizes far downstream of this wavemaker, the PVC is only marginally affected by the combustion. If the flame, in contrast to this, stabilizes close to the wavemaker and causes significant density stratification in its vicinity, the PVC is modified or completely suppressed. The suppression or modification of the PVC depends on the combination of density stratification and backflow in the flow field. If the flame is very short and completely located upstream of the wavemaker, the PVC can be established entirely in the region of burnt gases.

- *What is the role of the PVC for flame stabilization?*

The PVC was shown to strongly influence the heat release distribution and the mixing processes inside the combustor. When the PVC is excited, helical axial-radial eddies substantially increase the mixing between the jet and the inner recirculation zone. This leads to a significant cooling of the region close to the combustor inlet and, thereby, to a reduction of the reactivity of the mixture. Furthermore, the cooling leads to lower density gradients and, consequently, to an increased excitation of the PVC. The other way around, the suppression of the PVC leads to the suppression of the helical axial-radial eddies and, consequently, to weaker mixing. The resulting higher temperatures close to the combustor inlet increase the reactivity of the mixture, and the density gradients further inhibit the excitation of the PVC. In the presented cases, the detachment of the flame is related to an excitation of the PVC, which is suppressed when the flame is attached. The identified two way coupling between PVC and mixing causes a hysteresis during flame attachment and flame detachment.

- *How can the PVC be controlled?*

By the application of a low momentum (jet velocity is similar to bulk velocity), non-swirling axial jet on the centerline, the type of vortex breakdown inside a swirl-stabilized combustor can be successfully controlled. At high axial injection rates, the vortex breakdown type changes from the bubble type to the cone type. In this vortex breakdown state, the PVC, which present without axial injection, is completely suppressed, and a considerably weaker PVC located farther downstream and oscillating at a much lower frequency is excited. The modified flow field not only features a much weaker oscillation, but is also shown to provide an excellent basis for fuel-flexible combustor operation.

- *What determines the growth of axisymmetric coherent structures and what is their impact on the flame?*

Axisymmetric coherent structures usually appear as forced structures in the flow field when the combustor is operated at thermoacoustically unstable operating conditions.

The vortices interact with the flame and cause integral heat release fluctuations. Therefore, their growth essentially dominates the flame response to velocity perturbations. The growth of the vortices depends on the receptivity of the shear layers at the instability frequency. This receptivity can be analytically obtained from the time-averaged flow field, which is modified by the coherent structures themselves. At high oscillation amplitudes, this mean flow modification causes significantly lower amplification rates and, thus, a saturation of the axisymmetric coherent structures and the flame response.

- *How do the PVC and the axisymmetric structures interact?*

In practical combustion systems, the PVC and axisymmetric coherent structures frequently occur at the same time. Two different interaction mechanisms between the two types of coherent structures were found in the present thesis. Acoustic forcing modifies the time-averaged flow field and density field. Thereby, the global stability of the swirling flow field is changed and a naturally stable flow field can be destabilized or vice versa. The second interaction mechanism comprises the modulation of the linear growth rate and the eigenfrequency of a globally unstable flow field by the axisymmetric structures. In analogy to a parametrically excited oscillator, the effect of this modulation depends on the relation of the modulation frequency to the eigenfrequency. The PVC can be significantly damped by the axisymmetric structures or even amplified.



## Appendix A

# Influence of the Outlet Boundary Conditions on the Reacting Flow Field

<sup>5</sup>*During the design and testing process of swirl-stabilized combustors, it is often impractical to maintain identical outlet boundary conditions. Furthermore, it is a common practice to intentionally change the acoustic boundary conditions of the outlet in order to suppress thermoacoustic instabilities. In this appendix the susceptibility of the reacting flow field to downstream perturbations is assessed by the application of an area contraction at the outlet. Since combustion and fuel composition are shown to be important parameters for the influence of the boundary conditions on the flow field, highly steam-diluted flames are investigated in addition to dry flames at different equivalence ratios and degrees of swirl. The results reveal a clear correlation of the susceptibility of the flow field to downstream perturbations to both the inlet swirl number and the amount of dilatation caused by the flame. The concept of an effective swirl number downstream of the flame is applied to the results and is proven to be the dominating parameter. A theoretical explanation for the influence of this parameter is provided by the usage of the well-known theory of subcritical and supercritical swirling flows, where perturbations can propagate upstream solely in subcritical flows via standing waves. Knowledge of the flow state is of particular importance for the evaluation of combustion tests with differing exit boundary conditions and the results emphasize the need for realistic exit boundary conditions for numerical simulations.*

### A.1 Introduction

A typical combustor design and testing process involves several test facilities ranging from water tunnel facilities to multi-burner arrangements including atmospheric and pressurized combustion test rigs (e.g., Zajadatz et al., 2007; Schuermans et al., 2010). It is important

---

<sup>5</sup>The results presented in the present appendix were previously published in Terhaar et al. (2012). Bernhard Bobusch assisted during the LDV measurements.

that the results can be transferred from one stage to another. Naturally, the outlet boundary conditions cannot always be kept constant due to different test rig restrictions. Furthermore, in order to suppress self-excited thermoacoustic instabilities, it is common practice to intentionally change the acoustic outlet boundary conditions, for instance, by means of an area contraction (e.g, Kim et al., 2010; Mongia et al., 2003; Ćosić et al., 2012)).

The basic theory about the upstream effect of perturbations in swirling flows goes back to the work of Squire (1962) and Benjamin (1962) on vortex breakdown. Both used the approach of a cylindrical vortex flow with a superposed disturbance of small amplitude. If the mean flow field can sustain long inertia waves, perturbations can be transmitted upstream and the flow state is called subcritical. If the waves are swept downstream, the flow is termed supercritical and perturbations only affect the local flow. Both Squire and Benjamin related the phenomenon of vortex breakdown to a change from a supercritical to a subcritical flow state.

Escudier and Keller (1985) used the criticality theory to explain the different levels of influence of an area contraction at the outlet on the isothermal swirling flow field in a vortex tube at low and high swirl numbers. They assume that due to viscous effects, the subcritical flow after the vortex breakdown can either remain subcritical or recover to a supercritical state depending on the initial level of swirl and the length of the vortex tube. Carrying out LDA measurements in a water tunnel facility, they showed that for low levels of swirl, the application of an outlet area contraction has a negligible effect on the flow field. Hence, they assumed that the flow recovered to a supercritical flow state downstream of the vortex breakdown and before reaching the outlet. On the contrary, with high swirl, the application of an outlet area contraction led to significant changes within almost the entire flow field.

Regarding the transfer of their water tunnel results to the reacting flow field in a gas turbine combustor, they state that in practical situations, the flow typically returns to a supercritical state due to the combustion. That is, the axial velocity is accelerated sufficiently due to the higher temperatures and lower density downstream of the flame.

Hereby, they also explained the findings of Altgeld et al. (1983), who measured the flow field in a swirl-stabilized combustor and found that without combustion, negative velocities near the centerline arose at the combustor exit plane. This was not true for the reacting case. Escudier and Keller (1985) concluded that it is of fundamental importance for the combustion process whether the flow is subcritical or supercritical, and care must be taken when transferring cold flow results to the reacting conditions. Furthermore, they state that modifications of the outlet boundary conditions to prevent backflow (Altgeld et al., 1983) are questionable.

Li and Gutmark (2005) investigated the influence of an exhaust nozzle area contraction in a multi-swirl burner. At isothermal conditions they found that the amount of swirl determined whether the effect of the exhaust nozzle size was noticeable in the velocity field. At reacting conditions they measured emissions and the temperature field and found that, depending on the operating conditions, the influence of the exhaust nozzle either disappeared

or remained. In the latter case, the smaller exhaust nozzle led to higher  $\text{NO}_x$  emissions and a more heterogeneous temperature field.

The effect of combustion acceleration on confined swirling flows was more generally studied by Weber and Dugué (1992). One important finding of their work is that properties of the flow field, such as the reverse flow strength, depend on an effective swirl number, defined by the inlet swirl number and the ratio of the mean temperature downstream of the flame to the inlet air temperature, which is closely related to the density ratio upstream and downstream of the flame.

The density ratio in practical combustion systems mainly depends on the combustor inlet temperature, which is governed by the compressor pressure ratio, since the flame temperature is limited through  $\text{NO}_x$  regulations. Typical values of the density ratio in industrial heavy duty gas turbines, aeroengines, and aeroderivatives are in the range of 0.4 to 0.65 (Soares, 2007).

In atmospheric combustion tests, the air is not always preheated to the same temperatures as found in practical operation. Hence, the same amount of specific heat release (i.e., a similar temperature difference over the flame) leads to a significantly lower density ratio. For non-preheated combustion tests, this results in density ratios in the range of 0.15 to 0.35. For combustion tests at steam-diluted conditions, the inlet flow must be preheated in order to ensure stable combustion. Although near stoichiometric conditions are used, the temperature difference is comparable to dry lean combustion. As a result, the density ratios are significantly higher than for non-preheated or moderately preheated dry combustion.

The amount of initial swirl, as well as the presence of combustion, was shown to have a significant influence on the recovery of a subcritical flow to a supercritical flow state. Escudier and Keller (1985) altered the initial swirl number and Li and Gutmark (2005) changed the combustion conditions. Both found changes in the criticality of the flow. However, in each of the studies, only two flow configurations were investigated. No parametric studies have been reported to identify the critical configuration and the nature of the transition.

In the presented investigations, the temperature ratio over the flame is varied systematically for different swirl numbers under dry and steam-diluted conditions. At every operating condition, an area contraction at the outlet is applied and its influence on the flow field is measured. This influence is then used as an indicator for the upstream attenuation of a perturbation introduced into the flow field. For the investigated burner, several flame and flow field types were shown previously at different operating conditions (see Chapter 4). Furthermore, rapid transitions between the flow field types at the same operating conditions were encountered. Therefore, knowledge of the reacting flow field is needed in order to separate effects of the outlet boundary condition from the effects of combustion on the flow field.

The main idea of the present chapter is to quantify the effects of an area contraction on the reacting swirling flow field at different operating conditions and initial degrees of swirl. This is done by the introduction of two parameters that assess the upstream attenuation of the perturbation created by the area contraction at the outlet. A physical explanation for

the results is provided by the use of an effective swirl number and the well-known criticality theory.

The remainder of this chapter is structured as follows: First, the experimental approach and the investigated configuration are explained, and the effects of combustion, swirl number, and outlet contraction on the flow field are assessed. Subsequently, two parameters determining the effect of the outlet boundary conditions are introduced and the results of the parametric study are presented. Finally, the outcome of the parametric study is compared with good agreement to the results obtained by the application of a theoretical criterion derived by Benjamin (1962).

## A.2 Experimental Procedure

For the results presented in this chapter, the generic burner shown in Fig. 3.2a was used and the swirl number was adjusted between  $S = 0$  and  $S = 2$ . At the end of the 750 mm long, water cooled exhaust tube, an end orifice with a contraction ratio of 8:1 could be mounted in order to induce a perturbation into the swirling flow field. The application of the orifice resulted in an increased pressure in the combustor of about 1 mbar. The air was preheated and perfectly mixed with overheated steam upstream of the generic burner.

Radial profiles of the axial and tangential velocity were measured employing laser Doppler velocimetry (LDV). A two-component backscatter LDV system was mounted on a three-axis traverse system to measure the velocities at various axial and radial positions in the combustion chamber. The focal length of the LDV optics was set to 1000 mm, resulting in a spatial resolution of  $0.15 \text{ mm} \times 0.15 \text{ mm} \times 4 \text{ mm}$ . Reflections from the cylindrical surface of the combustion chamber inhibited measurements closer than 10-20 mm to the wall. Aluminum oxide particles with a nominal diameter of  $1 \mu\text{m}$  were seeded into the flow upstream of the swirl generator.

Deterioration of the silica glass at wet conditions and residuals of seeding particles at the wall limited the available measurement time. Therefore, only profiles of slightly more than half of the combustor flow were measured. This seemed sufficient as the mean flow is assumed to be axisymmetric.

Additionally, at selected operating conditions, particle image velocimetry (PIV) measurements at a horizontal plane containing the combustor axis were carried out. In contrast to the measurements presented in the previous chapters of this thesis, a low-speed, monoscopic PIV system (7 Hz), consisting of a 150 mJ per pulse Nd:YAG laser and one  $2048 \text{ px} \times 2048 \text{ px}$  CCD camera, was employed.

The images were processed with a final interrogation size of  $32 \text{ px} \times 32 \text{ px}$  and the interrogation window overlap was set to 50%, resulting in a vector spacing of 1.6 mm and a spatial resolution of 3.2 mm. The data was filtered for outliers and interpolated from adjacent interrogation areas.

Table A.1 gives an overview of the tested conditions. To calculate the density  $\rho_{\text{ad}}$  and temperature  $T_{\text{ad}}$  downstream of the flame, equilibrium conditions were calculated using Cantera



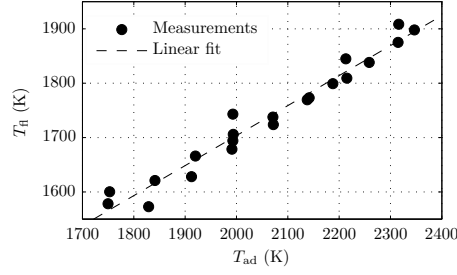


Figure A.1: Measured and calculated flame temperatures.

Table A.1: Combustor operating conditions.

Parameter	Velocity measurements	Emission measurements
$T_{in}$ in K	293-666	643
$S$	0.7-1.5	1.5
$\Omega$	0-0.3	0
$\phi$	0.41-0.94	0.45-0.75
$\rho_{fl}/\rho_{in}$	0.18-0.44	0.30-0.39
$Re$	22 000 - 38 500	22 000

and the GRI 3.0 mechanism (Smith et al., 2000). To account for heat losses into the combustor wall, temperature measurements using a suction pyrometer were carried out downstream of the reaction zone. The results, shown in Fig. A.1, reveal a simple correlation, which is valid in the investigated temperature range:

$$T_{fl} = 0.55T_{ad} + 600K. \quad (A.1)$$

This correlation is used to calculate the flame temperature  $T_{fl}$  in the remainder of this study. Details about the temperature measurements can be found in (Göke and Paschereit, 2013).

### A.3 Concept of an effective swirl number

The amount of swirl in the flow is defined by the swirl number, which is defined as the ratio of the axial flux of tangential momentum  $\dot{G}_{\Theta}$  to the axial flux of axial momentum  $\dot{G}_x$  normalized by a characteristic radius:

$$S = \frac{\dot{G}_{\Theta}}{R_b \dot{G}_x} = \frac{2\pi \int_0^{R_b} \rho W U r^2 dr}{R \cdot 2\pi \int_0^R \rho U^2 r dr}. \quad (A.2)$$

Here,  $R_b$  and  $R$  denote the burner outlet radius and the radius of the combustion chamber, respectively. Note, that the definition of  $\dot{G}_x$  does not account for the static pressure variation. The swirl number defined in Eqn. A.2 is also denoted as an alternative swirl number and was

found to be often of more physical meaning than the swirl number with the included pressure term (Weber and Dugué, 1992).

It has been observed that at combustion conditions, flow field parameters that depend on the swirl number, such as the size of the recirculation zones and the reverse flow strength, are similar to the parameters encountered at isothermal conditions and lower swirl numbers (e.g., Syred and Beér, 1974; Weber and Dugué, 1992). Escudier and Keller (1985) explained this decrease of effective swirl with the acceleration of the flow due to the density reduction over the flame. While the axial velocity of a particle passing the reaction zone is increased strongly, the angular momentum is almost conserved.

Sufficiently downstream of the reaction zone, temperature and density were found to be almost constant along a radial profile (Göke and Paschereit, 2013). If it is further assumed that the changes of the axial velocity due to combustion are dominated by a homogeneous acceleration over the flame ( $U \approx U_{\text{cold}} \rho_{\text{in}} / \rho_{\text{fl}}$ ), a simple relation for the inlet swirl number  $S$  and the effective swirl number  $S_{\text{eff}}$  downstream of the flame can be deduced from Eqn. A.2:

$$S_{\text{eff}} = \frac{2\pi \int_0^R \rho W \left( U_{\text{cold}} \frac{\rho_{\text{in}}}{\rho_{\text{fl}}} \right) r^2 dr}{R_b \cdot 2\pi \int_0^R \rho \left( U_{\text{cold}} \frac{\rho_{\text{in}}}{\rho_{\text{fl}}} \right)^2 r dr} = S \cdot \frac{\rho_{\text{fl}}}{\rho_{\text{in}}}. \quad (\text{A.3})$$

Here,  $\rho_{\text{fl}}/\rho_{\text{in}}$  denotes the density ratio obtained using the calculated flame temperature and the inlet temperature.

Note that the effective swirl number  $S_{\text{eff}}$  used in this study is based on a theoretical swirl number  $S$  at the burner outlet (Leuckel, 1967). When transferring it to other burners, the specific geometries, in particular the burner expansion ratio, must be accounted for.

The effective swirl number is shown in the presented work to be the dominating parameter for the susceptibility of the flow field to downstream perturbations.

## A.4 Results

### A.4.1 Isothermal Flow Field

Figures A.2 and A.3 depict the general effect of an outlet contraction on the isothermal flow field. In a region near the centerline, the direction of axial velocity changes from a homogeneous backflow to a flow in the forward direction. This leads to a change in the shape of the IRZ from a spherical to a V-shaped form. In the radial profiles measured at the downstream position ( $x/D_h = 10$ , Fig. A.3), in addition to the effects on the axial velocity near the centerline, it is evident that the maximum tangential velocity is considerably higher and the peak are shifts inwards.

These changes are accompanied by a significant increase in the turbulence level near the centerline. The velocity fluctuations are augmented in all three components but are particularly increased in the radial and tangential component. Hence, the two-dimensional turbulence in-

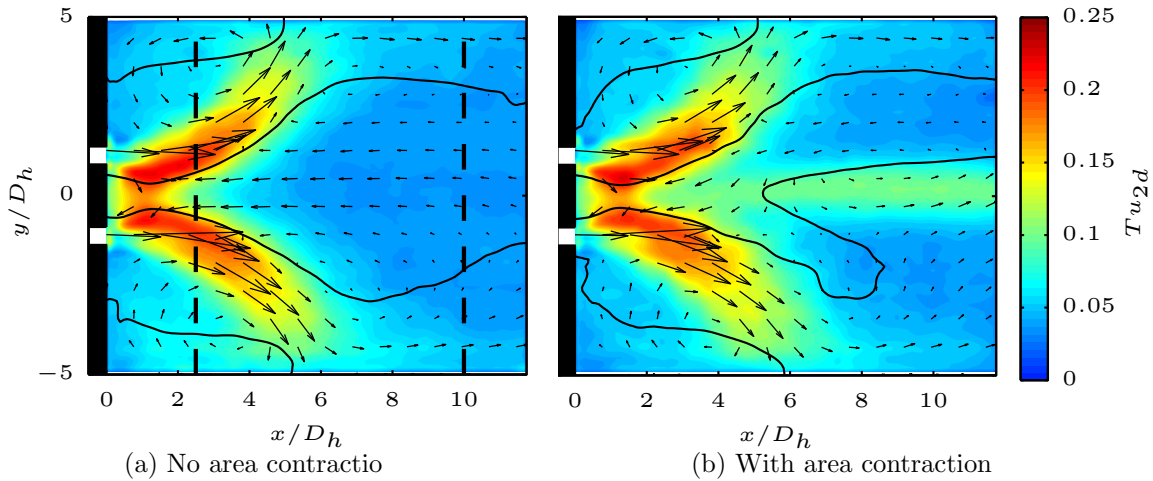


Figure A.2: Isothermal flow field at  $S = 0.7$  measured with PIV. Velocity vectors superimposed on the normalized turbulence intensity. Solid lines are isocontours of zero axial velocity. Dashed lines show measurement locations of LDV measurements.

tensity  $Tu_{2d}$  shown in Fig. A.2 somewhat underestimates the increase in turbulence intensity caused by the outlet contraction.

The higher turbulence near the centerline is believed to stem from the steeper gradient of the tangential velocity near the vortex center. Periodical and random movement of the core lead to higher fluctuations both in the measured radial and tangential velocities (Escudier et al., 2006). A similar general behavior has been described in literature (Escudier and Keller, 1985; Li and Gutmark, 2005; Escudier et al., 2006). For higher swirl numbers the mentioned effects become more pronounced and extend further upstream.

#### A.4.2 Reacting Flow Field

The reduction of the effective swirl intensity due to combustion can be observed in Fig. A.4. Velocity profiles for the highest measured swirl ( $S = 1.5$ ) at three operating conditions with different density ratios and, therefore, different accelerations of the flow due to heat release are shown. The velocities profiles are normalized by the combustor outlet velocity  $U_c$  (assuming the calculated flame temperatures). The tangential velocities are almost not affected by the acceleration, hence, a higher acceleration over the flame leads to lower normalized tangential velocities. This scaling can be observed very well by comparing the profiles of Fig. A.4 to profiles measured for different swirl numbers, but at the same operating conditions, as depicted in Fig. A.5. The profiles for the same swirl number but different density ratios show the same trends as the profiles for the same operating conditions but different swirl numbers. Note that, in contrast to Fig. A.4, the profiles depicted in Fig. A.5 are normalized with bulk velocity  $U_0$  at the combustor inlet.

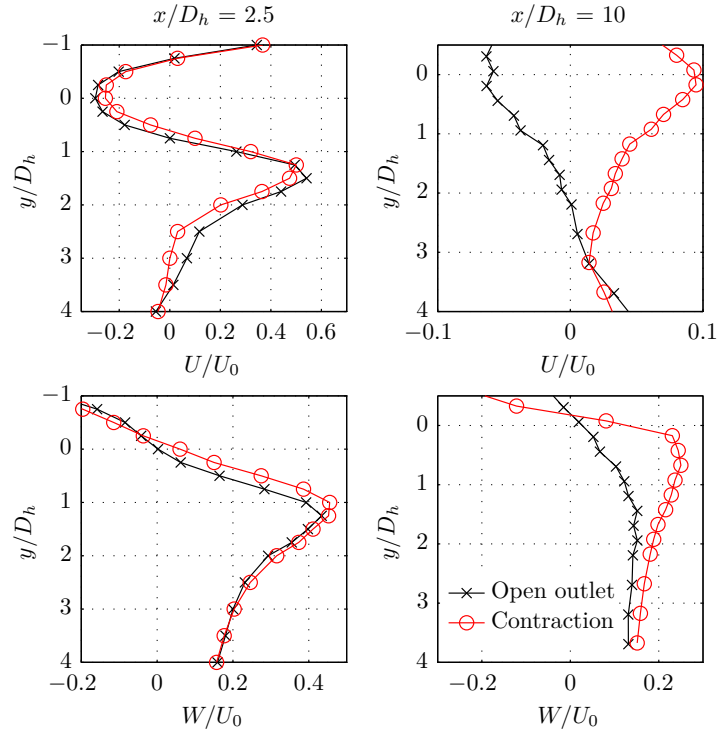


Figure A.3: Radial velocity profiles at isothermal conditions ( $S = 0.7$ ) with and without area contraction. Measured with LDV

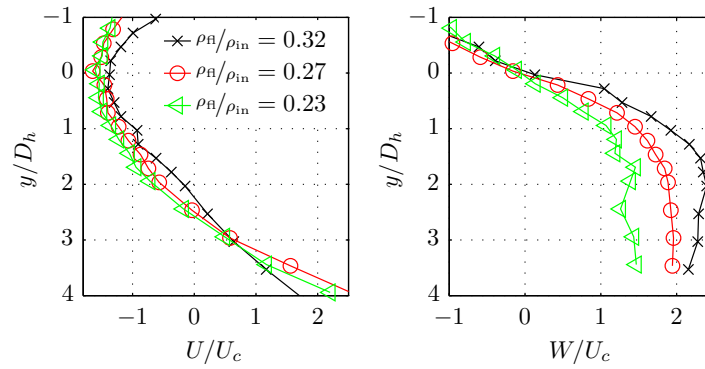


Figure A.4: Radial velocity profiles ( $x/D_h = 10$ ) at  $S = 1.5$  without area contraction at the outlet for 3 density ratios.

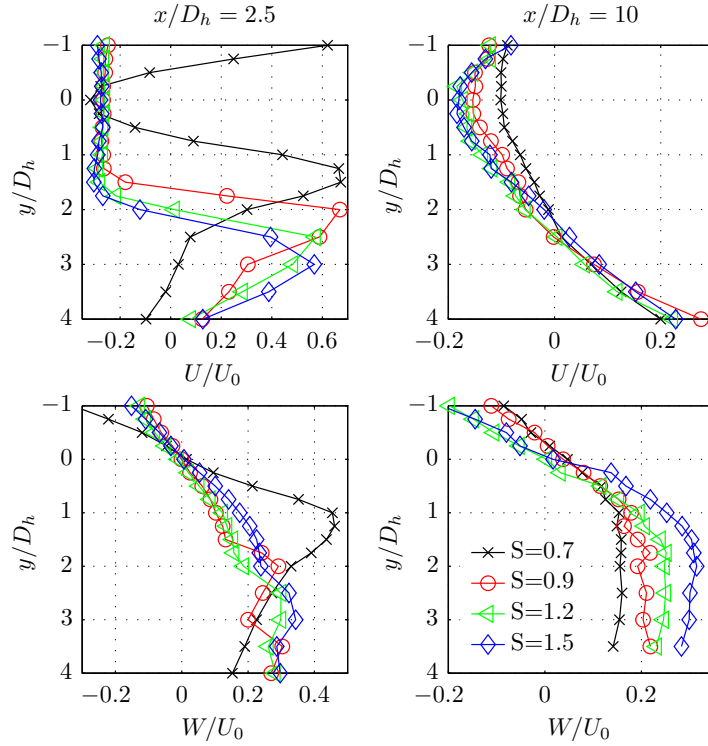


Figure A.5: Radial velocity profiles for various swirl numbers at combustion conditions ( $T_{\text{in}} = 527 \text{ K}$ ;  $\phi = 0.49$ ;  $\Omega = 0$ ) without area contraction.

#### A.4.3 Effect of outlet area contraction on the reacting flow field

Figure A.6 shows reacting flow fields for an inlet swirl number of  $S = 1.2$  and resulting effective swirl numbers of  $S_{\text{eff}} = 0.41$  and  $0.47$ . The deformation in the shape of the IRZ and the increase in the turbulence intensity near the centerline is evident at both conditions. However, they are more pronounced for the steam-diluted case ( $S_{\text{eff}} = 0.41$ ). Similar to the isothermal case, the increase in turbulence is likely to stem mainly from the steeper gradients of the tangential velocity component near the centerline.

A better insight into the influence of the outlet boundary condition on the flow field can be obtained by evaluating velocity profiles for differing outlet area contractions, as shown in Fig. A.7 and A.8. Radial profiles of axial and tangential velocities were measured for a high swirl number  $S = 1.5$  at two different operating conditions with high and low acceleration over the flame ( $\rho_{\text{fl}}/\rho_{\text{in}} = 0.19$  and  $0.35$ ,  $S_{\text{eff}} = 0.28$  and  $0.52$ , respectively). While the case with the high acceleration and the lower effective swirl number is not influenced by the area contraction, the case with low acceleration and the higher effective swirl number is significantly influenced. The effects of higher axial velocity near the centerline and an inwardly shifted higher peak of the tangential velocity, resulting in a steeper gradient, remain similar to the isothermal case.

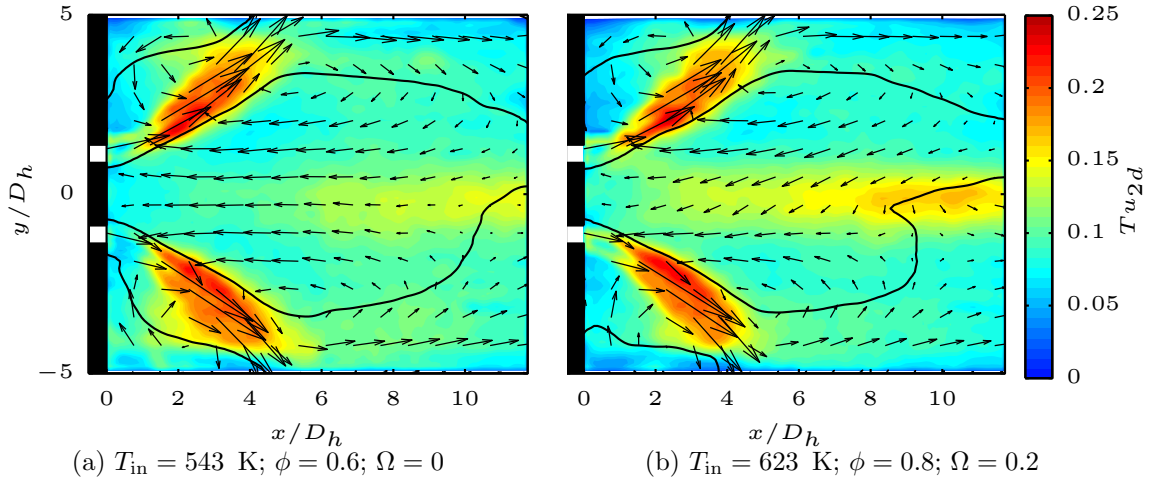


Figure A.6: Reacting flow fields at  $S = 1.2$  with area contraction. Solid lines are isocontours of zero axial velocity.

#### A.4.4 Parametric study

The results presented in Figs. A.6, A.7, and A.8 show the role of dilatation and inlet swirl number for the susceptibility of the flow field to downstream perturbations. An application of the criticality theory indicates that flow fields that show no influence of the outlet contraction must be of a supercritical flow state and flow fields that show an influence of the outlet contraction must be of a subcritical flow state. However, it can also be observed that the effect can be more or less pronounced depending on the operating conditions.

In order to quantitatively assess the effect of the outlet contraction on the velocity profiles, two parameters are introduced describing the most noticeable effects on the axial and tangential velocity. The first parameter  $p_x$  describes the excess axial velocity near the centerline caused by the acceleration of the flow passing through the area restriction. The second parameter  $p_\Theta$  describes the excess tangential velocity due to the constriction of the flow at the area contraction. Both parameters are calculated at the downstream position of  $x/D_h = 10$ , more than 850 mm upstream of the area contraction. By evaluating the parameters for different operating conditions, the upstream attenuation of the perturbation created at the area contraction, which is closely related to the criticality of the flow, can be quantitatively assessed.

$$p_x = \frac{1}{U_c} \int_{-0.5}^{0.5} (U_2 - U_1) \cdot d\left(\frac{x}{D_h}\right) \quad (\text{A.4})$$

$$p_\Theta = \frac{1}{\max(W_1)} \int_0^1 (W_2 - W_1) \cdot d\left(\frac{x}{D_h}\right) \quad (\text{A.5})$$

The subscripts 1 and 2 denote the undisturbed flow and the flow with a mounted area contraction, respectively. The parameters are normalized by the combustor outlet velocity  $U_c$  and the maximum swirl velocity of the undisturbed flow, respectively.

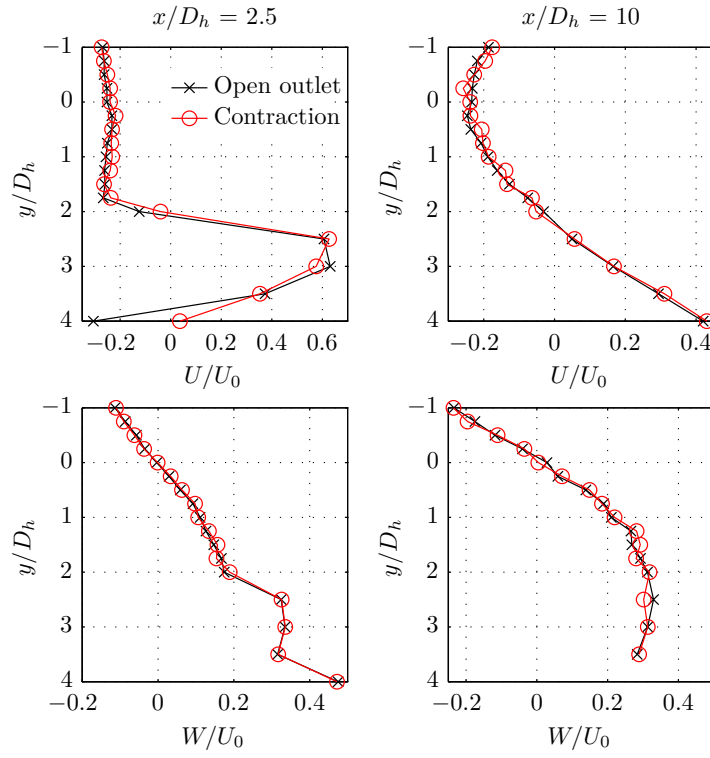


Figure A.7: Radial velocity profiles at  $S = 1.5$  for high acceleration due to heat release.

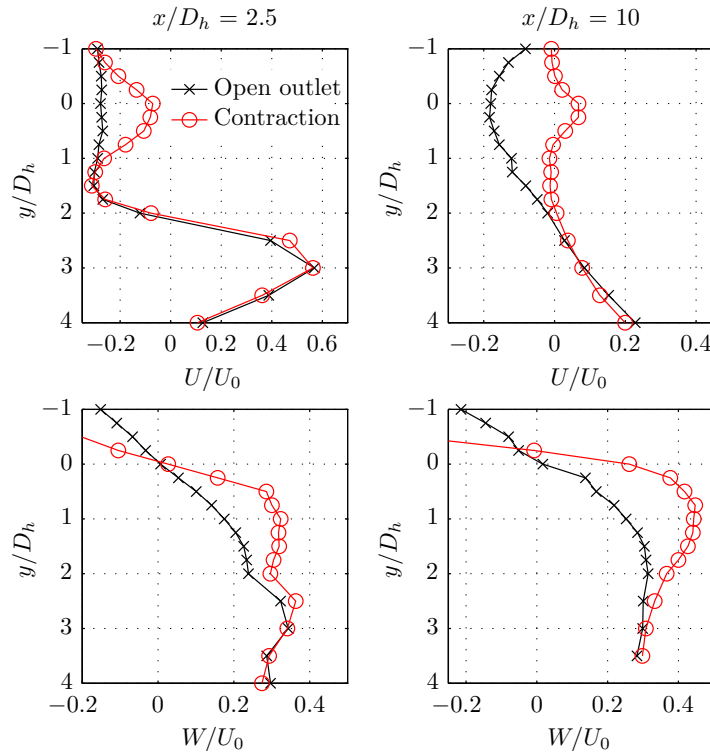


Figure A.8: Radial velocity profiles at  $S = 1.5$  for low acceleration due to heat release.

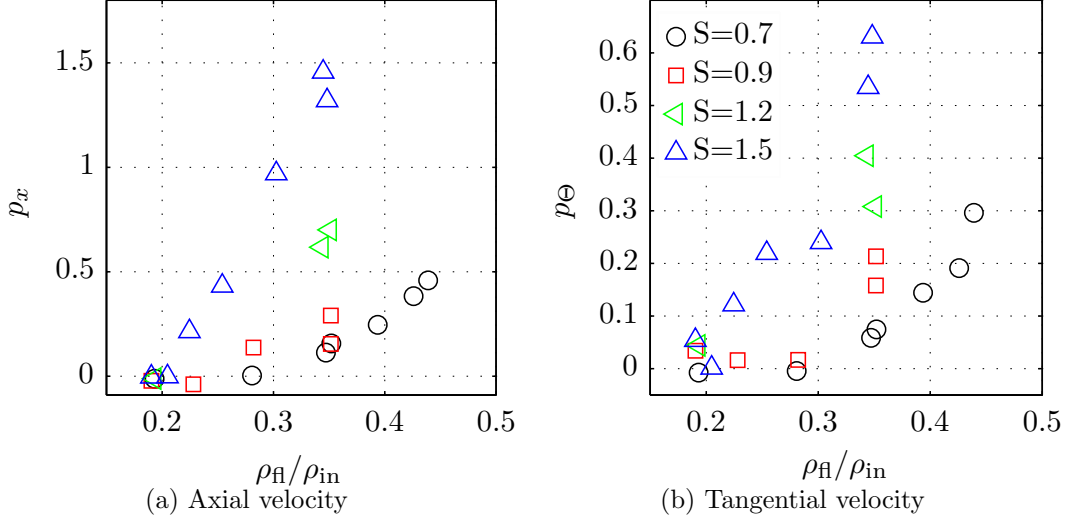


Figure A.9: Influence of the density ratio on the parameters  $p_x$  and  $p_\theta$  at different swirl numbers and combustor operating conditions.

It was observed during the measurements that for flow fields, showing a large influence of the area contraction ratio, the center of the vortex is slightly shifted from the centerline. This asymmetry, which can be also observed in Fig. A.2b, was reported previously by Escudier et al. (2006). To account for this when calculating  $p_\theta$ , the profile  $W_2$  is shifted so that  $W_2(x/D_h = 0) \equiv 0$ .

The influence of the inlet swirl number and the density ratio on the parameters  $p_x$  and  $p_\theta$  is shown in Fig. A.9. The expected trends can be observed: higher initial swirl numbers and higher density ratios (i.e., lower temperature ratios) lead to weaker attenuation of the downstream perturbation and, thus, higher values of  $p_x$  and  $p_\theta$ . For inlet swirl numbers of  $S = 0.7$  and  $S = 1.5$ , sufficient data is available to find that starting from a critical density ratio, the parameters increase almost linearly. The critical density ratio, however, depends on the amount of initial swirl. It is worth noting that Fig. A.9 and the following figures presenting the parameters  $p_x$  and  $p_\theta$  include dry measurements ( $\Omega = 0$ ) as well as highly steam-diluted measurements ( $\Omega = 0.3$ ).

The concept of the effective swirl number can be used to compare different inlet swirl numbers and different operating conditions. In Fig. A.10 the parameters  $p_x$  and  $p_\theta$  are shown as a function of the effective swirl number. It can be observed that the parameters match quite well for the different inlet swirl numbers. A linear regression of the parameter  $p_x$  that also fits reasonably well the isothermal measurements (not shown here) reveals the range of the critical effective swirl number ( $S_{eff} = 0.2$  to  $0.3$ ) at which the perturbation caused by the area contraction is fully attenuated at the measurement location. This critical effective swirl number is slightly lower for the low swirl case of  $S = 0.7$  than for  $S = 1.5$ . This is likely to stem from the different flow field shapes and flame shapes found at critical conditions for  $S = 0.7$  (detached flame) and  $S = 1.5$  (attached V-flame).



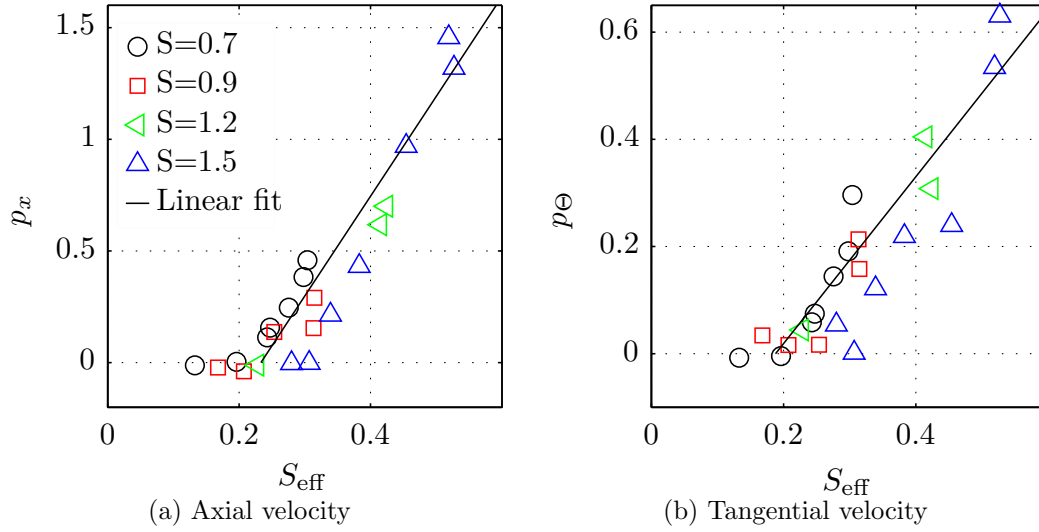


Figure A.10: Influence of the effective swirl number on the parameters  $p_x$  and  $p_\theta$  at different swirl numbers and combustor operating conditions.

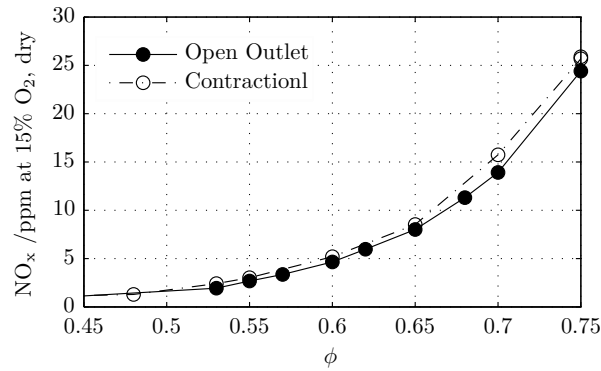


Figure A.11:  $\text{NO}_x$  emissions for premixed flames at subcritical conditions ( $S_{\text{eff}} = 0.45 - 0.58$ ).

In addition to the flow field measurements, an emission analysis was carried out for the operating conditions shown in Tab. 5.1. The results, presented in Fig. A.11, reveal that the  $\text{NO}_x$  emissions are not influenced significantly by the area contraction, even though the flow was clearly of a subcritical state ( $S_{\text{eff}} = 0.45 - 0.58$ ).

## A.5 Discussion

The results show that the upstream attenuation of a perturbation introduced at the outlet boundary condition depends on the effective swirl number after the flame. According to the results, a critical effective swirl number of  $S_{\text{eff}} = 0.2$  to  $S_{\text{eff}} = 0.3$  can be deduced. The flow field of detached flames seemed slightly more altered by the area contraction at the same effective swirl number.

The overall trend is in accordance to the criticality theory by Squire (1962) and Benjamin (1962) and the interpretation of Escudier and Keller (1985), in a way that higher axial velocities lead to supercritical flow states and higher tangential velocities lead to subcritical flow states where an upstream transport of perturbations is possible.

Both Squire and Benjamin developed criteria in order to test velocity profiles for their criticality. Squire provided a *rule of thumb* to compare the maximum tangential velocity to a constant axial velocity for three different vortex types. Li and Gutmark (2005) applied these rules replacing the constant axial velocity by the maximum axial velocity.

Leschziner and Hogg (1989) used a criterion based on Benjamin's work for an inviscid Rankine vortex to obtain the critical solid body rotational speed  $\omega_c$  for a given mean axial velocity  $U_c$ , combustion chamber diameter  $D_{cc}$ , and vortex radius  $r_a$ :

$$\frac{J_0\left(2\omega_c \frac{r_a}{U_c}\right)}{J_1\left(2\omega_c \frac{r_a}{U_c}\right)} = -\frac{r_a U_c}{\omega_c \left(\left(\frac{D_{cc}}{2}\right)^2 - r_a^2\right)}, \quad (\text{A.6})$$

where  $J_0$  and  $J_1$  denote Bessel functions of the first kind.

A solid body vortex with a rotational speed faster than the critical rotational speed  $\omega_c$  is considered to be subcritical and a slower rotating vortex is considered to be supercritical.

This criterion was applied to the measured velocities. As the assumption of a solid body vortex core is reasonably in line with the measured tangential velocity profiles at the downstream position ( $x/D_h = 10$ ), the vortex radius  $r_a$  and the actual solid body rotational speed  $\omega_m$  can be estimated with fair accuracy from the velocity data.

Hence, for every operating condition, a critical solid body rotational speed  $\omega_c$  can be obtained. The ratio of the estimated rotational speed to the critical solid body rotational speed can be introduced as the criticality factor  $\kappa$ .

$$\kappa = \frac{\omega_m}{\omega_c} \quad (\text{A.7})$$

Figure A.12 shows the criticality factor  $\kappa$  as a function of the effective swirl number  $S_{\text{eff}}$ . It can be observed that  $\kappa$  is close to unity for effective swirl numbers in the range of  $S_{\text{eff}} = 0.2$  to  $S_{\text{eff}} = 0.3$ . For very low effective swirl numbers, the supercritical state can be observed with values of  $\kappa$  smaller than unity. This matches the critical swirl number estimated from a linear regression of the parameters  $p_x$  and  $p_\Theta$  very well. Furthermore, it can be observed again that minor differences between the two flow field types of the low swirl number  $S = 0.7$  and the high swirl number  $S = 1.5$  exist.

The good correlation between the parameters  $p_x$  and  $p_\Theta$  and the criticality parameter  $\kappa$  can be observed in Fig. A.13b. For values of  $\kappa < 1$ , both  $p_x$  and  $p_\Theta$  remain constant near zero. Starting from  $\kappa = 1$ , both parameters grow almost linearly with  $\kappa$ . As  $\kappa$  already accounts for the changes in the flow field shape, no systematic differences between the low swirl number  $S = 0.7$  and the high swirl number  $S = 1.5$  can be observed.

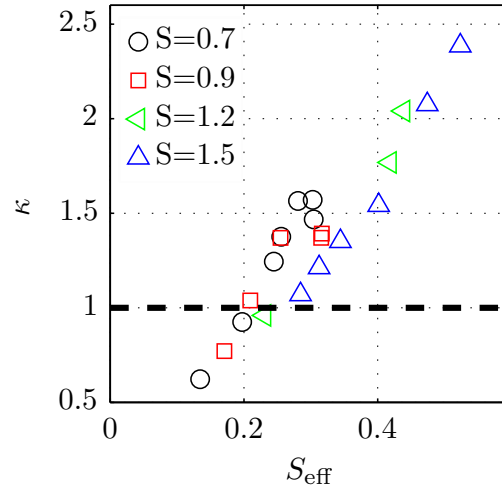


Figure A.12: Criticality parameter  $\kappa$  for different effective swirl numbers. Dashed line separates subcritical from supercritical flow.

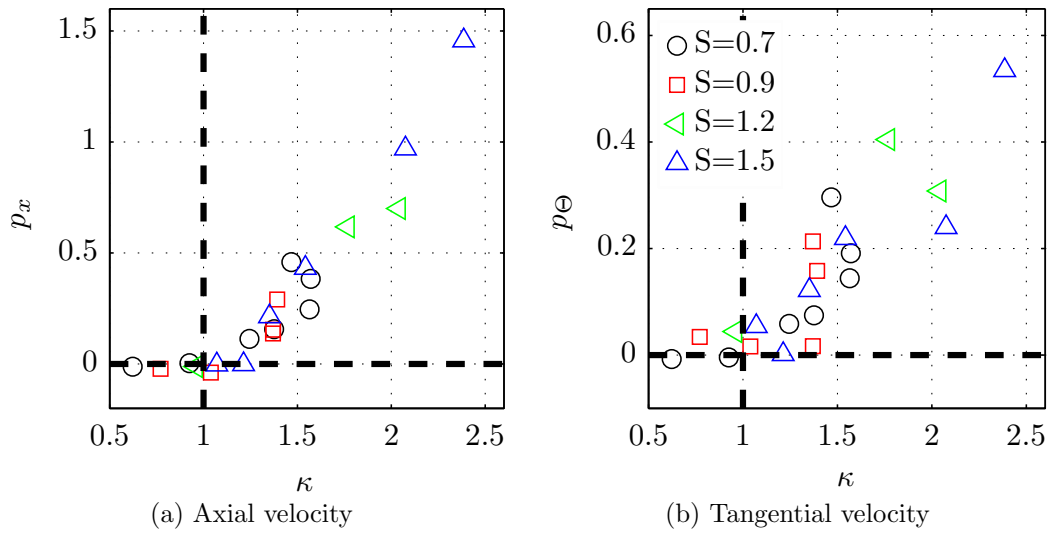


Figure A.13: Influence of the criticality parameter  $\kappa$  on  $p_x$  and  $p_\Theta$ .

Since  $\kappa$  can be calculated from single radial velocity profiles after the flame by application of Eqn. A.7, it can be used to predict whether or not the flow is subcritical and allows for the estimation of the influence of the outlet boundary condition on the flow field.

According to the criticality theory, the flow field is basically independent of the outlet boundary conditions if in the flow field between the measurement position (downstream of the flame) and the outlet, the flow recovers to a supercritical state at least once. Usually, this can be achieved due to viscous swirl attenuation and boundary layer growth. Under combustion conditions, heat loss to the exhaust tube must be further considered. Since the exhaust tube in the presented experiments is water cooled, it is assumed that the heat loss

effect increases the swirl number stronger than the weakening of the swirl due to viscous effects. Hence, the most supercritical position is assumed to be directly downstream or in the vicinity of the flame. This assumption seems to be valid since Fig. A.13b shows a very good dependence of the parameters  $p_x$  and  $p_\Theta$  on the effective swirl number  $S_{\text{eff}}$  (calculated with the flame temperature) and also on the criticality parameter  $\kappa$ . Even at subcritical conditions, an area contraction at the outlet had no significant influence on the measured  $\text{NO}_x$  emissions. This implies that from emission measurements of premixed flames only limited conclusions about the flow state can be drawn.

## A.6 Conclusions

Velocity measurements have been carried out in a swirl stabilized combustor for various swirl numbers and operating conditions including high rates of steam dilution. All measurements were conducted with an open outlet and an area contraction of 8:1. The qualitative effects on the velocity profiles, the shape of the IRZ and the turbulence distribution are the same as described by other authors. To quantitatively assess the upstream attenuation of the perturbation created at the outlet boundary condition, two parameters concerning the axial and tangential velocity distribution, respectively, were introduced.

To compare different inlet swirl numbers and combustor operating conditions, the concept of an effective swirl number was used and validated for the measured configurations. It was found that the susceptibility of the flow field to downstream perturbations mostly depends on this effective swirl number. When the effective swirl number was larger than a critical value of  $S_{\text{eff}} = 0.2$  to  $S_{\text{eff}} = 0.3$ , the parameters started to increase linearly. This linear behavior is valid for dry as well as for steam-diluted conditions.

A criticality criterion was applied to assess the criticality of the velocity profiles measured at the downstream position. The results of the analysis yield a critical effective swirl number of  $S_{\text{eff}} = 0.2$  to  $S_{\text{eff}} = 0.3$ , which matched very well with the results obtained from the parametric study.

For moderately preheated laboratory flames with low swirl numbers (that still ensure vortex breakdown), the outlet boundary conditions are of minor importance for the flow field. However, for well preheated very lean or highly diluted flames, such as steam-diluted flames, much higher effective swirl numbers are possible.

It is, therefore, of importance to be aware of the flow state and the outlet boundary conditions when comparing measurement results obtained on different test rigs or when changing the outlet boundary conditions in order to suppress thermoacoustic instabilities. Furthermore, it is known that the quality of numerical simulations depends significantly on the validity of the boundary conditions. However, the application of adequate subcritical outlet boundary conditions is still challenging (Leschziner and Hogg, 1989; Escudier et al., 2006) and due to limitations of the domain size, it is often impractical to simulate the entire flow field up to a state where the flow eventually recovers to a supercritical flow state.

No significant influence of an area contraction on the  $\text{NO}_x$  emissions was found for technically premixed flames.

If the swirl number is defined adequately and the burner geometry, in particular the burner expansion ratio, is taken into account, the usage of the effective swirl number, which is defined by the inlet swirl number and the operating conditions, allows for an estimation of whether the outlet boundary conditions have a significant effect on the flow field or may be neglected.



# Bibliography

- Acharya, V. S., Shin, D.-H., and Lieuwen, T. (2013). Premixed Flames Excited by Helical Disturbances: Flame Wrinkling and Heat Release Oscillations. *Journal of Propulsion and Power*, 29(6):1282–1291, doi: 10.2514/1.B34883.
- Adrian, R. J., Christensen, K. T., and Liu, Z.-C. (2000). Analysis and interpretation of instantaneous turbulent velocity fields. *Experiments in Fluids*, 29:275–290, doi: 10.1007/s003489900087.
- Altgeld, H., Jones, W., and Wilhelmi, J. (1983). Velocity measurements in a confined swirl driven recirculating flow. *Experiments in Fluids*, 1(2):73–78, doi: 10.1007/BF00266258.
- Anacleto, P. M., Fernandes, E. C., Heitor, M. V., and Shtork, S. I. (2002). Characterization of a strong swirling flow with precessing vortex core based on measurements of velocity and local pressure fluctuations. In *11th International Symposium on Application of Laser Techniques to Fluid Mechanics*.
- Baker, R., Hutchinson, P., Khalil, E., and Whitelaw, J. (1975). Measurements of three velocity components in a model furnace with and without combustion. *Symposium (International) on Combustion*, 15(1):553–559, doi: 10.1016/S0082-0784(75)80327-4.
- Balachandran, R., Ayoola, B. O., Kaminski, C. F., Dowling, A. P., and Mastorakos, E. (2005). Experimental investigation of the nonlinear response of turbulent premixed flames to imposed inlet velocity oscillations. *Combustion and Flame*, 143(1-2):37–55, doi: 10.1016/j.combustflame.2005.04.009.
- Barkley, D. (2006). Linear analysis of the cylinder wake mean flow. *Europhysics Letters (EPL)*, 75(5):750–756, doi: 10.1209/epl/i2006-10168-7.
- Bellows, B. D., Bobba, M. K., Seitzman, J. M., and Lieuwen, T. (2007). Nonlinear Flame Transfer Function Characteristics in a Swirl-Stabilized Combustor. *Journal of Engineering for Gas Turbines and Power*, 129(4):954–961, doi: 10.1115/1.2720545.
- Bender, C. and Büchner, H. (2005). Noise Emissions From a Premixed Swirl Combustor. In *Twelfth International Congress on Sound and Vibration, Lisbon, Portugal*.
- Benjamin, T. (1962). Theory of the vortex breakdown phenomenon. *Journal of Fluid Mechanics*, 14(04):593–629, doi: 10.1017/S0022112062001482.
- Berkooz, G., Holmes, P., and Lumley, J. L. (1993). The Proper Orthogonal Decomposition in the Analysis of Turbulent Flows. *Annual Review of Fluid Mechanics*, 25(1):539–575, doi: 10.1146/annurev.fl.25.010193.002543.

- Billant, P., Chomaz, J.-M., and Huerre, P. (1998). Experimental study of vortex breakdown in swirling jets. *Journal of Fluid Mechanics*, 376:183–219, doi: 10.1017/S0022112098002870.
- Boxx, I., Arndt, C. M., Carter, C. D., and Meier, W. (2010a). High-speed laser diagnostics for the study of flame dynamics in a lean premixed gas turbine model combustor. *Experiments in Fluids*, 52(3):555–567, doi: 10.1007/s00348-010-1022-x.
- Boxx, I., Stöhr, M., Carter, C. D., and Meier, W. (2009). Sustained multi-kHz flamefront and 3-component velocity-field measurements for the study of turbulent flames. *Applied Physics B*, 95(1):23–29, doi: 10.1007/s00340-009-3420-4.
- Boxx, I., Stöhr, M., Carter, C. D., and Meier, W. (2010b). Temporally resolved planar measurements of transient phenomena in a partially pre-mixed swirl flame in a gas turbine model combustor. *Combustion and Flame*, 157(8):1510–1525, doi: 10.1016/j.combustflame.2009.12.015.
- Briggs, R. (1964). *Electron-stream interaction with plasmas*. MIT Press, Cambridge, Massachusetts.
- Burke, M. P., Chaos, M., Ju, Y., Dryer, F. L., and Klippenstein, S. J. (2012). Comprehensive H<sub>2</sub>/O<sub>2</sub> kinetic model for high-pressure combustion. *International Journal of Chemical Kinetics*, 44(7):444–474, doi: 10.1002/kin.20603.
- Burmberger, S., Hirsch, C., and Sattelmayer, T. (2006). Designing a Radial Swirler Vortex Breakdown Burner. In *Proceedings of ASME Turbo Expo 2006 Power for Land, Sea and Air May 8-11, 2006, Barcelona, Spain*, ASME Paper: GT2006-90497. doi: 10.1115/GT2006-90497.
- Burmberger, S. and Sattelmayer, T. (2011). Optimization of the Aerodynamic Flame Stabilization for Fuel Flexible Gas Turbine Premix Burners. *Journal of Engineering for Gas Turbines and Power*, 133(10):101501, doi: 10.1115/1.4003164.
- Chigier, N. A. and Beer, J. M. (1964). Velocity and Static-Pressure Distributions in Swirling Air Jets Issuing From Annular and Divergent Nozzles. *Journal of Fluids Engineering*, 86(4):778–796, doi: 10.1115/1.3655954.
- Chomaz, J.-M. (2005). Global Instabilities in Spatially Developing Flows: Non-Normality and Nonlinearity. *Annual Review of Fluid Mechanics*, 37(1):357–392, doi: 10.1146/annurev.fluid.37.061903.175810.
- Chomaz, J.-M., Huerre, P., and Redekopp, L. (1988). Bifurcations to Local and Global Modes in Spatially Developing Flows. *Physical Review Letters*, 60(1):25–28, doi: 10.1103/PhysRevLett.60.25.
- Chomaz, J.-M., Huerre, P., and Redekopp, L. G. (1991). A frequency selection criterion in spatially developing flows. *Studies in Applied Mathematics*, 84:119–144.
- Coats, C. (1996). Coherent Structures in Combustion. *Progress in Energy and Combustion Science*, 22:427–509, doi: 10.1016/S0360-1285(96)00011-1.



- Cook, M. V. (2007). *Flight Dynamic Principles: A Linear Systems Approach to Aircraft Stability and Control Elsevier aerospace engineering series*. Butterworth-Heinemann, 3rd edition.
- Ćosić, B., Bobusch, B. C., Moeck, J. P., and Paschereit, C. O. (2012). Open-Loop Control of Combustion Instabilities and the Role of the Flame Response to Two-Frequency Forcing. *Journal of Engineering for Gas Turbines and Power*, 134(6):061502, doi: 10.1115/1.4005986.
- Ćosić, B., Moeck, J. P., and Paschereit, C. O. (2013). Nonlinear Instability Analysis for Partially Premixed Swirl Flames. *Combustion Science and Technology*, 186:713–736, doi: 10.1080/00102202.2013.876420.
- Ćosić, B., Terhaar, S., Moeck, J. P., and Paschereit, C. O. (2014). Response of a swirl-stabilized flame to simultaneous perturbations in equivalence ratio and velocity at high oscillation amplitudes. *Combustion and Flame*, in press, doi: 10.1016/j.combustflame.2014.09.025.
- Deans, S. R. (2007). *The Radon transform and some of its applications*. Dover, New York.
- Delbende, I., Chomaz, J.-M., and Huerre, P. (1998). Absolute/convective instabilities in the Batchelor vortex: a numerical study of the linear impulse response. *Journal of Fluid Mechanics*, 355:229–254, doi: 10.1017/S0022112097007787.
- Dolan, B., Villalva, R., Munday, D., Zink, G., Pack, S., and Gutmark, E. J. (2014). Flame Dynamics in a Multi-Nozzle Staged Combustor During High Power Operation. In *Proceedings of ASME Turbo Expo 2014, June 16-20, 2014, Düsseldorf, Germany*, ASME Paper GT2014-26164, pages 1–16. ASME, doi: 10.1115/GT2014-26164.
- Dowling, A. P. (1997). Nonlinear self-excited oscillations of a ducted flame. *Journal of fluid mechanics*, 346:271–290, doi: 10.1017/S0022112097006484.
- Drake, M. C. and Pitz, R. W. (1985). Comparison of turbulent diffusion flame measurements of OH by planar fluorescence and saturated fluorescence. *Experiments in Fluids*, 292:283–292, doi: 10.1007/BF00281776.
- Dunham, D., Spencer, A., McGuirk, J. J., and Dianat, M. (2009). Comparison of Unsteady Reynolds Averaged Navier–Stokes and Large Eddy Simulation Computational Fluid Dynamics Methodologies for Air Swirl Fuel Injectors. *Journal of Engineering for Gas Turbines and Power*, 131(1):011502, doi: 10.1115/1.2969096.
- Durox, D., Schuller, T., Noiray, N., and Candel, S. (2009). Experimental analysis of nonlinear flame transfer functions for different flame geometries. *Proceedings of the Combustion Institute*, 32(1):1391–1398, doi: 10.1016/j.proci.2008.06.204.
- Duwig, C., Ducruix, S., and Veynante, D. (2012). Studying the Stabilization Dynamics of Swirling Partially Premixed Flames by Proper Orthogonal Decomposition. *Journal of Engineering for Gas Turbines and Power*, 134(10):101501, doi: 10.1115/1.4007013.

- Emerson, B., O'Connor, J., Juniper, M. P., and Lieuwen, T. (2012). Density ratio effects on reacting bluff-body flow field characteristics. *Journal of Fluid Mechanics*, 706:219–250, doi: 10.1017/jfm.2012.248.
- Escudier, M. P. and Keller, J. J. (1985). Recirculation in swirling flow - A manifestation of vortex breakdown. *AIAA Journal*, 23(1):111–116, doi: 10.2514/3.8878.
- Escudier, M. P., Nickson, A. K., and Poole, R. J. (2006). Influence of outlet geometry on strongly swirling turbulent flow through a circular tube. *Physics of Fluids*, 18(12):125103, doi: 10.1063/1.2400075.
- Escudier, M. P. and Zehnder, N. (1982). Vortex-flow regimes. *Journal of Fluid Mechanics*, 115:105–121, doi: 10.1017/S0022112082000676.
- Findeisen, J., Gnirß, M., Damaschke, N., Schiffer, H.-P., and Tropea, C. (2005). 2D – Concentration Measurements Based on Mie Scattering using a Commercial PIV system. In *6th International Symposium on Particle Image Velocimetry, Pasadena, California, USA, September 21-23, 2005*.
- Freund, O., Schaefer, P., Rehder, H.-J., and Roehle, I. (2011). Experimental Investigations on Cooling Air Ejection at a Straight Turbine Cascade Using PIV and QLS. In *Proceedings of ASME Turbo Expo 2011, June 6-10, 2011, Vancouver, Canada*, ASME Paper GT2011-45296. doi: 10.1115/GT2011-45296.
- Froud, D., O'Doherty, T., and Syred, N. (1995). Phase Averaging of the Precessing Vortex Core in a Swirl Burner under Piloted and Premixed Combustion Conditions. *Combustion and Flame*, 100(3):407–412, doi: 10.1016/0010-2180(94)00167-Q.
- Gallaire, F. and Chomaz, J.-M. (2003). Mode selection in swirling jet experiments: a linear stability analysis. *Journal of Fluid Mechanics*, 494:223–253, doi: 10.1017/S0022112003006104.
- Gallaire, F., Ruith, M. R., Meiburg, E., Chomaz, J.-M., and Huerre, P. (2006). Spiral vortex breakdown as a global mode. *Journal of Fluid Mechanics*, 549:71–90, doi: 10.1017/S0022112005007834.
- Galley, D., Ducruix, S., Lacas, F., and Veynante, D. (2011). Mixing and stabilization study of a partially premixed swirling flame using laser induced fluorescence. *Combustion and Flame*, 158(1):155–171, doi: 10.1016/j.combustflame.2010.08.004.
- García-Villalba, M. and Fröhlich, J. (2006). LES of a free annular swirling jet - Dependence of coherent structures on a pilot jet and the level of swirl. *International Journal of Heat and Fluid Flow*, 27(5):911–923, doi: 10.1016/j.ijheatfluidflow.2006.03.015.
- García-Villalba, M., Fröhlich, J., and Rodi, W. (2007). Numerical Simulations of Isothermal Flow in a Swirl Burner. *Journal of Engineering for Gas Turbines and Power*, 129(2):377, doi: 10.1115/1.2364198.
- Gianetti, F. and Luchini, P. (2007). Structural sensitivity of the first instability of the cylinder wake. *Journal of Fluid Mechanics*, 581:167, doi: 10.1017/S0022112007005654.

- Giauque, A., Selle, L., Gicquel, L. Y., Poinso, T., Buechner, H., Kaufmann, P., and Krebs, W. (2005). System identification of a large-scale swirled partially premixed combustor using LES and measurements. *Journal of Turbulence*, 6:N21, doi: 10.1080/14685240512331391985.
- Göckeler, K., Terhaar, S., and Paschereit, C. O. (2013). Residence Time Distribution in a Swirling Flow at Nonreacting, Reacting, and Steam-Diluted Conditions. *Journal of Engineering for Gas Turbines and Power*, 136(041505):1–9, doi: 10.1115/1.4026000.
- Göke, S. (2012). *Ultra Wet Combustion: An Experimental and Numerical Study*. PhD thesis, TU Berlin.
- Göke, S. and Paschereit, C. O. (2013). Influence of Steam Dilution on Nitrogen Oxide Formation in Premixed Methane/Hydrogen Flames. *Journal of Propulsion and Power*, 29(1):249–260, doi: 10.2514/1.B34577.
- Göke, S., Terhaar, S., Schimek, S., Göckeler, K., and Paschereit, C. O. (2011). Combustion of Natural Gas, Hydrogen and Bio-Fuels at Ultra-Wet Conditions. In *Proceedings of ASME Turbo Expo 2011, June 6-10, 2011, Vancouver, Canada*, ASME Paper, GT2011-45696. doi: 10.1115/GT2011-45696.
- Goodwin, D. G. (2003). An Open Source, Extensible Software Suite for CVD Process Simulation. In *Proceedings of CVD XVI and EuroCVD Fourteen*.
- Güthe, F. and Schuermans, B. (2007). Phase-locking in post-processing for pulsating flames. *Measurement Science and Technology*, 18(9):3036–3042, doi: 10.1088/0957-0233/18/9/039.
- Hall, M. G. (1972). Vortex Breakdown. *Annual Review of Fluid Mechanics*, 4(1):195–218, doi: 10.1146/annurev.fl.04.010172.001211.
- Hermeth, S., Staffelbach, G. M., Gicquel, L. Y., and Poinso, T. (2014). Bistable flame stabilization in swirled flames and influence on flame transfer functions. *Combustion and Flame*, 161:184–196, doi: 10.1016/j.combustflame.2013.07.02.
- Huerre, P. and Monkewitz, P. A. (1990). Local and Global Instabilities in Spatially Developing Fluids. *Annual Review of Fluid Mechanics*, 22:473–537, doi: 10.1146/annurev.fl.22.010190.002353.
- ITTC (2008). Uncertainty Analysis Particle Imaging Velocimetry. In *ITTC - Recommended Procedures and Guidelines*, 7.5-01-03-03, pages 1–12.
- Iudiciani, P. and Duwig, C. (2011). Large Eddy Simulation of the Sensitivity of Vortex Breakdown and Flame Stabilisation to Axial Forcing. *Flow, Turbulence and Combustion*, 86(3-4):639–666, doi: 10.1007/s10494-011-9327-2.
- Ivanova, E., Noll, B. E., and Aigner, M. (2012). A Numerical Study on the Turbulent Schmidt Numbers in a Jet in Crossflow. *Journal of Engineering for Gas Turbines and Power*, 135(1):011505, doi: 10.1115/1.4007374.
- Ji, J. and Gore, J. (2002). Flow structure in lean premixed swirling combustion. *Proceedings of the Combustion Institute*, 29(1):861–867, doi: 10.1016/S1540-7489(02)80110-9.

- Jochmann, P., Sinigersky, A., Koch, R., and Bauer, H.-J. (2005). URANS Prediction of Flow Instabilities of a Novel Atomizer. In *Proceedings of ASME Turbo Expo 2005 Power for Land, Sea and Air June 6-9, 2005, Reno-Tahoe, Nevada, USA*, ASME Paper: GT2005-68072. doi:10.1115/GT2005-68072.
- Jones, J. P. (1964). On the explanation of vortex breakdown. In *IUTAM Symposium on vortex motion, Ann Arbor*.
- Juniper, M. P. (2006). The effect of confinement on the stability of two-dimensional shear flows. *Journal of Fluid Mechanics*, 565:171, doi:10.1017/S0022112006001558.
- Juniper, M. P. (2012). Absolute and Convective Instability in Gas Turbine Fuel Injectors. In *Proceedings of ASME Turbo Expo 2012, June 11-15, 2012, Copenhagen, Denmark*, ASME Paper GT-2012-68253, pages 1–10. doi:10.1115/GT2012-68253.
- Juniper, M. P. and Pier, B. (2014). The structural sensitivity of open shear flows calculated with a local stability analysis. *European Journal of Mechanics - B/Fluids*, doi:10.1016/j.euromechflu.2014.05.011.
- Juniper, M. P., Tammisola, O., and Lundell, F. (2011). The local and global stability of confined planar wakes at intermediate Reynolds number. *Journal of Fluid Mechanics*, 686:218–238, doi:10.1017/jfm.2011.324.
- Keller, J. J. (1995). Thermoacoustic oscillations in combustion chambers of gas turbines. *AIAA journal*, 33(12):2280–2287, doi:10.2514/3.12980.
- Khalil, S., Hourigan, K., and Thompson, M. C. (2006). Response of unconfined vortex breakdown to axial pulsing. *Physics of Fluids*, 18(3):038102, doi:10.1063/1.2180290.
- Khorrami, M., Malik, M., and Ash, R. (1989). Application of spectral collocation techniques to the stability of swirling flows. *Journal of Computational Physics*, 81(1):206–229, doi:10.1016/0021-9991(89)90071-5.
- Kim, K. T., Lee, J. G., Quay, B. D., and Santavicca, D. A. (2010). Spatially distributed flame transfer functions for predicting combustion dynamics in lean premixed gas turbine combustors. *Combustion and Flame*, 157(9):1718–1730, doi:10.1016/j.combustflame.2010.04.016.
- Kolář, V. (2007). Vortex identification: New requirements and limitations. *International Journal of Heat and Fluid Flow*, 28(4):638–652, doi:10.1016/j.ijheatfluidflow.2007.03.004.
- Konle, M., Kiesewetter, F., and Sattelmayer, T. (2007). Simultaneous high repetition rate PIV-LIF-measurements of CIVB driven flashback. *Experiments in Fluids*, 44(4):529–538, doi:10.1007/s00348-007-0411-2.
- Kröner, M., Fritz, J., and Sattelmayer, T. (2003). Flashback Limits for Combustion Induced Vortex Breakdown in a Swirl Burner. *Journal of Engineering for Gas Turbines and Power*, 125(3):693, doi:10.1115/1.1582498.
- Krüger, O., Duwig, C., Terhaar, S., and Paschereit, C. O. (2013). Large Eddy Simulations of Hydrogen Oxidation at Ultra-Wet Conditions in a Model Gas Turbine Combustor Applying

- Detailed Chemistry. *Journal of Engineering for Gas Turbines and Power*, 135(2):1–10, doi: 10.1115/1.4007718.
- Kuenne, G., Ketelheun, A., and Janicka, J. (2011). LES modeling of premixed combustion using a thickened flame approach coupled with FGM tabulated chemistry. *Combustion and Flame*, 158(9):1750–1767, doi: 10.1016/j.combustflame.2011.01.005.
- Lacarelle, A. (2011). *Modeling, control, and optimization of fuel / air mixing in a lean premixed swirl combustor using fuel staging to reduce pressure pulsations and NOx emissions*. PhD thesis, TU Berlin.
- Lacarelle, A., Faustmann, T., Greenblatt, D., Paschereit, C. O., Lehmann, O., Luchtenburg, D. M., and Noack, B. R. (2009). Spatiotemporal Characterization of a Conical Swirler Flow Field Under Strong Forcing. *Journal of Engineering for Gas Turbines and Power*, 131(3):031504, doi: 10.1115/1.2982139.
- Lambourne, N. C. and Bryer, D. W. (1961). The Bursting of Leading-Edge Vortices—Some Observations and Discussion of the Phenomenon. *Aeronautical Research Council Reports and Memoranda*, 3282:1–35.
- Lawson, N. J. and Wu, J. (1997). Three-dimensional particle image velocimetry: experimental error analysis of a digital angular stereoscopic system. *Measurement Science and Technology*, 1455:1455–1464, doi: 10.1088/0957-0233/8/12/009.
- Leibovich, S. (1978). The Structure of Vortex Breakdown. *Annual Review of Fluid Mechanics*, 10(1):221–246, doi: 10.1146/annurev.fl.10.010178.001253.
- Leibovich, S. (1984). Vortex stability and breakdown - Survey and extension. *AIAA Journal*, 22(9):1192–1206, doi: 10.2514/3.8761.
- Leschziner, M. A. and Hogg, S. (1989). Computation of highly swirling confined flow with a Reynolds stress turbulence model. *AIAA Journal*, 27(1):57–63, doi: 10.2514/3.10094.
- Lesshafft, L. and Huerre, P. (2007). Linear impulse response in hot round jets. *Physics of Fluids*, 19(2):024102, doi: 10.1063/1.2437238.
- Leuckel, W. (1967). Swirl intensities, swirl types and energy losses of different swirl generating devices. *IFRF Doc. Nr. G 2/a/16*, 2:1–53.
- Li, G. and Gutmark, E. J. (2005). Effect of exhaust nozzle geometry on combustor flow field and combustion characteristics. *Proceedings of the Combustion Institute*, 30(2):2893–2901, doi: 10.1016/j.proci.2004.08.189.
- Li, Z. S., Li, B., Sun, Z. W., Bai, X. S., and Aldén, M. (2010). Turbulence and combustion interaction: High resolution local flame front structure visualization using simultaneous single-shot PLIF imaging of CH, OH, and CH<sub>2</sub>O in a piloted premixed jet flame. *Combustion and Flame*, 157(6):1087–1096, doi: 10.1016/j.combustflame.2010.02.017.
- Liang, H. and Maxworthy, T. (2005). An experimental investigation of swirling jets. *Journal of Fluid Mechanics*, 525:115–159, doi: 10.1017/S0022112004002629.

- Lieuwen, T., McDonell, V., Petersen, E., and Santavicca, D. A. (2008). Fuel Flexibility Influences on Premixed Combustor Blowout, Flashback, Autoignition, and Stability. *Journal of Engineering for Gas Turbines and Power*, 130(1):011506, doi: 10.1115/1.2771243.
- Lieuwen, T. and Yang, V. (2005). *Combustion Instabilities in Gas Turbine Engines: Operational Experience, Fundamental Mechanisms, and Modeling*, volume 210 of *Progress in Astronautics and Aeronautics*. American Institute of Aeronautics and Astronautics, Reston and Va.
- Lilley, D. G. (1977). Swirl Flows in Combustion : A Review. *AIAA Journal*, 15(8), doi: 10.2514/3.60756.
- Lucca-Negro, O. and O'Doherty, T. (2001). Vortex breakdown: a review. *Progress in Energy and Combustion Science*, 27(4):431–481, doi: 10.1016/S0360-1285(00)00022-8.
- Meier, W., Boxx, I., Stöhr, M., and Carter, C. D. (2010). Laser-based investigations in gas turbine model combustors. *Experiments in Fluids*, 49(4):865–882, doi: 10.1007/s00348-010-0889-x.
- Meliga, P., Gallaire, F., and Chomaz, J.-M. (2012). A weakly nonlinear mechanism for mode selection in swirling jets. *Journal of Fluid Mechanics*, 699:216–262, doi: 10.1017/jfm.2012.93.
- Michalke, A. (1965). On spatially growing disturbances in an inviscid shear layer. *Journal of Fluid Mechanics*, 23(03):521–544, doi: 10.1017/S0022112065001520.
- Moeck, J. P., Bourgooin, J.-F., Durox, D., Schuller, T., and Candel, S. (2012). Nonlinear interaction between a precessing vortex core and acoustic oscillations in a turbulent swirling flame. *Combustion and Flame*, 159(8):2650–2668, doi: 10.1016/j.combustflame.2012.04.002.
- Moeck, J. P., Bourgooin, J.-F., Durox, D., Schuller, T., and Candel, S. (2013). Tomographic reconstruction of heat release rate perturbations induced by helical modes in turbulent swirl flames. *Experiments in Fluids*, 54(1498):1–17, doi: 10.1007/s00348-013-1498-2.
- Mongia, H. C., Held, T. J., Hsiao, G. C., and Pandalai, R. P. (2003). Challenges and progress in controlling dynamics in gas turbine combustors. *Journal of Propulsion and Power*, 19(5):822–829, doi: 10.2514/2.6197.
- Monkewitz, P. A. (1988). The absolute and convective nature of instability in two-dimensional wakes at low Reynolds numbers. *Physics of Fluids*, 31:999, doi: 10.1063/1.866720.
- Monkewitz, P. A. and Sohn, K. (1988). Absolute instability in hot jets. *AIAA Journal*, 26(8):911–916, doi: 10.2514/3.9990.
- Nitsche, W. and Brunn, A. (2006). *Strömungsmesstechnik*. Springer Berlin Heidelberg New York, 2nd edition.
- Oberleithner, K., Paschereit, C. O., Seele, R., and Wygnanski, I. J. (2012a). Formation of Turbulent Vortex Breakdown: Intermittency, Criticality, and Global Instability. *AIAA Journal*, 50(7):1437–1452, doi: 10.2514/1.J050642.

- Oberleithner, K., Paschereit, C. O., and Wygnanski, I. J. (2014). On the impact of swirl on the growth of coherent structures. *Journal of Fluid Mechanics*, 741:156–199, doi: 10.1017/jfm.2013.669.
- Oberleithner, K., Schimek, S., and Paschereit, C. O. (2012b). On The Impact of Shear Flow Instabilities on Global Heat Release Rate Fluctuations: Linear Stability Analysis of an Isothermal and a Reacting Swirling Jet. In *Proceedings of ASME Turbo Expo 2012, June 11-15, 2012, Copenhagen, Denmark*, ASME Paper GT2012-69774. doi: 10.1115/GT2012-69774.
- Oberleithner, K., Sieber, M., Nayeri, C. N., Paschereit, C. O., Petz, C., Hege, H.-C., Noack, B. R., and Wygnanski, I. J. (2011). Three-dimensional coherent structures in a swirling jet undergoing vortex breakdown: stability analysis and empirical mode construction. *Journal of Fluid Mechanics*, 679:383–414, doi: 10.1017/jfm.2011.141.
- Oberleithner, K., Terhaar, S., Rukes, L., and Paschereit, C. O. (2013). Why Non-Uniform Density Suppresses the Precessing Vortex Core. *Journal of Engineering for Gas Turbines and Power*, 135(121506):1–9, doi: 10.1115/1.4025130.
- Oertel, H. and Delfs, J. (2005). *Strömungsmechanische Instabilitäten*. Universitätsverlag, Karlsruhe.
- Palies, P., Durox, D., Schuller, T., and Candel, S. (2011). Nonlinear combustion instability analysis based on the flame describing function applied to turbulent premixed swirling flames. *Combustion and Flame*, 158(10):1980–1991, doi: 10.1016/j.combustflame.2011.02.012.
- Paredes, P., Hermanns, M., Le Clainche, S., and Theofilis, V. (2013). Order 10E4 speedup in global linear instability analysis using matrix formation. *Computer Methods in Applied Mechanics and Engineering*, 253:287–304, doi: 10.1016/j.cma.2012.09.014.
- Paschereit, C. O., Gutmark, E. J., and Weisenstein, W. (1999). Coherent structures in swirling flows and their role in acoustic combustion control. *Physics of Fluids*, 11(9):2667–2678, doi: 10.1063/1.870128.
- Paschereit, C. O., Gutmark, E. J., and Weisenstein, W. (2000). Excitation of thermoacoustic instabilities by interaction of acoustics and unstable swirling flow. *AIAA Journal*, 38(6):1025–1034, doi: 10.2514/2.1063.
- Paschereit, C. O., Schuermans, B., Polifke, W., and Mattson, O. (2002). Measurement of Transfer Matrices and Source Terms of Premixed Flames. *Journal of Engineering for Gas Turbines and Power*, 124(2):239–247, doi: 10.1115/1.1383255.
- Pier, B. (2002). On the frequency selection of finite-amplitude vortex shedding in the cylinder wake. *Journal of Fluid Mechanics*, 458:407–417, doi: 10.1017/S0022112002008054.
- Pier, B. (2003). Open-loop control of absolutely unstable domains. *Proceedings of the Royal Society A: Mathematical, Physical and Engineering Sciences*, 459(2033):1105–1115, doi: 10.1098/rspa.2002.1086.

- Pier, B. (2008). Local and global instabilities in the wake of a sphere. *Journal of Fluid Mechanics*, 603:39–61, doi: 10.1017/S0022112008000736.
- Provansal, M., Mathis, C., and Boyer, L. (1987). Benard-von Kármán instability: transient and forced regimes. *Journal of Fluid Mechanics*, 182:1–22, doi: 10.1017/S0022112087002222.
- Raffel, M., Willert, C. E., Wereley, S. T., and Kopenhans, J. (2007). *PIV - A Practical Guide*. Springer Berlin Heidelberg New York, 2nd edition.
- Rajaratnam, N. (1976). *Turbulent Jets (Vol.5 of Developments in Water Science)*. Elsevier Scientific Publishing Co., Amsterdam.
- Rayleigh, J. W. S. (1878). The Explanation of Certain Acoustical Phenomena. *Nature*, 18(455):319–321, doi: 10.1038/018319a0.
- Reau, N. and Tumin, A. (2002). On harmonic perturbations in a turbulent mixing layer. *European Journal of Mechanics - B/Fluids*, 21(2):143–155, doi: 10.1016/S0997-7546(01)01170-0.
- Rees, S. J. (2009). *Hydrodynamic instability of confined jets & wakes & implications for gas turbine fuel injectors*. Phd thesis, University of Cambridge.
- Reichel, T. G., Terhaar, S., and Paschereit, C. O. (2013). Flow Field Manipulation by Axial Air Injection to Achieve Flashback Resistance and its Impact on Mixing Quality. In *Proceedings of 43rd AIAA Fluid Dynamics Conference and Exhibit 24 - 27 June 2013, San Diego, CA*. American Institute of Aeronautics and Astronautics, doi: 10.2514/6.2013-2603.
- Reichel, T. G., Terhaar, S., and Paschereit, C. O. (2014). Increasing Flashback Resistance in Lean Premixed Swirl-Stabilized Hydrogen Combustion by Axial Air Injection. *Journal of Engineering for Gas Turbines and Power*, doi: 10.1115/1.4029119.
- Reynolds, W. C. and Hussain, A. K. M. F. (1972). The mechanics of an organized wave in turbulent shear flow. Part 3. Theoretical models and comparisons with experiments. *Journal of Fluid Mechanics*, 54(02):263–288, doi: 10.1017/S0022112072000679.
- Roehle, I., Schodl, R., Voigt, P., and Willert, C. E. (2000). Recent developments and applications of quantitative laser light sheet measuring techniques in turbomachinery components. *Measurement Science and Technology*, 11(7):1023–1035, doi: 10.1088/0957-0233/11/7/317.
- Roux, S., Lartigue, G., Poinso, T., Meier, U., and Bérat, C. (2005). Studies of mean and unsteady flow in a swirled combustor using experiments, acoustic analysis, and large eddy simulations. *Combustion and Flame*, 141(1-2):40–54, doi: 10.1016/j.combustflame.2004.12.007.
- Ruith, M. R., Chen, P., Meiburg, E., and Maxworthy, T. (2003). Three-dimensional vortex breakdown in swirling jets and wakes: direct numerical simulation. *Journal of Fluid Mechanics*, 486:331–378, doi: 10.1017/S0022112003004749.
- Sadanandan, R., Stöhr, M., and Meier, W. (2008). Simultaneous OH-PLIF and PIV measurements in a gas turbine model combustor. *Applied Physics B*, 90(3-4):609–618, doi: 10.1007/s00340-007-2928-8.



- Samarasinghe, J., Peluso, S., Szedlmayer, M., De Rosa, A., Quay, B. D., and Santavicca, D. A. (2013). Three-Dimensional Chemiluminescence Imaging of Unforced and Forced Swirl-Stabilized Flames in a Lean Premixed Multi-Nozzle Can Combustor. *Journal of Engineering for Gas Turbines and Power*, 135(10):1–7, doi:10.1115/1.4024987.
- Schadow, K. C. and Gutmark, E. J. (1992). Combustion instability related to vortex shedding in dump combustors and their passive control. *Progress in Energy and Combustion Science*, 18(2):117–132, doi:10.1016/0360-1285(92)90020-2.
- Schimek, S., Göke, S., Schrödinger, C., and Paschereit, C. O. (2012a). Flame Transer Measurements with CH<sub>4</sub> and H<sub>2</sub> Fuel Mixtures at Ultra Wet Conditions in a Swirl Stabilized Premixed Combustor. In *Proceedings of ASME Turbo Expo 2012, June 11-15, 2012, Copenhagen, Denmark*, ASME Paper GT2012-69788. doi:10.1115/GT2012-69788.
- Schimek, S., Moeck, J. P., Čosić, B., Terhaar, S., and Paschereit, C. O. (2012b). Amplitude-dependent Flowfield and Flame Response to Axial and Tangential Velocity Fluctuations. In *Proceedings of ASME Turbo Expo 2012, June 11-15, 2012, Copenhagen, Denmark*, ASME Paper GT2012-69785. doi:10.1115/GT2012-69785.
- Schimek, S., Moeck, J. P., and Paschereit, C. O. (2009). Design of a combustion test rig with high amplitude forcing capabilities for nonlinear flame transfer function. In *Proceedings of the 16th International Congress on Sound and Vibration, Krakow, Poland*.
- Schmid, P. J. (2010). Dynamic mode decomposition of numerical and experimental data. *Journal of Fluid Mechanics*, 656:5–28, doi:10.1017/S0022112010001217.
- Schuermans, B., Güthe, F., Pennell, D., Guyot, D., and Paschereit, C. O. (2010). Thermoacoustic Modeling of a Gas Turbine Using Transfer Functions Measured Under Full Engine Pressure. *Journal of Engineering for Gas Turbines and Power*, 132(11):111503, doi:10.1115/1.4000854.
- Sevilla, A. and Martínez-Bazán, C. (2004). Vortex shedding in high Reynolds number axisymmetric bluff-body wakes: Local linear instability and global bleed control. *Physics of Fluids*, 16(9):3460–3469, doi:10.1063/1.1773071.
- Smith, G. P., Golden, D. M., Frenklach, M., Moriarty, N. W., Eiteneer, B., Goldenberg, M., Bowman, C. T., Hanson, R. K., Song, S., Gardiner, W. C., Lissianski, V. V., and Qin, Z. (2000). GRI-Mech 3.0. [http://www.me.berkeley.edu/gri\\_mech/](http://www.me.berkeley.edu/gri_mech/).
- Soares, C. (2007). *Gas Turbines: A Handbook of Air, Land and Sea Applications*. Butterworth Heinemann.
- Soteriou, M. C. and Ghoniem, A. F. (1995). Effects of the free-stream density ratio on free and forced spatially developing shear layers. *Physics of Fluids*, 7(8):2036, doi:10.1063/1.868451.
- Spencer, A., McQuirk, J. J., and Midgley, K. (2008). Vortex Breakdown in Swirling Fuel Injector Flows. *Journal of Engineering for Gas Turbines and Power*, 130(2):021503, doi:10.1115/1.2799530.
- Squire, H. (1962). Analysis of the Vortex Breakdown Phenomenon. Part I. In *Miszellaneen der Angewandten Mechanik*, pages 306–312. Akademie Verlag Berlin.

- Steinberg, A. M., Boxx, I., Stöhr, M., Arndt, C. M., Meier, W., and Campbell, D. (2011). Influence of flow-structure dynamics on thermo-acoustic instabilities in oscillating swirl flames. In *47th AIAA/ASME/SAE/ASEE Joint Propulsion Conference and Exhibit, San Diego, California, July 31-3, 2011*, AIAA 2011-5554.
- Steinberg, A. M., Boxx, I., Stöhr, M., Carter, C. D., and Meier, W. (2010). Flow-flame interactions causing acoustically coupled heat release fluctuations in a thermo-acoustically unstable gas turbine model combustor. *Combustion and Flame*, 157(12):2250–2266, doi: 10.1016/j.combustflame.2010.07.011.
- Stöhr, M., Boxx, I., Carter, C. D., and Meier, W. (2011a). Dynamics of lean blowout of a swirl-stabilized flame in a gas turbine model combustor. *Proceedings of the Combustion Institute*, 33(2):2953–2960, doi: 10.1016/j.proci.2010.06.103.
- Stöhr, M., Boxx, I., Carter, C. D., and Meier, W. (2012). Experimental study of vortex-flame interaction in a gas turbine model combustor. *Combustion and Flame*, 159(8):2636–2649, doi: 10.1016/j.combustflame.2012.03.020.
- Stöhr, M. and Meier, W. (2007). Investigation of a Periodic Combustion Instability in a Swirl Burner Using Phase-Resolved PIV. In *Proceedings of the European Combustion Meeting*.
- Stöhr, M., Sadanandan, R., and Meier, W. (2009). Experimental study of unsteady flame structures of an oscillating swirl flame in a gas turbine model combustor. *Proceedings of the Combustion Institute*, 32(2):2925–2932, doi: 10.1016/j.proci.2008.05.086.
- Stöhr, M., Sadanandan, R., and Meier, W. (2011b). Phase-resolved characterization of vortex-flame interaction in a turbulent swirl flame. *Experiments in Fluids*, 51(4):1153–1167, doi: 10.1007/s00348-011-1134-y.
- Strangfeld, C., Göckeler, K., Terhaar, S., and Paschereit, C. O. (2011). 3D Visualisation of Measured Coherent Structures in a Swirling Water Flow. In *Proceedings of Lasermethoden in der Strömungsmesstechnik, 6.-8. September 2011, Ilmenau, Germany*.
- Syred, N. (2006). A review of oscillation mechanisms and the role of the precessing vortex core (PVC) in swirl combustion systems. *Progress in Energy and Combustion Science*, 32(2):93–161, doi: 10.1016/j.pecs.2005.10.002.
- Syred, N. and Beér, J. M. (1974). Combustion in swirling flows: A review. *Combustion and Flame*, 23(2):143–201, doi: 10.1016/0010-2180(74)90057-1.
- Terhaar, S., Bobusch, B. C., and Paschereit, C. O. (2012). Effects of Outlet Boundary Conditions on the Reacting Flow Field in a Swirl-Stabilized Burner at Dry and Humid Conditions. *Journal of Engineering for Gas Turbines and Power*, 134:111501, doi: 10.1115/1.4007165.
- Terhaar, S., Čosić, B., Paschereit, C. O., and Oberleithner, K. (2014a). Impact of Shear Flow Instabilities on the Magnitude and Saturation of the Flame Response. *Journal of Engineering for Gas Turbines and Power*, 136(071502):1–9, doi: 10.1115/1.4026530.
- Terhaar, S., Göckeler, K., Schimek, S., Göke, S., and Paschereit, C. O. (2011). Non-Reacting and Reacting Flow in a Swirl-Stabilized Burner for Ultra-Wet Combustion. In *Proceedings*

- of 41st AIAA Fluid Dynamics Conference and Exhibit 27 - 30 June 2011, Honolulu, Hawaii, AIAA Paper, 2011-3584. doi: 10.2514/6.2011-3584.
- Terhaar, S., Krüger, O., and Paschereit, C. O. (2015a). Flow Field and Flame Dynamics of Swirling Methane and Hydrogen Flames at Dry and Steam-Diluted Conditions. *Journal of Engineering for Gas Turbines and Power*, 137:041503, doi: 10.1115/1.4028392.
- Terhaar, S., Oberleithner, K., and Paschereit, C. O. (2014b). Impact of Steam Dilution on the Flame Shape and Coherent Structures in Swirl-Stabilized Combustors. *Combustion Science and Technology*, 186:889–911, doi: 10.1080/00102202.2014.890597.
- Terhaar, S., Oberleithner, K., and Paschereit, C. O. (2015b). Key parameters governing the precessing vortex core in reacting flows: An experimental and analytical study. *Proceedings of the Combustion Institute*, 35(3):3347–3354, doi: 10.1016/j.proci.2014.07.035.
- Terhaar, S., Paredes, P., Oberleithner, K., Theofilis, V., and Paschereit, C. O. (2014c). Investigation of the global mode in swirling combustor flows: experimental observations and local and global stability analysis. In *IUTAM ABCM Symposium on Laminar Turbulent Transition, Rio de Janeiro, Brazil, September 8-12, 2014*.
- Terhaar, S., Reichel, T. G., Schrödinger, C., Rukes, L., Oberleithner, K., and Paschereit, C. O. (2015c). Vortex Breakdown Types and Global Modes in Swirling Combustor Flows with Axial Injection. *Journal of Propulsion and Power*, 31(1):219–229, doi: 10.2514/1.B35217.
- Theofilis, V. (2003). Advances in global linear instability analysis of nonparallel and three-dimensional flows. *Progress in Aerospace Sciences*, 39(4):249–315, doi: 10.1016/S0376-0421(02)00030-1.
- Theofilis, V. (2011). Global Linear Instability. *Annual Review of Fluid Mechanics*, 43(1):319–352, doi: 10.1146/annurev-fluid-122109-160705.
- Thiria, B., Bouchet, G., and Wesfreid, J. E. (2007). On the relation between linear stability analysis and mean flow properties in wakes. *APS Letter*, APS/123-QE:1–11.
- Thummuluru, S. and Lieuwen, T. (2009). Characterization of acoustically forced swirl flame dynamics. *Proceedings of the Combustion Institute*, 32(2):2893–2900, doi: 10.1016/j.proci.2008.05.037.
- Tropea, C., Yarin, A. L., and Foss, J. F., editors (2007). *Springer Handbook of Experimental Fluid Mechanics*. Springer Berlin Heidelberg New York.
- Tummers, M. J., Hubner, A., Vanveen, E., Hanjalic, K., and Vandermeer, T. (2009). Hysteresis and transition in swirling nonpremixed flames. *Combustion and Flame*, 156(2):447–459, doi: 10.1016/j.combustflame.2008.10.027.
- Vanoverberghe, K. P., Van Den Bulck, E. V., and Tummers, M. J. (2003a). Confined annular swirling jet combustion. *Combustion Science and Technology*, 175(3):545–578, doi: 10.1080/00102200390123863.

- Vanoverberghe, K. P., Van den Bulck, E. V., Tummers, M. J., and Hübner, W. A. (2003b). Multiflame Patterns in Swirl-Driven Partially Premixed Natural Gas Combustion. *Journal of Engineering for Gas Turbines and Power*, 125(1):40, doi:10.1115/1.1520159.
- Voigt, P., Schodl, R., and Griebel, P. (1997). Using the Laser Light Sheet Technique in Combustion Research. In *Proc. 90th Symp. of AGARD-PEP on Advanced Non-intrusive Instrumentation for Propulsion Engines 1997*.
- Weber, R. and Dugué, J. (1992). Combustion accelerated swirling flows in high confinements. *Progress in Energy and Combustion Science*, 18(4):349–367, doi:10.1016/0360-1285(92)90005-L.
- Wicksall, D. M., Agrawal, A. K., Schefer, R. W., and Keller, J. O. (2005a). Influence of Hydrogen Addition on Flow Structure in Confined Swirling Methane Flame. *Journal of Propulsion and Power*, 21(1):16–24, doi:10.2514/1.4235.
- Wicksall, D. M., Agrawal, A. K., Schefer, R. W., and Keller, J. O. (2005b). The interaction of flame and flow field in a lean premixed swirl-stabilized combustor operated on H/CH/air. *Proceedings of the Combustion Institute*, 30(2):2875–2883, doi:10.1016/j.proci.2004.07.021.
- Wille, R. (1960). *Advances in Applied Mechanics Volume 6*. Academic Press.
- Willert, C. E., Hassa, C., Stockhausen, G., Jarius, M., Voges, M., and Klinner, J. (2006). Combined PIV and DGV applied to a pressurized gas turbine combustion facility. *Measurement Science and Technology*, 17(7):1670–1679, doi:10.1088/0957-0233/17/7/005.
- Williams, F. A. (2000). Progress in knowledge of flamelet structure and extinction. *Progress in Energy and Combustion Science*, 26(4-6):657–682, doi:10.1016/S0360-1285(00)00012-5.
- Zajadatz, M., Lachner, R., Bernero, S., Motz, C., and Flohr, P. (2007). Development and Design of Alstom’s Staged Fuel Gas Injection EV Burner for NOX Reduction. In *Proceedings of ASME Turbo Expo 2007 Power for Land, Sea and Air, May 14-17, 2007, Montreal Canada*, ASME Paper, GT2007-27730. doi:10.1115/GT2007-27730.
- Zeldovich, J. (1946). The Oxidation of Nitrogen in Combustion and Explosions. *Acta Physicochimica*, 21(4):577–628.